



HAL
open science

Innovative optical methods using fiber bundles for two-photon all-optical brain studies

Antonio Lorca Cámara

► **To cite this version:**

Antonio Lorca Cámara. Innovative optical methods using fiber bundles for two-photon all-optical brain studies. *Neurons and Cognition [q-bio.NC]*. Sorbonne Université, 2023. English. NNT : 2023SORUS563 . tel-04515008

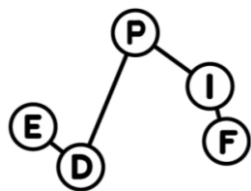
HAL Id: tel-04515008

<https://theses.hal.science/tel-04515008>

Submitted on 21 Mar 2024

HAL is a multi-disciplinary open access archive for the deposit and dissemination of scientific research documents, whether they are published or not. The documents may come from teaching and research institutions in France or abroad, or from public or private research centers.

L'archive ouverte pluridisciplinaire **HAL**, est destinée au dépôt et à la diffusion de documents scientifiques de niveau recherche, publiés ou non, émanant des établissements d'enseignement et de recherche français ou étrangers, des laboratoires publics ou privés.



THÈSE DE DOCTORAT DE SORBONNE UNIVERSITÉ

École doctorale 564 - Physique en Île-de-France

Préparée dans l'équipe de Microscopie d'Ingénierie du Front d'Onde - Département de Photonique
Institut de la Vision - Paris, France

Innovative optical methods using fiber bundles for two-photon all-optical brain studies

Présentée par

Antonio LORCA CÁMARA

Thèse soutenue publiquement le 15 décembre 2023

Devant le jury composé par :

Dr. Tobias BONHOEFFER (Rapporteur)

Dr. Yaniv ZIV (Rapporteur)

Dr. Hervé RIGNEAULT (Président du jury)

Dr. Hana UHLÍŘOVÁ (Examinatrice)

Dr. Volker BORMUTH (Examineur)

Dr. Valentina EMILIANI (Directrice de Thèse)

Dr. Nicolò ACCANTO (Co-encadrant)

*to my grandparents,
to my guide*

Acknowledgements

This manuscript represents the culmination of the extensive work I've undertaken over the past three and a half years. None of this would have been possible without the unwavering support and encouragement I've received from many of you, and I would like to express my gratitude to all of them.

First, I would like to express my gratitude to the jury members, Tobias Bonhoeffer, Yaniv Ziv, Hervé Rigneault, Hana Uhlířová and Volker Bormuth, who accepted the task of reviewing my work and participating in my PhD defense. I appreciate the time and effort you dedicated to evaluating and commenting on my manuscript and presentation, contributing significantly to the improvement of my scientific work.

Secondly, I would like to express my thanks to the members of the Wavefront-Engineering Microscopy group, of which I've had the extraordinary privilege to be a part.

- Valentina Emiliani, my supervisor, I owe you a profound debt of gratitude. Your belief in the various projects I've pursued has been instrumental in their success. You have not only taught me how to be a good scientist through your example but also demonstrated the value of perseverance in achieving our research goals. Your infectious happiness and sense of humor have made this journey all the more enjoyable.

- Nicolò Accanto, my co-supervisor and the person who has been closely working with me throughout these years. I think there is no words to express all the gratitude I have to you. When I, a somewhat naive student, decided to embark on a master's internship under your guidance, I had no idea how lucky I was. As the years have unfolded, and I've come to understand the challenges that come with pursuing a PhD, I've realized it wasn't as hard as it could have been, thanks to you and your attitude to face the problems. Your ever-present smile and your energy and time for helping me navigate through the complexities of experiments have made this journey far smoother than I could have imagined both inside and outside the lab.

- To Cecile Telliez and Joe, my companions in this PhD journey from the very beginning. We've been through it all, from the highs of exciting results to the lows of realizing that these results were wrong. Thank you for being there with me through all the discussions, and sometime complains, about the optics and biology. It's been 4 and a half years, and from the moment I arrived in Paris and met Cecile, both of us have come a long way, now approaching the finish line of our PhDs. I consider myself incredibly

fortunate to have met you and the other LUMI students who not only helped me to improve my French but also introduced me to the vibrant parties full of paints and “pichets”.

- Christophe Tourain, l'Atlas de ce laboratoire, et ce n'est pas pour l'ancienneté de la sculpture mais pour le précieux soutien que tu nous apportes. Sans toi, je serais encore en train d'imprimer de pièces pour mon système, de coller l'ordre zéro pour bloquer le laser ou de réparer une fibre cassée. To expertise technique a été inestimable. Mais aussi le soutien moral qui m'a aidé pendant les durs hivers, même si peut-être maintenant je les apprécie un peu plus, ou ton intérêt pour savoir comment se sont passées mes vacances ou mes courses.

- Francois Blot, the one I spent the most time with (aside from the mouse) in the setup, performing experiments that sometimes felt like playing the piano with the neurons. I'm deeply thankful for the invaluable biology knowledge I gained from you, the unofficial surgery trainings, and you spirit to delve into the complexities of optics and physics.

- Dimitri Tanese, Eirini Papagiakoumou, Ruth Sims, Emiliano Ronziti and Vincent de Sars. You've been instrumental during my PhD, offering enlightening discussions about the SLMs, holography, temporal focusing, lens compounds and possible aberration issues and the wavefront software and its development. Laurence Tricot, je tiens à te remercier pour les riches connaissances que j'ai acquises dans le domaine de la musique classique et aussi pour ton aide, en particulier vers la fin de ma thèse. Valeria Zampini, for introducing me to the world of neuroscience in the very beginning. Sol, I'm happy that you arrived to the lab to support the Spanish presence into the group. Benoit, I still remember the insightful notes you provided during my covid-intership about beam propagation. Chrisi, I promise to remember why the Christmas tree is not fluorescent. Aysha and Lien, thank you for your help in finding any optical and biological materials when I needed them.

- I would like to thanks the present and past PhD students: Clémence, Massilia, Clément and Florence, who introduced me to the life of a PhD and helped me in finding teaching opportunities at SU. You've been the best mentors with your recent experiences guiding the way. Many thanks Imane, who helped me a lot in the final steps of preparing and organizing my defense and to Ornella, Marie Louis and Stacy, I wish you the best for your PhDs and I hope you enjoy all what one could learn during these years. To Dimitri D. and Rafael, whom I had the pleasure of explaining the system, I'm glad that you will be continuing your PhD in this project.

Thirdly, I extend my gratitude to the entire photonics group.

- Gilles, Robert, and Pascal, for being part of my thesis advisory committee and for always being available to address any question or concern I had. Your excellent sense of humor and profound knowledge in optics were helpful during our discussions.

- Anis, for introducing me the hidden secrets of Paris and sharing enjoyable evenings in the quieter side of Paris. Hadrien, Benoit and José María thank you for always being available to lend me any optical equipment I needed.

Fourthly, I want to express my deep appreciation for the wonderful friends I made in this laboratory.

Grateful the moment we met each other. The breaks, lunchtimes and evenings we spent together of course were breaths of fresh air to momentarily forget all the issues within the lab. The snow trip to the north of Italy, where Elena learned to snow and Joe...well, Joe did DJoe. It was unforgettable. The occasional discussions with Esteban about cultural appropriations at the cantine for the lunch breaks and rambunctious conversations about life philosophy and the rational ones about Italian versus Spanish food reappeared all the time. I'll especially miss our evenings by the riverside or any Parisian garden full of rats ending with a nice bike tour. From now, you are welcome to visit me, where Elena will discover the amazing world of whales. Thank you for being such fantastic friends.

Finally, I would like to thank all my friends and family for always being by my side and witnessing my growth.

My parents, Consuelo and Antonio, deserve my deepest gratitude for their unconditional and infinite love and support, for believing in my dreams and in me. Your example has always been my guiding light. My sister, Mari, who has been a wonderful role model and made me to discover me the joys of travel. Thank you for generously offering your house as the best place for me to write my thesis this summer. To my godparents, Mari-Trini and Domingo, who introduced me to the awesome world of numbers and provided immeasurable advice. To my grandparents, whose lives have shown me the meaning of life itself. And to the people in Perú and Guate who taught me so much and showed me a different perspective of life, there are no words to express the profound impact you've had on me.

To my friends, Parra, Josué, MJ, Jorge and Quini, who have been with me since the bachelor and the secondary school days and continue to meet up at least once a year for a beer to see how we're growing older. To think about you is to think that amazing nights at the concerts of La Raiz, Izal, Vetusta or La Pegatina. My friends Roberto, Chesco, Jorge and Francis and all those nights in Murcia spent enjoying our time with some drinks and sharing incredible hospital stories that I could not possibly include here. To my

friends Irene and Mariángeles, for always supporting me in “whatever it is you are doing with mice”. To my friend Anna, who has been with me in Paris from the beginning and is always the best to talk about our favorite topics.

Lastly, to the person who has chosen to share and enjoy her life with. María, I want to thank you for your love, patience and for being by my side during the best moments of the past 4 years. Our travels to Menorca, Switzerland, Germany, Denmark, the Netherlands and all over France have been incredible adventures. Your infectious smile and laughter brighten everyone’s day, and your strength and determination inspire me to be a better person. Thank you for supporting and encouraging me, especially during the challenging times when I’m exhausted after a long and hard day of work or even after a marathon.

Summary

In neuroscience, advanced optical tools and techniques are required to map and manipulate brain circuits in living and freely behaving animals. Developments in two-photon microscopy and optogenetics have facilitated the performance of all-optical imaging and optogenetic photostimulation of neuronal populations with single-cell resolution, particularly in head-restrained animals. Furthermore, optical approaches like temporal focusing and computer-generated holography have enabled precise targeting of single or groups of neurons with single-cell resolution within a volume. These strategies have been used in pioneering experiments to, for example, influence animal behavior, affect perception and map connectivity *in vitro* and *in vivo* animals.

In the course of my thesis, I firstly focused on the development of a flexible two-photon fiberscope (2P-FENDO) capable of conducting all-optical brain investigations at near cellular resolution in freely moving mice. We employed a fiber bundle, and the exploited intrinsic inter-core delay dispersion of the bundle, with a GRIN lens to perform fast two-photon functional imaging and two-photon holographic photostimulation of single and multiple neurons with a $\sim 8 \mu\text{m}$ axial confinement within a field of view of $250 \mu\text{m}$ in diameter. 2P-FENDO will permit the simultaneous imaging and control of defined neuronal functions in the brain during naturalistic animal behaviors.

The second part of the thesis introduces a novel optical approach using a fiber bundle and a spatial light modulator for dual-color two-photon light patterning in three dimensions. This system achieves precise and reconfigurable targeting of large numbers of neurons with a good axial resolution ($\sim 20 \mu\text{m}$) within a $380 \times 380 \times 300 \mu\text{m}^3$ volume, capitalizing on the inter-core temporal delay and the lasers wavelength independency. Compared to previous three-dimensional light patterning systems, this approach simplifies the optical setup while maintaining good axial resolution independently of the resultant spot size, and it allows for the generation of two-dimensional and three-dimensional multicolor light patterns using a single beam path and two distinct laser wavelengths simultaneously.

Résumé

En neurosciences, des outils et techniques optiques avancés sont nécessaires pour imager et manipuler les circuits cérébraux chez des animaux vivants et en se comportant librement. Les développements en microscopie à deux photons et en optogénétique ont facilité la réalisation d'imageries entièrement optiques et de la photostimulation optogénétique de populations neuronales avec une résolution cellulaire unique, en particulier chez les animaux dont la tête est maintenue immobile. De plus, des approches optiques telles que la focalisation temporelle et l'holographie générée par ordinateur ont permis le ciblage précis de neurones individuels ou de groupes de neurones avec une résolution cellulaire unique dans un volume. Ces stratégies ont été utilisées dans des expériences novatrices pour, par exemple, influencer le comportement des animaux, affecter la perception et cartographier la connectivité *in vitro* et *in vivo* chez les animaux.

Au cours de ma thèse, j'ai d'abord axé mes recherches sur le développement d'une fibrescope flexible à deux photons (2P-FENDO) capable de mener des investigations cérébrales entièrement optiques à une résolution cellulaire proche, chez des souris se déplaçant librement. Nous avons utilisé un faisceau de fibres, et exploité la dispersion intrinsèque des retards intercœurs du faisceau, avec une lentille GRIN pour réaliser une imagerie fonctionnelle rapide à deux photons et une photostimulation holographique à deux photons de neurones individuels et multiples avec un confinement axial de $\sim 8 \mu\text{m}$ dans un champ d'excitation de $250 \mu\text{m}$ en diamètre. 2P-FENDO, peut permettre l'imagerie simultanée et le contrôle de réseaux neuronaux définis dans le cerveau pendant des comportements animaux naturalistes.

La deuxième partie de la thèse introduit une nouvelle approche optique utilisant un faisceau de fibres et un modulateur spatial de lumière pour le modelage bicouleur de la lumière à deux photons en trois dimensions. Ce système permet un ciblage précis et reconfigurable d'un grand nombre de neurones avec une résolution cellulaire unique ($\sim 20 \mu\text{m}$) dans un volume de $380 \times 380 \times 300 \mu\text{m}^3$, capitalisant sur le retard temporel intercœurs et l'indépendance en termes de longueur d'onde des lasers. Comparé aux systèmes précédents de modelage tridimensionnel de la lumière, cette approche simplifie la configuration optique tout en maintenant une bonne résolution axiale indépendamment de la taille résultante du spot, et il permet la génération de motifs de lumière multicolores bidimensionnels et tridimensionnels en utilisant un seul chemin de faisceau et deux longueurs d'onde laser distinctes simultanément.

Contents

Acknowledgments	3
Summary	7
Résumé	8
List of abbreviations	11
List of figures and tables	13
A. Introduction	15
A.1. The study of the brain using microscopy and optogenetics	15
A.2. Single and multiphoton microscopy	16
A.2.1 Single photon microscopy	16
A.2.2 Two-photon microscopy	17
A.2.3 Imaging techniques in two-photon microscopy	20
A.3. Optogenetics: molecular tools to study the brain	24
A.3.1 Genetically encoded indicators to read-out neuronal activity	24
A.3.2 Genetically encoded actuators to manipulate neuronal activity	26
A.4. Optical methods for optogenetics	28
A.4.1 Neuronal activity manipulation techniques in 2P microscopy	29
A.4.2 Computer generated holography	32
A.4.3 Temporal focusing combined with CGH	37
A.4.4 2P all-optical brain studies	39
A.4.5 Challenges of 2P all-optical brain studies	41
1. Freely moving	41
2. Simplicity and multicolor	44
A.5. Fiber Bundles	44
A.5.1 Ultrashort pulses propagation in fiber bundles	49
Group delay dispersion	49
Self-phase modulation	52
A.6. References	55
B. 2P all-optical studies in freely moving mice using a flexible fiber bundle	71
B.1. Introduction	71
B.1.1 The interest of brain studies in freely moving animals	71
B.1.2 Optical systems to study the brain in freely moving animals	73

1. Single-photon miniscopes	73
2. Two-photon miniaturized microscopes	75
3. Fiber bundle-based microscopes	76
B.2. 2P-FENDO	78
B.2.1 Paper	78
B.2.2 Elaboration on 2P-FENDO details	124
B.3. Recent advances enlarging the FOV of 2P-FENDO	127
B.3.1 Optical characterization of an enlarged FOV 2P-FENDO	134
B.3.2 Functional imaging with an enlarged FOV 2P-FENDO	135
B.3.3 In vivo all-optical experiment with an enlarged FOV 2P-FENDO	138
B.4. System perspectives	140
B.4.1 Review publication	142
B.5. References	143
C. Multicolor 2P light-patterning	168
C.1. Introduction	168
C.1.1 3D generation of TF-patterns	168
C.1.2 TF with multicolour illumination	173
C.1.3 Fiber bundles with multicolour illumination	176
C.2. Multicolor 2P light-patterning microscope using a fiber bundle	178
C.2.1 Paper	178
C.2.2 Details on the system for multicolour 3D light-patterning using a fiber bundle..	196
C.3. Discussion and future perspectives	197
C.4. References	200
D. General conclusion and future outlook	203

List of abbreviations

1P	One-Photon
2D	Two-Dimensions
2P	Two-Photon
3D	Three-Dimensions
3D-SHOT	3D-Scanless Holographic Optogenetics with Temporal focusing
3P	Three-Photon
AAV	Adeno Associated Virus
AOD	Acousto-Optic Deflector
CA1	Cornu Ammonis 1
CGH	Computer Generated Holography
ChR2	Channelrhodopsin-2
DCF	Dispersion-Compensation Fiber
DMD	Digital Micromirror Device
EM-CCD	Electron Multiplying-Charge Coupled Device
ETL	Electro-Tunable Lens
FACED	Free-space Angular-Chirp-Enhanced Delay
FLIT	Fast Light Targeting
fMRI	functional Magnetic Resonance Imaging
FOE	Field Of Excitation
FOV	Field Of View
FWHM	Full-Width at Half Maximum
GDD	Group Velocity Dispersion
GECI	Genetically Encoded Calcium Indicator
GEVI	Genetically Encoded Voltage Indicator
GFP	Green Fluorescent Protein
GPC	Generalized Phase Contrast
GRIN	Gradient Refractive INdex
GS	Gerchberg & Saxton
GtACR	<i>Guillardia theta</i> Anion-conducting ChannelRhodopsins
GVD	Group Velocity Dispersion

ICDD	Inter-Core Delay Dispersion
KCR	K ⁺ -selective Channelrhodopsin
LED	Light Emitting Diode
MAPSI	Miniscope with All-optical Patterned Stimulation and Imaging
MCF	Multi-Core Fiber
MEC	Medial Entorhinal Cortex
MEM	Micro-Electro-Mechanical
MMF	Multi-Mode Fiber
MTF-LS	Multiplex Temporal Focusing-Light Shaping
NA	Numerical Aperture
PMF	Polarized Maintained Fiber
PMT	PhotoMultiplier Tube
RAMP	Random Access MultiPhoton
ROI	Region Of Interest
sCMOS	Scientific Complementary Metal–Oxide–Semiconductor
SLM	Spatial Light Modulator
SNR	Signal-to-Noise Ratio
SPM	Self-Phase Modulation
TAG	Tunable Acoustic Gradient lens
TF	Temporal Focusing
VC	Visual Cortex

List of figures and tables

<i>Figure 1.</i> Principle of single-photon and two-photon excitation	19
<i>Figure 2.</i> Penetration depth in single and multiphoton microscopy	20
<i>Figure 3.</i> X/Y scanning strategies in multiphoton microscopy	24
<i>Figure 4.</i> Schematic diagram of GECIs	26
<i>Figure 5.</i> Examples of different opsin variants.....	28
<i>Figure 6.</i> Neuronal activity manipulation strategies	31
<i>Figure 7.</i> Principles of Computer-generated holography.....	33
<i>Figure 8.</i> Parameters of an optical system for CGH with a SLM.....	36
<i>Figure 9.</i> Implementation of Temporal Focusing combined with CGH.....	38
<i>Figure 10.</i> 2P All-optical investigations in retina circuits	40
<i>Figure 11.</i> Towards 2P holographic optogenetics in freely moving animals	43
<i>Figure 12.</i> Principles of Fujikura and Schott fiber bundles	47
<i>Figure 13.</i> Electric field amplitude profiles for all the guided modes of an optical fiber at a specific wavelength.....	49
<i>Figure 14.</i> Group Velocity Dispersion of an ultrashort laser pulse propagating in a dispersive medium.....	51
<i>Figure 15.</i> Dispersion-induced broadening of a Gaussian pulse inside a fiber.....	52
<i>Figure 16.</i> Self-phase modulation effect in a single core fiber	53
<i>Figure 17.</i> Self-phase modulation effect in a 5.5 μm core fiber	54
<i>Figure 18.</i> Spectral narrowing in a chirped Gaussian pulse.....	55
<i>Figure 19.</i> Miniaturized one-photon excitation microscope design	74
<i>Figure 20.</i> MINI2P for large-scale 2P calcium imaging in multiple brain regions	76
<i>Figure 21.</i> Optical setup of the Fiberscope and Characterization of holographic patterns.....	77
<i>Figure 22.</i> Group velocity dispersion compensation	124
<i>Figure 23.</i> Inter-core delays in the fiber bundle.....	125
<i>Figure 24.</i> Example of a GRIN lens of 1.3 mm diameter and 5 mm	127
<i>Figure 25.</i> Fiber bundles homogeneity comparison and GRIN lens and mini-objective aberrations comparison	131
<i>Figure 26.</i> Configurations to achieve a larger FOV and higher lateral resolution.....	134
<i>Figure 27.</i> Optical characterization of configuration 4.....	135
<i>Figure 28.</i> Imaging of spontaneous calcium activity in head-fixed mice	137
<i>Figure 29.</i> Imaging of spontaneous calcium activity in freely moving mice	138

<i>Figure 30.</i> High-resolution photostimulation in freely moving mice	140
<i>Figure 31.</i> Experimental setup and results of 3D-CGH.....	171
<i>Figure 32.</i> Optical setup of FLiT	173
<i>Figure 33.</i> Wavelength dependence of a diffraction grating.....	176
<i>Figure 34.</i> Simulation of beam propagation through a fiber bundle.....	177
<i>Figure 35.</i> View of the Wavefront V software	197
<i>Figure 36.</i> Encoding multicolor phase modulation into the SLM	199
<i>Table 1.</i> Fiber bundles parameters	128
<i>Table 2.</i> Lenses parameters	130

A. Introduction

A.1 The study of the brain using microscopy and optogenetics

Understanding how the brain works is a fundamental scientific goal that involves contributions from diverse fields. Scientists from various disciplines have all played a role in studying the brain's development, morphology, and physiology. They employ a range of tools and instruments to explore the brains of different animals. Comparing the brain to planet Earth, it can be explored using various imaging techniques, much like navigating through Google Maps. This exploration allows us to uncover the brain's complexities, similar to how a world atlas provides information about politics, topography, or traffic. Brain imaging reveals essential details about its microstructure, connectivity, and function. By figuratively "zooming in," we can observe the distinct boundaries of different brain areas, analogous to countries on a map. Additionally, further "zooming" in allows us to examine individual cells, much like observing cities in detail.

Just as Google Maps allows us to zoom in and out to explore different levels of detail, brain imaging techniques enable us to examine the brain at multiple levels, from macroscopic to microscopic. Functional magnetic resonance imaging (fMRI) provides a macroscopic view, mapping whole brain regions and functions. However, it possesses a millimetric resolution, non-sufficient for cellular or subcellular imaging ($< 15 \mu\text{m}$). On the opposite end of the spectrum of resolutions, advanced techniques like super-resolution and electron microscopy enable us to explore the brain at subcellular levels providing sub-nanoscale resolution within small micrometric volumes (Mazumder, N., Gangadharan, G., & Kistenev, 2022). It's akin to zooming in on cities to examine the fine details of buildings, streets, and even individual households. In between these two edges, optical microscopy enables from cellular to sub-cellular resolution, covering from hundreds to few micrometers' volumes in the brain. In this regime, it is possible to study brain regions of millimetric volumes keeping cellular resolution. All this made optically, allows to be non-invasive and to perform experiments in-vivo animals with the spatial and temporal resolution to measure the neuronal activity.

This thesis centers on the development of advanced optical approaches for two-photon (2P) all-optical manipulation of neuronal activity in mouse using optogenetics. In **chapter A**, I

summarize the different optical strategies and challenges of optogenetics to perform neuronal activity recording and manipulation in the brain and I introduce the use of fiber bundles for 2P all-optical studies. In **chapter B**, I focus on the use of flexible fiber bundles to perform optogenetics studies in freely moving mice with single-cell precision. In **chapter C**, I delve into the temporal properties of the fiber bundles to perform, with single-cell resolution, multicolor 3D light patterning. In chapters 2 and 3, I first introduce the state-of-the-art and fundamentals underlying each technique and then I present the obtained results and the discussions and futures perspectives. Lastly, in **chapter D**, I give general conclusions and future outlooks.

A.2 Single and multiphoton microscopy

The two primary techniques employed for imaging brain regions with cellular resolution are based on single photon and multiphoton microscopy.

A.2.1 Single photon microscopy

One-photon (1P) or single photon microscopy techniques, such as wide-field microscopy, confocal microscopy or selective plane illumination microscopy (Murphy and Davidson, 2013), rely on the fluorescence phenomena of a molecule absorbing and re-emitting photons (figure 1). In this process, the energy of one photon is absorbed by a molecule, inducing the excitation of an electron to a higher energy level (the energy gap is related to the incident light wavelength). The molecule then, generally relaxes non radiatively to a lower excited state (vibrational levels) from which a photon is emitted with lower energy than the absorbed one, resulting in the denominated Stokes shift. The fluorescence intensity is linearly related to the incoming light intensity ($F \propto I$).

The simplest type of 1P fluorescence microscopy is performed with a wide-field illumination of the entire sample containing fluorescent molecules, where, after illumination, the fluorescence light is collected while blocking the light used to excite the molecule with an optical filter, and detected by a detector such as a camera. Notably, Green Fluorescent Proteins (GFPs) are widely used due to their high brightness, photostability and excitation at optical wavelengths (Chalfie M, Tu Y, Euskirchen G, Ward WW, 1994; Tsien, 1998). 1P widefield microscopy, with GFPs expressed in the neurons, permits to image large regions on the surface of the brain (Waters, 2020). However, this method lacks axial sectioning, as the fluorescence is generated throughout all

along the excited path without spatial confinement, limiting the obtainable spatial resolution (Murphy and Davidson, 2013).

In confocal microscopy the excitation light is confined to a diffraction-limited point and scanned through the sample plane, and the fluorescence signal is detected by a single pixel detector, after passing through a pinhole, placed in the conjugated position with respect to the focal plane, which rejects the out-of-focus background light, achieving better axial confinement than with wide-field illumination (Pawley, 2010). *In-vivo* studies using confocal microscopy have been predominantly focused on shallow depths or transparent tissues (Fine *et al.*, 1988; Chiang *et al.*, 2023).

1P confocal microscopy presents some limitations due to the 1P illumination that limits the penetration depth into scattering tissues like the brain to few tens of micrometers, as shorter wavelengths are more scattered into the tissue and damage more the brain (Diaspro *et al.*, 2006). Moreover, the linear relationship between the excited light intensity and the collected fluorescence gives rise to increased background noise from planes situated above the focal plane which needs algorithms to extract the signal from the focal neuron from contaminants and signals from the out-of-focus cells (McNally *et al.*, 1999).

A.2.2 Two-photon microscopy

The theoretical demonstration of multiphoton absorption in 1931 (Goeppert-Mayer, 1931; Potma and Xie, 2008 for english translation) by Maria Goeppert Mayer along with experimental developments by Sheppard and Kompfner in 1978 (Sheppard, C. and Kompfner, 1978) led to the conceptualization of multiphoton microscopy. However, it was only in 1990 that the first experimental implementation based on 2P fluorescence microscopy was performed by W. Denk, J. Strickler and W. Webb in 1990 (W. Denk, J. H. Strickler, 1990; Helmchen and Denk, 2005). In 2P microscopy, electrons absorb two photons quasi-simultaneously (virtual state lifetime = 10^{-16} seconds, Xu and Webb, 1996). The photons are roughly half energy and double wavelength compared to the 1P excitation case (figure 1A). Consequently, the electrons are excited from the ground state to the vibrationally and electronically excited state. Upon electron relaxation and decay to the ground state, a photon of a shorter wavelength compared to the excitation laser is emitted (fluorescence). In this case, the generated fluorescence intensity depends nonlinearly on

the incident light intensity ($F \propto I^n$, where $n=2$ for 2P microscopy and $n=3$ in the case of three-photon microscopy (3P)). However, the probability of 2P absorption ($\text{Prob} \propto I^2 \delta_{2P}$) is much lower than 1P absorption, as it depends on the 2P cross section ($\delta_{2P} = \delta_{1P}^2 \cdot \tau_{LT} \approx 10^{-34} \text{ cm}^4/\text{photon} \cdot 10^{-16} \text{ s} = 10^{-49} \text{ cm}^4/\text{photon}$), which is very small compared to 1P microscopy ($\delta_{1P} = 10^{-17} \text{ cm}^2/\text{photon}$) (Xu and Webb, 2002; Papagiakoumou, Ronzitti and Emiliani, 2020), where τ_{LT} is the lifetime of the virtual state. The lower values of 2P cross section reduces the probability of 2P abortion, requiring different strategies to favor this phenomenon. In the early 2000's, femtosecond laser sources were developed with ultrashort pulsed lasers capable of delivering a large number of photons in just a few hundreds of femtoseconds. As the 2P fluorescence for ultrashort laser pulses can be expressed as: $S_{2P} \propto I^2 / \tau f$ (Xu *et al.*, 1996; Zipfel, Williams and Webb, 2003), where τ is the pulse duration and f is the laser repetition rate, the 2P absorption probability highly increases using ultrashort pulses. At the same time, the use of high-NA objectives allows to produce higher energy peaks by tightly focusing the light in diffraction-limited spot. The combination of high spatial and temporal confinement made it possible to achieve efficient 2P excitation (Helmchen and Denk, 2005).

In both 1P confocal and 2P microscopy, diffraction-limited spots are generally used to concentrate the light excitation into a small region. These spots are characterized by the beam waist w_0 at the focal plane, defined as $w_0 = \lambda/2NA$. Thus, higher objective numerical aperture (NA) reduces the beam waist. Moreover, the axial resolution obtained at the focal plane of the objective is defined by the full width at half maximum of the axial fluorescence profile and can be written as $\Delta z = 2 \cdot z_R$, where z_R is the Rayleigh range, $z_R = \pi \cdot w_0^2 / \lambda$ (Born and Wolf, 1986; Sheppard, 1996).

Even if the lateral and axial shape of a spot can be similar with 1P or 2P excitation, a key difference between 1P and 2P excitation is that the fluorescence (F) is directly proportional to the excitation intensity (I) in 1P excitation and proportional to the square of the intensity (I^2) in 2P excitation. Since the intensity at any position is in all the cases proportional to $1/z^2$ (energy conservation), the amount of fluorescence at every cross-sectional area (Φ) of the illuminated light cone (light cone area $A \propto z^2$) is $\Phi = F \cdot A = I \cdot A \propto 1/z^2 \cdot z^2$, which is constant for 1P excitation. By contrast, $\Phi = F \cdot A = I^2 \cdot A \propto 1/z^4 \cdot z^2$, which is proportional to $1/z^2$ for 2P excitation, giving a stronger localization of excitation effect and a higher optical sectioning (figure 1B-D). This results

in a reduction of absorption both above and below the focal plane, which also reduces the phototoxicity or the photobleaching into the tissue (Murphy and Davidson, 2013).

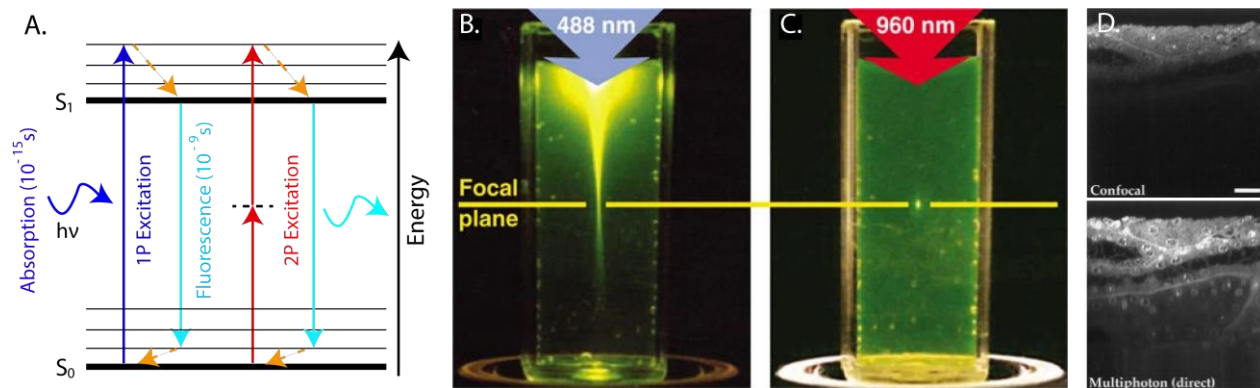


Figure 1. Principle of 1P and 2P excitation. **A.** Jablonski energy diagrams showing the excitation process in 1P and 2P excitation fluorescence microscopy. 1P excitation occurs when one photon ($h\nu$) is absorbed, promoting one electron to the excited state (S_1), blue arrow. Subsequently, the electron relaxes (vibrational relaxation, orange arrow) and decays to the ground state (S_0) releasing a photon at lower energy and wavelength, light blue arrow. In 2P excitation, the process occurs in a similar manner but the absorption is of two photons of half-energy quasi-simultaneously to excite the electron, red arrows. **B.** and **C.** Optical sectioning in the excitation volume generated by 1P and 2P excitation microscopy at 2 different wavelengths (Zipfel, Williams and Webb, 2003). **D.** Comparison of imaging penetration depth between 1P confocal microscopy and standard 2P microscopy (image adapted from Centonze and White, 1998).

2P microscopy presents several advantages over 1P microscopy for neuroscience applications when the excitation light propagates through the brain. Firstly, it leads to reduced out-of-focus fluorescence due to its higher axial confinement that decreases photobleaching. Secondly, it is more robust to scattering, which primarily depends on the size of the structures (d) and the excitation wavelength (λ) (Favre-Bulle *et al.*, 2015). In the visible and near infrared range of the spectrum, the longer excitation wavelengths allow deeper penetration depths in living tissues as the scattering coefficient decreases with the wavelength (figure 2). More specifically, this is due to a highly reduction of the Rayleigh scattering contributions ($d/\lambda \ll 1$) and a slight increase of Mie scattering ($d \approx \lambda$) (Bashkatov, Genina and Tuchin, 2011; Jacques, 2013). The penetration depth can be increased from $\sim 100 \mu\text{m}$ in 1P microscopy (Theer and Denk, 2006) to $\sim 1.6\text{mm}$ with 2P microscopy (Kobat *et al.*, 2009; Kobat, Horton and Xu, 2011). Finally, light penetration in biological tissues is not only hampered by the scattering but also by the medium absorption, which prevents the incoming photons to reach the focal volume. The absorption free path (l_{abs}) refers to the average distance traveled by a photon through tissue before being absorbed. In the 600-1150

μm range, there exist the so-called transparency window where I_{abs} is maximized, as most components of brain tissue minimally absorb at these wavelengths. As the scattering is lower with longer excitation wavelengths, 2P microscopy it therefore more suitable for image deep structures in the brain with cellular and subcellular resolution. Finally, there exists another window between 1650-1850 nm, which is characterized by a relative minimum in absorption that, combined with the lower scattering, makes 3P excitation possible to access even deeper region within the brain (Horton *et al.*, 2013; Cheng *et al.*, 2014; Chen *et al.*, 2018; Wang *et al.*, 2020; Streich *et al.*, 2021).

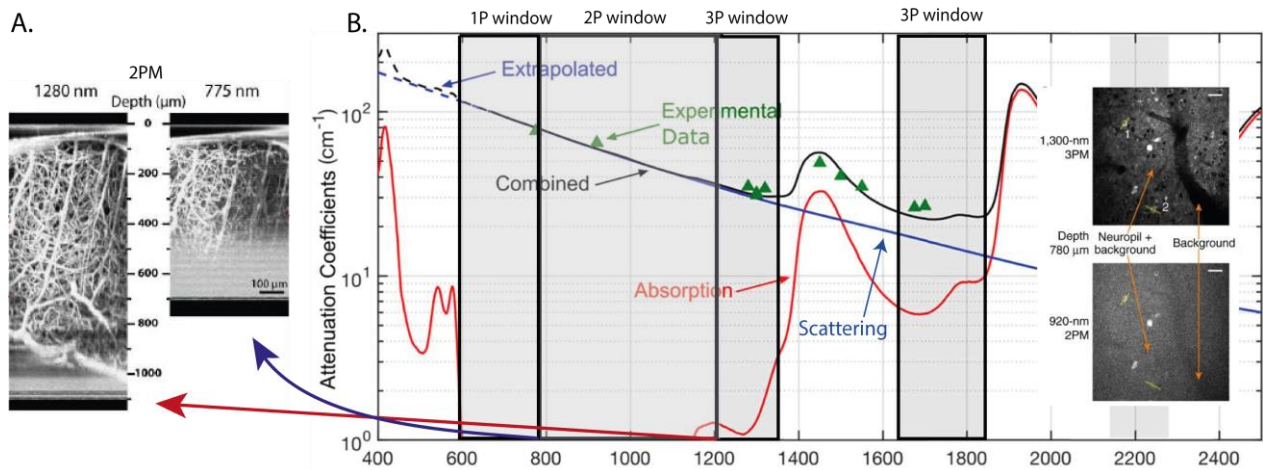


Figure 2. Penetration depth in single and multiphoton microscopy. **A.** In vivo 2P microscopy images of cortical vasculature in a mouse brain. Maximum intensity side projections of normalized image stacks for 1280 nm 2P microscopy (2PM) and for 775 nm 2PM are shown on the left and right, respectively (adapted from Kobat *et al.*, 2009). **B.** Absorption and scattering coefficients of biological tissue for different wavelengths and the combination of both coefficients. 3P excitation at higher wavelengths allowing deeper brain imaging with high-resolution of single cells compared with 2P excitation (775-1280 nm) and 1P excitation (600-775 nm) (adapted from Gigan *et al.*, 2022).

A.2.3 Imaging techniques in 2P microscopy

In a conventional 2P microscope, images are acquired by point-scanning the 2D field of excitation (FOE) using a diffraction-limited spot. The lateral scanning of the spot through the focal plane is achieved with the help of a scanning device, such as galvanometric mirrors (W. Denk, J. H. Strickler, 1990) (figure 3). To precisely focus the diffraction-limited spot onto the sample, 2P microscopes usually use a high NA objective (NA \sim 1) lens. These objectives enable high axial resolution (\sim 2 μm) in a FOE of $<1 \text{ mm}^2$ (Oheim *et al.*, 2001). In this configuration, the scanning device is placed at the conjugated plane of the objective's back aperture, introducing different

angles to laterally move the spot within the focal plane. Subsequently, the fluorescence signal emitted by the sample is collected and detected by photomultiplier tubes (PMTs), synchronized with the scanning device to generate the final 2D image. Such systems allow for high-resolution brain imaging with large FOEs and at detection speeds of 5-20 frames per second (Hz) (Grienberger *et al.*, 2022). Additionally, 3D images can be acquired by adjusting the axial position of the focusing objective to capture different focal planes.

Recent advances in optical techniques have been directed towards expanding the FOE for simultaneous recording of a greater number of neurons and achieving faster acquisition frame rates to capture rapid dynamic biological processes. A conventional scanning unit typically consists of two galvanometric mirrors, including a fast mirror (1-12 kHz) and a slow one (few to hundreds Hz) (figure 3). These mirrors are directed by signals to deflect the light at specific angles. The fast mirror scans a line, while the slow mirror laterally shifts this line to cover a 2D FOV. Galvanometric mirrors offer flexible capabilities in terms of their scanning speed and amplitude, making them versatile tools that can be modified. However, their raster scanning mode may not be sufficient for high frame rate functional imaging. To address this limitation, galvanometric mirrors can be replaced by faster scanning devices such as polygon mirrors (Kim, Buehler and So, 1999; Keller and Ahrens, 2015) or resonant mirrors (Fan *et al.*, 1999; Nguyen *et al.*, 2001). Polygonal mirrors, shaped as multi-faceted polygons, are rapidly rotated at a constant speed to scan a single line. Resonant mirrors, a variant of galvanometric mirrors, scan the sample at their resonant frequency (4-12 kHz), which enables much faster scanning of a single line (80 μ s per line). When combined with a galvanometric mirror for the slow axis scan, this approach has demonstrated substantial frame rate enhancement, achieving speeds of up to 30 Hz (Fan *et al.*, 1999; Lecoq, Orlova and Grewe, 2019).

Similar devices such as digital micromirror devices (DMDs) (Cheng *et al.*, 2016) or micro-electro-mechanical (MEM) scanners (Miyajima, H. and Asaoka, N. and Isokawa, T. and Ogata, M. and Aoki, Y. and Imai, M. and Fujimori, O. and Katashiro, M. and Matsumoto, 2003; Piyawattanametha *et al.*, 2006, 2009) are also employed. Additionally, non-mechanical movement devices like acousto-optic deflectors (AODs) provide an alternative solution for random access multiphoton (RAMP) microscopy, unhindered by mechanical inertia (Lechleiter, Lin and Sieneart, 2002; Salomé *et al.*, 2006). AODs utilize an acoustic wave that propagates through a medium to

periodically alter its refractive index, effectively modifying a phase grating. This alteration diffracts the excitation beam at specific angles, depending on the created grating's periodicity (Pavone and Shoham, 2020). Employing a pair of AODs oriented perpendicularly enables steering the laser beam along both the x and y directions. An additional pair of AODs, placed in the conjugate plane of the first pair, controls the z-focusing of the beam to generate a 3D scanning image (Akemann *et al.*, 2015). It is important to note that this microscopy technique does not raster scan the excitation beam through all the sample but it only sequentially scans the regions of interest at kilohertz speeds (Villette *et al.*, 2019). Various other systems exist for z-directional scanning, including the electro-tunable lens (ETL) or the tunable acoustic gradient lens (TAG). These devices modulate the beam divergence to change the focal plane of the excitation beam.

Not only new technological devices have improved the speed to monitor the neuronal activity, but also several optical configurations have shown an increase of the effective speed of the resonant scanner (Xiao, Davison and Mertz, 2021; Xiao, Giblin, *et al.*, 2023). Other techniques perform ultrafast 2P fluorescence imaging (3 kHz) in the brain *in vivo* by adding smart scanning strategies (such as the FACED module) that scan multiple spots in the sample plane with a single scanning device (Wu *et al.*, 2020; Meng *et al.*, 2022).

Other approaches have extended the excitation volume, including multifocal excitation (Kim *et al.*, 2007; Cheng *et al.*, 2011; Zhang *et al.*, 2019), line scanning such as light-sheet microscopy (Supatto *et al.*, 2011; Truong *et al.*, 2011; Bouchard *et al.*, 2015) or multiple line scanning across the focal plane at multiple angles to obtain recording rates up to 1 kHz (Kazemipour *et al.*, 2019). Fast imaging frequencies can be also achieved by extending the excitation axially by creating multiple spots in the z direction (Beaulieu *et al.*, 2020) or creating a line in the axial direction with a Bessel beam strategy (figure 3)(Lu *et al.*, 2017). Ultra-fast 2P imaging with a large excitation spot is achievable combined with temporal focusing strategies to obtain a good optical sectioning (Vaziri and Shank, 2010). This approach increases the illuminated region with the spot, consequently increasing the frame rate up to 160 Hz in a FOE of 0.5x0.5 mm² (Prevedel *et al.*, 2016).

The combination of new fast scanning devices and adapted scanning strategies enables to monitor the neuronal activity with higher speeds, reaching up to 10 kHz (Duemani Reddy *et al.*,

2008). For applications where a larger FOE is desired, lower NA objectives are used at the expense of lower axial resolutions (Stirman *et al.*, 2016), creating mesoscopic functional 2P imaging microscopes (McConnell *et al.*, 2016; Sofroniew *et al.*, 2016). These systems use customized objectives (Clough *et al.*, 2021; Yu *et al.*, 2021) and multiple scanning devices with the proper aberration free lenses (Bumstead, 2018), which allow the recording of Fields of view (FOVs) of $> 9.5 \text{ mm}^2$ at frame rates of 4 Hz (Stirman *et al.*, 2016; Lecoq, Orlova and Grewe, 2019).

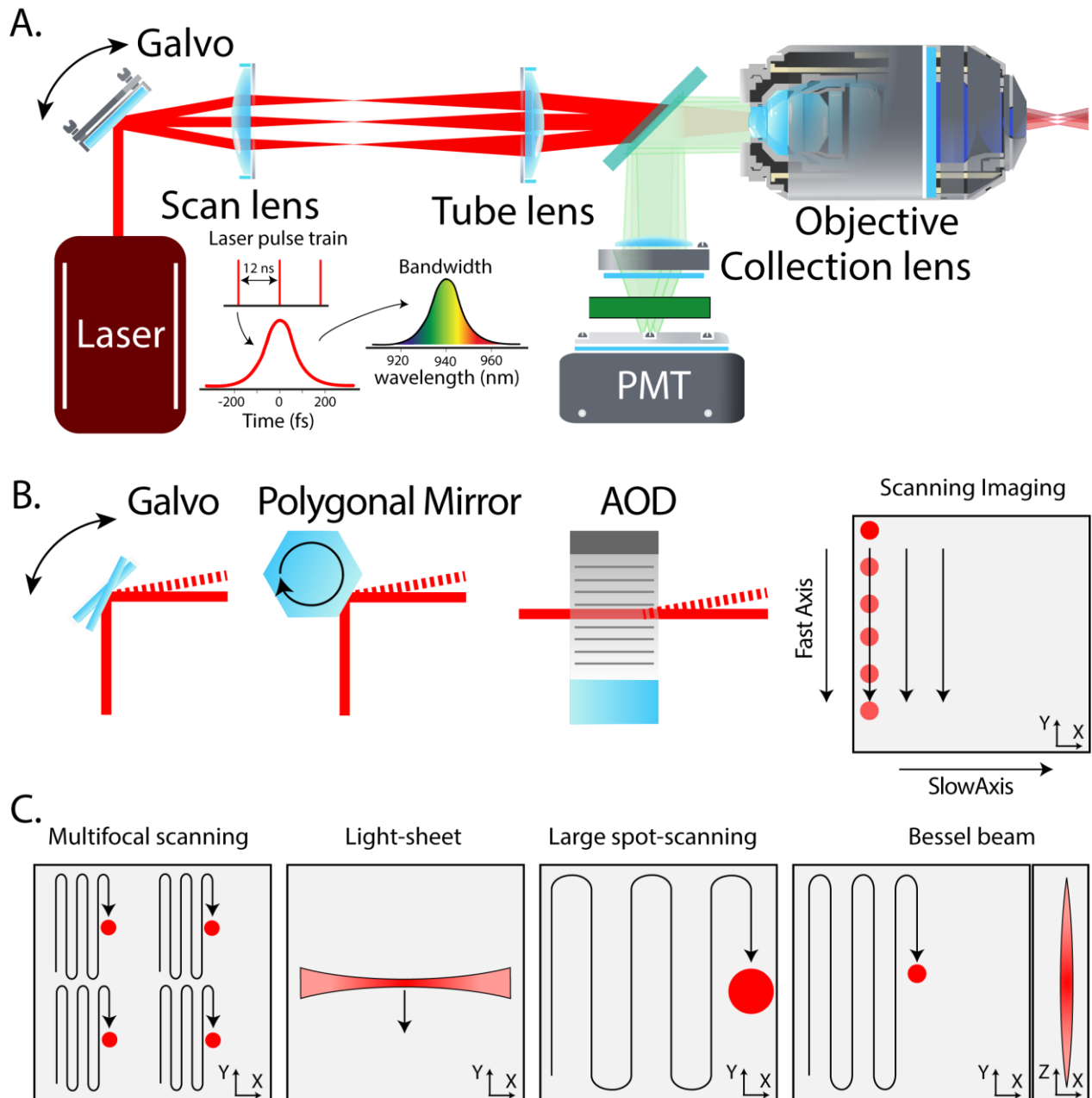


Figure 3. X/Y scanning strategies in multiphoton microscopy. **A.** Schematics of a 2P point-scanning microscope. The light emitted by an ultrashort laser, in this case an 80 MHz repetition rate laser, pulse duration 150 fs and central wavelength 940 nm (10 nm bandwidth). The excitation beam is scanned (X/Y) using galvanometric mirrors and focalized by an objective in the same plane. The fluorescence signal is reflected by a dichroic mirror, filtered and detected by a PMT. **B.** Different scanning devices. From left to right: galvanometric mirror, polygonal mirror and AOD. Right. Example of scanning strategy with two galvanometric mirrors with the fast mirror scanning the fast axis and the slow mirror scanning the slow axis to cover the entire 2D FOE. **C.** Different optical scanning strategies. Multifocal scanning where multiple spots are created at the same time and the scanned through the FOE. Light sheet microscope where an enlarged spot in the X direction is scanned for fast 2D imaging. Large spot scanning system where a large diameter excitation spot is scanned. Bessel beam scanning where the beam is enlarged in the Z direction for 3D imaging.

A.3 Optogenetics: molecular tools to study the brain

In 2005, the term "optogenetics" was coined to describe the technology that uses light to control the activity of genetically modified neurons (Boyden *et al.*, 2005). Since then, optogenetics has evolved into a non-invasive method for studying neurons in the brain (Deisseroth, 2015; Emiliani *et al.*, 2022). While optogenetics typically refers to the use of light to control neuronal activity, in this chapter, I will use the term optogenetics in a more general meaning, referring to the approaches to read-out the neuronal activity by using genetically encoded indicators and to manipulate this activity with genetically encoded light-gated actuators.

A.3.1 Genetically encoded indicators to read-out neuronal activity

Neural communication relies on electrical transients, which are generated by the depolarization and hyperpolarization of cell membranes. These transients can be measured using genetically encoded functional indicators (Martin, 2012). Optical monitoring of neural activity commonly involves measuring two types of signals: changes in intracellular calcium concentration related to electrical spikes (calcium imaging) and fluctuations in membrane potential (voltage imaging). For that, genetically encoded calcium indicators (GECIs) such as GCaMP (Nakai, Ohkura and Imoto, 2001; Grienberger and Konnerth, 2012; Rose *et al.*, 2014; Lin and Schnitzer, 2016; Zhang *et al.*, 2023) and genetically encoded voltage indicators (GEVIs) (Kralj *et al.*, 2011; Hochbaum *et al.*, 2014; Hou, Venkatachalam and Cohen, 2014; Gong *et al.*, 2015) are used, respectively.

GECIs have seen extensive use and development, with laboratories regularly producing enhanced variants exhibiting improved brightness, sensitivity, and signal-to-noise ratio (Paredes *et al.*, 2008). GECIs are used to detect neuronal activity since electrical transients, i.e. an action potential, induce a depolarization of the plasma membrane leading to the opening of voltage-gated Ca^{2+} channels and an increasing in intracellular Ca^{2+} concentration. This increase in Ca^{2+} concentration results in a conformation change of the GECI molecule, when bounded to Ca^{2+} , so that it gives higher fluorescence (figure 4). These indicators, combined with optical methods, allow the recording of neuronal activity in hundreds of neurons in the brain in living animals (Prevedel *et al.*, 2016; Demas *et al.*, 2021). The combination of 2P excitation and GECIs have allowed the study the dynamics of neuronal circuits over multiple spatial and temporal scales (Chen *et al.*, 2013; Stringer *et al.*, 2019; Yu *et al.*, 2019).

Advanced 2P microscopy approaches for calcium imaging have enabled to record calcium activity of thousands of neurons distributed in extended FOE (Sofroniew *et al.*, 2016). For instance, thousands of neurons across multiple areas have been recorded in a $3 \times 3 \text{ mm}^2$ square FOE at 7.5 Hz of acquisition rate with a PMT (Ota *et al.*, 2021). These systems allow to obtain high signal-to-noise ratios and single-cell resolution. Spatio-temporal sculpted light techniques, as the ones previously introduced, have allowed to perform volumetric calcium imaging in the mouse brain in a 1.2 mm^3 volume at up to 17 Hz (Weisenburger *et al.*, 2019). Not only a large number of neurons in large brain regions can be recorded with 2P microscopy techniques but also sub-cellular structures such as the neuronal dendrites and spines can be recorded with high spatial resolution with such optical microscopic strategies (Pryazhnikov *et al.*, 2018).

While calcium indicators are extensively utilized to record neuronal activity, it is important to note that they have a limitation as they are indirect reporters of electrical activity. Precisely, the kinetics of calcium transients are considerably slower than the action potentials, attributed to the prolonged inactivation of voltage-gated calcium channels and the slower kinetics of calcium extrusion, which are 10- to 100-fold longer than an action potential spike (Dana *et al.*, 2019). As a result, accurately determining the precise timing of events or resolving spike timing on fast trains can pose challenges.

To overcome these limitations, GEVIs are used as they directly translate changes in the membrane potential of neurons into a variation of fluorescence. GEVIs have the potential to precisely detect single action potentials and subthreshold changes in potential of the neurons. Moreover, as GEVIs respond to changes in membrane in either direction, it is possible to detect both the activation (depolarization) and the inhibition (hyperpolarization) of the neuronal activity when an increase or decrease of voltage is produced, respectively. Voltage imaging has been mostly used with 1P excitation (Quicke *et al.*, 2019) both *in vitro* (Brinks, Klein and Cohen, 2015; Chamberland *et al.*, 2017) and *in vivo* (Gong *et al.*, 2015; Kannan *et al.*, 2018; Roome and Kuhn, 2018; Villette *et al.*, 2019; Xiao, Cunningham, *et al.*, 2023). Thanks to the recent advances in kHz imaging strategies, 2P excitation voltage imaging of more sensitive and photostable voltage indicators have been recently performed (Li *et al.*, 2020; Wu *et al.*, 2020; Evans *et al.*, 2023; Sims *et al.*, 2023).

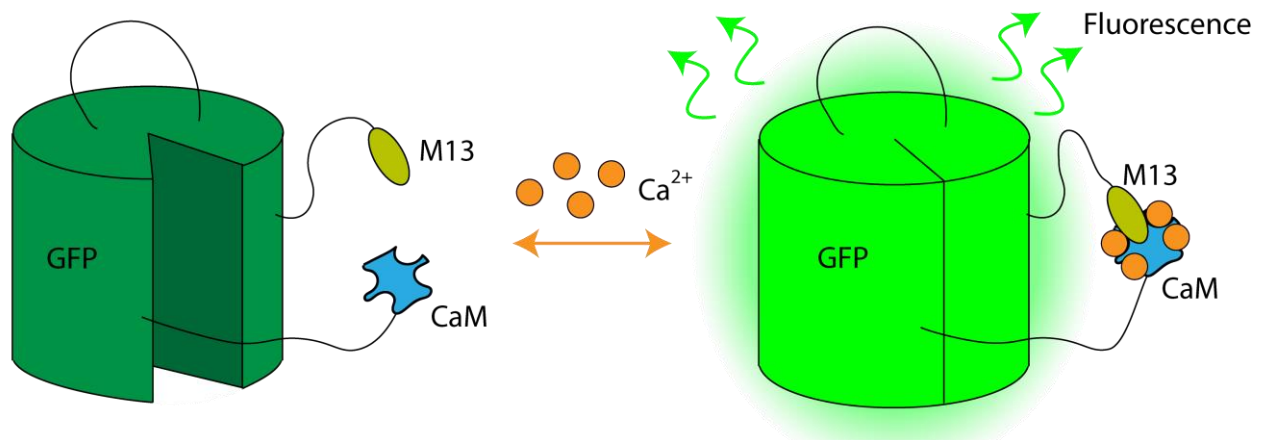


Figure 4. Schematic diagram of GECIs. The fusion of a fluorescent protein (such as GFP) to a specific binding domain can be used to report on the production of certain signaling molecules. GCaMP sensor consist on a molecular switch that contains calmodulin (CaM) and M13 inserted into the GFP (left). The addition of Ca^{2+} ions, induce CaM to bind with M13, which leads to increase of the GFP fluorescence (right).

A.3.2 Genetically encoded actuators to manipulate neuronal activity

Although optical stimulation of neurons dates back to 1971, when laser radiation was used to scan the surface of the ganglion of the marine mollusk *Aplysia californica* to map cellular interconnections (Fork, 1971), the term "optogenetics" was coined approximately two decades ago by Boyden *et al.* to describe the modern neuroscience tool that enables genetically targeted optical

control of neural activity (Boyden *et al.*, 2005). Since then, optogenetic actuators have revolutionized our understanding of neuronal function and continue to drive advancements in the field of neuroscience.

Genetically encoded actuators (Martin, 2012) play a crucial role in the manipulation of neuronal activity, complementing the advancements in genetically encoded functional indicators. These optogenetic actuators are categorized into two main types: those that activate neuronal cells (depolarization) and those that inhibit neuronal activity (hyperpolarization). Among all the different types of actuators that have been discovered or engineered, microbial opsins have emerged as the most widely adopted approach in optogenetics (figure 5).

As an example, Channelrhodopsin-2 (ChR2), a prominent microbial opsin, is a light-gated ion conducting channel that enables the influx of sodium ions (Na^+), leading to neuronal depolarization within an incredibly fast timeframe of 1-2 milliseconds upon visible light illumination (Bamann *et al.*, 2008). Such millisecond-scale precision allows for the generation of events that mimic the patterns of endogenous single-spike action potentials (Boyden *et al.*, 2005). Conversely, halorhodopsin and archaerhodopsin or GtACRs and KCRs act as inhibitory opsins (Vierock *et al.*, 2022), inducing hyperpolarization of neurons through the opening of chloride ion (Cl^-) and proton (H^+) pumps or chloride ion (Cl^-) and potassium ion (K^+) channels, respectively. These opsins elicit hyperpolarization within 8-15 milliseconds after visible light illumination (Han and Boyden, 2007). On the past years, researchers have been dedicated to developing new variants of these opsins, either from the same species or different ones, with enhanced characteristics such as faster kinetics, heightened sensitivity, and diverse absorption spectra (Emiliani *et al.*, 2022).

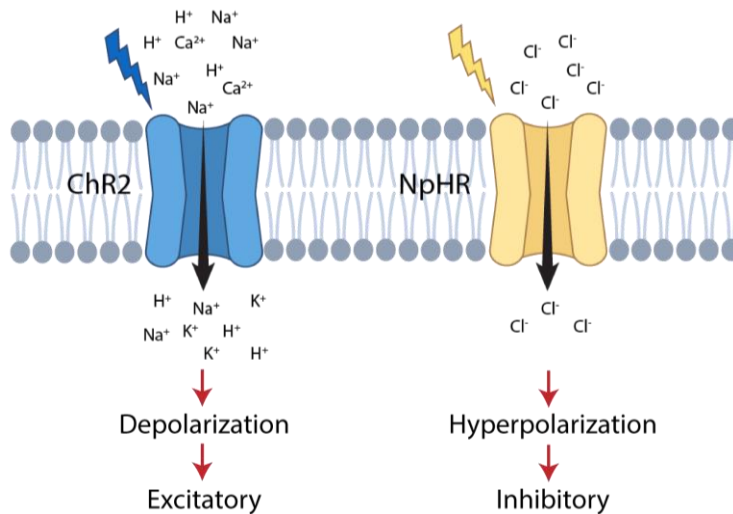


Figure 5. Examples of different opsin variants. Upon exposure to blue light, Channelrhodopsins (ChR2) allows cations to enter the cell causing a depolarization of the cell membrane and an excitatory response of the cell. In contrast, Halorhodopsin (NpHR) upon exposure to yellow light, results in a hyperpolarization and an inhibitory response of the cell with the entrance of anions (Cl^-) into the cell (Adapted from Guru *et al.*, 2015).

Targeting specificity is a crucial consideration in the realm of optogenetic tools. The task of achieving selective expression of light-sensitive proteins in specific cell types while excluding others is a labor-intensive process. To accomplish this, various methods are employed, such as transfection, viral transduction, or the creation of transgenic lines (Pastrana, 2010). Specific promoters or recombinase-based conditional systems, such as the Cre-lox systems (Sauer, 1987; Sauer and Henderson, 1988), are frequently utilized to restrict the expression of light-sensitive proteins to genetically identified neuronal population.

A.4 Optical methods for optogenetics

Over the past two decades, the development of optogenetics, along with the illumination of genetically encoded opsins in neurons, has revolutionized neuroscience enabling for the first time the mapping of neuronal function with cell type specificity or analyzing local circuits activity in a non-invasive manner (Boyden *et al.*, 2005; Mancuso *et al.*, 2011; Yizhar *et al.*, 2011). Initially, 1P microscopes used visible light delivered in a wide-field configuration (figure 6A) (Werley, Chien and Cohen, 2017). However, with this illumination approach, cellular specificity relied solely on genetic targeting strategies that allow opsins' expression in specific cellular types. This strategy

offers limited insights into the mechanisms that regulate neuronal circuit functions, as neurons of the same class may exhibit diverse response patterns (Ohki *et al.*, 2005; Curtis and Kleinfeld, 2009; O'Connor, Huber and Svoboda, 2009), while wide-field illumination only allows for the synchronous activation of entire populations of neurons, controlling them collectively. To address questions concerning the fine-scale organization of the neuronal circuits, such as determining how many neurons are needed to trigger a specific behavior or identifying dominant nodes in neuronal circuits, the spatial resolution of the illumination light need to be scaled-down to the level of individual neurons. To achieve this, optogenetics has developed new, non-invasive, illumination methods that offer single-cell spatial resolution and millisecond temporal precision for manipulating individual cells or subgroups of cells within the same genetically identified population (Ronzitti *et al.*, 2017). Among them, 1P excitation has been used to achieve single-cell precision manipulation of multiple neurons using fast scanning devices that target one by one the desired neurons (Bechtold, Hohenstein and Schmidt, 2013; Akemann *et al.*, 2015; Nadella *et al.*, 2016; Szalay *et al.*, 2016), or patterned light to target multiple neurons simultaneously (Farah, Reutsky and Shoham, 2007; Wang *et al.*, 2007; Guo, Hart and Ramanathan, 2009; Wyart *et al.*, 2009; Arrenberg *et al.*, 2010; Grossman *et al.*, 2010; Stirman *et al.*, 2011; Zhu *et al.*, 2012). 2P excitation approaches have the advantage of overcoming the limitation of tissue scattering, favoring deep light penetration and axial confinement. However, traditional 2P approaches are deficient because of the low conductivity (Feldbauer *et al.*, 2009) and channel density (Nagel *et al.*, 2002, 2003) in most optogenetic actuators, requiring the development of advanced optical strategies.

A.4.1 Neuronal activity manipulation techniques in 2P microscopy

Two main strategies for 2P optogenetics have emerged in the last years, which can be categorized based on whether the illumination light is focused into a diffraction-limited spot that is rapidly steered across the neuron(s) or the light illuminates with an extended spot the entire neuronal soma(s). In the following paragraphs, I will describe these different light-targeting strategies.

- **Scanning strategies.** Initially, the idea of using a static diffraction-limited spot to precisely target individual neurons deep within the brain was explored. However, this approach

encountered limitations due to the low conductance of the opsin channels, preventing the generation of action potentials by simply activating the few opsin molecules contained in the confined spot. To overcome these limitations, in 2009 Rickgauer and Tank refined the strategy for 2P photostimulation by implementing a sequential opsin-channel recruitment that involves fast scanning of diffraction-limited spot across the cell soma (Rickgauer and Tank, 2009). This approach was applied first in cultured cells and later *in vivo* (Prakash *et al.*, 2012). Different scanning methods, such as raster or spiral scanning, were tested to maximize the stimulation efficiency. The illumination time (T) or temporal resolution to generate the desired response (action potential, inhibition, behavior response,...) in N neurons using this strategy is given by (Ronzitti *et al.*, 2017): $T = N \cdot [n \cdot t_{\text{dwell}} + (n-1) \cdot t_{\text{cell}}] + (N-1) \cdot t_{\text{move}} = N \cdot T_{\text{dwell}} + (N-1) \cdot t_{\text{move}}$. Here, n represents the number of points that illuminate each cell, t_{dwell} is the dwell time per position, t_{cell} the scanning time from one point to another within the same cell, and t_{move} the scanning time from one cell to another. The key concept here is the total time that the spot spends in scanning a neuron, $T(N=1) = T_{\text{dwell}}$, which must be shorter than the decay time (τ_{off}) of the opsin and define the temporal resolution of this approach. This ensures that the generated serially evoked depolarizations integrate efficiently. It is important to note that with spiral scanning, the total illumination time T_{dwell} depends on the scan parameters such as the illumination power, time or scan length within the cell and the opsin kinetics and expression. Generally, this strategy has been used with slow decay time opsins ($\tau_{\text{off}} = 5\text{-}30$ ms) (Rickgauer and Tank, 2009; Packer *et al.*, 2015), limiting the possibility to generate spikes at fast frequencies (Emiliani *et al.*, 2015).

For multi-cell excitation, each cell is sequentially visited and spiral scanned (figure 6B), which inherently limits the maximum number of cells that can be photoactivated or inhibited within a few milliseconds to just a few (Xue *et al.*, 2022). To address this limitation, spiral scanning can be combined with Spatial Light Modulators (SLMs), that are used to multiplex the diffraction-limited spot, creating multiple holographic diffraction-limited spots at every desired cellular target (as described in more details in A.4.2). Then, these spots are simultaneously spiral scanned on each neuron (Packer *et al.*, 2012, 2015). The illumination time of N neurons for this system can then be defined as $T \approx n \cdot (t_{\text{dwell}} + t_{\text{cell}}) = T_{\text{dwell}}$.

- Parallel strategies.** Parallel or scanless illumination generates an excitation spot that is tailored to illuminate a defined cell structure (dendrite, spine, soma). To illuminate the entire neuronal soma, an enlarged spot of $\sim 15 \mu\text{m}$ diameter is commonly used (Rickgauer, Deisseroth and Tank, 2014). Two strategies can be employed to generate enlarged excitation spots. In the first one, a simple configuration uses a low-NA Gaussian beam (Bittner, Andrasfalvy and Magee, 2012; Pégard *et al.*, 2017), which is sequentially moved from one cell to another to photostimulate multiple neurons. The illumination time in this case is given by $T = N \cdot t_{\text{dwell}} + (N-1) \cdot t_{\text{move}}$ (Rickgauer and Tank, 2009; Peron and Svoboda, 2011; Rickgauer, Deisseroth and Tank, 2014). The second strategy uses a SLM to generate an extended spot using generalized phase contrast (GPC) (Papagiakoumou *et al.*, 2010; Bañas and Glückstad, 2017) or computer-generated holography (CGH) (Papagiakoumou *et al.*, 2008; Bègue *et al.*, 2013; Hernandez *et al.*, 2016; Accanto *et al.*, 2018; Forli *et al.*, 2018). These approaches enable to multiplex targets in 2D or in 3D in the case of CGH (figure 6C) (introduced in A.4.2) (Papagiakoumou *et al.*, 2008, 2010, 2013; Bègue *et al.*, 2013; Szabo *et al.*, 2014). In this case, the illumination time to stimulate N cells is independent of N and is only limited by the single cell dwell time: $T = t_{\text{dwell}}$, needed to, e.g., trigger an action potential in a single cell. However, since the illumination is now distributed over larger areas, the power demand is higher than in scanning approaches.

In the parallel strategy, the illumination is independent on the number of targets and only depends on the stimulation parameters, including the illumination time and power, the spot size and shape and on the opsin used.

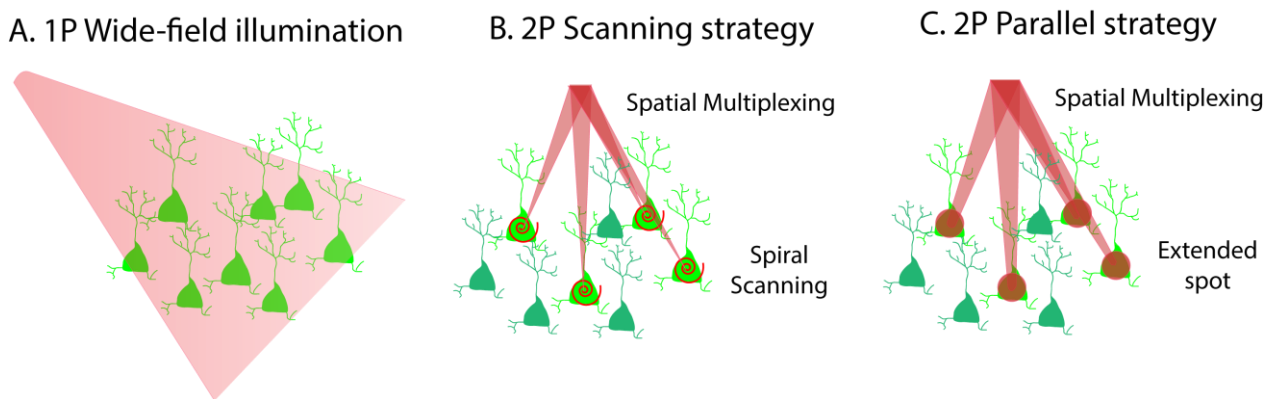


Figure 6. Neuronal activity manipulation strategies. **A.** 1P wide-field light stimulation targeting all opsin-express cells. **B.** 2P light stimulation with a scanning approach where multiple cells targeted

with a diffraction-limited spot are spirally scanned at the same time with galvanometric mirrors. C. 2P light stimulation using a parallel approach where large excitation spots target the entire desired cells simultaneously reducing the total time to photostimulate the opsins expressed in the neurons.

A.4.2 Computer generated holography

Computer-generated holography (CGH) is a technique that utilizes a SLM, a device based on a liquid crystal matrix, which can be controlled to modify the phase of a coherent optical wavefront (figure 7). The modulation of the incident beam with a phase profile or a hologram that is calculated and displayed onto the SLM allows to modify therefore the excitation wavefront in order to create arbitrary beam shapes into the sample plane. The phase calculation is performed using an iterative Fourier transforms-based algorithm between the focal plane and the back focal plane, known as the Gerchberg & Saxton (GS) algorithm (Gerchberg, 1971). To achieve a desired pattern at the focal plane, the GS algorithm computes the phase to be displayed in the SLM, i.e. at the back focal plane. Recent developments have introduced new algorithms that enhance computation speed and optimize the optical intensity distribution at the focal plane (Pégard *et al.*, 2017; Eybposh *et al.*, 2020).

CGH allows the generation of arbitrary and complex shapes, which can be multiplexed into a 2D or 3D volume to cover single or multiple targets simultaneously. However, as GS algorithm converges faster if the phase at the sample plane is a free parameter, the electric field at the focal plane have pseudo-random phases at neighboring points that interfere either constructively or destructively, causing intensity inhomogeneities called speckle (Ronzitti *et al.*, 2017). Various methods exist to smooth the phase profile of the spots to remove the speckles in the patterns, but they come with drawbacks such as reduced light efficiency in terms of transmitted power and a compromise in temporal resolution (Amako, Miura and Sonehara, 1995; Lutz *et al.*, 2008; Golan *et al.*, 2009; Guillon *et al.*, 2017; Aharoni and Shoham, 2018; Eybposh *et al.*, 2022).

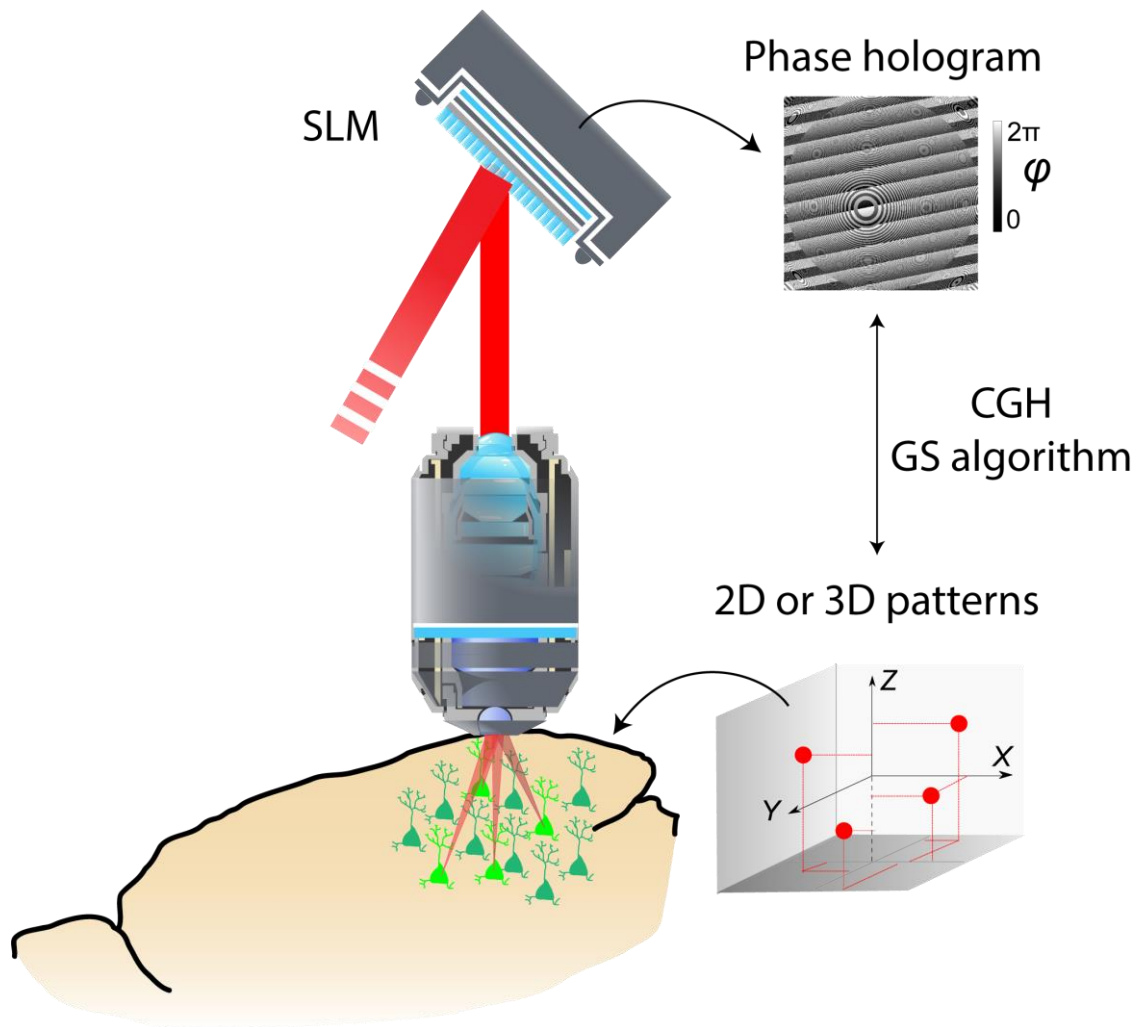


Figure 7. Principles of computer-generated holography. The laser beam illuminates the SLM which display a computer-generated phase hologram to reproduced the desired pattern at the focal plane. This hologram can reproduce 2D and 3D light patterns from a GS computer-based iterative algorithm. This pattern will multiplex the incoming beam to target the illumination at the desired neurons.

In the following, I will introduce some of the important parameters that should be considered while using liquid-crystal SLMs with CGH such as the FOE they can access, the diffraction efficiency in this FOE, the light losses and the SLM time speed.

1) The FOE is restricted by the maximal lateral displacement that the crystals or pixels of the SLM can introduce. The maximal deflection angle (θ) is related to the spatial period of diffraction grating (Λ) by this relation $m \cdot \lambda = \Lambda \cdot \sin(\theta)$, where m is the diffraction order ($m=1$ for the first order) and λ the central laser wavelength. In the case of the SLM, the minimal spatial

period is given by $\Lambda = 2 \cdot d_{\text{SLM}}$, where d_{SLM} is the pitch of the SLM. The entire screen of the SLM (L) is defined as $L = N \cdot d_{\text{SLM}}$, where N is the number of crystals in a square $N \times N$ matrix that composes the SLM. Considering small angles approximation ($\sin(\theta) \sim \theta$), we can represent the maximum deflection angle in terms of the pixel size of the SLM: $\theta_{\text{MAX}} = \lambda / 2 \cdot d_{\text{SLM}}$. Using the maximal deflection angle, the maximal lateral displacement at the sample plane (Δx_{MAX}), after the excitation objective (focal length = f_{obj}), can be expressed as: $\Delta x_{\text{MAX}} = \theta_{\text{MAX}} \cdot f_{\text{obj}}$ (figure 8A). Typically, a telescope system with magnification M is introduced between the SLM and the excitation objective to match the size of the SLM with the objective's back aperture pupil, filling its aperture. With this consideration, the expression we obtain that: $\Delta x_{\text{MAX}} = \lambda \cdot f_{\text{obj}} / 2 \cdot d_{\text{SLM}} \cdot M$. Therefore, the maximal FOE diameter is: $\text{FOE}_{\text{MAX}} = 2 \cdot \Delta x_{\text{MAX}} = \lambda \cdot f_{\text{obj}} / d_{\text{SLM}} \cdot M$ (Golan *et al.*, 2009).

For a given SLM size, if the system magnification M is fixed, it is possible to increase the maximal FOE by reducing the pixel size and increasing the number of pixels N into the SLM. However, as the pixels size are smaller, larger deflection angles on the beam are produced introducing higher dispersion of the light, which can introduce aberrations in the optical lenses placed after the SLM (Bumstead, 2018). Another consideration is the tradeoff between the FOE and the resolution. To obtain a relation between these two parameters, we consider that we fill the objective back aperture. With that, we can achieve the diffraction-limited lateral resolution: $\text{PSF}_x = \lambda / 2 \cdot \text{NA}$. Moreover, geometrically, the diameter of the pupil's objective is: $\phi_{\text{obj}} = 2 \cdot \text{NA} \cdot f_{\text{obj}}$. If the magnification system between the SLM and the objective is designed such that they match, $L \cdot M = N \cdot d_{\text{SLM}} \cdot M = \phi_{\text{obj}}$. By combining these equations, we express: $d_{\text{SLM}} = 2 \cdot \text{NA} \cdot f_{\text{obj}} / N \cdot M$. Finally, we can derive the relationship between the FOE and the resolution: $\text{FOE}_{\text{MAX}} = \lambda \cdot f_{\text{obj}} / d_{\text{SLM}} \cdot M = \lambda \cdot N / 4 \text{NA} = \text{PSF}_x \cdot N / 2$. From this, it's apparent that, for a given SLM, an increase of the maximum FOE leads to a broader PSF, consequently resulting in a reduction of optical resolution. Similarly, it is shown that the maximal axial excitation field FOE_z , for spots generated in a 3D volume, can be expressed as: $\text{FOE}_z = n \cdot \lambda \cdot f_{\text{obj}} / d_{\text{SLM}} \cdot M \cdot \text{NA}$, where n is the refractive index of the immersion medium.

2) As the SLM is a diffractive element, it generates different diffraction orders. We can express the diffraction efficiency of the light intensity diffracted at the order m (ξ_m) as a function

of the number of pixels used in the SLM (N_x) to create a displacement x : $\xi_m = \left(\frac{\sin(\pi(m/Nx))}{\pi(m/Nx)} \right)^2$ (Benton and Bove, 2008). The number of pixels N for a displacement x can be expressed as: $N = \lambda \cdot f_{obj} / d_{SLM} \cdot M \cdot x$.

Combining these two equations and considering the order $m=1$ of diffraction of the SLM, we obtain the relationship between the diffraction efficiency of the SLM and the lateral displacement in X and Y . $\xi(X, Y) = \text{sinc}^2(d_{SLM} \cdot M \cdot X / \lambda \cdot f_{obj}) \times \text{sinc}^2(d_{SLM} \cdot M \cdot Y / \lambda \cdot f_{obj})$ (figure 8B).

This equation links the power loss for a spot displaced at a certain distance from the center of the FOE, where the efficiency is 100%. It leads to an inhomogeneous optical power density over the entire FOE, which needs to be corrected to create uniform spots at any X, Y position. Thereby, a diffraction efficiency correction is commonly used in systems using SLMs to create constant light illumination spots patterns in the excitation volume (Golan *et al.*, 2009; Hernandez *et al.*, 2016).

3) Commonly, the SLM modulates and sends the 1st diffractive order to the sample plane. However, zeroth order is also produced from the non-modulated light, which appears in the middle of the FOE of the image plane. The zeroth order arises from various factors. First, it results from the empty spaces between the liquid crystals that directly reflect the incoming light, accounting for about 5-10% of the illuminated SLM area. Second, losses occur in the protective glass of the SLM, which is commonly designed to operate within a broad band of wavelengths. Lastly, due to the complexity of the phase profile, when complex patterns with significant high frequency phase variations are required, the overall diffraction efficiency of the phase pattern decreases, resulting in the addition of light into high diffraction orders or to the zeroth-order component (Goodman and Silvestri, 1970; Persson, Engström and Goksör, 2012; Ronzitti *et al.*, 2012).

Various strategies exist to remove the zeroth order in the sample plane (Palima and Daria, 2007; Hernandez *et al.*, 2014). One approach involves diverging the zeroth-order light over a large area by using cylindrical or spherical lenses, taking advantage of the non-linearity of the 2P excitation effect. The SLM then modulates the 1st order by adding the phase of a cylindrical lens to the displayed hologram to counterbalance and compensate for the aberration introduced with the physical spherical or cylindrical lenses placed in front of the SLM. Since the zeroth order is non-modulated by the SLM, it will remain with the aberrations and it will be removed from the FOE in

the sample plane (figure 8C). Another straightforward strategy is to physically block the zero order in an imaged plane before the sample plane. This can be achieved by adding a beam blocker, which also blocks a region in the center of the FOE where it will not be possible to generate spots.

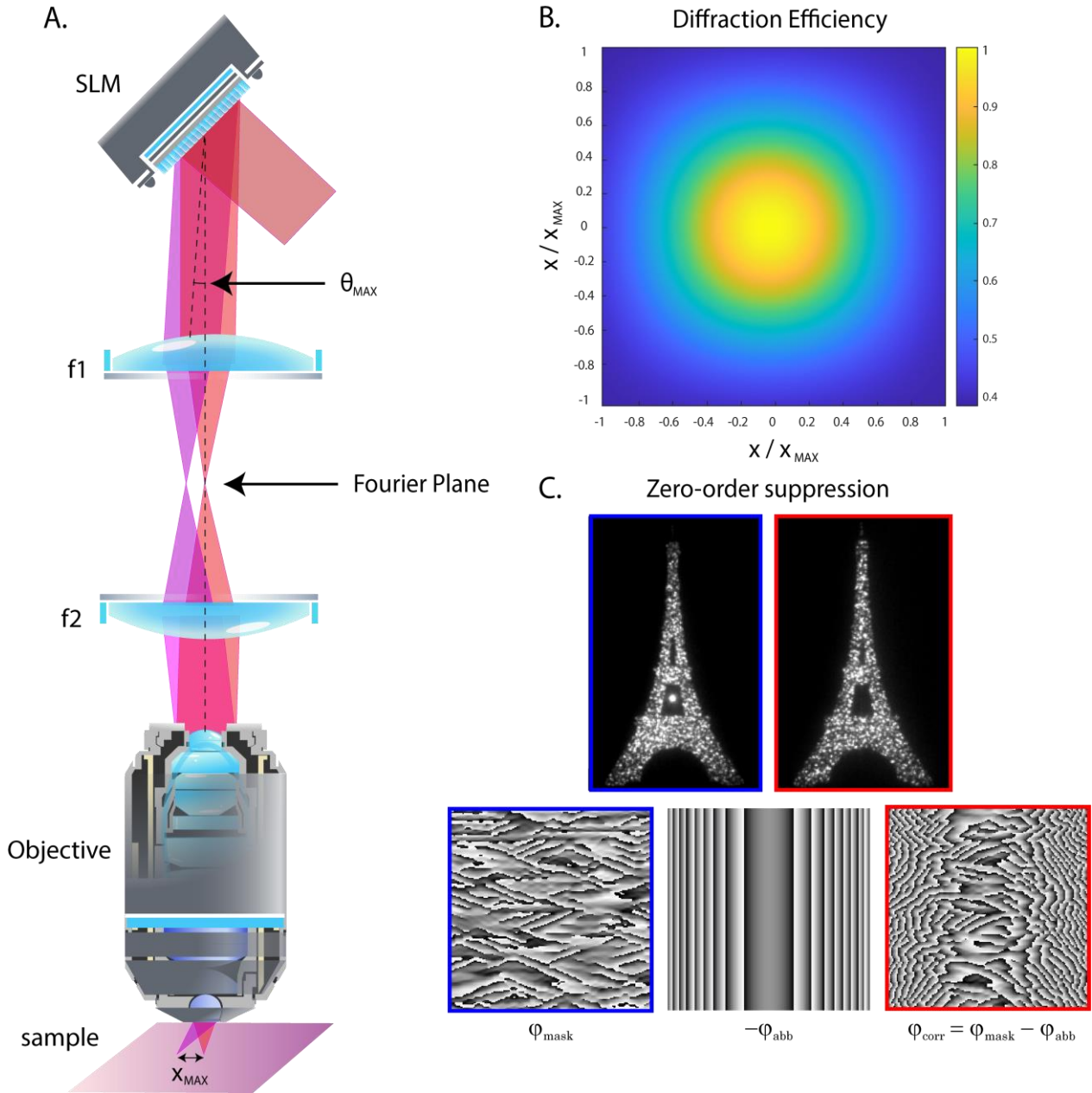


Figure 8. Parameters of an optical system for CGH with a SLM. **A.** Schematic representation of an optical system for CGH application in microscopy using a SLM. Two lenses (f_1 and f_2) are placed in a $4f$ configuration to image the SLM screen at the objective BFP. The maximal deflection angle of the SLM is represented as well as its maximal lateral displacement at the focal plane. **B.** Graphical representation of the diffraction efficiency. The X/Y axis are normalized with the

maximal lateral displacement for a given optical configuration. **C.** Zero-order correction shown in a 2P fluorescence image (blue square) where the spot in the middle (the zero order) of the Eiffel tower pattern (1st diffraction order φ_{mask}) is removed with a cylindrical lens placed in front of the SLM. The Eiffel tower pattern is preserved (red square) without any aberration by digitally counterbalancing ($-\varphi_{\text{abb}}$) with the SLM the aberration induced by the cylindrical lens (adapted from Hernandez *et al.*, 2014).

4) CHG is commonly used with approaches in which sequential generation of independent illumination patterns is achieved by projecting multiple holograms at a speed that is limited by the liquid crystal SLM refresh rate (60-300 Hz) and the cells illumination time (few to tens of ms). Recent advancements in SLM technology have enabled to achieve higher refresh rates, of 300-600 Hz (Thalhammer *et al.*, 2013; Marshel *et al.*, 2019). Additionally, optical strategies for ultrafast sequential light targeting have been developed (Faini *et al.*, 2023). The strategies involve dividing the SLM into multiple vertically aligned holograms that are rapidly scanned at the kHz rate.

Finally, when using large 2P excitation spots, a limitation arises as the axial resolution scales with the square of the lateral spot size when using low-NA spots or GPC and linearly with the lateral spot size in the case of CGH (Papagiakoumou, Ronzitti and Emiliani, 2020). Therefore, when creating extended excitation spots to stimulate the entire cell body, the single-cell axial resolution is lost. In the brain, neuronal circuits are extremely dense structures packed into 3D tissue (Helmstaedter, 2013), making it crucial to stimulate these structures with single-cell axial resolution. To overcome this limitation the generation of low-NA spots, GPC or CGH are combined with temporal focusing (TF) (Oron, Tal and Silberberg, 2005; Zhu *et al.*, 2005).

A.4.3 Temporal focusing combined with CGH

TF uses a diffraction grating to diffract the different spectral components of an ultrashort laser beam at various angles (Oron, Tal and Silberberg, 2005; Zhu *et al.*, 2005). The dispersion of the colors of the beam are then recombined after the objective, at the focal plane, where the grating is reimaged and all the colors of the laser spectra come together again. This dispersion leads to a broader pulse duration in all out-of-focus planes, which is then recompressed to its shortest value only at the focus of the excitation objective, broadening again when propagating away (figure 9A-C). The implementation of TF with a diffraction grating allows to decouple the dependence between lateral size of the spot and its axial resolution (Papagiakoumou *et al.*, 2008). CGH

combined with TF can be performed simultaneously with the diffraction grating placed after the SLM, in the focal plane of a lens placed in between the SLM and the grating. This innovative combination offers the potential to extend the size of the illumination spot, thereby enabling fast and precise excitation of multiple targets in 2D with single-cell axial resolution (figure 9B) (Papagiakoumou *et al.*, 2008; Ronzitti *et al.*, 2017; Papagiakoumou, Ronzitti and Emiliani, 2020). As it will be discussed in chapter 3, extending CGH with TF (CGH-TF) for light targeting in 3D can also be performed, but is not straightforward and requires to use multiple optical devices (Hernandez *et al.*, 2016; Pégard *et al.*, 2017; Accanto *et al.*, 2018; Faini *et al.*, 2023).

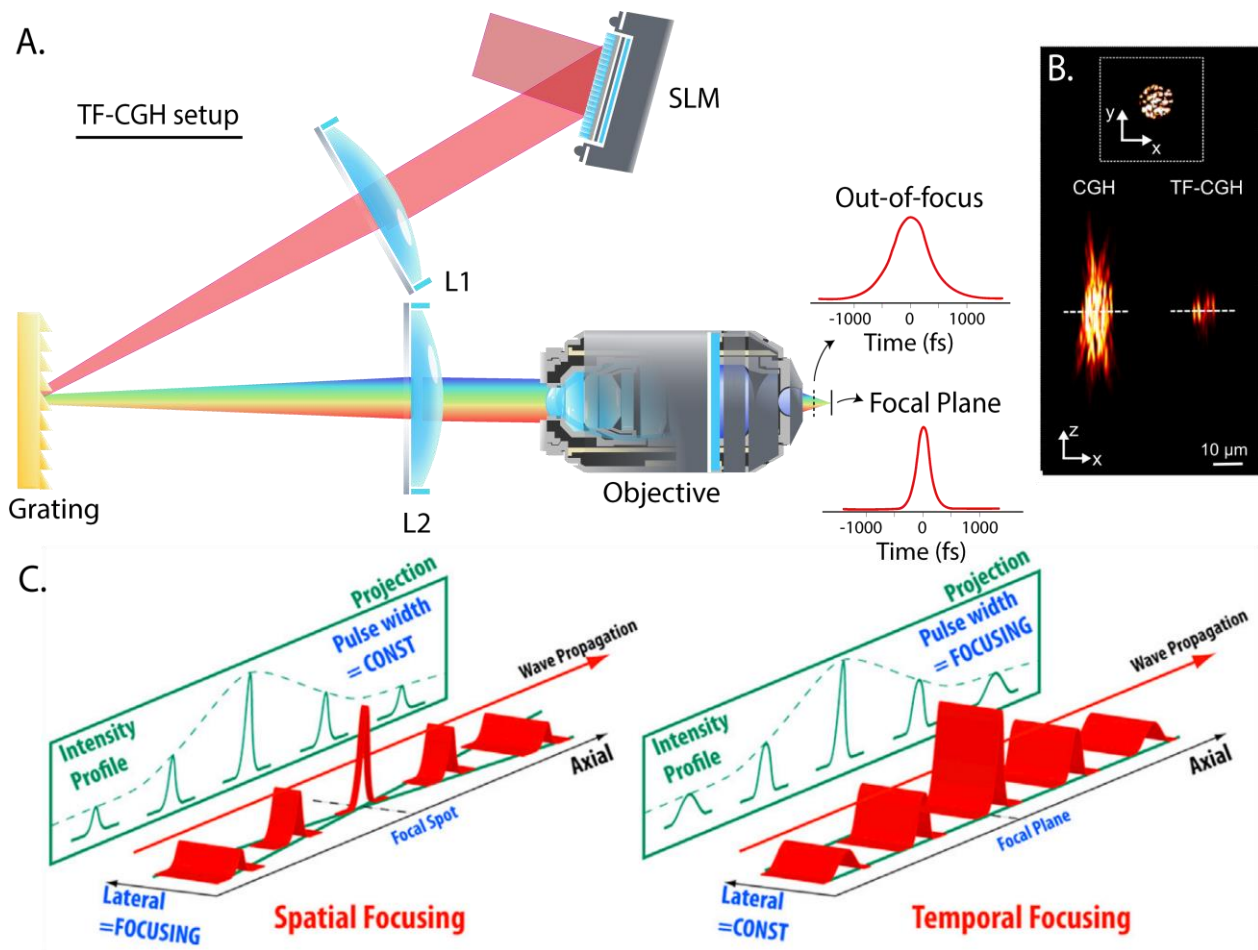


Figure 9. Implementation of TF combined with CGH. **A.** The SLM generates a 2D illumination pattern on a diffraction grating that is then imaged at the objective focal plane. The different wavelengths of an ultrashort laser pulse are dispersed by a diffractive grating. The different color components are recombined only at the focal plane achieving its shortest pulse duration. The laser beam illuminates the SLM which display a phase hologram to reproduced the desired pattern at the focal plane. **B.** Comparison between CGH without and with TF. Axial optical sectioning is

achieved thanks to TF that reduce the out-of-focus 2P excitation where the peak intensities of the femtosecond laser pulses are too weak to generate significant 2P absorption (adapted from Papagiakoumou, Ronzitti and Emiliani, 2020). **C.** Representation of the axial propagation of a temporally focused beam where the photons are not only focalized spatially (left) but also temporally (right) at the focal plane, thus reducing the out-of-focus excitation probability (adapted from So, Yew and Rowlands, 2013).

A.4.4 2P all-optical brain studies

Optogenetics can be implemented using all-optical systems where light-targeting photostimulation and functional imaging are performed simultaneously using genetically encoded reporters and actuators. The initial demonstration of 2P-all optical investigations were conducted in awake mice co-expressing the opsin C1V1 and the GCaMP3 calcium indicator (Rickgauer, Deisseroth and Tank, 2014; Packer *et al.*, 2015). In these experiments, two high-power ultrafast laser sources emitting at 920 and 1064 nm were used for imaging and photostimulation, respectively. Employing a scanning light-targeting approach, in which multiple diffraction-limited spots are generated by a SLM and then spirally scanned over multiple neurons, this configuration enabled, coupled with functional imaging, to trigger calcium transients in tens of neurons co-expressing the opsin and the calcium indicator (Packer *et al.*, 2015).

Since then, similar approaches have been used to link neuronal circuits manipulation to mice behavior, such as their response to sensory or cognitive input (e.g., orientated grating or cued action) (Carrillo-Reid *et al.*, 2019; Marshel *et al.*, 2019; Gill *et al.*, 2020; Robinson *et al.*, 2020; Daie, Svoboda and Druckmann, 2021; Russell *et al.*, 2022).

These experiments demonstrated the feasibility of 2P activation of individual neurons' activity while simultaneously recording spontaneous neuronal activity in a FOV of 240 μm (Carrillo-Reid *et al.*, 2019) in the visual cortex of awake mice. For example, in all-optical experiments with computational analysis of physiological data obtained from the recorded neuronal activity, specific neurons displaying a high degree of functional coupling to many other neurons have been identified. This coupling can be replicated by manipulating those cells (Carrillo-Reid *et al.*, 2019). Precisely, using 2P holographic optogenetics in the mouse visual cortex, behavioral performance (licking) in response to a visual task (visual stimuli) was altered by repetitively stimulating a group of neurons with single-cell precision. This behavior change could subsequently

be reproduced with a reduced external stimulus and by optogenetically activating an ensemble of neurons responsible of that behavior, creating a causal role of neuronal ensembles in visually guided behavior.

Another advantage of all-optical optogenetics is to simultaneously image and control neuronal activity at different axial planes, enabling a precise interrogation of multi-layered circuits. For example, the manipulation of a group of neurons at single-cell resolution using CGH-TF, combined with 2P imaging, such as with GCaMP, provides a means to investigate the contributions of individual neurons within dense networks such as the retinal circuit. Functional connectivity in the mouse retina, involving different types of cells (e.g., rod bipolar cells and ganglion cells), was studied by selectively activating individual and defined groups of rod bipolar cells while recording the activity evoked in connected ganglion cells. This approach allows the derivation of the receptive field that describes how one group of cells impacts the other type (figure 10) (Spampinato *et al.*, 2022).

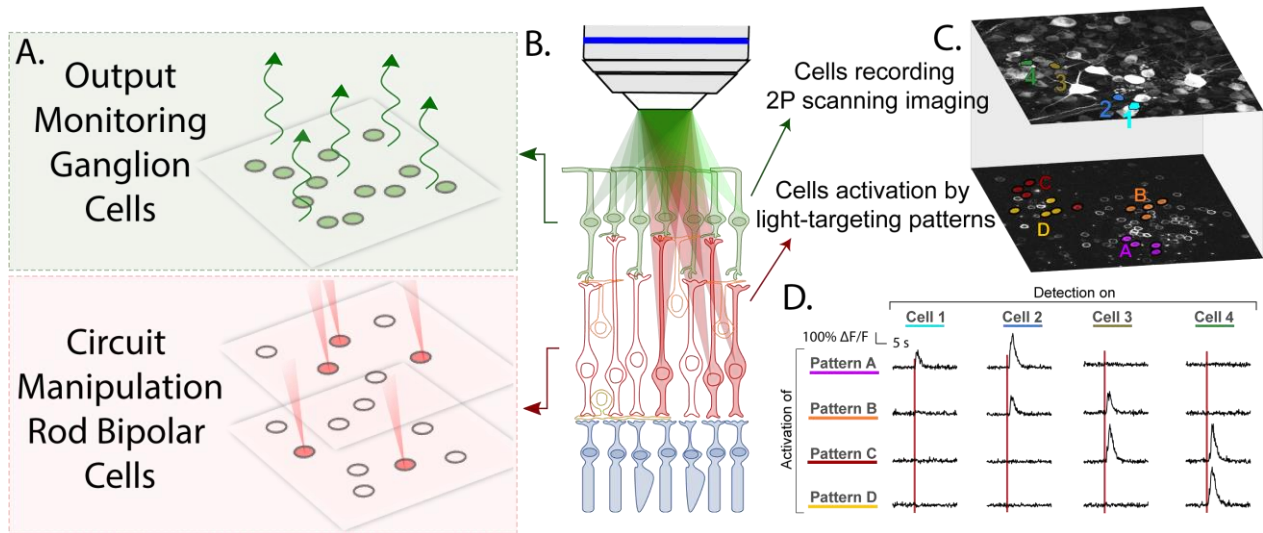


Figure 10. 2P all-optical investigations in retina circuits. **A.** Scheme of 2P optogenetics manipulation of retinal information at single-cell resolution and 2P imaging recording of the retinal output signal to dissect retinal circuits. **B.** Schematics of simultaneous photoactivation of groups of Rod Bipolar Cells (RBCs) by using a SLM and TF and functional imaging of Ganglion Cells (GCs) via 2P raster scan. **C.** CoChR/GFP-expressing RBCs (up) and GCaMP6-expressing GCs (down) within the same XY FOV located on retina layers 60 μm axially apart. Different colors correspond to different patterns of photoactivation across RBCs (up) and different monitored GCs (down). **D.** Calcium response induced on different GCs cells upon photoactivation of RBCs with different illumination patterns. Each row corresponds to a different pattern of stimulation in the

RBC layer as shown in C. Each line corresponds to the response of a different GC as shown in C. The red line indicates the timing of the holographic stimulation (adapted from Spampinato *et al.*, 2022).

A.4.5 Challenges of 2P all-optical brain studies

In this section, I will discuss several key challenges that could significantly broaden the applications of 2P optogenetics that were addressed during my PhD such as 1) performing these studies in freely moving animal or 2) with a more compact and simple system for lasers with multiple colors.

1. Freely moving: Currently, 2P all-optical experiments in mouse brain have been performed in head fixed animals. This is a limitation when studying neuronal circuits implicated in tasks related to orientation, navigation, complex motion tasks or social behavior, requiring freely moving mice (Cai *et al.*, 2016; Murugan *et al.*, 2017; Wang *et al.*, 2017; Levy *et al.*, 2019; Giovanniello *et al.*, 2020; Olson *et al.*, 2020; Karigo *et al.*, 2021; Parker *et al.*, 2022).

To overcome this limitation, several systems have been miniaturized to record the neuronal activity in freely moving animal, including head-mounted 1P wide-field miniscopes (Aharoni and Hoogland, 2019; Aharoni *et al.*, 2019), 2P or 3P miniaturized microscopes connected to a single optical fiber with a portable scanning unit attached to the animal's head (figure 11A) (Helmchen *et al.*, 2001; Göbel *et al.*, 2004; Duemani Reddy *et al.*, 2008; Sawinski *et al.*, 2009; Zong *et al.*, 2017, 2021; Klioutchnikov *et al.*, 2020, 2023; Park *et al.*, 2020; Li *et al.*, 2021) or 1P or 2P systems using a bundle of optical fibers with the scanning and beam manipulation unit placed before the bundle (figure 11B) (Szabo *et al.*, 2014; Ozbay *et al.*, 2018).

Most of these systems can only perform imaging in freely moving mice while only few configurations have so far enabled all-optical circuit manipulation. Among them, few systems have been developed to perform wide-field 1P excitation to photostimulate the same (Stamatakis *et al.*, 2018) or a different (de Groot *et al.*, 2020) brain area as the recorded one. Patterned light for multi-target optogenetic photostimulation has been also performed combining 1P excitation with a DMD (Zhang *et al.*, 2021), by coupling a standard bench microscope to a fiber bundle and attaching the output facet of the fiber to a mini-objective (figure 11B) (Szabo *et al.*, 2014). All these systems used 1P excitation light for both recording and manipulating the neuronal activity. This introduced

several limitations due to the use of visible wavelengths and 1P excitation, which hindered deep illumination from the brain's surface and the spatial resolution of the targeted light to manipulate individual neurons in a dense neuronal population.

The main goal of my PhD has been to develop a 2P fiber-based microscope, 2P-FENDO (Accanto*, Blot*, Lorca-Cámara* *et al.*, 2023), to perform for the first time 2P optogenetics and 2P imaging in freely moving mice. This system is specifically designed for fast recording neuronal activity and performing high-resolution optogenetic stimulation in freely moving mice, using 2P excitation coupled to a multicore fiber. In chapter 2, I will present the state of the art of existing optical strategies to study the neuronal activity in freely moving mice and the details of 2P-FENDO. The details will include a description of the setup's characterization when using a fiber bundle and a gradient refractive index (GRIN) lens, its application in conducting 2P all-optical studies in freely moving mice, and the recent advancements made to enhance the capabilities of 2P-FENDO.

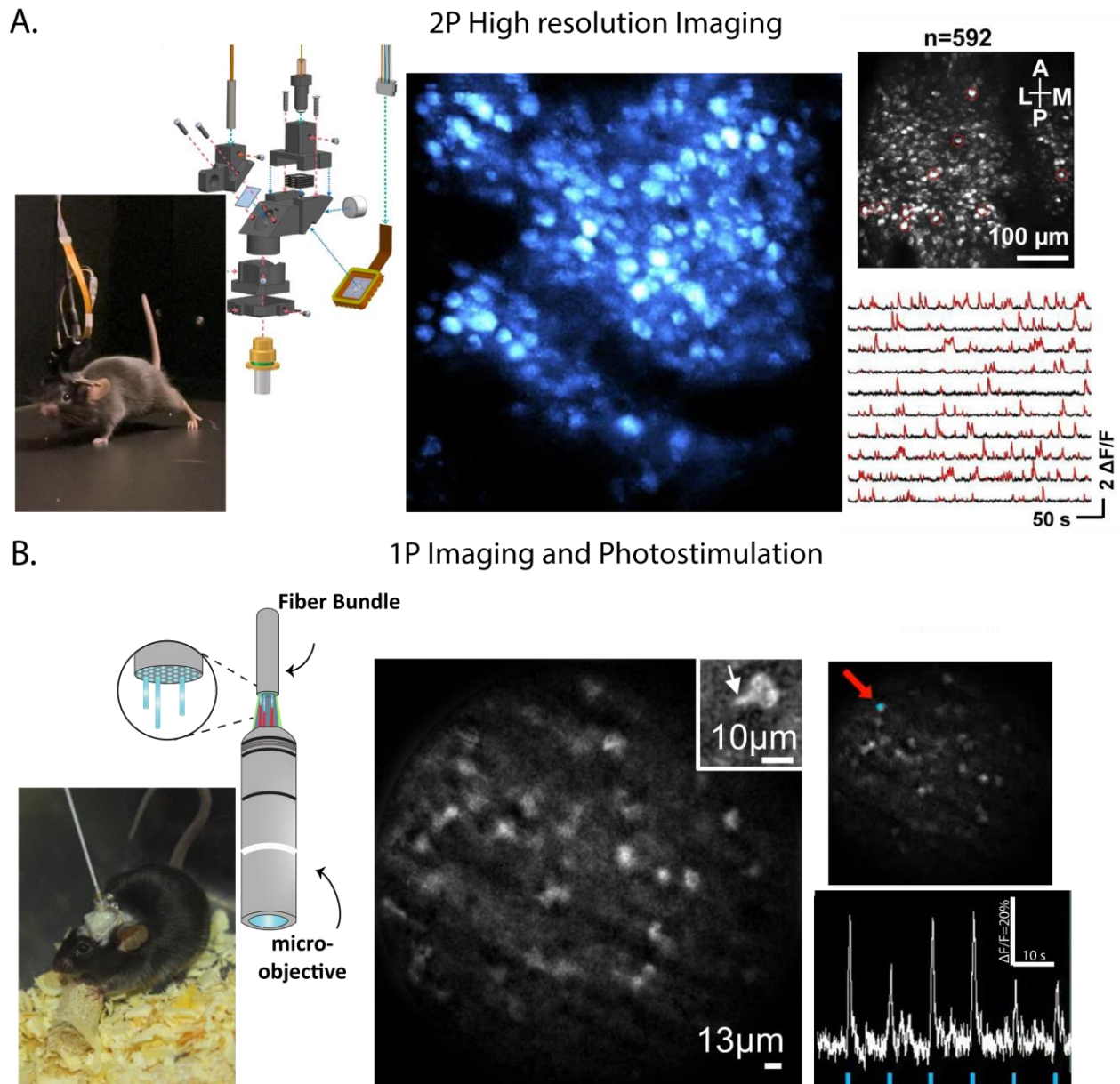


Figure 11. Towards 2P holographic optogenetics in freely moving animals. 2P microscopes could be directly coupled to an optical fiber or a miniaturized and head mounted microscope. **A.** 2P high resolution system that allows the recording of hundreds of neurons simultaneously with a single core fiber attached to a miniaturized and light miniscope (adapted from Zong *et al.*, 2021). **B.** 1P fiberscope to perform all optical experiments with 1P imaging and 1P holographic optogenetics through a fiber bundle and a micro-objective. Single-cell resolution is achieved near the surface of the brain and single cell optogenetic stimulation is achieved as shown in the calcium activity traces, where the activity increases when the neuron is stimulated (time of stimulation indicated with the blue lines) (adapted from Szabo *et al.*, 2014).

2. Simplicity and multicolor: 2P optogenetics can be performed with a scanless approach by using CGH and TF (TF-CGH) to create multiple extended spots that illuminate simultaneously the desired neurons with single-cell resolution. Most implementations using this strategy can only achieve 2P optogenetic photostimulation with high temporal precision within a 2D region, which corresponds to the image plane of the diffraction grating. To extend experiments to a 3D region, additional optical elements are generally required beyond the diffraction grating for TF and a single SLM. For example, an additional SLM or a static phase mask can be used together with the diffraction grating for TF, which is placed in between the two SLMs (or a SLM and a phase mask) (Accanto *et al.*, 2018). Other systems also use a rotating diffuser or a galvanometric mirror to achieve multiple spots in 3D with single-cell precision (Faini *et al.*, 2023). However, these systems are non-straightforward to align and synchronize as they used multiple devices, increasing the overall complexity and cost of the experiment. Finally, the use of multiple lasers at different central wavelengths for multicolor experiments aligned into the same beam path complexifies more the system. The use of a diffraction grating for TF, which disperse each wavelength of the lasers at different angles, need an additional beam switching element to recombined the different wavelengths to focalize them at the same focal plane.

To overcome these challenges, during my PhD I developed a new approach for multicolor, single-cell targeting in a 3D volume by replacing the diffraction grating for TF with a multicore optical fiber bundle. This system reduces significantly the complexity of previously described setups. Additionally, due to the replacement of the diffraction grating with a fiber bundle, which randomizes the phase among its different cores at the output, the system becomes nearly wavelength independent. It is shown that this system can be used to multicolor experiments where two lasers at different wavelengths are coupled into the fiber bundle, to perform multicolor 3D light patterning with high resolution. This can be important for experiments that require dual-color imaging and photostimulation of the same or different subsets of neurons, or dual color activation and inhibition of the same cell to control its activity. In chapter 3, I will provide an overview of the current state of 3D light targeting approaches, and I described and characterized a new approach (Lorca-Cámara *et al.*, 2024), with a comparison with existing strategies.

A. 5. Fibers Bundles

Throughout my PhD, fiber bundles have played a central role in our developed systems due to their various advantages that allowed us to overcome the challenges presented previously. In this section, I introduce fiber bundles, elucidating its optical properties and showing how ultrashort laser pulses propagates through them to perform 2P all-optical studies. I will particularly focus on the temporal and spectral broadening introduced by fiber bundles and delve into potential compensation techniques.

Optical fiber bundles are constructed by bundling together hundreds or even thousands of individual fiber cores, forming an elongated and flexible form of optical waveguide. These bundles can vary in size depending on factors such as the dimensions of the individual cores or the total number of cores within the bundle. This leads to bundle diameters ranging from a few hundred of micrometers to several millimeters, with lengths spanning from several centimeter to a few meters (figure 12). In most cases, fiber bundles are crafted from either glass or polymers. Among the glass materials, fused silica (SiO_2) stands out as a popular choice for various applications. This is due to its numerous beneficial properties, which have already been extensively employed in optical fiber communications, fiber lasers and amplifiers, as well as fiber-optic sensors (Snyder and Love, 1983).

In terms of the silica properties, silica boasts excellent optical transparency across a broad spectrum, in particular within the infrared region, where it exhibits low absorption and scattering losses. Silica fibers can be conveniently cleaved, polished or fused to achieve flat and clean surfaces. Their mechanical strength against pulling or bending is notably high, though this attribute naturally depends on factors such as fiber thickness and the number of cores. For instance, minimal bending radius ($< 1\text{cm}$) is obtained for a 1.65mm diameter fiber bundle composed by 18k cores (Schott fiber bundle) whereas a 0.55mm diameter fiber bundle composed by 15k cores (Fujikura fiber bundle) achieve a bending radius of 30 cm. The variations in bending radius are primarily attributed to differences in the fabrication process. The Schott fiber bundle is produced using a leaching process, which contributes to its enhanced flexibility and a much smaller bending radius compared to the Fujikura fiber bundle. Silica fibers are chemical stable, being resistant to water, humidity and even high temperatures. The refractive index of these fibers can be altered by introducing diverse dopant materials. This doping can encompass not only the fiber core but also the cladding surrounding the cores as the NA of the fiber depends on the refractive index of the

cores (n_1) and the cladding (n_2): $NA = \sqrt{n_1^2 - n_2^2}$. This results in a diverse range of NA values, mostly between 0.1 and 1 with different dopant materials. Notably, silica fibers also exhibit high damage threshold with short laser pulses (Gambling, 2000; Paschotta, 2020e).

For the fabrication of the fiber bundles, there is a wide range of methods, although a common prerequisite usually is a fiber preform in which, typically, a cylindrical optical glass is used for drawing the optical fiber. In the case of multiple cores fibers, like fiber bundles, individual single-core fibers are assembled together to yield a bundle. The arrangement of single-core fibers often adopts a hexagonal pattern, although circular, rectangular, irregular, and alternative configurations can also be employed (figure 12). The creation of single-core employs diverse techniques such as vapor deposition strategies or the rod-in tube method. In the latter approach, a glass rod is inserted into a lower refraction index glass tube that are connected by heating. The subsequent process involves pulling out cooling the fiber to solidified it. The fiber core diameter can be precisely controlled via manipulation of the pulling speed and the temperature, thereby ensuring a constant fiber core diameter throughout. Once all the fibers are assembled, a thin polymer coating is typically applied for protective purposes, followed by curing. Acrylate or silicone materials are frequently chosen for these coatings due to their capacity for high-temperature resistance (Wang *et al.*, 2006; Paschotta, 2020b).

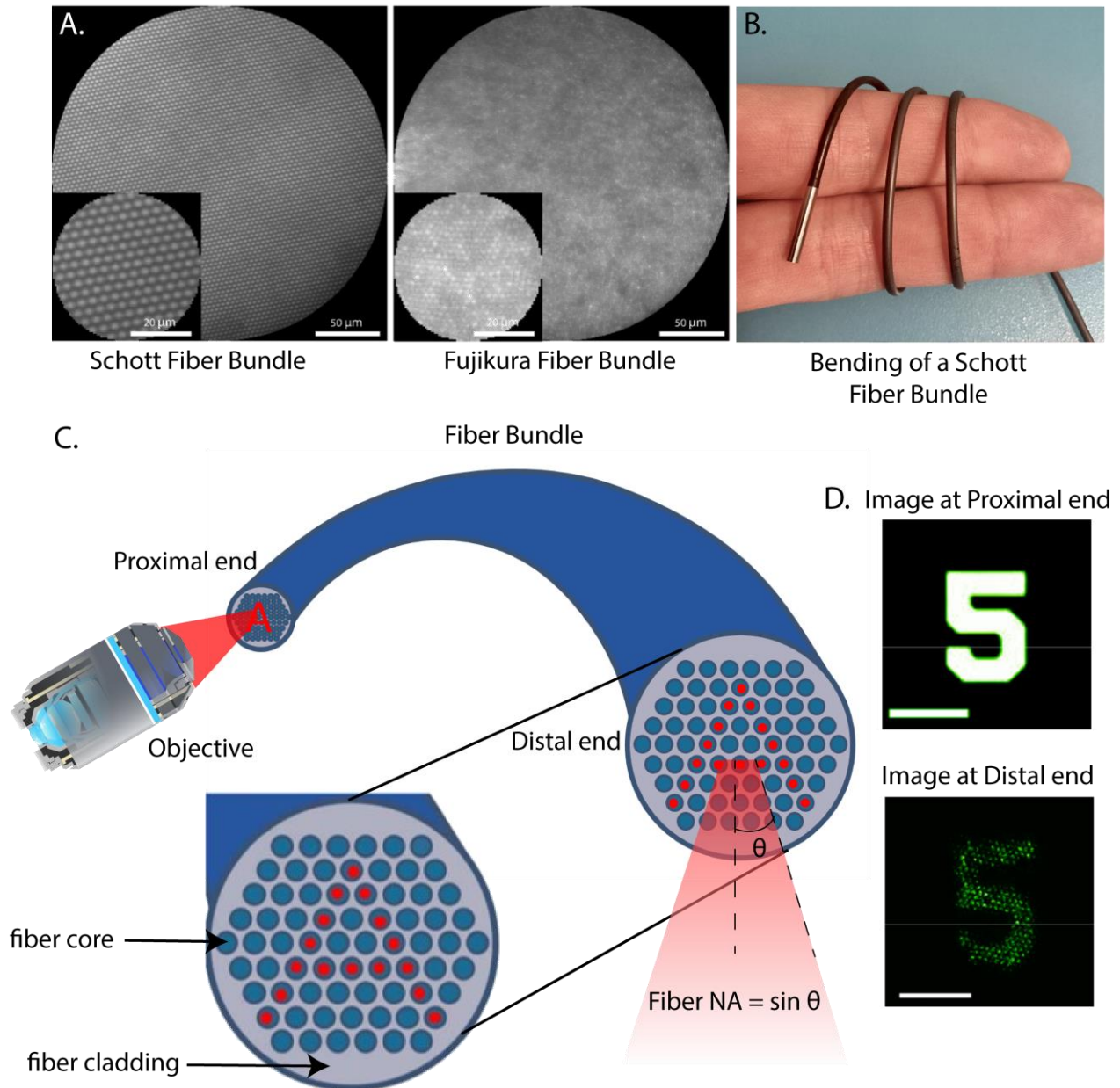


Figure 12. Principles of Fujikura and Schott fiber bundles. **A.** Measured 2P fluorescence when the fiber bundles are illuminated and imaged into a uniform rhodamine sample. Imaged and zoomed views of a 1.1 mm (left) diameter Schott fiber bundle and 0.55 mm diameter Fujikura fiber bundle (right) with 8 μm diameter fiber cores (left) and 4 μm diameter fiber cores (right) with hexagonal configurations. **B.** Example of the bending of a Schott fiber bundle of 1.1 mm diameter, 0.9 m length and 18k cores of 8 μm diameter fiber cores. **C.** Schematic of light launching the proximal end of the fiber bundle with an illumination NA similar to the fiber NA with a certain pattern (letter A) and the same pattern emerging from the distal end through the illuminated cores with an angle given by the fiber NA. **D.** Original image transmitted to the proximal end of the fiber bundle and experimental image captured at the distal end of the fiber bundle (adapted from Porat *et al.*, 2016).

The fiber bundles are characterized by three crucial parameters: the core size, the inter-core distance and the NA of the fiber. The typical core sizes (a) of these bundles range from 3 to 20 micrometers. To quantify the number of modes that propagates through the cores, the V number is employed, a dimensionless parameter defined as:

$$V = \frac{2\pi}{\lambda} \cdot a \cdot NA$$

The number of modes that are present in the case of the fiber bundles used during my thesis ($a = 4 - 5 \mu\text{m}$, $NA = 0.2 - 0.3$) are between 2 - 6 modes, which are close to a single mode fiber propagation than to a multimode fiber (> 100 modes). For a given laser wavelength, the total electric field distribution in a multimode fiber results from a superposition of contributions from the different modes. The intensity profile is influenced not only by the powers attributed to all the modes, but also by their relative phases. This dynamic interplay can lead to constructive or destructive interference of diverse modes at specific locations within the fiber. Both the powers and optical phases are initially determined by the launching conditions, and the relative phases (and thus the interference conditions) evolve further due to the mode-dependent propagation constants (Bhatia, Rustagi and John, 2014; Sivankutty *et al.*, 2016).

In comparison to single-mode fibers, multimode fibers and fiber bundles have a lower NA of 0.2 - 0.3, accompanied by higher propagation losses without bending as irregularities between the core-cladding interface can scatter the light more efficiently. Launching light into a multimode fiber or a fiber bundle is easier as they have greater tolerances concerning the spatial location and propagation angle of the incident light (figure 13). However, specific requirements must be met to effectively launch light into the fiber bundle. For instance, the input light's angles should not exceed the arcsin of the fiber bundle NA. Another requirement, to minimize power losses, it is important to ensure that the incoming light exclusively interacts with the fiber cores and avoids the cladding. In fiber bundles with a hexagonal arrangement, power losses can exceed 50% if the light encompasses the entire bundle, leading to substantial absorption of the light by the cladding (Paschotta, 2020a). Fiber bundles transmission properties can also vary with the incident illumination angle. The illumination can also introduce autofluorescence and Raman scattering due to the refraction index variations in the fiber bundles. This is more pronounced when using UV

light but it is also presented in the IR range. The autofluorescence effect represent an increase of the background signal when performing imaging (Udovich *et al.*, 2008).

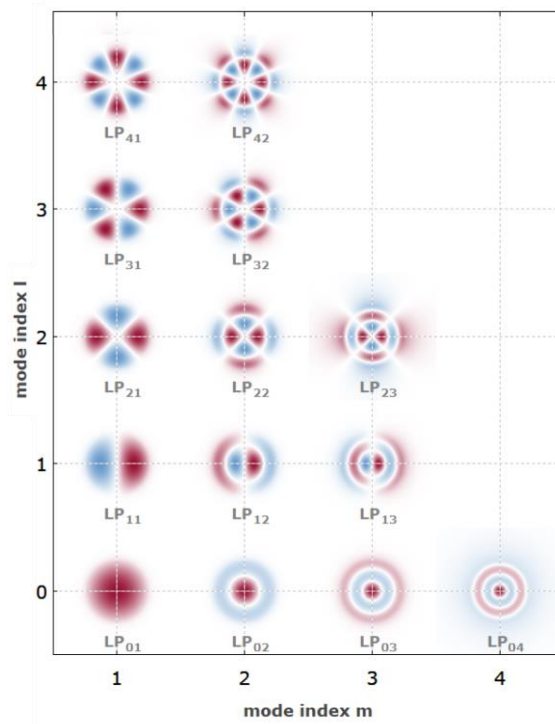


Figure 13. Electric field amplitude profiles for all the guided modes of an optical fiber at a specific wavelength. The fundamental mode (LP₀₁) with an approximately Gaussian intensity distribution, and a number of higher-order modes with more complicated spatial profiles are shown (Paschotta, 2020c).

A.5.1 Ultrashort pulses propagation in fiber bundles

The electromagnetic wave propagation through dispersive nonlinear media like the optical fibers introduce some effects that have been studied and that have been considered during my PhD while using ultrashort light pulses.

Group Delay Dispersion

Light propagation inside a dielectric medium depends on the optical frequency ω . This effect, referred to as chromatic dispersion, results from the dependence of the refraction index of the medium on the frequency $n(\omega)$. This dependence can be approximated by the Sellmeier equation (Arregger, 1973) :

$$n^2(\omega) = 1 + \sum_{j=1}^m \frac{B_j \omega_j^2}{\omega_j^2 - \omega^2}$$

where ω_j are the resonance frequencies of the medium and B_j is the strength of each resonance j . Fibers are normally made with bulk-fused silica, whose parameters for this equation can be found in (Malitson, 1965). Fiber dispersion is particularly manifested when working with ultrashort pulses as different colors travel at different speed $c/n(\omega)$ as it happens with fiber bundles and 2P microscopy. This effect can be accounted expanding the mode-propagation constant β in a Taylor series about the central frequency ω_0 at which the laser spectrum is centered:

$$\beta(\omega) = n(\omega) \frac{\omega}{c} = \beta_0 + \beta_1(\omega - \omega_0) + \frac{1}{2}\beta_2(\omega - \omega_0)^2 + \dots$$

where $\beta_1 = 1/v_g$ and v_g represent the group velocity, i.e., the speed of the envelope of the optical pulse. β_2 represents the dispersion of the group velocity and is responsible for pulse broadening. It is possible to quantify the total dispersion by the dispersion parameter D that is related to β_2 :

$$D = \frac{d\beta_1}{d\lambda} = -\frac{2\pi c}{\lambda^2} \beta_2$$

This dependency describes the phenomenon call group velocity dispersion (GVD) (figure 14). Depending on the sign of the GVD parameter, the fiber can exhibit normal dispersion as $D < 0$ ($\beta_2 > 0$) or anomalous dispersion if $D > 0$ ($\beta_2 < 0$). The contribution of D depends on the fiber-design parameters such as the core radius or the core-cladding index. Therefore, there exist fibers designed to compensate for the dispersion effect, known as dispersion-compensation fibers (DCFs). In standard silica fibers, $\beta_2 \sim +35 \text{ fs}^2/\text{mm}$ at 800 nm and $\beta_2 \sim -26 \text{ fs}^2/\text{mm}$ at 1500 nm, being $\beta_2 \sim 0$ at 1300 nm. It is also important to define the group delay dispersion (GDD), as the GVD by unit length. For long fiber bundles the group delay dispersion can be important. For example, with a 2-meter fiber bundle the GDD can be $> +40000 \text{ fs}^2$ at 1000nm.

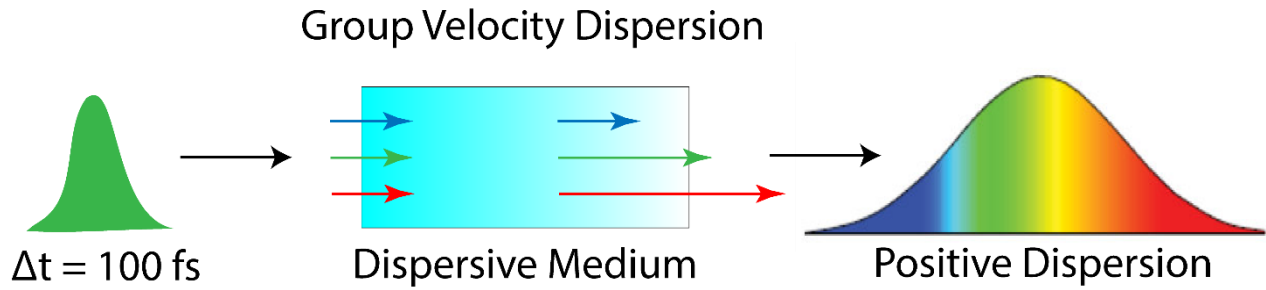


Figure 14. Group Velocity Dispersion of an ultrashort laser pulse propagating in a dispersive medium. The spectral components of the laser pulse (blue, green and red arrows) propagate at a different speed in the medium, introducing a delay. In this case, a positive chirp (dispersion) delays more the short wavelength compared to the long wavelengths so that the initial pulse is broadened after propagating through the dispersive medium.

The effect of GVD on optical pulses propagating inside a fiber bundle for a Gaussian pulse of amplitude $U(z, T)$ can be analytically determined for any time T at any distance z inside the fiber:

$$U(z, T) = \frac{T_0}{(T_0^2 - i\beta_2 z)^{1/2}} \exp\left(-\frac{T^2}{2(T_0^2 - i\beta_2 z)}\right),$$

where T_0 is the temporal pulse width (Marcuse, 1980).

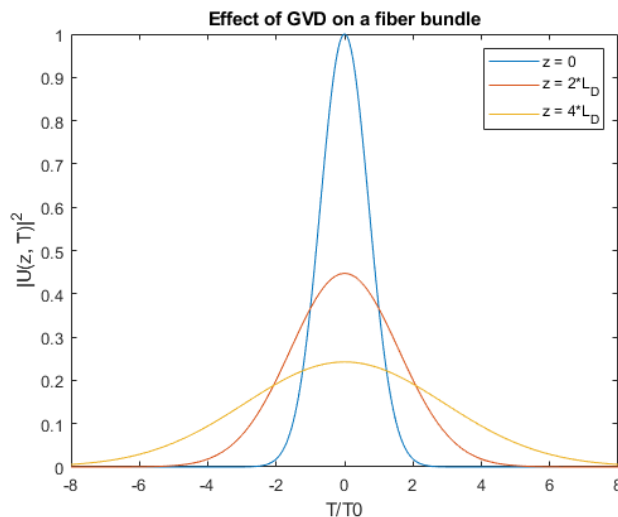


Figure 15. Dispersion-induced broadening of a Gaussian pulse inside a fiber at $z = 0, z = 2L_D$ and $z = 4L_D$. $L_D = T_0^2/\beta_2$. Group velocity dispersion at 1030 nm $\beta_2 = 1060 \text{ fs}^2/\text{m}$ and $T_0 = 150 \text{ fs}$.

In figure 15 it is clearly shown that pulse shapes can vary in function of the fiber length for this example where a Gaussian beam is propagated through a silica fiber bundle. Depending on the specific situation, GVD can have different important effects. It is responsible for either dispersive temporal broadening or compression of ultrashort pulses, like in this case, depending on the dispersion properties of the fiber bundle and the wavelength used.

To compensate for pulse broadening caused by GVD, techniques such as dispersion-compensating fiber (Jones *et al.*, 2007) or glass rods (for anomalous dispersion fibers) can be designed. These methods are used to counterbalance the fiber's dispersion, resulting in a final GVD close to zero. Additionally, modifiable chirping systems with two diffraction gratings are mostly used to compensate for the dispersion pulse broadening introduced by GVD, so that the final pulse duration is similar to the original laser pulse duration (Treacy, 1969). During my thesis, I employed the latter approach, which involved incorporating a pulse compressor inside the lasers, to compensate for the dispersion introduced primarily by the fiber bundle but also by other optical components within the systems I worked with.

Self-Phase Modulation

The Kerr effect is a nonlinear optical phenomenon that occurs when light propagates through crystal and glasses, including fiber bundles. This effect manifests when high intensity light (I) from an ultrashort pulse propagates through these materials, modifying their refractive index according to:

$$n(T) = n_1 + n_2 I(T),$$

where n_1 and n_2 are the linear and nonlinear refractive indices, respectively, and I is proportional to the square of the electric field at any time T. For silica fibers, the nonlinear index is $\sim 3 \cdot 10^{-16} \text{ cm}^2/\text{W}$. The temporal variation leads to Self-Phase Modulation (SPM), which depends on the pulse's temporal profile, its wavelength and intensity (Stolen, R.H., Ashkin, 1973;

Bahaa E. A. Saleh, 1991). SPM leads to spectral narrowing or broadening of optical pulses (Fisher and Bischel, 1975) and becomes important when high power is used as the nonlinear phase shift can be expressed as:

$$\phi_{NL}(T) = n_2 I(T) \omega_0 L / c,$$

where L is the fiber length.

It is possible to describe the nonlinear spectral narrowing or broadening from the nonlinear phase. When the pulse propagates through a fiber, new frequency components are generated: $\omega(T) = \omega_0 + \delta\omega(T)$, where $\delta\omega(T) = d\phi_{NL}(T)/dT$ that is referred to as frequency chirping. These new frequencies can be different from the initial pulse spectrum and therefore they can broaden or narrow the pulse spectrum after the propagation through the fiber. For instance, for an unchirped Gaussian pulse, SPM induce spectral broadening (pulse narrowing) as shown in figure 16.

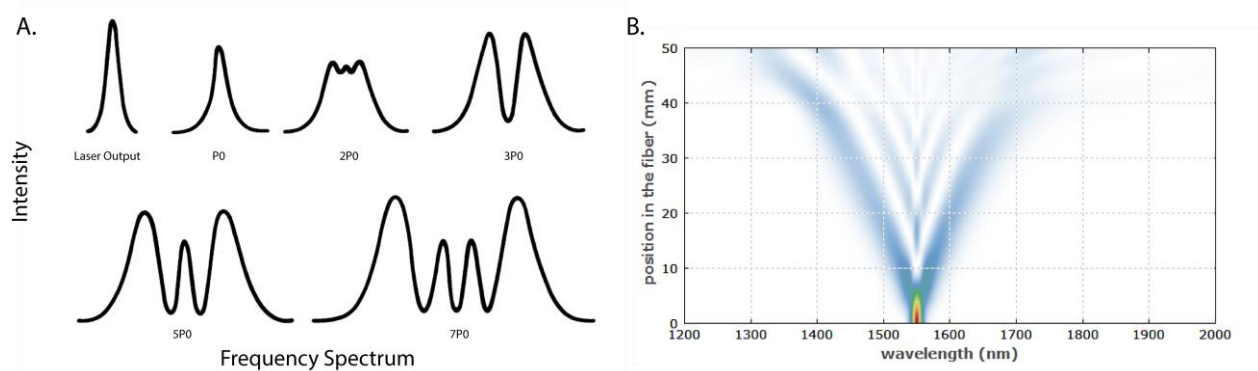


Figure 16. Self-phase modulation effect in a single core fiber. **A.** An initial unchirped Gaussian pulse of 180 fs is propagated through a 3.35 μm silica single core fiber at different powers per core (from P0 to 7P0), where P0 is the threshold peak power that induces the SPM effect. **B.** Simulation of the propagation of an ultrashort pulse in a fiber, where self-phase modulation is the dominant effect on the pulse within the first 30 mm of propagation distance (Paschotta, 2020d).

If the initial pulse is chirped, SPM leads to spectral narrowing (Stolen and Lin, 1978). As shown in figure 17, the spectrum of the initial pulse (figure 17A) is narrowed after propagation through a single core fiber (figure 17B). The direct consequence of the spectral narrowing when high peak powers of ultrashort pulses propagate through a fiber is the pulse broadening (Helmchen,

Tank and Denk, 2002; Lelek *et al.*, 2007; Kalashyan *et al.*, 2012; Choi and So, 2014; Lefort *et al.*, 2014).

Figure 17 illustrates the pulse broadening due to SPM of a chirped Gaussian pulse after the propagation in a 5.5 μm fiber. SPM can be reduced by using low peak energies, by reducing the fiber length or by compensating it inducing spectral broadening by propagating the transform-limited pulse into polarized maintained fibers (PMF) (Lefort *et al.*, 2014).

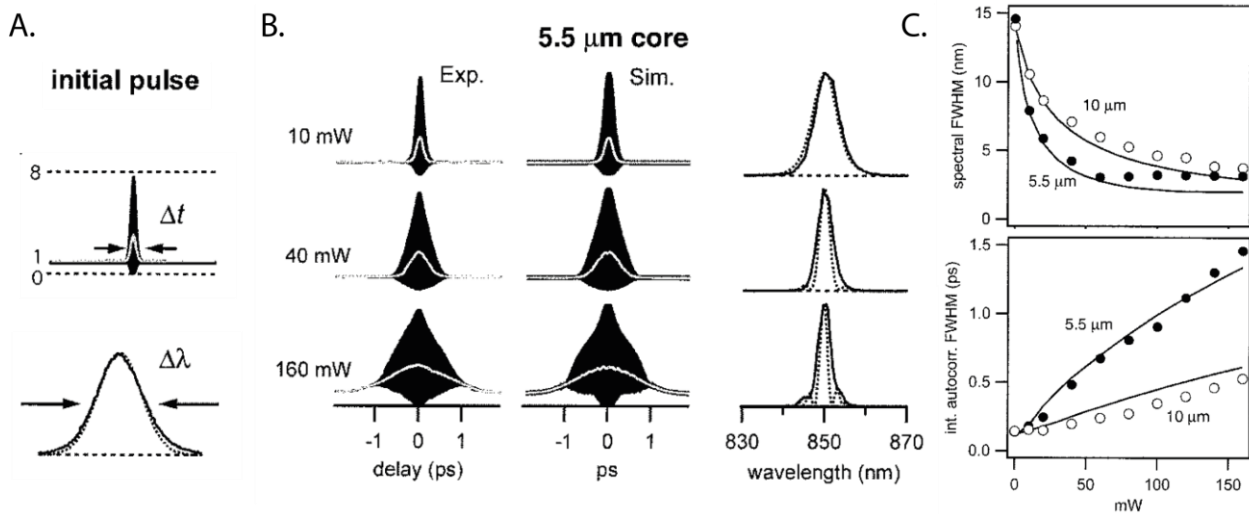


Figure 17. Self-phase modulation effect in a 5.5 μm core fiber as a function of the average transmitted power. **A.** Autocorrelation traces (up) and normalized spectrum (down) for the initial pulse. **B.** Experimental (left) and simulated (middle) autocorrelations, and spectra (right, simulated spectra dashed) for a 5.5 μm core fiber at three different power levels. **C.** Pulse broadening and spectral compression as a function of average transmitted power. FWHM of (A.) intensity autocorrelation and (B.) spectrum for a 5.5 μm core fiber (filled circles) and a 10 μm core fiber (open circles). The solid curves represent the numerical simulations (adapted from Helmchen, Tank and Denk, 2002).

The spectral narrowing, or pulse broadening, due to SPM have been also measured by employing the same fiber bundle as the one used during my PhD. In this case, Ozbay *et al.*, 2018 measured the output pulse spectrum and the spectrum after propagating a chirped ultrashort laser pulse (initial pulse duration 80 fs, 910 nm central wavelength, 80 MHz repetition rate) through a Fujikura fiber bundle (figure 18). Different powers per core where used (1 mW and 40 mW) showing that for high powers per core the pulse spectrum is narrower due to the effect of SPM.

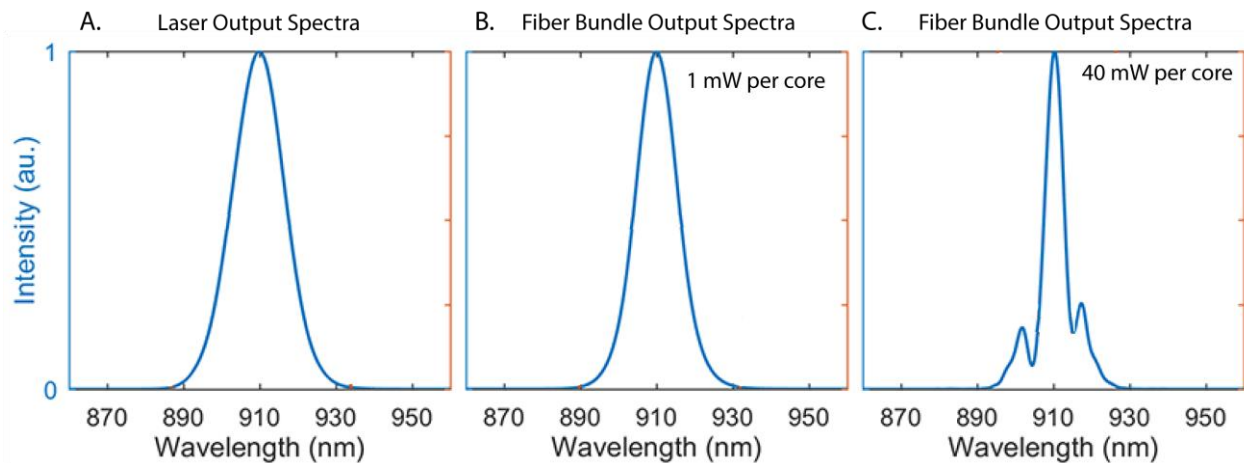


Figure 18. Spectral narrowing in a chirped Gaussian pulse. **A.** Measured spectral intensities of the laser pulse at the output of the laser, **B.** at the output of the fiber bundle with low power per core (1mW) and **C.** with high power per core (40mW) that induces spectral narrowing, i.e. pulse broadening, due to SPM effect (adapted from Ozbay *et al.*, 2018).

A.6 References

- Accanto, N. *et al.* (2018) 'Multiplexed temporally focused light shaping for high-resolution multi-cell targeting', *Optica*, 5(11), p. 1478. doi: 10.1364/optica.5.001478.
- Accanto, N. *et al.* (2023) 'A flexible two-photon fiberscope for fast activity imaging and precise optogenetic photostimulation of neurons in freely moving mice', *Neuron*, 111(2), pp. 176-189.e6. doi: 10.1016/j.neuron.2022.10.030.
- Aharoni, D. *et al.* (2019) 'All the light that we can see: a new era in miniaturized microscopy', *Nature Methods*, 16(1), pp. 11–13. doi: 10.1038/s41592-018-0266-x.
- Aharoni, D. and Hoogland, T. M. (2019) 'Circuit investigations with open-source miniaturized microscopes: Past, present and future', *Frontiers in Cellular Neuroscience*, 13(April), pp. 1–12. doi: 10.3389/fncel.2019.00141.
- Aharoni, T. and Shoham, S. (2018) 'Phase-controlled, speckle-free holographic projection with applications in precision optogenetics', *Neurophotonics*, 5(02), p. 1. doi: 10.1117/1.nph.5.2.025004.
- Akemann, W. *et al.* (2015) 'Fast spatial beam shaping by acousto-optic diffraction for 3D non-linear microscopy', *Opt. Express*, 23(22), pp. 28191–28205. doi: 10.1364/OE.23.028191.
- Amako, J., Miura, H. and Sonehara, T. (1995) 'Speckle-noise reduction on kinoform reconstruction using a phase-only spatial light modulator', *Appl. Opt.*, 34(17), pp. 3165–3171. doi: 10.1364/AO.34.003165.
- Arregger, C. E. (1973) 'Light transmission optics: D. Marcuse Van Nostrand Reinhold Company, 1972. Bell Laboratories Series, pp 444, £12.25', *Optics & Laser Technology*, 5(2), p. 93. doi: [https://doi.org/10.1016/0030-3992\(73\)90045-5](https://doi.org/10.1016/0030-3992(73)90045-5).

- Arrenberg, A. B. *et al.* (2010) 'Optogenetic control of cardiac function.', *Science (New York, N.Y.)*, 330(6006), pp. 971–974. doi: 10.1126/science.1195929.
- Bahaa E. A. Saleh, M. C. T. (1991) *Fundamentals of Photonics, John Wiley & Sons, Ltd.* John Wiley & Sons, Ltd. doi: 10.1002/0471213748.
- Bamann, C. *et al.* (2008) 'Spectral characteristics of the photocycle of channelrhodopsin-2 and its implication for channel function.', *Journal of molecular biology*, 375(3), pp. 686–694. doi: 10.1016/j.jmb.2007.10.072.
- Bañás, A. and Glückstad, J. (2017) 'Holo-GPC: Holographic Generalized Phase Contrast', *Optics Communications*, 392, pp. 190–195. doi: <https://doi.org/10.1016/j.optcom.2017.01.036>.
- Bashkatov, A. N., Genina, E. A. and Tuchin, V. V. (2011) 'Optical properties of skin, subcutaneous, and muscle tissues: A review', *Journal of Innovative Optical Health Sciences*, 4(1), pp. 9–38. doi: 10.1142/S1793545811001319.
- Beaulieu, D. R. *et al.* (2020) 'Simultaneous multiplane imaging with reverberation two-photon microscopy', *Nature Methods*, 17(3). doi: 10.1038/s41592-019-0728-9.
- Bechtold, P., Hohenstein, R. and Schmidt, M. (2013) 'Beam shaping and high-speed, cylinder-lens-free beam guiding using acousto-optical deflectors without additional compensation optics', *Opt. Express*, 21(12), pp. 14627–14635. doi: 10.1364/OE.21.014627.
- Bègue, A. *et al.* (2013) 'Two-photon excitation in scattering media by spatiotemporally shaped beams and their application in optogenetic stimulation', *Biomedical Optics Express*, 4(12), p. 2869. doi: 10.1364/boe.4.002869.
- Benton, S. A. and Bove, V. M. (2008) 'Holographic Imaging'. Wiley, p. 783850.
- Bhatia, N., Rustagi, K. C. and John, J. (2014) 'Single LP_{0,n} mode excitation in multimode fibers', *Opt. Express*, 22(14), pp. 16847–16862. doi: 10.1364/OE.22.016847.
- Bittner, K. C., Andrasfalvy, B. K. and Magee, J. C. (2012) 'Ion Channel Gradients in the Apical Tuft Region of CA1 Pyramidal Neurons', *PLOS ONE*, 7(10), pp. 1–7. doi: 10.1371/journal.pone.0046652.
- Born, M. and Wolf, E. (1986) *Principles of Optics*.
- Bouchard, M. B. *et al.* (2015) 'Swept confocally-aligned planar excitation (SCAPE) microscopy for high speed volumetric imaging of behaving organisms.', *Nature photonics*, 9(2), pp. 113–119. doi: 10.1038/nphoton.2014.323.
- Boyden, E. S. *et al.* (2005) 'Millisecond-timescale, genetically targeted optical control of neural activity', *Nature Neuroscience*, 8(9), pp. 1263–1268. doi: 10.1038/nn1525.
- Brinks, D., Klein, A. J. and Cohen, A. E. (2015) 'Two-Photon Lifetime Imaging of Voltage Indicating Proteins as a Probe of Absolute Membrane Voltage', *Biophysical Journal*, 109(5), pp. 914–921. doi: <https://doi.org/10.1016/j.bpj.2015.07.038>.
- Bumstead, J. R. (2018) 'Designing a large field-of-view two-photon microscope using optical invariant analysis',

Neurophotonics, 5(02), p. 1. doi: 10.1117/1.nph.5.2.025001.

Cai, D. J. *et al.* (2016) 'A shared neural ensemble links distinct contextual memories encoded close in time', *Nature*, 534(7605), pp. 115–118. doi: 10.1038/nature17955.

Carrillo-Reid, L. *et al.* (2019) 'Controlling Visually Guided Behavior by Holographic Recalling of Cortical Ensembles', *Cell*, 178(2), pp. 447–457.e5. doi: 10.1016/j.cell.2019.05.045.

Centonze, V. E. and White, J. G. (1998) 'Multiphoton excitation provides optical sections from deeper within scattering specimens than confocal imaging', *Biophysical Journal*, 75(4), pp. 2015–2024. doi: 10.1016/S0006-3495(98)77643-X.

Chalfie M, Tu Y, Euskirchen G, Ward WW, P. D. (1994) 'Green fluorescent protein as a marker for gene expression.', *Science.*, 11(263 (5148)), pp. 802–5. doi: 10.1126/science.8303295.

Chamberland, S. *et al.* (2017) 'Fast two-photon imaging of subcellular voltage dynamics in neuronal tissue with genetically encoded indicators', *eLife*, 6, pp. 1–35. doi: 10.7554/eLife.25690.

Chen, B. *et al.* (2018) 'Rapid volumetric imaging with Bessel-Beam three-photon microscopy', *Biomed. Opt. Express*, 9(4), pp. 1992–2000. doi: 10.1364/BOE.9.001992.

Chen, T.-W. *et al.* (2013) 'Ultrasensitive fluorescent proteins for imaging neuronal activity', *Nature*, 499(7458), pp. 295–300. doi: 10.1038/nature12354.

Cheng, A. *et al.* (2011) 'Simultaneous two-photon calcium imaging at different depths with spatiotemporal multiplexing.', *Nature methods*, 8(2), pp. 139–142. doi: 10.1038/nmeth.1552.

Cheng, J. *et al.* (2016) 'Ultrafast axial scanning for two-photon microscopy via a digital micromirror device and binary holography', *Optics Letters*, 41(7), p. 1451. doi: 10.1364/ol.41.001451.

Cheng, L.-C. *et al.* (2014) 'Measurements of multiphoton action cross sections for multiphoton microscopy', *Biomed. Opt. Express*, 5(10), pp. 3427–3433. doi: 10.1364/BOE.5.003427.

Chiang, J. C. B. *et al.* (2023) 'In-vivo corneal confocal microscopy: Imaging analysis, biological insights and future directions', *Communications Biology*, 6(1), pp. 4–10. doi: 10.1038/s42003-023-05005-8.

Choi, H. and So, P. T. C. (2014) 'Improving femtosecond laser pulse delivery through a hollow core photonic crystal fiber for temporally focused two-photon endomicroscopy', *Scientific Reports*, 4(1), p. 6626. doi: 10.1038/srep06626.

Clough, M. *et al.* (2021) 'Flexible simultaneous mesoscale two-photon imaging of neural activity at high speeds', *Nature Communications*, 12(1), pp. 1–7. doi: 10.1038/s41467-021-26737-3.

Curtis, J. C. and Kleinfeld, D. (2009) 'Phase-to-rate transformations encode touch in cortical neurons of a scanning sensorimotor system.', *Nature neuroscience*, 12(4), pp. 492–501. doi: 10.1038/nn.2283.

Daie, K., Svoboda, K. and Druckmann, S. (2021) 'Targeted photostimulation uncovers circuit motifs supporting short-

term memory', *Nature Neuroscience*, 24(2), pp. 259–265. doi: 10.1038/s41593-020-00776-3.

Dana, H. *et al.* (2019) 'High-performance calcium sensors for imaging activity in neuronal populations and microcompartments', *Nature Methods*, 16(7), pp. 649–657. doi: 10.1038/s41592-019-0435-6.

Deisseroth, K. (2015) 'Optogenetics: 10 years of microbial opsins in neuroscience', *Nature Neuroscience*, 18(9), pp. 1213–1225. doi: 10.1038/nn.4091.

Demas, J. *et al.* (2021) 'High-speed, cortex-wide volumetric recording of neuroactivity at cellular resolution using light beads microscopy', *Nature Methods*, 18(9), pp. 1103–1111. doi: 10.1038/s41592-021-01239-8.

Diaspro, A. *et al.* (2006) 'Multi-photon excitation microscopy', *BioMedical Engineering Online*, 5, pp. 1–14. doi: 10.1186/1475-925X-5-36.

Duemani Reddy, G. *et al.* (2008) 'Three-dimensional random access multiphoton microscopy for functional imaging of neuronal activity.', *Nature neuroscience*, 11(6), pp. 713–720. doi: 10.1038/nn.2116.

Emiliani, V. *et al.* (2015) 'All-optical interrogation of neural circuits', *Journal of Neuroscience*, 35(41), pp. 13917–13926. doi: 10.1523/JNEUROSCI.2916-15.2015.

Emiliani, V. *et al.* (2022) 'Optogenetics for light control of biological systems', *Nature reviews methods primers*, 2, p. 55.

Evans, S. W. *et al.* (2023) 'A positively tuned voltage indicator for extended electrical recordings in the brain', *Nature Methods*, 20(7), pp. 1104–1113. doi: 10.1038/s41592-023-01913-z.

Eybposh, M. H. *et al.* (2020) 'DeepCGH: 3D computer-generated holography using deep learning', *Optics Express*, 28(18), p. 26636. doi: 10.1364/oe.399624.

Eybposh, M. H. *et al.* (2022) 'Advances in computer-generated holography for targeted neuronal modulation.', *Neurophotonics*, 9(4), p. 41409. doi: 10.1117/1.NPh.9.4.041409.

Faini, G. *et al.* (2023) 'Ultrafast light targeting for high-throughput precise control of neuronal networks', *Nature communications*, 14(1), p. 1888. doi: 10.1038/s41467-023-37416-w.

Fan, G. Y. *et al.* (1999) 'Video-rate scanning two-photon excitation fluorescence microscopy and ratio imaging with cameleons', *Biophysical Journal*, 76(5), pp. 2412–2420. doi: 10.1016/S0006-3495(99)77396-0.

Farah, N., Reutsky, I. and Shoham, S. (2007) 'Patterned optical activation of retinal ganglion cells.', *Annual International Conference of the IEEE Engineering in Medicine and Biology Society. IEEE Engineering in Medicine and Biology Society. Annual International Conference*, 2007, pp. 6368–6370. doi: 10.1109/IEMBS.2007.4353812.

Favre-Bulle, I. A. *et al.* (2015) 'Scattering of Sculpted Light in Intact Brain Tissue, with implications for Optogenetics', *Scientific Reports*, 5(1), p. 11501. doi: 10.1038/srep11501.

Feldbauer, K. *et al.* (2009) 'Channelrhodopsin-2 is a leaky proton pump', *Proceedings of the National Academy of*

Sciences of the United States of America, 106(30), pp. 12317–12322. doi: 10.1073/pnas.0905852106.

Fine, A. *et al.* (1988) 'Confocal microscopy: applications in neurobiology', *Trends in Neurosciences*, 11(8), pp. 346–351. doi: 10.1016/0166-2236(88)90056-2.

Fisher, R. A. and Bischel, W. K. (1975) 'Numerical studies of the interplay between self-phase modulation and dispersion for intense plane-wave laser pulses', *Journal of Applied Physics*, 46(11), pp. 4921–4934. doi: 10.1063/1.321476.

Fork, R. L. (1971) 'Laser stimulation of nerve cells in *Aplysia*.', *Science*, 171(3974), pp. 907–908. doi: 10.1126/science.171.3974.907.

Forli, A. *et al.* (2018) 'Two-Photon Bidirectional Control and Imaging of Neuronal Excitability with High Spatial Resolution In Vivo', *Cell Reports*, 22(11). doi: 10.1016/j.celrep.2018.02.063.

Gambling, W. A. (2000) 'The rise and rise of optical fibers', *IEEE Journal of Selected Topics in Quantum Electronics*, 6(6), pp. 1084–1093. doi: 10.1109/2944.902157.

Gerchberg, R. W. and S. W. O. (1971) 'A Practical Algorithm for the Determination of Phase from Image and Diffraction Plane Pictures', *Optik*, 35, pp. 237–246. doi: 10.1070/qe2009v039n06abeh013642.

Gill, J. V. *et al.* (2020) 'Precise Holographic Manipulation of Olfactory Circuits Reveals Coding Features Determining Perceptual Detection', *Neuron*, 108(2), pp. 382–393.e5. doi: 10.1016/j.neuron.2020.07.034.

Giovanniello, J. *et al.* (2020) 'A central amygdala-globus pallidus circuit conveys unconditioned stimulus-related information and controls fear learning', *Journal of Neuroscience*, 40(47), pp. 9043–9054. doi: 10.1523/JNEUROSCI.2090-20.2020.

Göbel, W. *et al.* (2004) 'Miniaturized two-photon microscope based on a flexible coherent fiber bundle and a gradient-index lens objective', *Optics Letters*, 29(21), p. 2521. doi: 10.1364/ol.29.002521.

Goeppert-Mayer, M. (1931) 'Über Elementarakte mit zwei Quantensprüngen', *Annalen der Physik*, pp. 273–294. doi: 10.1002/andp.19314010303.

Golan, L. *et al.* (2009) 'Design and characteristics of holographic neural photo-stimulation systems', *Journal of Neural Engineering*, 6(6). doi: 10.1088/1741-2560/6/6/066004.

Gong, Y. *et al.* (2015) 'High-speed recording of neural spikes in awake mice and flies with a fluorescent voltage sensor.', *Science (New York, N.Y.)*, 350(6266), pp. 1361–1366. doi: 10.1126/science.aab0810.

Goodman, J. W. and Silvestri, A. M. (1970) 'Some Effects of Fourier-Domain Phase Quantization', *IBM J. Res. Dev.*, 14(5), pp. 478–484. doi: 10.1147/rd.145.0478.

Grienberger, C. *et al.* (2022) 'Two-photon calcium imaging of neuronal activity', *Nature Reviews Methods Primers*, 2(1), p. 67. doi: 10.1038/s43586-022-00147-1.

Grienberger, C. and Konnerth, A. (2012) 'Imaging calcium in neurons.', *Neuron*, 73(5), pp. 862–885. doi: 10.1016/j.neuron.2012.02.011.

de Groot, A. *et al.* (2020) 'Ninscope, a versatile miniscope for multi-region circuit investigations', *eLife*, 9, pp. 1–24. doi: 10.7554/eLife.49987.

Grossman, N. *et al.* (2010) 'Multi-site optical excitation using ChR2 and micro-LED array.', *Journal of neural engineering*, 7(1), p. 16004. doi: 10.1088/1741-2560/7/1/016004.

Guillon, M. *et al.* (2017) 'Vortex-free phase profiles for uniform patterning with computer-generated holography', *Opt. Express*, 25(11), pp. 12640–12652. doi: 10.1364/OE.25.012640.

Guo, Z. V., Hart, A. C. and Ramanathan, S. (2009) 'Optical interrogation of neural circuits in *Caenorhabditis elegans*.', *Nature methods*, 6(12), pp. 891–896. doi: 10.1038/nmeth.1397.

Guru, A. *et al.* (2015) 'Making Sense of Optogenetics', *International Journal of Neuropsychopharmacology*, 18(11), p. pyv079. doi: 10.1093/ijnp/pyv079.

Han, X. and Boyden, E. S. (2007) 'Multiple-color optical activation, silencing, and desynchronization of neural activity, with single-spike temporal resolution.', *PLoS one*, 2(3), p. e299. doi: 10.1371/journal.pone.0000299.

Helmchen, F. *et al.* (2001) 'A miniature head-mounted two-photon microscope: High-resolution brain imaging in freely moving animals', *Neuron*, 31(6), pp. 903–912. doi: 10.1016/S0896-6273(01)00421-4.

Helmchen, F. and Denk, W. (2005) 'Deep tissue two-photon microscopy', *Nature Methods*, 2(12), pp. 932–940. doi: 10.1038/nmeth818.

Helmchen, F., Tank, D. W. and Denk, W. (2002) 'Enhanced two-photon excitation through optical fiber by single-mode propagation in a large core', *Applied Optics*, 41(15), p. 2930. doi: 10.1364/ao.41.002930.

Helmstaedter, M. (2013) 'Cellular-resolution connectomics: challenges of dense neural circuit reconstruction.', *Nature methods*, 10(6), pp. 501–507. doi: 10.1038/nmeth.2476.

Hernandez, O. *et al.* (2014) 'Zero-order suppression for two-photon holographic excitation', *Optics Letters*, 39(20), p. 5953. doi: 10.1364/ol.39.005953.

Hernandez, O. *et al.* (2016) 'Three-dimensional spatiotemporal focusing of holographic patterns', *Nature Communications*, 7. doi: 10.1038/ncomms11928.

Hochbaum, D. R. *et al.* (2014) 'All-optical electrophysiology in mammalian neurons using engineered microbial rhodopsins.', *Nature methods*, 11(8), pp. 825–833. doi: 10.1038/nmeth.3000.

Horton, N. G. *et al.* (2013) 'In vivo three-photon microscopy of subcortical structures within an intact mouse brain.', *Nature photonics*, 7(3), pp. 205–209. doi: 10.1038/nphoton.2012.336.

Hou, J. H., Venkatachalam, V. and Cohen, A. E. (2014) 'Temporal dynamics of microbial rhodopsin fluorescence

reports absolute membrane voltage.', *Biophysical journal*, 106(3), pp. 639–648. doi: 10.1016/j.bpj.2013.11.4493.

Jacques, S. L. (2013) 'Optical properties of biological tissues: A review', *Physics in Medicine and Biology*, 58(14), pp. 5007–5008. doi: 10.1088/0031-9155/58/14/5007.

Jones, R. *et al.* (2007) 'Silicon photonic tunable optical dispersion compensator', *Opt. Express*, 15(24), pp. 15836–15841. doi: 10.1364/OE.15.015836.

Kalashyan, M. *et al.* (2012) 'Ultrashort pulse fiber delivery with optimized dispersion control by reflection gratings at 800 nm', *Opt. Express*, 20(23), pp. 25624–25635. doi: 10.1364/OE.20.025624.

Kannan, M. *et al.* (2018) 'Fast, in vivo voltage imaging using a red fluorescent indicator', *Nature Methods*, 15(12), pp. 1108–1116. doi: 10.1038/s41592-018-0188-7.

Karigo, T. *et al.* (2021) 'Distinct hypothalamic control of same- and opposite-sex mounting behaviour in mice', *Nature*, 589(7841), pp. 258–263. doi: 10.1038/s41586-020-2995-0.

Kazemipour, A. *et al.* (2019) 'Kilohertz frame-rate two-photon tomography', *Nature Methods*, 16(8), pp. 778–786. doi: 10.1038/s41592-019-0493-9.

Keller, P. J. and Ahrens, M. B. (2015) 'Visualizing whole-brain activity and development at the single-cell level using light-sheet microscopy.', *Neuron*, 85(3), pp. 462–483. doi: 10.1016/j.neuron.2014.12.039.

Kim, K. H. *et al.* (2007) 'Multifocal multiphoton microscopy based on multianode photomultiplier tubes', *Opt. Express*, 15(18), pp. 11658–11678. doi: 10.1364/OE.15.011658.

Kim, K. H., Buehler, C. and So, P. T. C. (1999) 'High-speed, two-photon scanning microscope'.

Klioutchnikov, A. *et al.* (2020) 'Three-photon head-mounted microscope for imaging deep cortical layers in freely moving rats', *Nature Methods*, 17(5), pp. 509–513. doi: 10.1038/s41592-020-0817-9.

Klioutchnikov, A. *et al.* (2023) 'A three-photon head-mounted microscope for imaging all layers of visual cortex in freely moving mice', *Nature Methods*, 20(4), pp. 610–616. doi: 10.1038/s41592-022-01688-9.

Kobat, D. *et al.* (2009) 'Deep tissue multiphoton microscopy using longer wavelength excitation', *Optics Express*, 17(16), p. 13354. doi: 10.1364/oe.17.013354.

Kobat, D., Horton, N. G. and Xu, C. (2011) 'In vivo two-photon microscopy to 1.6-mm depth in mouse cortex', *Journal of Biomedical Optics*, 16(10), p. 1. doi: 10.1117/1.3646209.

Kralj, J. M. *et al.* (2011) 'Optical recording of action potentials in mammalian neurons using a microbial rhodopsin.', *Nature methods*, 9(1), pp. 90–95. doi: 10.1038/nmeth.1782.

Lechleiter, J. D., Lin, D. T. and Sieneart, U. (2002) 'Multi-photon laser scanning microscopy using an acoustic optical deflector', *Biophysical Journal*, 83(4), pp. 2292–2299. doi: 10.1016/S0006-3495(02)73989-1.

Lecoq, J., Orlova, N. and Grewe, B. F. (2019) 'Wide. Fast. Deep: Recent advances in multiphoton microscopy of in vivo

- neuronal activity', *Journal of Neuroscience*, 39(46), pp. 9042–9052. doi: 10.1523/JNEUROSCI.1527-18.2019.
- Lefort, C. *et al.* (2014) 'Sub-30-fs pulse compression and pulse shaping at the output of a 2-m-long optical fiber in the near-infrared range', *Journal of the Optical Society of America B*, 31(10), p. 2317. doi: 10.1364/josab.31.002317.
- Lelek, M. *et al.* (2007) 'Coherent femtosecond pulse shaping for the optimization of a non-linear micro-endoscope', *Optics Express*, 15(16), p. 10154. doi: 10.1364/oe.15.010154.
- Levy, D. R. *et al.* (2019) 'Dynamics of social representation in the mouse prefrontal cortex', *Nature Neuroscience*, 22(12), pp. 2013–2022. doi: 10.1038/s41593-019-0531-z.
- Li, A. *et al.* (2021) 'Twist-free ultralight two-photon fiberscope enabling neuroimaging on freely rotating/walking mice', *Optica*, 8(6), p. 870. doi: 10.1364/optica.422657.
- Li, B. *et al.* (2020) 'Two-Photon Voltage Imaging of Spontaneous Activity from Multiple Neurons Reveals Network Activity in Brain Tissue', *iScience*, 23(8), p. 101363. doi: <https://doi.org/10.1016/j.isci.2020.101363>.
- Lin, M. Z. and Schnitzer, M. J. (2016) 'Genetically encoded indicators of neuronal activity', *Nature Neuroscience*, 19(9), pp. 1142–1153. doi: 10.1038/nn.4359.
- Lorca-Cámara, A. *et al.* (2024) 'A multicolor two-photon light-patterning microscope exploiting the spatio-temporal properties of a fiber bundle', *Biomedical Optics Express*. doi: 10.1364/BOE.507690.
- Lu, R. *et al.* (2017) 'Video-rate volumetric functional imaging of the brain at synaptic resolution.', *Nature neuroscience*, 20(4), pp. 620–628. doi: 10.1038/nn.4516.
- Lutz, C. *et al.* (2008) 'Holographic photolysis of caged neurotransmitters', *Nature Methods*, 5(9), pp. 821–827. doi: 10.1038/nmeth.1241.
- Malitson, I. H. (1965) 'Interspecimen Comparison of the Refractive Index of Fused Silica', *J. Opt. Soc. Am.*, 55(10), pp. 1205–1209. doi: 10.1364/JOSA.55.001205.
- Mancuso, J. J. *et al.* (2011) 'Optogenetic probing of functional brain circuitry.', *Experimental physiology*, 96(1), pp. 26–33. doi: 10.1113/expphysiol.2010.055731.
- Marcuse, D. (1980) 'Pulse distortion in single-mode fibers', *Appl. Opt.*, 19(10), pp. 1653–1660. doi: 10.1364/AO.19.001653.
- Marshall, J. H. *et al.* (2019) 'Cortical layer-specific critical dynamics triggering perception', *Science*, 365(6453). doi: 10.1126/science.aaw5202.
- Martin, J.-R. (2012) *Genetically Encoded Functional Indicators*. Springer.
- Mazumder, N., Gangadharan, G., & Kistenev, Y. V. (2022) *Advances in Brain Imaging Techniques*. Springer Nature. doi: 10.1007/978-981-19-1352-5.
- McConnell, G. *et al.* (2016) 'A novel optical microscope for imaging large embryos and tissue volumes with sub-

cellular resolution throughout', *eLife*. Edited by M. E. Bronner, 5, p. e18659. doi: 10.7554/eLife.18659.

McNally, J. G. *et al.* (1999) 'Three-Dimensional Imaging by Deconvolution Microscopy', *Methods*, 19(3), pp. 373–385. doi: <https://doi.org/10.1006/meth.1999.0873>.

Meng, G. *et al.* (2022) 'Ultrafast two-photon fluorescence imaging of cerebral blood circulation in the mouse brain in vivo', *Proceedings of the National Academy of Sciences of the United States of America*, 119(23), pp. 1–11. doi: 10.1073/pnas.2117346119.

Miyajima, H. and Asaoka, N. and Isokawa, T. and Ogata, M. and Aoki, Y. and Imai, M. and Fujimori, O. and Katashiro, M. and Matsumoto, K. (2003) 'A MEMS electromagnetic optical scanner for a commercial confocal laser scanning microscope', *Journal of Microelectromechanical Systems*, 12(3), pp. 243–251. doi: 10.1109/JMEMS.2003.809961.

Murphy, D. B. and Davidson, M. W. (2013) *Fundamentals of Light Microscopy and Electronic Imaging*, Wiley-Blackwell. doi: 10.1002/9781118382905.

Murugan, M. *et al.* (2017) 'Combined Social and Spatial Coding in a Descending Projection from the Prefrontal Cortex', *Cell*, 171(7), pp. 1663–1677.e16. doi: 10.1016/j.cell.2017.11.002.

Nadella, K. M. N. S. *et al.* (2016) 'Random-access scanning microscopy for 3D imaging in awake behaving animals.', *Nature methods*, 13(12), pp. 1001–1004. doi: 10.1038/nmeth.4033.

Nagel, G. *et al.* (2002) 'Channelrhodopsin-1: A Light-Gated Proton Channel in Green Algae', *Science*, 296(5577), pp. 2395–2398. doi: 10.1126/science.1072068.

Nagel, G. *et al.* (2003) 'Channelrhodopsin-2, a directly light-gated cation-selective membrane channel', *Proceedings of the National Academy of Sciences*, 100(24), pp. 13940–13945. doi: 10.1073/pnas.1936192100.

Nakai, J., Ohkura, M. and Imoto, K. (2001) 'A high signal-to-noise Ca²⁺ probe composed of a single green fluorescent protein', *Nature Biotechnology*, 19(2), pp. 137–141. doi: 10.1038/84397.

Nguyen, Q. T. *et al.* (2001) 'Construction of a two-photon microscope for video-rate Ca²⁺ imaging', *Cell Calcium*, 30(6), pp. 383–393. doi: 10.1054/ceca.2001.0246.

O'Connor, D. H., Huber, D. and Svoboda, K. (2009) 'Reverse engineering the mouse brain.', *Nature*, 461(7266), pp. 923–929. doi: 10.1038/nature08539.

Oheim, M. *et al.* (2001) 'Two-photon microscopy in brain tissue: Parameters influencing the imaging depth', *Journal of Neuroscience Methods*, 111(1), pp. 29–37. doi: 10.1016/S0165-0270(01)00438-1.

Ohki, K. *et al.* (2005) 'Functional imaging with cellular resolution reveals precise micro- architecture in visual cortex', *Nature*, 433(February), pp. 1–8. Available at: <http://reid.med.harvard.edu/pdf/ohki-chung-chng-kara-reid-2005-nature.pdf%5Cnpapers2://publication/uuid/3B881569-E951-4C6D-9943-2069A3CED7B2>.

Olson, J. M. *et al.* (2020) 'Secondary Motor Cortex Transforms Spatial Information into Planned Action during Navigation', *Current Biology*, 30(10), pp. 1845–1854.e4. doi: 10.1016/j.cub.2020.03.016.

Oron, D., Tal, E. and Silberberg, Y. (2005) 'Scanningless depth-resolved microscopy', 13(5), pp. 1468–1476.

Ota, K. *et al.* (2021) 'Fast, cell-resolution, contiguous-wide two-photon imaging to reveal functional network architectures across multi-modal cortical areas', *Neuron*, 109(11), pp. 1810-1824.e9. doi: 10.1016/j.neuron.2021.03.032.

Ozby, B. N. *et al.* (2018) 'Three dimensional two-photon brain imaging in freely moving mice using a miniature fiber coupled microscope with active axial-scanning', *Scientific Reports*, 8(1), pp. 1–14. doi: 10.1038/s41598-018-26326-3.

Packer, A. M. *et al.* (2012) 'Two-photon optogenetics of dendritic spines and neural circuits', *Nature Methods*, 9(12), pp. 1202–1205. doi: 10.1038/nmeth.2249.

Packer, A. M. *et al.* (2015) 'Simultaneous all-optical manipulation and recording of neural circuit activity with cellular resolution in vivo', *Nature Methods*, 12(2), pp. 140–146. doi: 10.1038/nmeth.3217.

Palima, D. and Daria, V. R. (2007) 'Holographic projection of arbitrary light patterns with a suppressed zero-order beam', *Appl. Opt.*, 46(20), pp. 4197–4201. doi: 10.1364/AO.46.004197.

Papagiakoumou, E. *et al.* (2008) 'Patterned two-photon illumination by spatiotemporal shaping of ultrashort pulses', *Optics Express*, 16(26), p. 22039. doi: 10.1364/oe.16.022039.

Papagiakoumou, E. *et al.* (2010) 'Scanless two-photon excitation of channelrhodopsin-2', *Nature Methods*, 7(10), pp. 848–854. doi: 10.1038/nmeth.1505.

Papagiakoumou, E. *et al.* (2013) 'Functional patterned multiphoton excitation deep inside scattering tissue', *Nature Photonics*, 7(4), pp. 274–278. doi: 10.1038/nphoton.2013.9.

Papagiakoumou, E., Ronzitti, E. and Emiliani, V. (2020) 'Scanless two-photon excitation with temporal focusing', *Nature Methods*, 17(6), pp. 571–581. doi: 10.1038/s41592-020-0795-y.

Paredes, R. M. *et al.* (2008) 'Chemical calcium indicators.', *Methods (San Diego, Calif.)*, 46(3), pp. 143–151. doi: 10.1016/j.ymeth.2008.09.025.

Park, H.-C. *et al.* (2020) 'High-speed fiber-optic scanning nonlinear endomicroscopy for imaging neuron dynamics in vivo', *Optics Letters*, 45(13), p. 3605. doi: 10.1364/ol.396023.

Parker, P. R. L. *et al.* (2022) 'Distance estimation from monocular cues in an ethological visuomotor task', *eLife*, 11. doi: 10.7554/eLife.74708.

Paschotta, R. (2020a) *Fiber bundles*. Available at: https://www.rp-photonics.com/fiber_bundles.html.

Paschotta, R. (2020b) *Fiber Fabrication*. Available at: https://www.rp-photonics.com/fiber_fabrication.html.

Paschotta, R. (2020c) *LP Modes*. Available at: https://www.rp-photonics.com/lp_modes.html.

Paschotta, R. (2020d) *Self-Phase Modulation*. Available at: https://www.rp-photonics.com/self_phase_modulation.html.

- Paschotta, R. (2020e) *Silica Fibers*. Available at: https://www.rp-photonics.com/silica_fibers.html.
- Pastrana, E. (2010) 'A toolset for the proficient geneticist', *Nature Methods*, 7(7), p. 488. doi: 10.1038/nmeth0710-488a.
- Pavone, F. S. and Shoham, S. (2020) 'Two-Photon Microscopy in the Mammalian Brain', *Handbook of Neurophotonics*, pp. 55–80. doi: 10.1201/9780429194702-4.
- Pawley, J. (2010) *Handbook of Biological Confocal Microscopy*. 3rd edn. Edited by 2010 Springer Science & Business Media. Springer US. doi: 10.1007/978-0-387-45524-2.
- Pégard, N. et al. (2017) 'Three-dimensional scanless holographic optogenetics with temporal focusing (3D-SHOT)', *Nature Communications*, 8(1). doi: 10.1038/s41467-017-01031-3.
- Peron, S. and Svoboda, K. (2011) 'From cudgel to scalpel: toward precise neural control with optogenetics.', *Nature methods*, 8(1), pp. 30–34. doi: 10.1038/nmeth.f.325.
- Persson, M., Engström, D. and Goksör, M. (2012) 'Reducing the effect of pixel crosstalk in phase only spatial light modulators', *Opt. Express*, 20(20), pp. 22334–22343. doi: 10.1364/OE.20.022334.
- Piyawattanametha, W. et al. (2006) 'Fast-scanning two-photon fluorescence imaging based on a microelectromechanical systems two-dimensional scanning mirror', *Optics Letters*, 31(13), p. 2018. doi: 10.1364/ol.31.002018.
- Piyawattanametha, W. et al. (2009) 'In vivo brain imaging using a portable 29 g two-photon microscope based on a microelectromechanical systems scanning mirror', *Optics Letters*, 34(15), p. 2309. doi: 10.1364/ol.34.002309.
- Porat, A. et al. (2016) 'Widefield lensless imaging through a fiber bundle via speckle correlations', *Opt. Express*, 24(15), pp. 16835–16855. doi: 10.1364/OE.24.016835.
- Potma, E. and Xie, X. (2008) *Handbook of biological nonlinear optical microscopy*. Edited by M. Peter, So; Br.
- Prakash, R. et al. (2012) 'Two-photon optogenetic toolbox for fast inhibition, excitation and bistable modulation', *Nature Methods*, 9(12), pp. 1171–1179. doi: 10.1038/nmeth.2215.
- Prevedel, R. et al. (2016) 'Fast volumetric calcium imaging across multiple cortical layers using sculpted light.', *Nature methods*, 13(12), pp. 1021–1028. doi: 10.1038/nmeth.4040.
- Pryazhnikov, E. et al. (2018) 'Longitudinal two-photon imaging in somatosensory cortex of behaving mice reveals dendritic spine formation enhancement by subchronic administration of low-dose ketamine', *Scientific Reports*, 8(1), p. 6464. doi: 10.1038/s41598-018-24933-8.
- Quicke, P. et al. (2019) 'Single-neuron level one-photon voltage imaging with sparsely targeted genetically encoded voltage indicators', *Frontiers in Cellular Neuroscience*, 13(February), pp. 1–12. doi: 10.3389/fncel.2019.00039.
- Rickgauer, J. P., Deisseroth, K. and Tank, D. W. (2014) 'Simultaneous cellular-resolution optical perturbation and

imaging of place cell firing fields', *Nature Neuroscience*, 17(12), pp. 1816–1824. doi: 10.1038/nn.3866.

Rickgauer, J. P. and Tank, D. W. (2009) 'Two-photon excitation of channelrhodopsin-2 at saturation', *Proceedings of the National Academy of Sciences of the United States of America*, 106(35), pp. 15025–15030. doi: 10.1073/pnas.0907084106.

Robinson, N. T. M. *et al.* (2020) 'Targeted Activation of Hippocampal Place Cells Drives Memory-Guided Spatial Behavior', *Cell*, 183(6), pp. 1586-1599.e10. doi: 10.1016/j.cell.2020.09.061.

Ronzitti, E. *et al.* (2012) 'LCoS nematic SLM characterization and modeling for diffraction efficiency optimization, zero and ghost orders suppression.', *Optics express*, 20(16), pp. 17843–17855. doi: 10.1364/OE.20.017843.

Ronzitti, E. *et al.* (2017) 'Recent advances in patterned photostimulation for optogenetics', *Journal of Optics (United Kingdom)*. Institute of Physics Publishing. doi: 10.1088/2040-8986/aa8299.

Roome, C. J. and Kuhn, B. (2018) 'Simultaneous dendritic voltage and calcium imaging and somatic recording from Purkinje neurons in awake mice', *Nature Communications*, 9(1), p. 3388. doi: 10.1038/s41467-018-05900-3.

Rose, T. *et al.* (2014) 'Putting a finishing touch on GECIs', *Frontiers in Molecular Neuroscience*, 7. doi: 10.3389/fnmol.2014.00088.

Russell, L. E. *et al.* (2022) 'All-optical interrogation of neural circuits in behaving mice', *Nature Protocols*, 17(7), pp. 1579–1620. doi: 10.1038/s41596-022-00691-w.

Salomé, R. *et al.* (2006) 'Ultrafast random-access scanning in two-photon microscopy using acousto-optic deflectors.', *Journal of neuroscience methods*, 154(1–2), pp. 161–174. doi: 10.1016/j.jneumeth.2005.12.010.

Sauer, B. (1987) 'Functional expression of the cre-lox site-specific recombination system in the yeast *Saccharomyces cerevisiae*.', *Molecular and cellular biology*, 7(6), pp. 2087–2096. doi: 10.1128/mcb.7.6.2087-2096.1987.

Sauer, B. and Henderson, N. (1988) 'Site-specific DNA recombination in mammalian cells by the Cre recombinase of bacteriophage P1.', *Proceedings of the National Academy of Sciences of the United States of America*, 85(14), pp. 5166–5170. doi: 10.1073/pnas.85.14.5166.

Sawinski, J. *et al.* (2009) 'Visually evoked activity in cortical cells imaged in freely moving animals', *Proceedings of the National Academy of Sciences of the United States of America*, 106(46), pp. 19557–19562. doi: 10.1073/pnas.0903680106.

Sheppard, C. and Kompfner, R. (1978) 'Scanning optical microscope', *IEE Review*, 26(2), pp. 166–172. doi: 10.1049/ep.1980.0088.

Sheppard, C. J. R. (1996) 'Image formation in three-photon fluorescence microscopy', *Bioimaging*, 4(3), pp. 124–128. doi: 10.1002/1361-6374(199609)4:3<124::AID-BIO2>3.0.CO;2-2.

Sims, R. R. *et al.* (2023) 'Scanless two-photon voltage imaging', *Research Square*, Under revi. doi: 10.21203/RS.3.RS-2412371/V1.

Sivankutty, S. *et al.* (2016) 'Single-Shot Polarimetry Imaging of Multicore Fibers', in *Frontiers in Optics 2016*. Optica Publishing Group, p. FF1A.5. doi: 10.1364/FIO.2016.FF1A.5.

Snyder, A. W. and Love, J. D. (1983) *Optical waveguide theory, TA - TT -*. London SE - VIII, 734 p. ; 24 cm: Chapman and Hall London. doi: LK - <https://worldcat.org/title/911300756>.

So, P. T. C., Yew, E. Y. S. and Rowlands, C. (2013) 'High-throughput nonlinear optical microscopy.', *Biophysical journal*, 105(12), pp. 2641–2654. doi: 10.1016/j.bpj.2013.08.051.

Sofroniew, N. J. *et al.* (2016) 'A large field of view two-photon mesoscope with subcellular resolution for in vivo imaging', *eLife*, 5(JUN2016), pp. 1–20. doi: 10.7554/eLife.14472.

Spampinato, G. L. B. *et al.* (2022) 'All-optical inter-layers functional connectivity investigation in the mouse retina', *Cell Reports Methods*, 2(8), p. 100268. doi: <https://doi.org/10.1016/j.crmeth.2022.100268>.

Stamatakis, A. M. *et al.* (2018) 'Simultaneous optogenetics and cellular resolution calcium imaging during active behavior using a miniaturized microscope', *Frontiers in Neuroscience*, 12(JUL), pp. 1–16. doi: 10.3389/fnins.2018.00496.

Stirman, J. N. *et al.* (2011) 'Real-time multimodal optical control of neurons and muscles in freely behaving *Caenorhabditis elegans*', *Nature Methods*, 8(2), pp. 153–158. doi: 10.1038/nmeth.1555.

Stirman, J. N. *et al.* (2016) 'Wide field-of-view, multi-region, two-photon imaging of neuronal activity in the mammalian brain', *Nature Biotechnology*, 34(8). doi: 10.1038/nbt.3594.

Stolen, R.H., Ashkin, A. (1973) 'Optical Kerr effect in glass waveguide', *Applied Physics Letters*, 22(6), pp. 294–296. doi: 10.1103/PhysRevA.100.063831.

Stolen, R. H. and Lin, C. (1978) 'Self-phase-modulation in silica optical fibers', *Phys. Rev. A*, 17(4), pp. 1448–1453. doi: 10.1103/PhysRevA.17.1448.

Streich, L. *et al.* (2021) 'High-resolution structural and functional deep brain imaging using adaptive optics three-photon microscopy', *Nature Methods*, 18(10), pp. 1253–1258. doi: 10.1038/s41592-021-01257-6.

Stringer, C. *et al.* (2019) 'High-dimensional geometry of population responses in visual cortex', *Nature*, 571(7765), pp. 361–365. doi: 10.1038/s41586-019-1346-5.

Supatto, W. *et al.* (2011) 'Advances in multiphoton microscopy for imaging embryos.', *Current opinion in genetics & development*, 21(5), pp. 538–548. doi: 10.1016/j.gde.2011.08.003.

Szabo, V. *et al.* (2014) 'Spatially selective holographic photoactivation and functional fluorescence imaging in freely behaving mice with a fiberscope', *Urology*, 84(6), pp. 1157–1169. doi: 10.1016/j.neuron.2014.11.005.

Szalay, G. *et al.* (2016) 'Fast 3D Imaging of Spine, Dendritic, and Neuronal Assemblies in Behaving Animals', *Neuron*, 92(4), pp. 723–738. doi: <https://doi.org/10.1016/j.neuron.2016.10.002>.

Thalhammer, G. *et al.* (2013) 'Speeding up liquid crystal SLMs using overdrive with phase change reduction', *Opt. Express*, 21(2), pp. 1779–1797. doi: 10.1364/OE.21.001779.

Theer, P. and Denk, W. (2006) 'On the fundamental imaging-depth limit in two-photon microscopy', *Journal of the Optical Society of America A*, 23(12), p. 3139. doi: 10.1364/josaa.23.003139.

Treacy, E. (1969) 'Optical pulse compression with diffraction gratings', *IEEE Journal of Quantum Electronics*, 5(9), pp. 454–458. doi: 10.1109/JQE.1969.1076303.

Truong, T. V *et al.* (2011) 'Deep and fast live imaging with two-photon scanned light-sheet microscopy.', *Nature methods*, 8(9), pp. 757–760. doi: 10.1038/nmeth.1652.

Tsien, R. Y. (1998) 'The green fluorescent protein', *Annual Review of Biochemistry*, 67, pp. 509–544. doi: 10.1146/annurev.biochem.67.1.509.

Udovich, J. A. *et al.* (2008) 'Spectral background and transmission characteristics of fiber optic imaging bundles', *Appl. Opt.*, 47(25), pp. 4560–4568. doi: 10.1364/AO.47.004560.

Vaziri, A. and Shank, C. V. (2010) 'Ultrafast widefield optical sectioning microscopy by multifocal temporal focusing', *Optics Express*, 18(19), p. 19645. doi: 10.1364/oe.18.019645.

Vierock, J. *et al.* (2022) 'WiChR, a highly potassium-selective channelrhodopsin for low-light one- and two-photon inhibition of excitable cells', *Science Advances*, 8(49), pp. 1–18. doi: 10.1126/sciadv.add7729.

Villette, V. *et al.* (2019) 'Ultrafast Two-Photon Imaging of a High-Gain Voltage Indicator in Awake Behaving Mice', *Cell*, 179(7), pp. 1590-1608.e23. doi: 10.1016/j.cell.2019.11.004.

W. Denk, J. H. Strickler, W. W. W. (1990) 'Two-photon laser scanning fluorescence microscopy', *Science*, 248(4951), pp. 73–76.

Wang, S. *et al.* (2007) 'All Optical Interface for Parallel, Remote, and Spatiotemporal Control of Neuronal Activity', *Nano Letters*, 7(12), pp. 3859–3863. doi: 10.1021/nl072783t.

Wang, T. *et al.* (2020) 'Quantitative analysis of 1300-nm three-photon calcium imaging in the mouse brain', *eLife*, 9, pp. 1–22. doi: 10.7554/eLife.53205.

Wang, X. *et al.* (2006) 'A review of the fabrication of optic fiber', in *Proc.SPIE*, p. 60341D. doi: 10.1117/12.668147.

Wang, X. *et al.* (2017) 'Deconstruction of Corticospinal Circuits for Goal-Directed Motor Skills', *Cell*, 171(2), pp. 440-455.e14. doi: 10.1016/j.cell.2017.08.014.

Waters, J. (2020) 'Sources of widefield fluorescence from the brain.', *eLife*, 9. doi: 10.7554/eLife.59841.

Weisenburger, S. *et al.* (2019) 'Volumetric Ca²⁺ Imaging in the Mouse Brain Using Hybrid Multiplexed Sculpted Light Microscopy', *Cell*, 177(4). doi: 10.1016/j.cell.2019.03.011.

Werley, C. A., Chien, M.-P. and Cohen, A. E. (2017) 'Ultrawidefield microscope for high-speed fluorescence imaging

and targeted optogenetic stimulation', *Biomedical Optics Express*, 8(12), p. 5794. doi: 10.1364/boe.8.005794.

Wu, J. *et al.* (2020) 'Kilohertz two-photon fluorescence microscopy imaging of neural activity in vivo', *Nature Methods*. doi: 10.1038/s41592-020-0762-7.

Wyart, C. *et al.* (2009) 'Optogenetic dissection of a behavioural module in the vertebrate spinal cord', *Nature*, 461(7262), pp. 407–410. doi: 10.1038/nature08323.

Xiao, S., Giblin, J. T., *et al.* (2023) 'High-throughput deep tissue two-photon microscopy at kilohertz frame rates', *Optica*, 10(6), pp. 763–769. doi: 10.1364/OPTICA.487272.

Xiao, S., Cunningham, W. J., *et al.* (2023) 'Large-scale deep tissue voltage imaging with targeted illumination confocal microscopy'.

Xiao, S., Davison, I. and Mertz, J. (2021) 'Scan multiplier unit for ultrafast laser scanning beyond the inertia limit', *Optica*, 8(11), pp. 1403–1404. doi: 10.1364/OPTICA.445254.

Xu, C. *et al.* (1996) 'Multiphoton fluorescence excitation: New spectral windows for biological nonlinear microscopy', *Proceedings of the National Academy of Sciences of the United States of America*, 93(20), pp. 10763–10768. doi: 10.1073/pnas.93.20.10763.

Xu, C. and Webb, W. W. (1996) 'Measurement of two-photon excitation cross sections of molecular fluorophores with data from 690 to 1050 nm', *Journal of the Optical Society of America B*, 13(3), p. 481. doi: 10.1364/josab.13.000481.

Xu, C. and Webb, W. W. (2002) 'Multiphoton Excitation of Molecular Fluorophores and Nonlinear Laser Microscopy', *Topics in Fluorescence Spectroscopy*, 5, pp. 471–540. doi: 10.1007/0-306-47070-5_11.

Xue, Y. *et al.* (2022) 'Three-dimensional multi-site random access photostimulation (3D-MAP)', *eLife*, 11, pp. 1–27. doi: 10.7554/ELIFE.73266.

Yizhar, O. *et al.* (2011) 'Optogenetics in neural systems.', *Neuron*, 71(1), pp. 9–34. doi: 10.1016/j.neuron.2011.06.004.

Yu, C. H. *et al.* (2021) 'Diesel2p mesoscope with dual independent scan engines for flexible capture of dynamics in distributed neural circuitry', *Nature Communications*, 12(1). doi: 10.1038/s41467-021-26736-4.

Yu, J. *et al.* (2019) 'Recruitment of GABAergic Interneurons in the Barrel Cortex during Active Tactile Behavior', *Neuron*, 104(2), pp. 412–427.e4. doi: <https://doi.org/10.1016/j.neuron.2019.07.027>.

Zhang, J. *et al.* (2021) 'All-optical imaging and patterned stimulation at cellular resolution with a one-photon endoscope'.

Zhang, T. *et al.* (2019) 'Kilohertz two-photon brain imaging in awake mice', *Nature Methods*, 16(11), pp. 1119–1122. doi: 10.1038/s41592-019-0597-2.

Zhang, Y. *et al.* (2023) *Fast and sensitive GCaMP calcium indicators for imaging neural populations*, *Nature*. Springer

US. doi: 10.1038/s41586-023-05828-9.

Zhu, G. *et al.* (2005) 'Simultaneous spatial and temporal focusing of femtosecond pulses.', *Optics Express*, 2005/03/21, 13(6), pp. 2153–2159. doi: 83023 [pii].

Zhu, P. *et al.* (2012) 'High-resolution optical control of spatiotemporal neuronal activity patterns in zebrafish using a digital micromirror device.', *Nature protocols*, 7(7), pp. 1410–1425. doi: 10.1038/nprot.2012.072.

Zipfel, W. R., Williams, R. M. and Webb, W. W. (2003) 'Nonlinear magic: Multiphoton microscopy', *Nature Biotechnology*, 21(11), pp. 1369–1377. doi: 10.1038/nbt899.

Zong, W. *et al.* (2017) 'Fast high-resolution miniature two-photon microscopy for brain imaging in freely behaving mice', *Nature Methods*, 14(7), pp. 713–719. doi: 10.1038/nmeth.4305.

Zong, W. *et al.* (2021) 'Miniature two-photon microscopy for enlarged field-of-view, multi-plane and long-term brain imaging', *Nature Methods*, 18(1), pp. 46–49. doi: 10.1038/s41592-020-01024-z.

B. 2P all-optical studies in freely moving mice using a flexible fiber bundle

This chapter focuses on the recent optical advancements that have been developed to record and manipulate neuronal activity in freely moving animals. Subsequently, I present the central objective of my PhD, which is to conduct 2P all-optical studies in freely moving mice by using a flexible fiber bundle.

B.1 Introduction

B.1.1 The interest of brain studies in freely moving animals

Studying animals' behaviors in their natural, unrestrained state is essential for understanding crucial neuronal processes. This significance becomes particularly evident when animals are involved in complex motor tasks, engage in spatial navigation within their natural environment, or interact socially with other animals or with their surroundings. I will give here few examples of recent results that explored the behaviors of freely moving rodents in different situations. Such experiments could not be carried out in head restrained conditions and thus serve as example of the importance of study neuronal processing during natural behavior.

A study in the visual cortex of mice during the estimation of jumping distances enabled to investigate how neural circuits convert sensory information into motor output (Parker *et al.*, 2022). Mice used vision to accurately calculate distances when jumping across variable gaps while researchers recorded the neuronal activity in the visual cortex. Subsequently, through wide-field optogenetic inhibition of the visual cortex, responsible for distance estimation, it was possible to impair jumping performance. This unique insight into the interplay between sensory processing and motor control can only be effectively explored in freely moving animals.

Single-photon miniscopes have been used to record animals' neural activity during navigation and learning new tasks, revealing brain plasticity mechanisms and neural circuit adaptations to varying behavioral contexts (Ghosh *et al.*, 2011; Cai *et al.*, 2016). An exemplary study of the role of secondary motor cortex (M2) in processing environmental information was

recently performed in freely moving rats (Olson *et al.*, 2020). It was observed how the animals use the spatial information in a maze to plan actions during the navigation. It was shown that neurons recorded with electrodes in M2 integrate the position, route and orientation in the maze and this was used to plan and execute left/right turning actions. This enabled researchers to identify M2 as a key structure that controls planning and execution during spatial navigation, representing a base to study the processing of spatial cognition into motor output (Olson *et al.*, 2020).

As a third example, interactions with the surroundings have been also investigated in freely moving mice. External factors (food reward, tones, electric shock) have been used to study fear learning in the amygdala brain region and defensive behavior, which is involved in a range of adaptive behaviors that require the animal to be freely moving to naturally react to the different stimuli presented (Grewe *et al.*, 2017; Giovanniello *et al.*, 2020). These results have implications in the understanding of memory formation and learning in the brain in natural behaving animals.

Finally, social and sexual interactions are also important to be investigated in freely moving animal (Kingsbury *et al.*, 2019; Levy *et al.*, 2019; Karigo *et al.*, 2021b, 2021a). A study in freely moving mice investigated the neural basis of social interactions by examining interbrain neural activity correlations in pairs of socially interacting mice with a single-photon miniscope (Kingsbury *et al.*, 2019). The findings revealed that during social interactions, mice exhibited synchronized activity in the dorsal medial PFC, with these interbrain correlations dependent on the nature of the interaction. The results shown that synchronized activity could not be solely attributed to coordinated behavior but appeared to reflect future social interactions and dominance relationships in a competitive (dominant-subordinate) context.

As the previously described experiments clearly show, like many others (Händel and Schölvinck, 2019), it is fundamental to study neuronal activity in correlation with certain types of animal behaviors in their natural environment, i.e. in freely moving animals. Not only this, but different studies also showed that head fixed animals present higher stress levels (Rector and Harper, 1991) and can induce significant differences in the neuronal responses (Aghajan *et al.*, 2015; Liberti *et al.*, 2022), which might bias the interpretation of the results. For all these reasons, in the recent years and being the framework of this thesis, it has been fundamental to develop new and powerful optical systems to record and manipulate neuronal activity of different brain areas

during animal behavior (Aharoni and Hoogland, 2019; Aharoni *et al.*, 2019; Klioutchnikov and Kerr, 2023).

B.1.2 Optical systems to study the brain in freely moving animals

In order to optically investigate the neuronal circuits in freely moving rodents, three main strategies have been proposed: 1) single-photon miniscopes; 2) two-photon miniaturized microscopes; and 3) fiber bundle-based microscopes.

1. Single-photon miniscopes. These devices typically employ a Light Emitting Diode (LED) source, a small sCMOS (Scientific Complementary Metal–Oxide–Semiconductor), and miniaturized optics such as GRIN lenses, within a device that weighs less than 5g (figure 19) (Ghosh *et al.*, 2011; Park *et al.*, 2011). Such integrated miniature microscopes have been extensively used for wide-field Ca²⁺ activity imaging studies in freely moving mice and rats (> 200 publications, Kim and Schnitzer, 2022), birds and monkeys (Roberts *et al.*, 2017; Kondo *et al.*, 2018; Bollimunta *et al.*, 2021). Since the first demonstrations of single-photon miniscopes (Ghosh *et al.*, 2011; Park *et al.*, 2011), commercial one-photon miniscopes as well as open-source wide-field miniscopes have been developed, such as the UCLA Miniscope (Cai *et al.*, 2016), FinchScope (Liberti *et al.*, 2017), CHEndoscope (Jacob *et al.*, 2018), MiniScope (Zhang *et al.*, 2019) and NINscope (de Groot *et al.*, 2020), that can record hundreds of neurons at >20 Hz imaging rate, across FOVs >0.34 mm² (Ziv *et al.*, 2013; Juneau *et al.*, 2020; Guo *et al.*, 2023; Scherrer *et al.*, 2023).

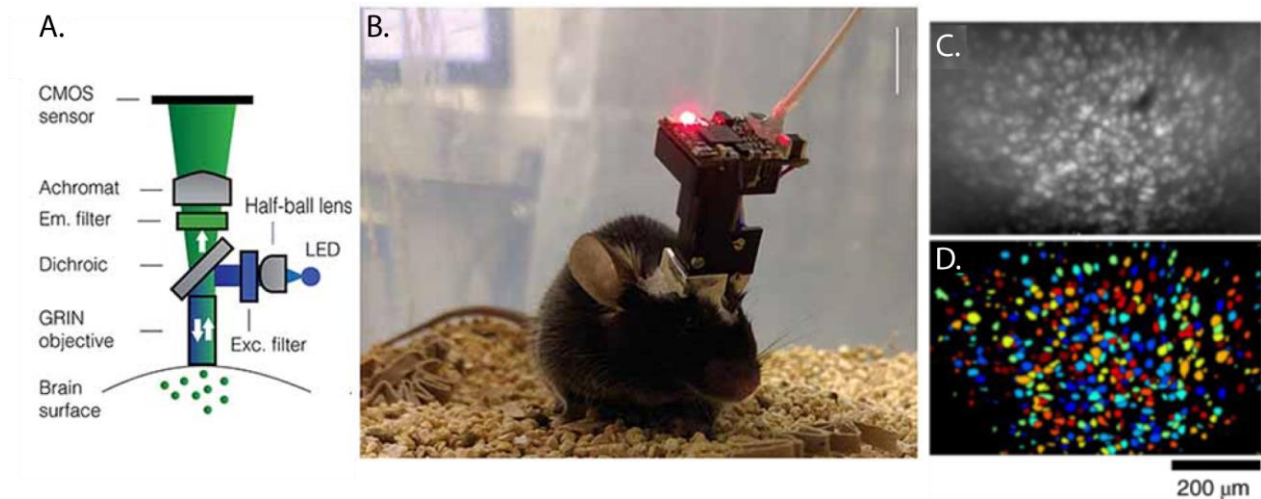


Figure 19. Miniaturized 1P excitation microscope design. **A.** Typical design of a miniaturized 1P excitation microscope used in combination with a GRIN lens and an excitation LED light source that is reflected down toward the specimen and transmitting emitted fluorescence goes up to the imaging detector, a sCMOS sensor. **B.** First-generation of the open-source UCLA Miniscope (3 g), which is mounted, *via* a baseplate, on a mouse head for the duration of the recording session. **C.** Maximum projection of a 10-minute motion-corrected Miniscope recording of hippocampal CA1 pyramidal neurons labeled with GCaMP6f. **D.** Spatial footprints of identified neurons from the recording in C.

All the systems mentioned above present relatively simple optical designs, with the use of miniaturized cameras and illumination LEDs placed directly above the sample and have been extensively used for functional imaging in freely moving rodents. Subsequently, the development of miniscopes with multicolor illumination has enhanced the capabilities of 1P miniscopes, allowing simultaneous wide-field one-photon imaging and optogenetics stimulation (Stamatakis *et al.*, 2018; Srinivasan *et al.*, 2019; de Groot *et al.*, 2020). For example, a system with two LED light sources and an excitation filter for each source, at 430-460 nm for the imaging path and a 590-650 nm for the optogenetic path (Stamatakis *et al.*, 2018), successfully allowed imaging and photostimulation in freely moving mice. Another system replaced the LEDs with 1P fiber lasers, such as the simple modification of the UCLA miniscope, allowing for multiple and flexible light sources illumination through the same fiber and remains light-weight (~1.9 g). However, the use of wide-field illumination has limited these applications to shallow depths from the focalizing optics, low signal to noise ratios (SNRs) in the recorded neuronal activity, and high background signals, with devices that often remaining voluminous (25x15x15 mm³, Zhang *et al.*, 2021) on a mouse head, which have similar dimensions.

To gain precision in the optogenetic photostimulation, a single-photon miniscope have been recently proposed using a miniaturized and light DMD that enabled optogenetic photostimulation with spatial light patterning on freely moving mice (MAPSI system, Zhang *et al.*, 2021). This device achieved a lateral resolution of $\sim 10\ \mu\text{m}$ for patterned stimulation of individual neurons within a $250\ \mu\text{m}$ -wide FOV. However, due to the single-photon excitation used, the penetration depth of the patterned stimulation spots was limited to shallow depths ($< 50\ \mu\text{m}$) and the axial resolution ranged $30\text{-}40\ \mu\text{m}$, which cannot ensure precise single-cell targeting within densely populated neuronal regions. Additionally, it is worth noting that, unlike miniscopes that typically weigh less than 5g, this system weighs 7.8g, accounting for 25-30% of the animal's total weight, which imposes significant movement constraints on the animal.

2. Two-photon miniaturized microscopes. To overcome the limitations of single-photon miniscopes, in the early 2000s, fiber-based microscopes have been proposed to rely 2P excitation microscopes from the tabletop to the mouse brain. Precisely, in these systems, the integration of single-core fibers, along with commercial MEMS scanning mirrors or piezoelectric-based fiber scanning unit, has led to the development of fiber-based miniaturized two-photon microscopes (Helmchen *et al.*, 2001; Bao *et al.*, 2008; Piyawattanametha *et al.*, 2009; Sawinski *et al.*, 2009; Ducourthial *et al.*, 2015; Zong *et al.*, 2017, 2021; Li *et al.*, 2021; Zong *et al.*, 2022; Zhao, Zhu, *et al.*, 2023) and three-photon microscopes (Klioutchnikov *et al.*, 2020, 2022; Zhao, Chen, *et al.*, 2023). Their optical sectioning capabilities, improved spatial resolution, and extended imaging depths offer substantial benefits for many research applications, thanks to the use of 2P excitation. For example, one of the most advanced 2P single-core-based miniaturized microscope offers cellular and subcellular resolution imaging across a three-dimensional FOV of $400\times 400\times 200\ \mu\text{m}^3$ at frame rates $> 4\ \text{Hz}$, all within a 2.4 g device (Zong *et al.*, 2022) (figure 20A) that includes a fast and ultralight tunable lens composed by 4 μTlens that axially scan the beam (figure 20B). This system has been used with different customized mini-objectives (figure 20C) to access brain regions such as the visual cortex (VC), the medial entorhinal cortex (MEC) or the hippocampus CA1 region, enabling the detection of neuronal Ca^{2+} activity in more than 400 neurons within each brain region (figure 20D-F). However, 2P miniaturized microscopes have not, until now, integrated high-resolution optogenetic neuronal stimulation. This limitation arises from the use of single-core fibers, which lack the capability to transmit multiple light patterns to manipulate simultaneously different neurons positioned at various locations within the recorded FOV.

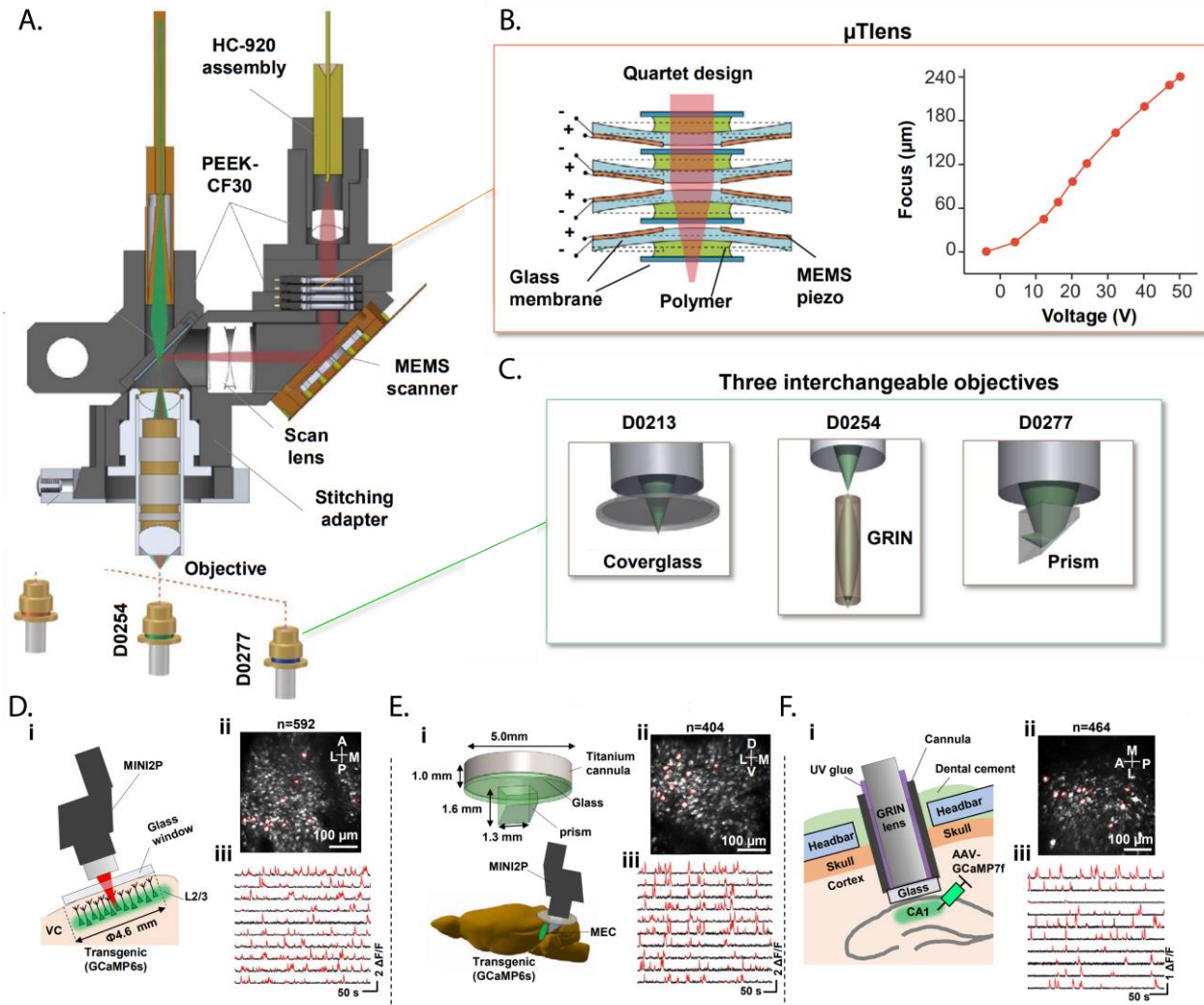


Figure 20. MINI2P for large-scale 2P calcium imaging in multiple brain regions. **A.** Schematic of MINI2P with key components such as a MEMS mirror for lateral scanning and the single-core fiber (HC-920). **B.** Set of 4 μ Tlens for axial scanning, covering a 200 μm range. **C.** Customized mini-objects for 3 different imaging applications at the VC, MEC and CA1. **D-F.** On the left of each panel: Representative image of the 2P miniaturized miniscope at different brain regions (VC, MEC, CA1 respectively). On the right of each panel: Examples of the recorded FOV and calcium traces from neurons marked in red circles of GCaMP6s transgenic mouse freely moving (Zong *et al.*, 2022).

3. Fiber bundle-based microscopes. The third option involves the use of fiber bundles (introduced in A.5) integrated with a standard microscope, where the scanning imaging system is located at the optical table (Göbel *et al.*, 2004; Dussaux *et al.*, 2018). One major advantage of fiber bundles is its possibility to be integrated with patterned holographic illumination that are produced at the proximal end of the fiber bundle and transmitted through its multiple cores to the distal end,

where the patterns are focused into the brain using mini-objectives or miniaturized lenses (Szabo *et al.*, 2014). A first example of this approach was developed in our lab using 1P imaging and 1P photostimulation through a fiber bundle to enable the manipulation of multiple selected neurons within a desired FOV with near single-cell axial resolution ($\sim 20 \mu\text{m}$) (Szabo *et al.*, 2014). In this setup, a SLM and a DMD generated illumination patterns for both holographic photostimulation (excitation at 473 nm) and imaging (excitation at 491 nm), respectively, that are then transmitted through a fiber bundle and a mini-objective to the brain (figure 21). By co-injecting mice with GCaMP5-G and ChR2, the system could control one or more neurons while simultaneously recording neuronal activity in a $240 \mu\text{m}$ -wide FOV in freely moving mice. However, it is important to note the limited penetration depth ($< 60 - 100 \mu\text{m}$) inherent in a 1P excitation system and the use of a large mini-objective (2.8 mm in diameter), that cannot be implanted deep in the brain for endoscopy.

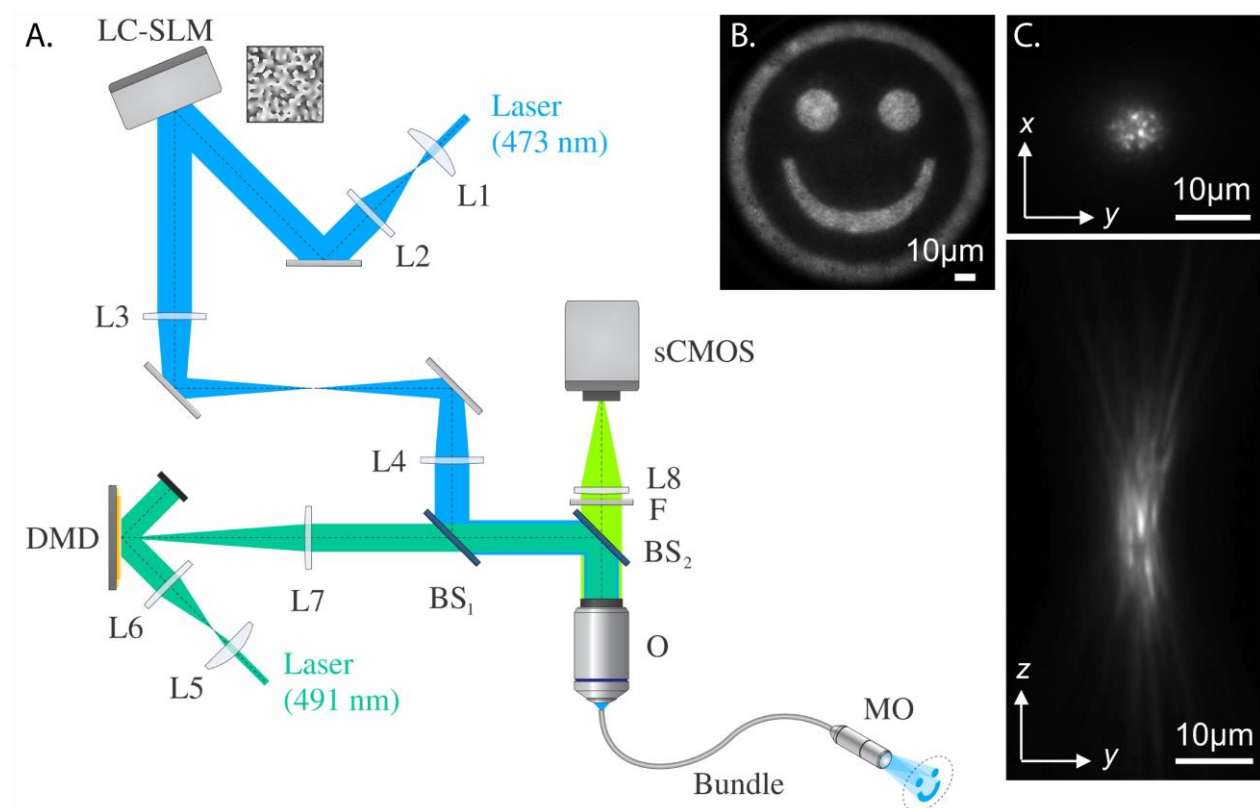


Figure 21. Optical setup of the fiberscope and characterization of holographic patterns. **A.** The fiberscope is composed of two illumination paths: one for photoactivation with CGH (blue path), including a SLM, and a second for fluorescence imaging (dark green path), incorporating a DMD. Backward fluorescence (light green path) is detected on a sCMOS camera. These paths are coupled

to the sample using a fiber bundle attached to a mini-objective. **B.** A “Happy face” illumination pattern generated with the SLM and recorded with the fiberscope showing the full FOV (240 μm in diameter) that was accessible for photoactivation. **C.** Sections of photoactivation beam along the x-y plane (top) and y-z plane (bottom) for a 5 μm -diameter spot with an axial resolution of 18 μm (Szabo *et al.*, 2014).

To tackle these challenges, during my PhD we wanted to overcome the limitation of the previous system by using a smaller mini-objective and 2P excitation. To this end, we developed a two-photon fiberscope (2P-FENDO, Accanto*, Blot*, Lorca-Cámara* *et al.*, 2023) using a fiber bundle and leveraging its intrinsic temporal properties to achieve a good axial resolution. In a FOV of 250 μm in diameter, our system demonstrates both functional imaging at frame rates of up to 50 Hz and precise optogenetics manipulation of selected groups of cells with an axial confinement of 8 μm . This represents the first demonstration of neuronal manipulation with near single-cell resolution using two-photon excitation in freely moving mice. The two-photon regime allows us to access deeper layers of the brain, limited by the working distance of the GRIN lens (200 μm).

B.2 2P-FENDO

B.2.1 Paper

My primary focus within this project was the development of the optical system for both 2P imaging and 2P photostimulation through the fiber bundle, the system’s characterization, and the execution of experiments to troubleshoot and validate the system’s efficacy in real freely moving mice experimental conditions, conducting 2P all-optical studies in freely moving mice (Accanto*, Blot*, Lorca-Cámara* *et al.*, 2023).

A flexible two-photon fiberscope for fast activity imaging and precise optogenetic photostimulation of neurons in freely moving mice

Nicolò Accanto^{1*}, François G. C. Blot^{1*}, Antonio Lorca-Cámara^{1*}, Valeria Zampini¹, Florence Bui¹, Christophe Tourain¹, Noam Badt², Ori Katz², and Valentina Emiliani^{1,3}

¹ Sorbonne Université, INSERM, CNRS, Institut de la Vision, F-75012 Paris, France

² Department of Applied Physics, Hebrew University of Jerusalem, Jerusalem 9190401, Israel.

³Lead Author

* These authors contributed equally

Contact: nicolo.accanto@inserm.fr, valentina.emiliani@inserm.fr

Summary

We developed a flexible two-photon microendoscope (2P-FENDO) capable of all-optical brain investigation at near cellular resolution in freely moving mice. The system performs fast two-photon (2P) functional imaging and 2P holographic photostimulation of single and multiple cells using axially confined extended spots. Proof-of-principle experiments were performed in freely moving mice co-expressing jRCaMP7s and the opsin ChRmine in the visual or barrel cortex. On a field of view of 250 μm in diameter, we demonstrated functional imaging at a frame rate of up to 50 Hz and precise photostimulation of selected groups of cells. With the capability to simultaneously image and control defined neuronal networks in freely moving animals, 2P-FENDO will enable a precise investigation of neuronal functions in the brain during naturalistic behaviors.

Keywords

microendoscopy; 2-photon optogenetic photostimulation; freely moving mice; computer-generated holography; 2-photon calcium imaging; all-optical neuronal circuit manipulation; optical fiber bundles; GRIN lenses

Introduction

A key question in neuroscience is to understand the links between neuronal activity and behavior. This complicated task demands powerful tools to map activity patterns and precisely manipulate

selected neurons in the brain circuits of living and freely behaving animals¹. Combined advances in multiphoton-microscopy and optogenetic sensors and actuators have provided the technology for *in vivo*, single-cell precise, all-optical imaging and optogenetic manipulation of neuronal circuits in head-restrained animals²⁻¹⁰. The next essential step is to extend such technologies to the study of brain circuits in animals that can freely perform behavioral tasks engaging the circuits of interest. If several systems were previously reported for imaging neuronal activity in freely moving rodents¹¹⁻¹⁹, a precise optogenetic photostimulation approach allowing to manipulate neuronal activity at the single-cell level during natural behavior is still missing.

Current systems capable of imaging in freely moving rodents can be grouped into three main categories: one-photon (1P) head-mounted wide-field microscopes, two- or three-photon (2P, 3P) systems coupled to a single optical fiber with a portable scanning unit attached to the animal head, and 1P or 2P systems based on a bundle of optical fibers in which the scanning and beam manipulation unit is placed before the bundle.

1P head-mounted miniaturized microscopes (or miniscopes) come with a simple optical set up and, due to their wide field illumination, can perform functional imaging of large fields of view (FOV) (up to $\sim 1\text{mm}^2$) at high acquisition frame rates (20-100 Hz)^{11,20}. However, their lack of optical sectioning produces relatively high background fluorescence and 1P excitation limits the imaging depth to few tens of μm below the miniscope objective lens.

2P or even 3P miniaturized-microscopes^{14,15,19,21-27} generally use a single optical fiber as a point source and a miniaturized scanning unit, attached to the animal skull, to scan the excitation light across the focal plane. These systems outperform 1P miniscopes in optical resolution and penetration depth, enabling high quality recordings²⁷ up to 40 Hz on FOVs of $400\times 400\ \mu\text{m}^2$.

Optogenetic manipulation in freely moving animals using the previous approaches remains challenging. Different 1P miniscope versions were combined with wide-field photostimulation of the same²⁸ or different¹³ brain areas with respect to the imaging FOV, but lacked cellular resolution. Recently, a newer system²⁹ incorporated a digital micromirror device (DMD) for 1P patterned photostimulation, but only achieved a penetration depth of $\sim 30\ \mu\text{m}$ and an axial resolution of $30\ \mu\text{m}$. On the other hand, multi-photon miniaturized-microscopes, where light is delivered on the sample through a single optical fiber are not compatible with the simultaneous generation of patterned light for multi-target optogenetic photostimulation.

Alternatively, patterned illumination can be reached by using a fiber bundle microscope^{16-18,30}, in which a bundle of optical fibers relays a regular-sized microscope to the animal head. Such an

approach broadens the capabilities of the system and makes it compatible with advanced optical techniques, such as computer-generated holography. A first fiber bundle microscope combined with 1P-structured illumination and 1P-holographic light patterning could indeed perform optogenetic photostimulation with near cellular resolution, in freely moving mice. However, the use of 1P excitation with short penetration depth, the large size and the short working distance of the micro-objective limited this approach to the shallow depth of $60\ \mu\text{m}^{16}$. Larger penetration depths and better axial sectioning in fiber bundle microscopes could be reached by replacing 1P with 2P excitation^{18,31}. However, in this case, the difficulty in propagating high energy laser pulses through fiber bundles, limited the imaging speed¹⁸ to 2.5 Hz on a FOV of $\sim 200 \times 200\ \mu\text{m}^2$. Most importantly, 2P optogenetic photostimulation through a fiber bundle-based microscope has not yet been demonstrated.

In this work we overcome these limitations by developing a flexible two-photon endoscope (2P-FENDO) based on a fiber bundle and a gradient index (GRIN) lens for fast 2P functional imaging and 2P holographic photostimulation of single and multiple cells in freely moving animals. To achieve this, we make use of extended and more efficient 2P excitation spots for both imaging and photostimulation and demonstrate that, by exploiting the intrinsic inter-core delay dispersion of the fiber bundle, 2P-FENDO keeps single-cell axial resolution independently of the size of the excitation spots. Using mice injected with ChRmine and jRCaMP7s in the visual and barrel cortex, we demonstrated functional imaging at up to 50 Hz on a FOV of $250\ \mu\text{m}$ in diameter, at a depth of up to $150\ \mu\text{m}$ and, for the first time, 2P multi-target photostimulation in freely moving animals.

Results

Inter core delay dispersion and optical axial resolution characterization

The optical setup (**Fig. 1A** and **Methods** for details) consists of two different optical paths for imaging and photostimulation. The imaging laser is an ultrafast fiber laser (Alcor, Spark Lasers) that is scanned by a galvo-resonant scanner at the entrance of the fiber bundle. The photostimulation laser is a low repetition rate fiber laser (Goji, Amplitude) that is spatially shaped by a SLM (Hamamatsu) using computer-generated holography (CGH) to generate single or multiple excitation spots at the imaging plane. The imaging and photostimulation lasers are focused by a 0.3 NA objective at the entrance of the endoscope. The micro-endoscope is composed of a 2-m long fiber bundle (Fujikura, diameter of $550\ \mu\text{m}$, 15000 fiber cores) and a commercial, chromatic and field corrected GRIN lens (Grintech, diameter of 1.3 mm) placed above the cranial window. In practice, the GRIN lens behaves

like a doublet, re-imaging the output facet of the fiber bundle at the sample plane (see **Supplementary Fig.1**) with a certain magnification factor (see **Table 1**).

High-speed 2P imaging is achieved by scanning with a galvo-resonant scanner an excitation spot of variable size, at the entrance of the fiber bundle. A motorized iris on the path to the fiber bundle is used to change the imaging spot size and thus the total amount of power at the focal plane so to keep the power/core < 10 mW, which corresponds to the threshold for nonlinear effects, such as self-phase modulation (SPM) to occur³¹⁻³⁵. SPM has the detrimental effect of decreasing the wavelength bandwidth transmitted by the fiber, thus increasing the pulse length and decreasing the 2P excitation efficiency, and cannot be easily compensated for. The emitted fluorescence is collected through the same GRIN objective + fiber bundle system, separated from the laser light using a dichroic mirror, and detected by a high yield EM-CCD camera (Andor IXon Ultra 888).

Single or multi target photostimulation is achieved by projecting at the entrance of the fiber bundle a two-dimensional distribution of holographic spots generated by a SLM placed at the Fourier plane of the microscope objective pupil.

To increase imaging speed and photostimulation efficiency, 2P-FENDO uses excitation spots of 10-20 μm in diameter for imaging, and 10 μm in diameter for photostimulation (matching the size of a neuron). In a classical optical setup, this would result in a drastic loss in axial resolution, which could undermine the advantages of using 2P excitation. As illustrated in **Fig. 1B-C**, 2P-FENDO circumvents this problem by taking advantage of the pulse propagation properties inside the fiber bundle.

Fujikura fiber bundles³⁶, as well as bundles of different types³⁷, generally present a certain degree of core-to-core variation in size and shape. This results in an inter-core delay dispersion (ICDD), meaning that pulses coupled at the same time through different cores arrive at the sample plane at slightly different times, thus decreasing the out of focus 2P interaction with one another (**Fig. 1B**). We quantified this effect by interferometric measurements (**Fig. 1C** and **Supplementary Fig. 1A**) in which an ultrafast pulse from a Ti:sapph laser was split into two arms. One arm was sent through the fiber bundle, and the reference arm was delayed using an adjustable delay line. Using off-axis optical coherent tomography³⁸ and demodulation, we extracted the time cross-correlation of the reference arm and the fiber bundle arm. Since we imaged the fiber onto a camera, we effectively measured the electric field on each core separately. This technique allowed us to differentiate between different modes in each core by using a spatial filter applied to each core in post-processing, and therefore to selectively measure the arrival time of the pulse in the first mode. We found that the measured average ICDD for different types of Fujikura fibers is in the range of 1 to 2 ps/m. With our imaging and photostimulation lasers both

producing pulses of ~ 150 fs, we experimentally confirmed that after propagation through 2 m of fiber, such ICDD values are sufficient to decouple in time the different cores, thus maintaining good axial resolution even for large 2P excitation spots (**Fig. 2**). We measured the axial profile for two different GRIN lenses with high numerical aperture (NA) on the sample side and with chromatic and field corrections. The parameters of the two GRIN lenses are listed in **Table 1**. The axial profiles are dominated by a narrow central Lorentzian peak of full width at half maximum (FWHM) of 7-9 μm . As the 2P spots are made larger, (> 50 μm ; **Fig. 1d**) a broader pedestal starts to appear, which might result in out of focus excitation. To understand the physical origin of the pedestal, one can think that, as the excitation spot becomes larger, more fiber cores are simultaneously illuminated, which increases the probability that pulses from different cores will experience similar temporal delays, thus contributing to out of focus excitation. To avoid the consequent loss of axial sectioning, we always kept the imaging and photostimulation spots at a diameter < 20 μm , which for both GRIN lenses was unaffected by the pedestal component (see **Supplementary Fig. 2**).

In vivo and in vitro depth resolved imaging with different GRIN lenses

We first assessed the capability of 2P-FENDO, with the two different GRIN lenses, to image fixed non-scattering samples (pollen grains, **Fig. 3A**), scattering samples (fixed brain slices, **Fig. 3B**, first and third row), and *in vivo* TdTomato and jRCaMP7s expressing neurons in head-fixed and anesthetized mice (**Fig. 3B**, second and fourth row) with axial sectioning. For that, we acquired z stacks of the selected samples by moving together the fiber bundle and the GRIN lens, with a z step motor, relative to the brain surface (**Fig. 3B**).

The main difference between the two GRIN lenses is the magnification (M in **Table 1**) and thus the size of the FOV (122 μm and 250 μm respectively) and the lateral resolution (~ 1 μm and ~ 2 μm respectively). GRIN 1 has higher lateral resolution, it is thus more adapted to see small features at the sample, with a FOV limited to a diameter of 125 μm (**Fig. 3A-B upper panels**). GRIN 2 offers larger FOVs (250 μm in diameter) with lower resolution that still allows to discriminate individual cells (**Fig. 3A-B lower panels**, see **STAR Methods** for a detailed explanation). As better explained in **STAR Methods** and illustrated in **Supplementary Fig. 3**, to extend the working distance of the GRIN lenses below the cranial window for experiments *in vivo*, we always placed the GRIN lens in contact with the fiber bundle (i.e., at a smaller distance with respect to the input working distance, see **Table 1**) and used protected cover glasses on top of the brain surface of a thickness of ~ 100 μm , which is ~ 70 μm smaller than the cover glasses the GRIN

lenses are designed for. This resulted in sufficient working distance to image at depths of 150-200 μm through the cover glass with minor added aberrations.

We also demonstrated morphological imaging of TdTomato expressing neurons through 2P-FENDO by using a 1040 nm fiber laser (**Fig. 3B**). This opens the possibility for functional imaging of red shifted calcium indicators³⁹, which would not be efficiently excited by a 920 nm laser. As **Fig. 3** demonstrates, in all cases, the good axial confinement produced by the ICDD of the Fujikura fiber enabled achieving a good optical sectioning (for the complete stack data, see **Supplementary videos 1**), even in fixed highly scattering samples (brain slices) and most importantly for *in vivo* imaging.

***In vivo* functional calcium imaging in freely moving animals**

We assessed the capability of 2P-FENDO to perform functional calcium imaging at the highest achievable speed and optogenetic photostimulation *in vivo* in freely moving mice, with small movement artefacts, excellent long-term stability and without obstructing animals' free motions (**Fig. 4-6**). For the following experiments we always used GRIN 2, which gives access to a larger FOV. We co-injected an AAV9 viral vector for jRCaMP7s⁴⁰ expression together with an AAV1 vector for expression of the opsin ChRmine (AAV1.hSyn.ChRmine.mScarlet.Kv2.1.WPRE, see Ref. ³), both under h-synapsin promoter, delivered by stereotaxic injections in primary visual cortex (V1) or primary somatosensory barrel cortex (wS1). Four to eight weeks post injection, the cranial window surgery was performed under ketamine/xylazine anesthesia and the animals were given at least 3 days of recovering before the first day of imaging. For experiments in freely moving animals, we used a custom made, lightweight (Impl.1/2/3 + joint=0.7g, **Fig. 4E**) holder for the fiber and the GRIN lens that could be attached to the mouse head. The implant was positioned over the cranial window of the head fixed animal maintained under isoflurane anesthesia, on the first day of the imaging sessions. Once a region of interest was identified, the implant was cemented over the window and experiments were performed in the hours following the surgery (see **Methods** for details on preparations). The fiber bundle was then removed at the end of each session and inserted back in the following days to repeat experiments on the same FOV. For all the freely moving experiments, the space between the GRIN lens tip and the cranial window was filled with index matching oil for microscope objectives, to prevent easy evaporation that would happen in case of water immersion. As shown in **Supplementary Fig. 3**, and discussed in **STAR Methods**, this had the result of moving the actual focal plane of few μm towards the brain surface, with neglectable other effects on the optical properties.

In successive experimental days, the animal was maintained 20-30 min under isoflurane anesthesia to position the fiber in the implant. Each experiment was spaced of at least 3 days to allow for the recovery of the animal.

We first characterized the imaging properties of 2P-FENDO by measuring the spontaneous activity of jGCaMP7s expressing neurons in freely moving mice (**Fig. 4 and Supp. Video 2**). The recordings were performed in cortical superficial layers (between 70 μm and 150 μm from the brain surface) at different imaging frame rates (from 2Hz to 50 Hz), with powers ranging from 85 to 155 mW (see **Supplementary Table1**).

We used a semi-automatized analysis (see **Methods**) based on CaImAn⁴¹, a software for calcium imaging data analysis, to correct for motion artefacts, select regions of interest (ROIs), extract the calcium traces (corrected for neuropil activity and with baseline subtraction, DF/F signal), and quantify the signal to noise ratio (SNR). As shown in the exemplary graphs of **Fig. 4A-D** (5 different measurement days on 3 different mice), we were consistently able to detect calcium transients in multiple neurons with reliable SNR at acquisition frame rates as high as 20 Hz. A significant drop in the SNR occurred when trying to image at the frame rate of 50 Hz (**Fig. 4 D**) with consequent losses of detectable cells, indicating that more laser power, or different imaging strategies (see **Discussion**) should be used to achieve higher frame rates.

Video recordings of the mouse in the cage were simultaneously acquired during the calcium imaging acquisitions, which allowed us to correlate the motion artefacts of the FOV with the movements of the animal and the relative speed, obtained by analyzing the videos of the mice with DeepLabCut⁴². For each frame in the acquisition (total duration of 300s per acquisition), we estimated the average motion of the FOV by using the resulting values of the planar non-rigid motion correction algorithm of CaImAn⁴¹ (see **Methods**). In **Fig. 4F** we report the average motion artefacts over the acquisition periods in which the animal was moving in the cage at lower (< 5 cm/s) or higher (> 5 cm/s) speeds. Motion artefacts were on average around 2 μm , with peaks that could reach 8 μm for a short time, and a slight tendency on some cases (such as in **Fig. 4F**, FOV2) to increase when the mouse was moving at higher speeds.

A critical property that a head mounted system should demonstrate is its capability to allow recordings in moving animals without restricting their locomotion. To confirm that the fiber bundle did not hamper free movements or alter normal behavior we recorded trajectories, speeds and accelerations for different animals with and without the attached fiber. The results are shown in **Fig. 5A-C**, from which one can clearly deduce a similar level of locomotion for the control and implanted animals. Finally, as

Fig. 5D demonstrates, with the described implant, we could reliably perform optical experiments for hours with a relatively stable FOV.

***In vivo* holographic photostimulation in freely moving animals**

We next demonstrated the capability of 2P-FENDO to perform, for the first time, high resolution 2P photostimulation of a single or multiple targets in freely moving mice. After acquiring a reference image of the FOV, we selected the single or multiple neurons to target and generated with the SLM the corresponding holograms which also contained the corrections to achieve uniform light distribution across the FOV (**Supplementary Fig. 4A-B**). Precisely, the SLM diffraction efficiency, but most importantly the residual aberration of the GRIN lens⁴³⁻⁴⁵, caused a marked decrease of the two-photon fluorescence (2PF) on the edges of the FOV. To compensate for this, we generated corrected holograms to send more laser power to off-centered holographic spots (~ 2 times more than in the center), which resulted in uniform 2PF emitted from each location at the sample plane. We always used holographic spots of 10 μm to photostimulate neurons, corresponding to an axial resolution of 9 μm at the center and < 14 μm at the edges of the FOV, respectively (**Supplementary Fig. 4C**).

We photostimulated ChRmine expressing cells (**Supplementary Fig. 4D**) with a low repetition rate laser (10 MHz, 1030 nm, 150 fs) by using 10 μm holographic spots and sending a train of 10 pulses of 20 ms in duration at a frequency of 4.2 Hz with a power (measured at the GRIN lens output) of 30-40 mW at the center of the FOV (**Supplementary Fig. 4E**), which was smoothly increased for off-center spots until reaching 60-80 mW at the edges of the FOV, to compensate for the GRIN lens aberrations.

Fig. 6A, B show representative traces of one FOV in which we sequentially photostimulated different groups of neurons (**Fig. 6A and Supp. Video 3**) or individual neurons one by one (**Fig. 6B**). We repeated each photostimulation pattern for three consecutive times, with an interval of 50 s, as shown in the DF/F traces of **Fig. 6A**. To quantify the response of targeted cells to photostimulation, we averaged the DF/F signal over the three consecutive repetitions, generating the average $\langle \text{DF}/\text{F} \rangle$ shown in the rectangular boxes of **Fig. 6a** (in **Fig. 6B** we only show the average $\langle \text{DF}/\text{F} \rangle$ traces). As explained in the **Methods**, we used $\langle \text{DF}/\text{F} \rangle$ to compare the mean signal 2s before $\langle \text{DF}/\text{F} \rangle_{\text{Before}}$ and after $\langle \text{DF}/\text{F} \rangle_{\text{After}}$ photostimulation to assess if a neuron was or not photo-activated and to calculate the induced increase of fluorescence signal $\langle \text{DF}/\text{F} \rangle_{\text{Photostim}} = \langle \text{DF}/\text{F} \rangle_{\text{After}} - \langle \text{DF}/\text{F} \rangle_{\text{Before}}$ in response to photostimulation. A neuron was considered photostimulated if $\langle \text{DF}/\text{F} \rangle_{\text{Photostim}}$ was greater than 3 times the standard deviation of the baseline signal.

As shown in the traces of **Fig. 6A, B** we were able to selectively photo-activate only the neurons of interest, inducing responses on average of $\langle \text{DF}/\text{F} \rangle_{\text{Photostim}} \approx 25\%$, with very little cross activation of

non-targeted cells (marked with red rectangles on the average traces). As a proof of the stability of the system, in **Fig. 6A** we also indicate the starting time of each acquisition with respect to the first one. As also shown in **Fig. 5**, we could reliably perform imaging and photostimulation experiments on the same FOV for hours (see also **Supplementary Video 2**).

As quantified in the population graphs of **Fig. 6 C, D**, (representing the average behavior over 50 different photostimulation sequences, 5 different days of measurement on 3 mice) cross activation of non-targeted cells was only visible at distances $< 30 \mu\text{m}$ from one of the targeted cells, after which the activation probability and the $\langle \text{DF}/F \rangle_{\text{Photostim}}$ decayed to zero. The ensemble of data in **Fig. 6C** could be fitted with a single exponential decay function $A \cdot \exp(-x/k)$, with x vector of distances from the photostimulated cells, A normalization factor, $k=20 \pm 5 \mu\text{m}$ characteristic decay distance, confirming the high spatial selectivity of the photostimulation experiments. Overall, these results demonstrate that 2P-FENDO has enough sensitivity and it is sufficiently robust to allow cell selective photostimulation in freely moving animals.

Discussion

We have developed a novel fiber-based microscope, named 2P-FENDO for the 2P all-optical control and high-speed imaging of neuronal activity in head-fixed and freely moving mice with cellular resolution. This was demonstrated using 2P holographic photostimulation and 2P imaging in the cortex (L1, L2/3) of mice injected with the opsin ChRmine and/or the calcium indicator jRCaMP7s.

We have used 10-20 μm diameter imaging and 10 μm diameter photostimulation spots, which enabled increasing the total photon flux while keeping the power per core below the threshold for self-phase modulation ($\approx 10 \text{ mW}$ for 80 MHz repetition rate lasers³¹⁻³⁵) (**STAR Methods**). We have demonstrated that the inter-core delay dispersion properties of the fiber bundle efficiently decouple the 2P excitation from different cores, thereby maintaining axially confined ($< 8 \mu\text{m}$ at the center of the FOV, $< 14 \mu\text{m}$ at the edges) excitations almost independently of the lateral spot size. When illuminating multiple cores simultaneously, the pulses from each core reach the output fiber facet at slightly different times. The GRIN lens is then used to re-image the output facet at the sample plane. In practice, at any given time, even if multiple cores are excited together at the fiber entrance, only one focus appear at the sample plane, as all the other cores are delayed differently (within few ps) by the fiber bundle. The fiber bundles used here thus behave as temporal multiplexing devices, similar to previously investigated systems used for imaging⁴⁶⁻⁴⁸, with the notable difference that the number of multiplexed points in this case can be as large as the number of cores in the bundle (~ 15000), as opposed to the < 100 of previous works.

By using this illumination approach combined with a high detection efficiency EM-CCD camera, we have demonstrated up to 50 Hz functional imaging capability on a FOV of 250 μm in diameter (see **STAR Methods** for possible strategies to enlarge further the FOV), which represents to our knowledge the fastest acquisition speed so far demonstrated in 2P fiber-bundle microscopes. Even at the highest acquisition speed, the total power sent to the sample (**STAR Methods**) was always kept well below the reported illumination threshold (≈ 250 mW) for persistent measurable brain damage⁴⁹. Higher acquisition speeds with sufficient SNR could be reached by adapting the scanning strategy, for instance by scanning only on the cells of interest, such as in random access microscopy⁵⁰, or by using the unique capability of 2P-FENDO to generate static holographic spots.

We have demonstrated single and multi-target 2P photostimulation using holographic spots of 10 μm and an average power per cell of 30-80 mW. Considering the losses through the fiber and the need to compensate for aberrations of the GRIN lens, with the current laser (10 MHz; 1030 nm, 5W) we could photostimulate ~ 10 neurons simultaneously, a number that could be easily increased by using commercially available higher power (up to 60 W) and lower repetition rate (< 1 MHz) lasers.

Previous studies^{6,7,9,51-55} have shown that small cortical subnetworks (< 30 neurons) distributed on FOVs comparable in size with what is currently reachable through 2P-FENDO, can encode for perception, or bias learned behavioral tasks. It was also shown that the manipulation of few highly connected “*hub*” cells can control the synchronicity of larger neuronal networks^{6,55}. We therefore anticipate that 2P-FENDO, will enable to similarly affect behavioral outputs through the manipulation of defined microcircuits.

Over conventional 1P miniscopes^{11,13,20,28}, 2P-FENDO shows superior axial resolution and thus z sectioning capabilities and larger penetration depth. Multiphoton miniaturized microscopes based on the use of a single optical fiber and a miniaturized scanner unit^{15,19,26,27} offer higher spatial resolution and thus superior imaging quality, mainly because the lateral resolution is not limited by the inter-core spacing as in fiber bundles. Compared to these systems, 2P-FENDO uses a larger illumination spot with no cost in the axial resolution, enabling 50 Hz imaging acquisitions albeit with the lower imaging resolution imposed by the fiber bundle. Compared to previously demonstrated fiber bundle based 2P microscopes¹⁸, 2P-FENDO has a much higher acquisition speed and uses smaller and implantable probes. With respect to all these systems, 2P-FENDO is the only technology today capable of cell-precise multitarget 2P photostimulation in freely moving animals, which greatly increases the spectrum of applications within the reach of flexible microendoscopes. With respect to our previously demonstrated 1P fiber bundle system¹⁶, 2P-FENDO presents all the advantages of 2P excitation, a higher acquisition speed and the use of a smaller GRIN lens, suitable for deep implants.

A major advantage of 2P-FENDO is the simplicity of its implementation. For imaging it only requires minor modifications of a standard 2P imaging system (larger imaging spot and camera detection), without the need of miniaturized scanning units and complex custom-made optical architectures, which are typical of 2P miniaturized microscopes^{15,19,26,27}. Furthermore, considering that good axial resolution is obtained thanks to the ICDD effect of the fiber, 2P-FENDO does not require additional techniques, such as temporal focusing⁵⁶, to maintain axial resolution for extended holographic spots. This will also enable to use of the same microscope for head restrained and freely moving experiments.

Contrary to previous works^{45,57,58} performed in standard 2P microscopes, in which we used SLMs to create multiple 2P excitations distributed in three dimensions, working with a fiber bundle prevents the SLM from axially shifting the generated patterns. As a result, in this configuration the SLM can only be used to target neurons located at one focal plane, which coincides with the imaging plane. By adding an axially shifting device, such as a tunable lens^{18,27} or a step motor⁵⁹ after the fiber, one could simultaneously shift the imaging and photostimulation planes. By imaging at 20 Hz per plane, this could enable the subsequent acquisition of ~5 different planes at the total speed of 4 Hz. However, adding more optical components (such as tunable lenses) would also increase the complexity, volume and weight of the resulting device.

Camera detection strategies, combined with multipoint illumination, were demonstrated to be able to detect fluorescence signal down to 300 μm in brain tissue^{60,61}, after which the images become too blurred because of scattering effects. In this manuscript we have demonstrated imaging until depths of about 200 μm , limited by the working distances of the GRIN lens. Optimization of surgical techniques and miniaturization of implants represent further developments of endoscopic technologies for investigation of neuronal circuits located deep in the brain. Combined with GRIN lens brain implantation strategies, 2P-FENDO can be employed to investigate functions of selected neurons in brain regions unreachable by multiphoton microscopy such as the hypothalamus⁶², the amygdala neuronal circuits⁶³, or the thalamus⁶⁴. For this, both GRIN lenses used in here (see **Table 1**) have a total diameter of 1.3 mm, which is comparable to previously implanted GRIN lenses^{51,65,66}.

When performing photostimulation experiments in freely moving animals, the stability of the implant is of great importance to reliably photostimulate the targeted cells. We have demonstrated an average displacement of the FOV, of around 2 μm during acquisitions of 300s, smaller than the size of a cell, and a long-term stability of the implant. However, we have also observed movements of the FOV larger than 5 μm , even if for short periods of time. For repetitive photostimulations, this

limitation could be overcome with the implementation of an active feedback loop that registers in real time the movement of the FOV and corrects the phase on the SLM to recenter the photostimulation pattern.

2P holographic photostimulation, combined with adequate optogenetic tools⁶⁷, makes it possible to selectively activate or inhibit specific neurons or discrete networks within a larger population, even among a molecularly indistinguishable sub-type. This ability, together with that of precisely controlling the spike timing, is fundamental to probe possible causal links between perception, neuronal activity and behavior, which are hard to understand with functional imaging alone^{1,3,9}. Probing the role of spike timing and synchronicity in specific networks (e.g., in the visual cortex for sensory perception), or driving a specific temporal activity in relevant subgroups of neurons to trigger an appropriate behavioral response, are challenges that can be addressed with a 2P holographic photostimulation system⁶⁸. Yet, most experiments exploring neuronal network activity are performed in head-fixed conditions, tempering the impact of animal free motion on neuronal processing. Recent works^{69,70} showed for example that three-dimensional head motion modulates visual integration in primary visual cortex V1. The heterogeneity in directionality and timing of single-cell responses in V1 resulting from head motion uncovered a multitude of network dynamics that cannot be observed in head fixed conditions. With the capability to simultaneously image and control neuronal activity with single-cell resolution in freely moving animals, 2P-FENDO will enable to identify and challenge these emerging networks dynamics in order to unravel the complex brain processes hidden behind naturalistic behavior.

Acknowledgments

We acknowledge support from the IHU FOReSIGHT grant (Grant P-ALLOP3-IHU-000), the Fondation Bettencourt Schueller (Prix Coups d'élan pour la recherche française), the Axa research funding the 'Agence National de la Recherche' (grants ANR 19-CE19-0001-01, 2MEnHoloMD) the Human Frontiers Science Program (Grant RGP0015/2016), Imagine Nano, the ERC advanced Grant HOLOVIS (ERC-2019-AdG; Award no. 885090), the ERC Horizon 2020 H2020-ICT (DEEPER, 101016787), Israel Science Foundation (1361/18), Israeli Ministry of Science and Technology (Grant 712845). We would like to thank Serge Charpak, Marine Tournissac and Manon Omnès (Vision Institute, Paris) for helpful discussions and pilot imaging experiments, Andrea Giovannucci for help with CalmAn, Aaron Benson Wong (ErasmusMC Rotterdam) for help in calcium imaging data analysis, Vincent de Sars for WaveFront IV software development, and Manuel Simonutti, Julie Degardin and Quenol Cesar from the animal facility of the Institut de la vision, for their help and support on animal experimentation.

Declaration of interest

The authors declare that they have no known competing financial interests or personal relationships that could have appeared to influence the work reported in this paper.

Author Contributions

N.A., A.L.C. and C.T. built the optical setup. N.A. and A.L.C. developed the acquisition software and performed the optical characterization. O.K. conceived the experiment for measuring the inter core delay dispersion. N.B. measured and analysed the inter core delay dispersion. F.G.C.B. and C.T. designed and developed the implant for freely moving experiments. F.G.C.B., V.Z. and F.B. developed the surgical procedures and performed viral injections. V.Z. and F.B. acquired in vivo and in vitro z-stacks and preliminary calcium imaging data in vivo. F.G.C.B. and A.L.C. performed imaging and photostimulation experiments in freely moving mice. N.A., F.G.C.B. and A.L.C. analysed the data. N.A., F.G.C.B. and V.E. wrote the paper with the contribution of all the authors. N.A. and V.E. conceived and supervised the project.

Figures and legends

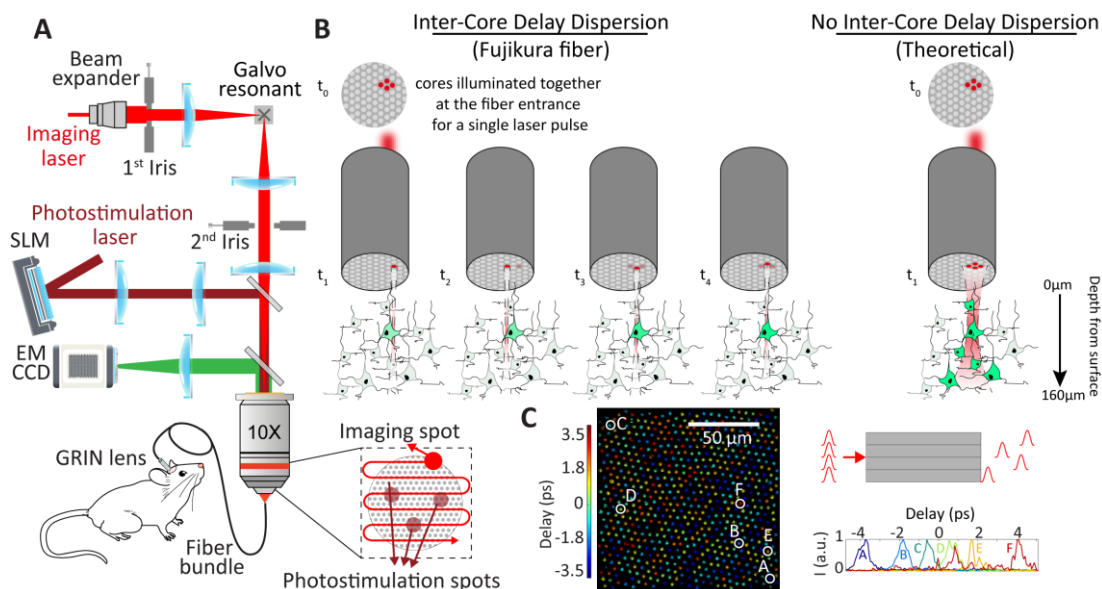


Figure 1. Optical set-up of the flexible two-photon endoscope (2P-FENDO). A) Schematics of the optical setup. B) Representation of the effect of the inter-core delay dispersion on the axial sectioning capabilities for an extended excitation spot. Left: through the Fujikura fiber bundle the incoming laser pulse simultaneously illuminates different cores at t_0 , but is outcoupled from each core at slightly different times (t_1 to t_4). As the pulses from each core do not interact with each other at the sample, the axial resolution

corresponds to the single core axial resolution, which ensures imaging and photostimulation with single-cell axial confinement. Right: through a theoretical fiber bundle with no inter-core delay dispersion, the laser pulses from each core are outcoupled simultaneously and interact at the sample, resulting a much worse axial confinement. **C)** Measurement and schematic representation of the delays experienced by a laser pulse when propagating through multiple cores of a 60 cm Fujikura fiber bundle (details in **Supplementary Figure 1**).

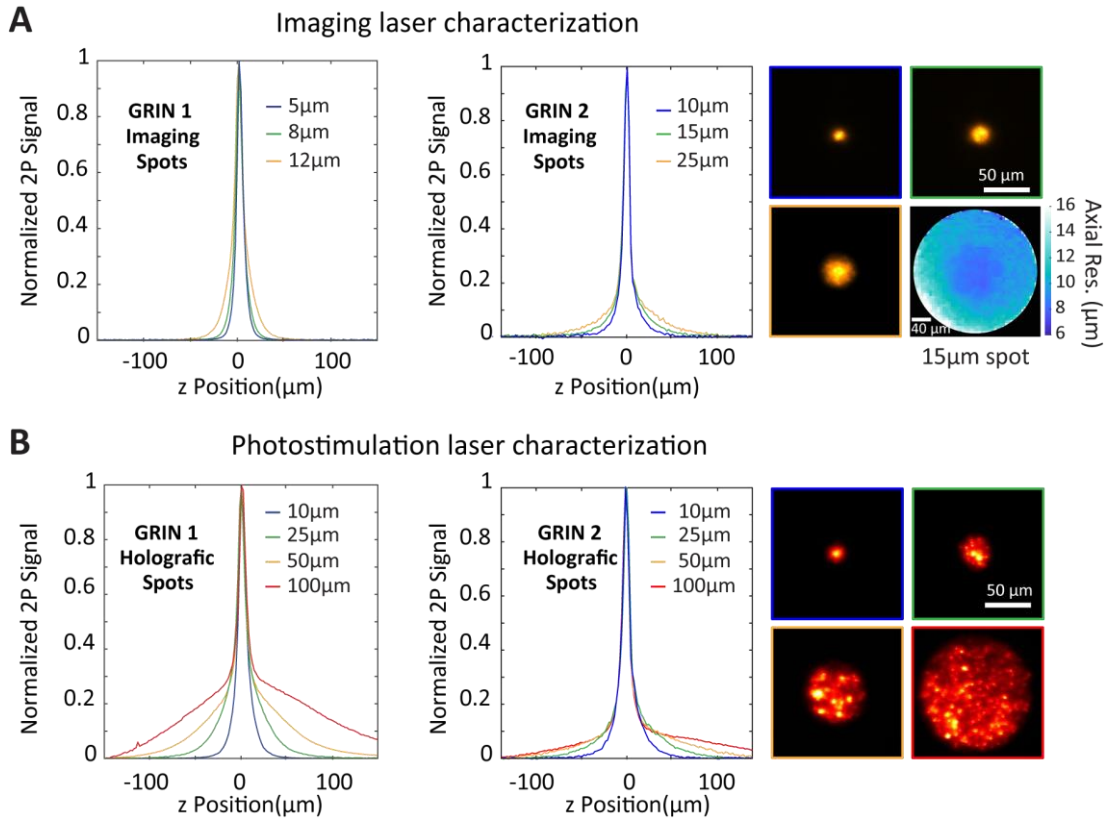


Figure 2. Axial resolutions characterization. Axial resolution measurements for extended spots of different sizes for the imaging (**A**) and photostimulation (**B**) lasers respectively and for the two different GRIN lenses (left: GRIN 1, right: GRIN2). In the case of the imaging laser, the different spot sizes were obtained with different apertures of the motorized iris, for the photostimulation laser, they correspond to different sizes of the holographic spots produced by the SLM. The axial resolutions were measured by moving the distal end of the fiber plus the GRIN lens together in z using a vertical step motor while recording the emitted 2P fluorescence from a thin ($\sim 1 \mu\text{m}$) rhodamine layer with the camera detector. The space between the GRIN lens and the rhodamine layer was filled with water, i.e. the GRIN lens was used in water immersion conditions. The axial full width at half maximum of the central Lorentzian peaks

is as narrow as 7 μm for the imaging laser and 9 μm for the photostimulation one. The two-dimensional images on the excitation spots on the right were acquired with GRIN2 (see Table 1). In **A**) the bottom right image represents the position-dependent axial resolution, calculated as the full width at half maximum of the Lorentzian peak, for a 15 μm imaging spot that was raster scanned across the whole fiber bundle. The axial resolution is ~ 7 μm at the center and increases to ~ 13 μm at the edges of the FOV. The indicated spot sizes refer to the spot at the sample plane. For subsequent experiments the imaging spot size was maintained below 20 μm which does not affect the resolution (see **Supplementary Figure 2**).

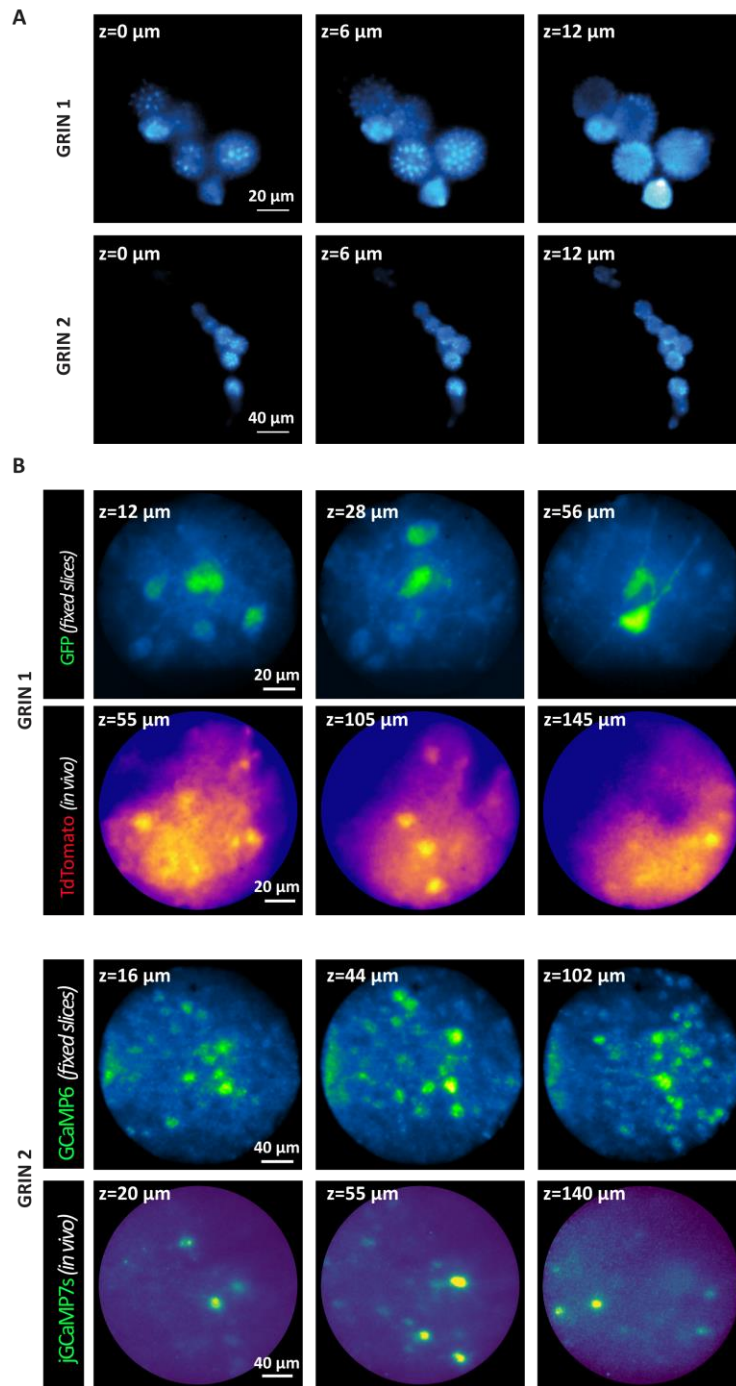


Figure 3. Imaging capabilities of 2P-FENDO. A) 2P z-stacks of pollen grains with two different GRIN lenses. B). Upper panel: 2P z-stacks with GRIN1 of GFP labelled hippocampal brain slices (upper row) and *in vivo* TdTomato labelled cortical neurons in injected mouse (lower row). Lower panel: 2P z-stacks with GRIN2 of GCaMP6 labelled cortical brain slices (upper row) and *in vivo* jGCaMP7s labelled cortical neurons in injected mouse (lower row). GFP and jGCaMP7s labelled neurons were imaged with 920 nm laser and

TdTomato with 1040 nm laser. Because of the higher magnification of GRIN1, the sharp edges of pollen grains as well as neuronal processes are clearly visible, whereas with GRIN2 we have access to a twice bigger FOV. For example, of z-stacks see **Suppl. Video 1**.

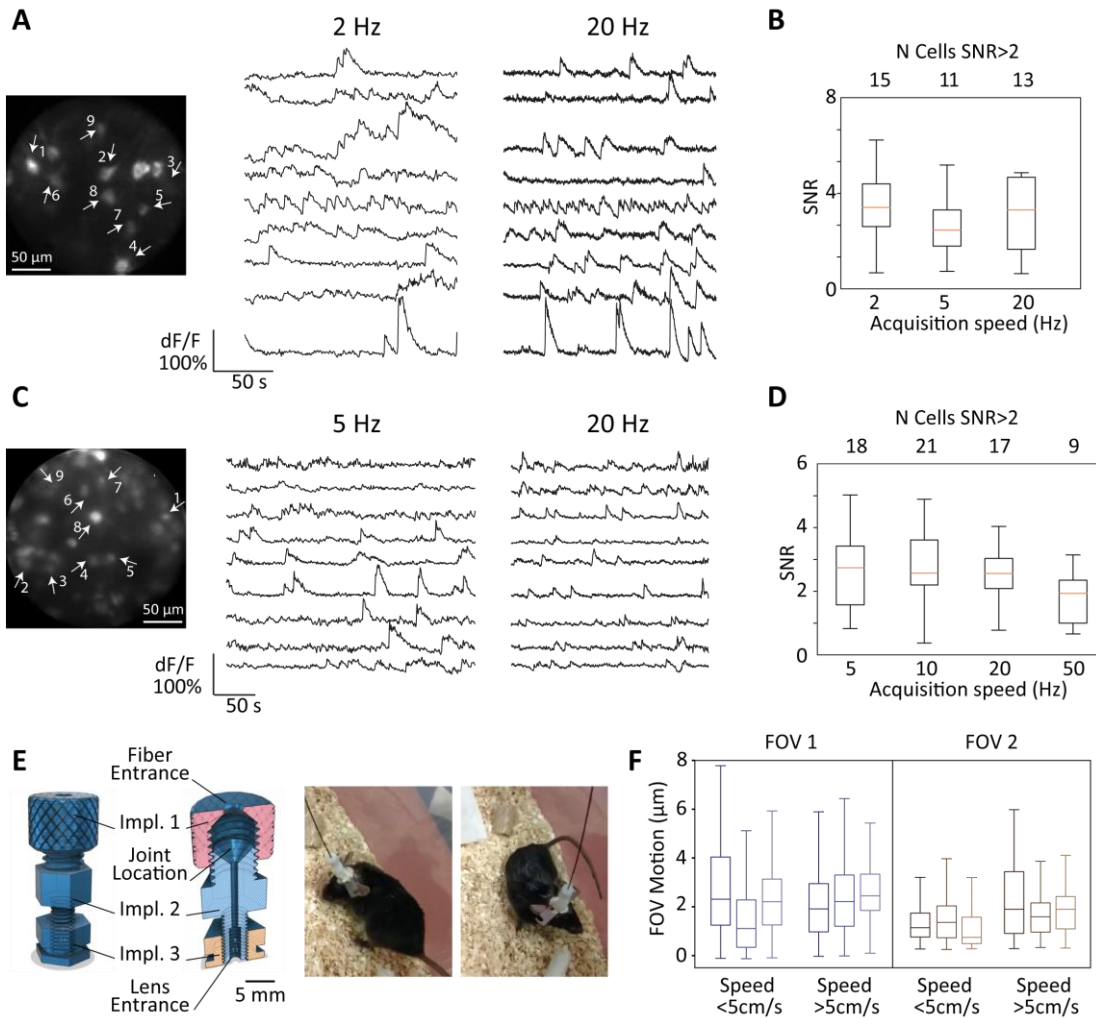


Figure 4. Imaging of spontaneous calcium activity in freely moving mice. **A & C.** Two representative FOVs in two different mice with corresponding calcium transients (dF/F) for 9 selected cells for each FOV imaged at low (2 or 5 Hz) and high (20 Hz) acquisition speeds. Imaging power and spot size were 135 mW and 16 μm at all the imaging rates. **B & D.** SNR quantification and number of cells with SNR higher than 2 for the two FOVs as a function of the acquisition speed. **E.** Image of the implant, a lightweight, simple to produce and cost-effective holder for the fiber and the GRIN lens. This implant is composed of three elements carved from a nylon screw (RS Pro, nylon, socket hexagonal male/female, 30 mm, M4 x M, RS code: 325-801), assembled with a joint (**HLC-11** orange cone washer). The fiber (0.65 mm outer diameter) passes in the first element of the implant (Impl.1), through an opening of 0.7mm, then through the joint (1.1 mm

inner diameter), and halfway through the second element (Impl.2). Once the Impl.1 and 2 are screwed together the joint compresses to clench the fiber within the implant. The GRIN lens (1.3 mm outer diameter) is introduced in the Impl.2 from the other end, to come directly in contact with the fiber. The openings of Impl.2 are centered for the optimal alignment of the fiber and the lens. A third element (Impl.3) screws onto Impl.2 to act as a chuck, clenching the lens in position. The fully assembled implant was positioned over the cranial window of the anesthetized/head fixed animal, performed as previously described. Once a region of interest is identified, the implant is cemented over the window. Impl.3 is the sole element to be permanently fixed onto the animal's head, thus allowing to make the system fully detachable by unscrewing Impl.2 from Impl.3. The relative position of Impl.2 in Impl.3 also changes the distance between the lens and the sample, allowing to manually change the focal plan of imaging. The total weight of the implant (Impl.1/2/3 + joint) is 0.7g. Scale bar = 5mm. Representation images of a mouse in its cage with the implant and the fiber bundle fixed on the head. **F.** Quantification of the lateral non-rigid motion of the FOV for three different acquisitions (different color hues) of total duration of 300 s in 2 representative FOVs of animals #1/2, see **Supplementary Table1**, for low (< 5cm/s) and high (> 5cm/s) movement speed of the mouse in the cage. Acquisition examples are presented in **Suppl. Video 2**.

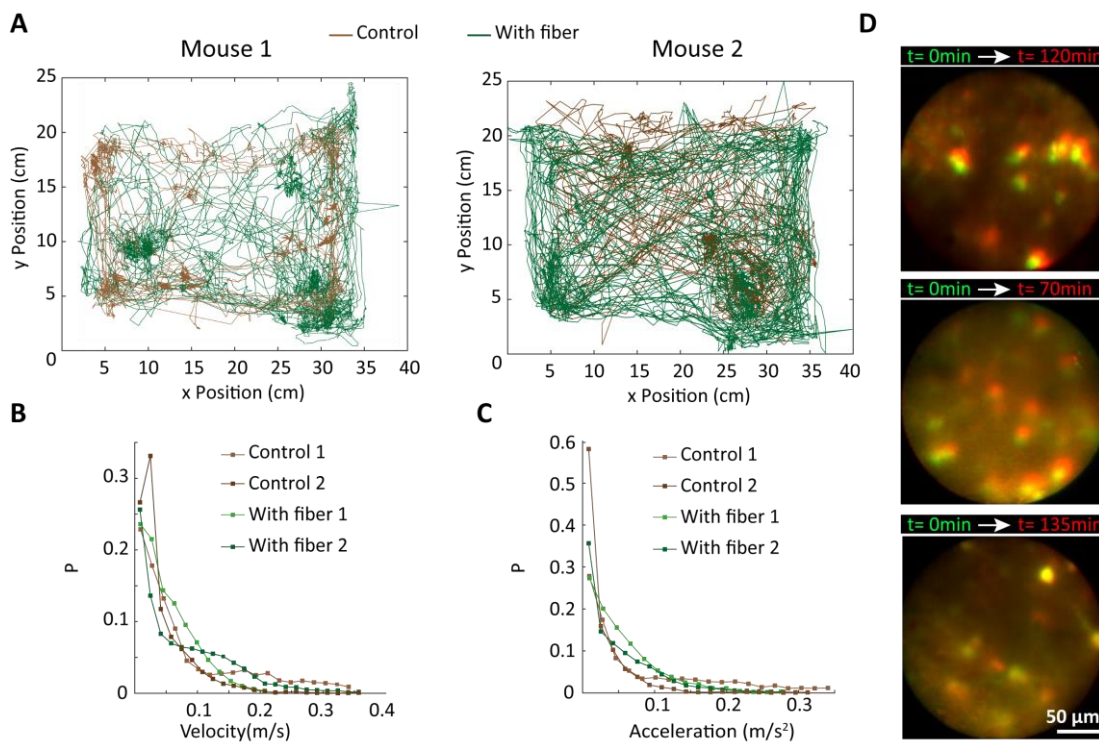


Figure 5. Mice movement with or without fiber, and long-term stability of the implant. A. Position tracking of two different mice for a time of 10-20 minutes, when the fiber bundle was in the implant and,

on a different day, without the fiber bundle (only with head plate and implant, called control in figure). In all cases animals were anesthetized for 20 minutes with isoflurane to have the same starting conditions. **B-C.** Probability distribution of the mouse velocity and acceleration showing no significant difference between the control (with no fiber) and with fiber condition. **D.** Examples FOVs of long time (> 1h) in 3 different mice in freely moving conditions to illustrate stability of the FOV. Each image is the superposition of two images, one acquired at the beginning (in green) and one at the end (in red) of the experimental session. The total displacement over the entire session is < 20 μm .

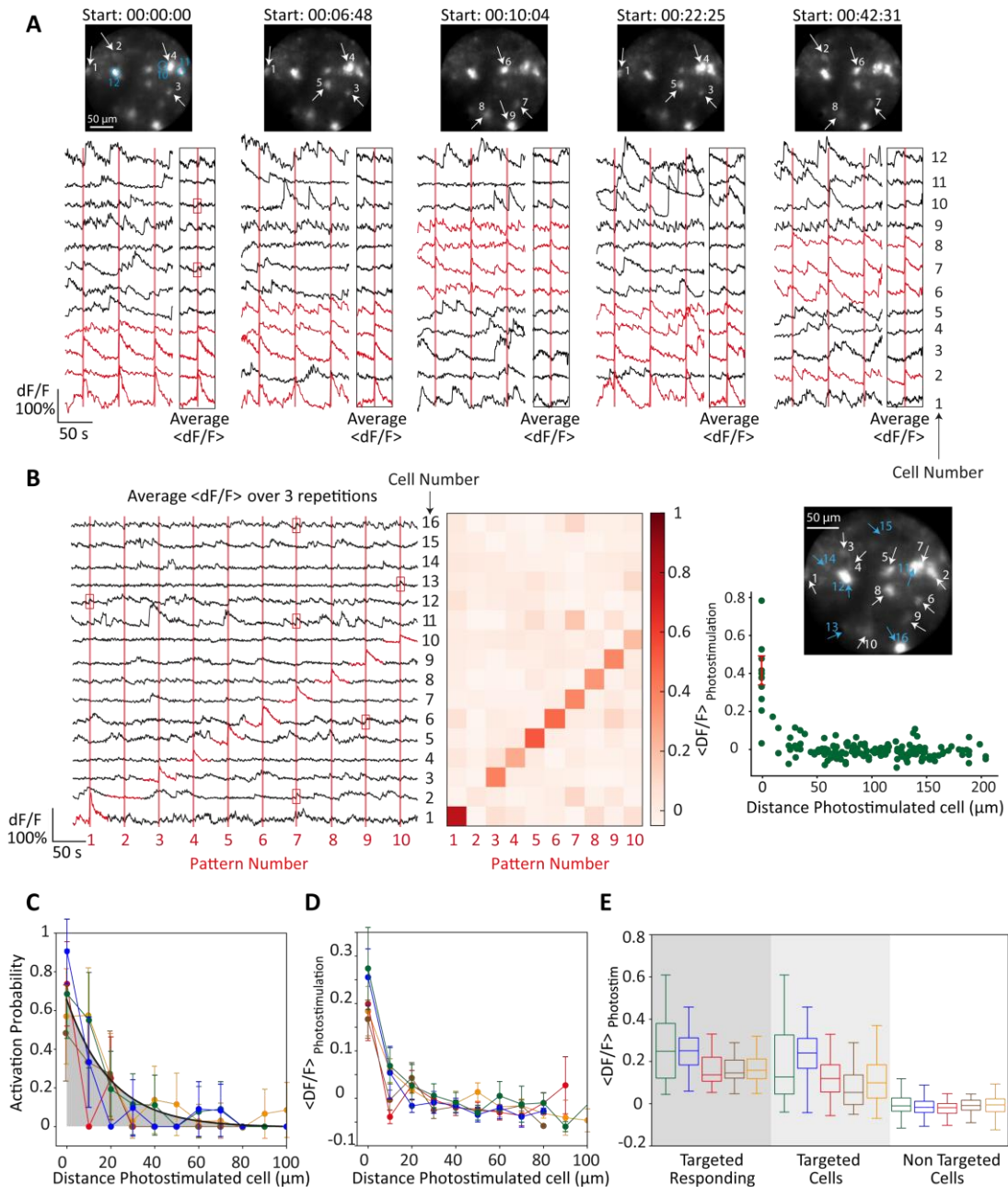


Figure 6. High resolution photostimulation in freely moving mice. A. Photostimulation of different groups of 4 neurons. Photostimulated neurons are indicated by arrows in the different z projections of each acquisition, and their calcium traces are plotted in red. For each group of neurons, the photostimulation was repeated 3 times, and the average signal was calculated and plotted as “Average $\langle dF/F \rangle$ ”. The starting time of each experiment relatively to the first acquisition is indicated on the top. **B.** Photostimulation of 10 different neurons, one by one. Left: Average $\langle dF/F \rangle$ traces over 3 photostimulation repetitions for every neuron. Traces of neurons photostimulated are plotted in red. Red frames highlight instances of increased activity for non-targeted neurons concomitant with the photostimulation period. Middle: heat map representing the average fluorescence change $\langle dF/F \rangle_{\text{Photostim}}$ upon photostimulation for photostimulated neurons (1-10) and control neurons (11-16) for each photostimulation pattern. Right: z-projection of the FOV showing targeted (white arrows) and non-targeted (blue arrows) neurons. Plot of $\langle dF/F \rangle_{\text{Photostim}}$ for each neuron as a function of the distance from the photostimulated cell. All example data are taken from one FOV in animal #2, see **Supplementary Table 1**. **C-E.** Population analysis of the photostimulation efficiency on 5 different FOVs and 3 different mice. Each color corresponds to a different FOV. **C.** Activation probability of neurons as a function of the distance from the photostimulated cells. The black solid line is a fit with an exponential decay, the gray region refers to the area underneath the fit. **D.** $\langle DF/F \rangle_{\text{Photostim}}$ for neurons that show a positive response to the photostimulation as a function of the distance from the photostimulated cells. In **C** and **D** in the case of multi-target photostimulation, we considered the distance from the closest photostimulated cell. **E.** Average $\langle DF/F \rangle_{\text{Photostim}}$ for targeted and responding; targeted (both responding and non-responding); and non-targeted neurons, showing a significant difference in the response for targeted and non-targeted neurons. See the main text and Methods, for a detailed explanation of how $\langle DF/F \rangle_{\text{Photostim}}$ and the activation probability were calculated. Data are taken from one FOV in animals #2/3/4, see **Supplementary Table 1**. Power distribution correction and photostimulation paradigm are detailed in see **Supplementary Figure 4**. Acquisition examples are presented in **Suppl. Video 3**.

	Input NA	Output NA	M	Input Work. Dist. (μm)	Output Work. Dist. (μm)	GRIN diameter (mm)	FOV diameter (μm)	Lateral res. (μm)
GRIN 1 GT-MO- 070-016- ACR-	0.16	0.7	4. 5	200	300, not corrected for	1.3	122, limited by	~ 1 , limited by inter-

VISNIR-30-20					cover glass		bundle diameter	core distance
GRIN 2 GT-MO-080-032-ACR-VISNIR-08CG-20	0.32	0.7	2.2	200	80, below 170 μ m cover glass	1.3	250, limited by bundle diameter	\sim 2, limited by inter-core distance

Table 1. Parameters of the two GRIN lenses. Input/output NA refer to the numerical aperture of the GRIN lenses on the fiber and sample side respectively. M is the magnification of the GRIN lens. Input and output working distances refer to the nominal working distance of the GRIN lenses on the fiber and sample side respectively. Input (output) working distances are specified for air (water) immersion respectively. Both GRIN lenses are suitable for imaging through a cover glass on the sample side, even if GRIN 1 is not specifically designed for that. The field of view and lateral resolution depend on the physical size of the fiber bundle (550 μ m in diameter, 15000 total cores), its core-to-core distance (\sim 4.5 μ m), and on the magnification of the GRIN lens, in the way described in **STAR Methods**.

STAR Methods

Key Resources Table

REAGENT or RESOURCE	SOURCE	IDENTIFIER
Bacterial and virus strains		
AAV9-CMV-GFP-WPRE	Xiong <i>et al</i> J Clin Invest. 2015	Addgene Cat#67634
AAV1.CAG.tdTomato	Edward Boyden lab	Addgene Cat#59462-AAV1
AAV9-syn-jGCaMP7s-WPRE	Dana <i>et al</i> Nat Methods. 2019	Addgene Cat#104487-AAV9
AAV1-hSyn-ChRmine-mscarlet-Kv2.1-WPRE	Marshel <i>et al</i> Science. 2019	Addgene Cat#130995
Chemicals, peptides, and recombinant proteins		
Dexazone (Dexamethasone) - Virbac	Centravet	Cat#DEX216
Laocaine (Lidocaine) - MSD	Centravet	Cat#LAO001

Rompun 2% (Xylazine) - Bayer	Centravet	Cat#ROM001
Ketamidol (Ketamine) - Axience	Axience Santé Animale	Cat#152500
Lubrithal (Eye gel) - Dechra	Centravet	Cat#LUB001
Buprenorphine	Axience Santé Animale	Cat#151244
Isoflurane	Axience Santé Animale	Cat#153613
Antisedan-ANTIDORM	Axience Santé Animale	Cat#152494
Tetric Evoflow A1-IVOCLAR	Dentaltix	Ca#45TE595953
Experimental models: Organisms/strains		
C57BL/6J	Janvier Labs	https://janvier-labs.com/fiche_produit/2-c57bl-6jrj/
Software and algorithms		
WaveFront IV	Emiliani's Lab	Available from: vincent.de-sars@inserm.fr
MATLAB 2020b	Mathworks	https://www.mathworks.com/
FIJI/ImageJ 2.0.0	ImageJ	https://imagej.net/software/fiji/
LabView 2016	National Instruments	https://www.ni.com/fr-fr/shop/labview.html
DeepLabCut 2.1	Mathis's Lab (Mathis et al. 2018)	https://github.com/DeepLabCut/DeepLabCut
CalmAn 1.9.7	Flatiron Institute	https://github.com/flatironinstitute/CalmAn
Other		
Laser Spark Alcor - ALCOR 920-4	Spark Alcor	https://spark-lasers.com/produit/alcor/

EM-CCD Camera iXon Ultra 888	Andor - Oxford Instruments	https://andor.oxinst.com/products/ixon-emccd-cameras-for-physical-science
Laser Goji	Amplitude	https://amplitude-laser.com/products/femtosecond-lasers/goji/
LCOS-SLM X10468-07	Hamamatsu	http://www.hamamatsu.com.cn/UserFiles/DownFile/Product/20130920095320007.pdf
Image Fiber FIGH-15-600N	Fujikura	https://www.fujikura.co.jp/eng/products/optical/appliedoptics/03/2050110_12902.html
GRIN Lens 1: GT-MO-070-016-ACR-VISNIR-30-20	Grintech	https://www.grintech.de/fileadmin/user_upload/Datenblaetter/High-NA_chromatic_and_field_corrected_Endomicroscopic_Imaging_Objectives.pdf
GRIN Lens 2: GT-MO-080-032-ACR-VISNIR-08CG-20	Grintech	https://www.grintech.de/fileadmin/user_upload/Datenblaetter/High-NA_chromatic_and_field_corrected_Endomicroscopic_Imaging_Objectives.pdf

RESOURCE AVAILABILITY

Lead contact

Extended information and requests for resources should be directed to the lead contact, Dr. Valentina Emiliani (valentina.emiliani@inserm.fr).

Materials availability

This study did not generate new unique reagents, mouse lines or optical elements. Commercially available resources are indicated in the [key resources table](#).

Data and Code Availability

- All data reported in this paper will be shared by the lead contact upon request.
- This paper does not report original code.
- Any additional information required to reanalyze the data reported in this paper is available from the lead contact upon request.

Experimental model and subject details

Mouse lines and knockout genetics

Wild-type males and females C57BL/6J mice (Janvier Labs) were used for experiments. All experiments were performed in accordance with EU Directive 2010/63. The protocols were reviewed by the local animal experimentation ethics committee (CETEA n.44) and authorized by the French Ministry of Research and Education (#201803261541580). Advices on procedures, refinement of animal experimentation standards, and pain and distress management are provided by the Local Animal Welfare Office. Animals are housed in 2-5 per cage, with a light-dark cycle of 12+12 hours, and food and water ad libitum.

METHOD DETAILS

Imaging setup

The imaging laser was an ultrafast fiber laser (Spark Alcor, central wavelength of 920 nm, pulse duration of 150 fs, total power of 4 W, repetition rate of 80 MHz), whose output power was controlled by using a lambda half waveplate and a polarizing beam splitter. The internal laser compressor was set to $\sim -90000 \text{ fs}^2$ to compensate for the fiber dispersion. The laser beam was first magnified using a 5X beam expander. It was then sent through a motorized iris to control the size of the beam at the fiber (and therefore at the sample), in this way we could control the imaging power by changing the imaging spot size without effective changes in the power/core. This enabled to keep the power per core always lower than the onset of self-phase modulations effects ($\sim 10 \text{ mW/core}$). The galvo-resonant mirrors were placed in a Fourier plane of both the iris and the fiber entrance. The beam passing through the motorized iris was focused at the entrance of the galvo-resonant mirrors using 3 lenses ($f_1=200 \text{ mm}$, $f_2=60 \text{ mm}$, $f_3=500 \text{ mm}$, for simplicity in the scheme of the setup in Fig.1 only one lens between the first iris and the galvo-resonant mirrors is shown). After the galvo-resonant mirrors,

a first lens ($f_4=400$ mm) created an intermediate imaging plane where we placed a second iris that was perfectly imaged at the fiber entrance using one lens ($f_5=200$ mm) and a microscope objective (Olympus, UPLFLN 10X, 0.3 NA). The second iris prevented the beam to be scanned outside of the fiber region, thus avoiding unwanted thermal and nonlinear effects that might come from the fiber coating or the fiber holder. The average power measured after the second iris was $\sim 50\%$ of the power measured before. This is because, to uniformly illuminate the fiber entrance, the second iris cut the outer parts of the scanned regions, where galvo and resonant scanners decrease their speeds and spend more time. The fluorescence emission from the sample was collected through the endoscope and the same 10X microscope objective. A long pass dichroic beam splitter was then used to separate it from the incoming laser beam and reflect it to the EM-CCD camera (Andor Ultra 888, 1024×1024 pixels, pixel size $13.3 \times 13.3 \mu\text{m}^2$). The camera was used in crop mode with a sub array of 512×512 pixels corresponding to a maximum frame rate of 94 fps. A 180 mm focal length lens was used to focus the fluorescence onto the camera after passing through 2 IR blocking filters (Thorlabs TF1). To select green (for GFP and GCaMP7) or red (for TdTomato) fluorescence emission, a flip motor (Thorlabs MFF102) switched from a green to a red emission filter.

Photostimulation setup

The photostimulation laser was a low repetition rate fiber laser (Goji, central wavelength of 1040 nm, pulse duration of 150 fs, total power of 5 W, repetition rate of 10 MHz, internal laser compressor set to $\sim -90000 \text{ fs}^2$) whose power was controlled by a lambda half waveplate and a polarizing beam splitter. The laser beam was magnified by a 5X beam expander and spatially shaped by an SLM (LCOS-SLM X10468-07, Hamamatsu Photonics, resolution 800×600 pixels, $20 \mu\text{m}$ pixel size). Two lenses ($f_{1\text{SLM}}=250$ mm and $f_{2\text{SLM}}=300$ mm) conjugated the SLM plane with the entrance of the microscope objective (Olympus, UPLFLN 10X, 0.3 NA). A short pass dichroic mirror was used to recombine the photostimulation and imaging beams before entering the microscope objective. The laser beam was made slightly divergent with the beam expander before arriving to the SLM, which applied a defocus to the beam to compensate the divergence. In this way we separated in z the planes of the 0th and 1st diffraction order of the SLM. A small beam blocker was then used to block the 0th order (see Ref.⁷¹).

Fiber and GRIN lens specifications

The fiber bundle used in the experiments was a 2 meter commercially available bundle (Fujikura model FIGH-15-600N), which was coupled to chromatic and field corrected GRIN micro-objectives (Grintech models GT-MO-080-032-ACR-VISNIR-08CG-20 or GT-MO-070-016-ACR-VISNIR-30-20,

diameter of 1.3 mm). The chromatic correction allows both the fluorescence and two laser wavelengths, for imaging and photostimulation, to be focused on the same plane.

The diameter of the FOV (D_{FOV}) currently accessible to 2P-FENDO is limited by the diameter of the optical fiber bundle (D_{Bundle}) and the magnification of the GRIN lenses (M_{GRIN}), according to the relation $D_{FOV} = D_{Bundle}/M_{GRIN}$. At the same time, the lateral resolution (d_{xy}) is limited by the intercore distance within the fiber bundle ($d_{intercore} \approx 4.5 \mu m$ in for the current fiber bundle) and M_{GRIN} , according to $d_{xy} = d_{intercore}/M_{GRIN}$. To enlarge the FOV without affecting the lateral resolution of the system, one could use a bundle with a larger diameter, matching the GRIN lens diameter (~ 1 mm). Similar bundles are commercially available but have a reduced flexibility with respect to the ones used in this work, which would restrain too much the movements of the mice. The only alternative could be to reduce the magnification of the GRIN lens, which in turn depends on the ratio between the NA on the sample side and that on the fiber side according to $M_{GRIN} = NA_{sample}/NA_{fiber}$. Reducing the NA on the sample side could therefore enlarge the FOV at the expenses of the detected fluorescence signal. Additionally, a lower NA could be obtained with a GRIN lens of a smaller diameter (GRIN lenses with a diameter as small as 300 μm are already commercially available with NAs of 0.5), which might be beneficial to reduce further the size of the endoscope. However, reducing the GRIN lens magnification would also cause a decrease in the lateral resolution. To compensate for this, one might use fiber bundles with more closely spaced cores, which are already commercially available (such as the S series from Fujikura).

GRIN lens 2 is designed to be at a distance, $d=200 \mu m$ from the fiber bundle, and to produce a working distance, WD, of 80 μm (in water or brain tissue) below a cover glass of 170 μm in thickness (see **Table 1** in the main manuscript). To increase this value and reach deeper cortical layer (L2/3), we have proceeded as follows: 1) we kept the GRIN lens always in contact with the fiber bundle, which increased the working distance in brain tissue of $\sim 70 \mu m$; 2) we used cover glasses of thickness of $\sim 100 \mu m$, which further increased the working distance of $\sim 60 \mu m$, taking into account the refractive index mismatch between glass and water (or brain). With these modifications, we could reach a working distance of ~ 150 to 200 μm below the cover glass for in vivo experiments in the water immersion configuration (see **Supplementary Fig. 3**). GRIN lens 2 is specified by the manufacturer (Grintech) to work in water (or brain tissue) after the protective cover glass. To keep as much as possible these ideal conditions, in all the experiments on rhodamine, fixed brain slices, pollen grains, head-fixed animals the space between the GRIN lens and the cover glass was filled with water. To prevent water evaporation, experiments in freely moving mice, in which the GRIN lens is cemented on top of the craniotomy for several days, the space

between the GRIN lens and the cover glass was filled with a drop of index matching oil for microscope objectives. This, as shown in Ref.^{72,73} has the effect of shifting the effective focal plane, as better quantified in **Supplementary Fig. 3**. In the oil immersion configuration, the maximum attainable working distance is lower, namely ~ 120 to $160 \mu\text{m}$.

For the characterization and the head-fixed experiments the fiber and GRIN lens were held on two separated mounts and could be moved one respect to the other by using a three-dimensional translation stage.

Power measurements

Because of the filling factor of the fiber bundle ($\sim 50\%$ transmission when using a large spot encompassing multiple cores), the infra-red transmission of the low NA objective ($\sim 80\%$ at 920 nm and $\sim 60\%$ at 1030 nm) used to focus the laser inside the fiber and the coupling between the GRIN lens and the fiber bundle ($\sim 90\%$ efficiency), the total transmission for the imaging laser is $\sim 35\%$ and for the photostimulation laser is $\sim 27\%$. This value can be increased by using a higher transmission lens in the infra-red range but will still be ultimately limited by the filling factor of the fiber bundle.

For the photostimulation laser one additionally has to account for the 70% efficiency of the SLM (considering reflection efficiency, zero order losses, diffraction efficiency losses), and the transmission of polarization optics (λ half waveplates and polarizers to control the power, beam expander to enlarge the beam at the SLM, additional lenses to get to the objective pupil). Considering all this, we measured a total available photostimulation power after the endoscope of 600 mW , when starting with a 5 W laser.

Because the imaging spot is scanned at the fiber entrance by using a galvo-resonant scanner, in order to completely fill the fiber, we scanned the laser beam on a square of lateral dimension of $\sim 600 \mu\text{m}$, where the diameter of the fiber bundle is $\sim 550 \mu\text{m}$. This ensures uniform illumination of the fiber bundle. In order to prevent the laser beam to hit the fiber cladding, which could possibly damage the fiber, we clipped the beam by using an iris placed in the first image plane after the scanners. Because the resonant scanner passes more time on the edges, in which it slows down and turns around, than in the center, a large amount of the total power is lost on the iris (or, if an iris were not used, it would be lost outside of the fiber). In our system, the average power measured after the GRIN lens while scanning the entire FOV was 50% of the power measured when the beam was static (not scanned) at the fiber entrance.

Signal comparison between core-by-core scanning and multi-core illumination.

A key property of 2P-FENDO, which enables faster acquisition speeds with respect to previous 2P fiber bundle approaches is the optimized illumination and detection scheme. By making an extended excitation spot, and detecting the 2P fluorescence with a high quantum efficiency and low readout noise EMCCD camera, 2P-FENDO gains in the total amount of photons detected per cell, which is ultimately the signal one is interested in when performing calcium imaging. Let us consider the case of a fiber bundle with a filling factor of 50% ($F=0.5$) and compare the two-photon signal (2PS) coming from a cell that occupies $N=20$ cores of the fiber bundle in two different cases: 1) The scanning microscope configuration, in which a laser intensity I is focused on a diffraction limited spot that is scanned on the cell on a total time T . Each core is thus illuminated for a total time that is $T/(N/F) = T/(2N)$ in the case of a 50% filling factor. This is because the scanning beam at the fiber entrance has to scan also on the dark space in between different cores. The detection is performed with a PMT that has a quantum efficiency of $\sim 40\%$. To avoid damage of the fiber, which mainly happens because during scanning one also scans in the space between fiber cores, the scanning configuration is practically limited to power values < 100 mW; 2) The 2P-FENDO configuration in which every core is excited simultaneously for a total time T with the same intensity I_{max} , just below the threshold for self-phase modulation (SPM) to occur, which was measured to be roughly 10 mW per core^{1–4}. The detection is performed with an EMCCD camera that has a quantum efficiency of $\sim 90\%$. For simplicity we will assume a twice higher quantum efficiency for the camera than for the PMT. In the ideal case, in which the 2PS scales quadratically with the laser intensity, we obtain:

$$2PS_{Scan}^{Ideal} \propto A I^2 T F = A I^2 \frac{T}{2}$$

$$2PS_{FENDO}^{Ideal} \propto I_{max}^2 T N$$

Where we have introduced a scaling factor A representing the ratio between the quantum efficiency of the PMT and the camera ($A=0.5$ in this case).

However, when using small core fibers or fiber bundles, SPM results in a longer pulse at the fiber output. This, in turns, means that the quadratic relation between the 2P signal and the excitation power breaks down above 10 mW, and the 2P signal grows sub-optimally, eventually only scaling linearly as the power is further increased (see for instance Ref.^{18,32,34,35}). For instance, from Ref.³⁵, a laser pulse of 150 fs at the fiber output for a power of 10 mW becomes ~ 1 ps when the power is increased to 100 mW. If we call $S_{core}(I)$ the 2PS from a single core of the fiber bundle as a function of the laser intensity, we can write the previous equations as:

$$2PS_{\text{Scan}} = A S_{\text{core}}(I) T F$$

$$2PS_{\text{FENDO}} = S_{\text{core}}(I = I_{\text{max}}) T N$$

If we limit to powers per cores < 100 mW, considering that $\text{Score}(I=100\text{mW}) \approx 15 * \text{Score}(I=I_{\text{max}}=10\text{mW})$, 2P-FENDO, thanks to the wider illumination and the higher camera quantum efficiency is able to detect 2.5 or 5 times the signal when using N=10 or N=20 cores and total power of 100 mW or 200 mW. This ultimately allows 2P-FENDO to increase proportionally the acquisition speed with respect to 2P scanning techniques when using comparable laser powers

Controlling software and synchronization with photostimulation.

A custom-designed software written in LabVIEW was used to control the motorized iris at the imaging laser, the galvo-resonant scanners, the photostimulation laser power, the fast shutter to control the photostimulation timing, the z step motor used to move vertically the micro-endoscope, and the XY position stage that moved the anesthetized mouse with respect to the endoscope.

A custom-designed software, Wavefront-Designer IV, written in C++ and using the open graphic library Qt 4.8.7, controlled the SLM for the dynamic CGH configuration, using Gerchberg-Saxton-based algorithms. The software also included the phase corrections for the first-order Zernike aberrations.

The EM-CCD camera was controlled with its software (Andor Solis) and externally synchronized with the LabVIEW software for z-stack and photostimulation experiments.

During photostimulation a fast shutter was used to let through the Goji laser for 10 ms every 140 or 225 ms. The EM-CCD camera was used in external exposure mode and turned off between 25 to 40 ms in correspondence to the periods of Goji illumination. With this we removed completely any artifact that might come from the direct excitation of fluorescence from the photostimulation laser. For a better visualization of the photostimulation protocol, see **Supplementary Fig. 4**

Viral vectors injections and surgical procedure for in-vivo experiments.

Stereotaxic injections were performed to deliver high titer adeno-associated viral vectors to cortical neurons of 5-8-weeks-old mice for expression of GFP, TdTomato, the calcium reporter jGCaMP7s, the opsins ChRmine, or jGCaMP7s+ChRmine. The following viral constructs were used (viral concentration in the order of 10^{12} vp/ml): AAV9-CMV-GFP-WPRE (Vision Institute vector core facility, Paris), AAV1.CAG.tdTomato (Addgene), AAV9-syn-jGCaMP7s-WPRE (Addgene), AAV1-hSyn-

ChRmine-mscarlet-Kv2.1-WPRE (plasmid from Addgene), or a mixture 2:1 of AAV9-syn-jGCaMP7s-WPRE + AAV1-hSyn-ChRmine-mscarlet-Kv2.1-WPRE. Imaging and photostimulation experiments were performed 3-15 weeks after injection. All surgical procedures were performed in sterile conditions on mice anesthetized with intraperitoneal injection of a mixture of ketamine (60-80 mg/Kg) - xylazine (5-8 mg/Kg). Eyes were protected with ophthalmic gel, and the animal was placed on the stereotaxic frame. The anti-inflammatory dexamethasone sodium phosphate (0.01 mg/g) and analgesic buprenorphine (0.1mg/Kg) were injected subcutaneously before surgery. Lidocaine 2% was injected subcutaneously before opening the skin. Body temperature was kept constant at 37°C and anesthesia parameters were monitored all along the experiments (homeothermic system, Kent Scientific). Subcutaneous injections of 0.1 ml sterile saline solution ensured rehydration all along the experiments.

For viral vectors injections, a craniotomy of 0.5-0.7 mm was made on the skull overlying V1 or wS1 cortex, and 1µl solution containing the viral vector was delivered at 150-50 µm depth from the brain surface. Skin was sutured and mouse recovered from anesthesia. Buprenorphine was injected 8-12 hours after surgery.

The cranial window surgery was performed 3-15 weeks after injection. A cranial window of 3-3.5 mm was made above and centered on the viral injection site. Dura was removed while keeping the brain surface moist with sterile saline solution. A 3 mm cover glass (#0, 0.085 to 0.13 mm thickness; Multichannel System) was placed on top of the craniotomy and sealed with dental cement (Tetric EvoFlow A2, Ivoclar). The head plate was then fixed with dental cement.

Mice were given at least 3 days to recover from the cranial window surgery done under ketamine/xylazine. On experimental day one, mice were maintained head-fixed under isoflurane anesthesia (<1.5%) for 40min. The region with best expression of opsin and calcium reporter was identified under 2P FENDO. Then the fiber/GRIN lens holder was fixed with dental cement over the window.

For *in vivo* freely moving imaging and photostimulation experiments, mice were let recover in their home cage. The light and short isoflurane anesthesia allowed for fast recovery, in the order of minutes. At the end of the recording session (3-4h) mice were put back on isoflurane (<5 min) to remove the fiber from the holder. At the start of every following session, mice were maintained 20 min head-fixed under isoflurane anesthesia to set-up the fiber back in the holder. With this holder system and cranial window surgical methodology, animals were recorded for successive experiments for up to 1.5 months.

The only limitation being the growth of fibrotic tissue commonly observed in chronic windows that will end up blocking optical access.

Axial resolution measurements

For characterizing the axial resolution and performances of the 2P-FENDO, both for the imaging and photostimulation lasers, the 2P fluorescence from a thin ($\sim 1 \mu\text{m}$) spin-coated fluorescent layer of rhodamine-6G in polymethyl methacrylate 2% w/v in chloroform was collected through the endoscope and sent to the camera detector. By using a z-step motor (Thorlabs DDS100), the endoscope (fiber+ GRIN lens) was scanned over the desired z range to collect 3D stacks of images. We performed the analysis of the recorded stacks with MATLAB and ImageJ. The 2P fluorescence values were obtained by integrating the intensity of all the pixels in a circular area containing the (imaging or holographic) spot, for each plane of the recorded stack. Reported values for the axial confinement were the fit of the axial profile of the spots with a Lorentzian model and referred to the FWHM of the curves.

Motion correction and movement estimation

We used CalmAn⁴¹ to quantify and correct for the motion of the FOV, by using patched non-rigid motion correction. We used patches of 30-60 μm . For each frame f in the acquisition and for each patch p , we thus obtained the x and y displacement of the FOV in μm , called $d_x(f, p)$ and $d_y(f, p)$, from which we calculated the total displacement, according to $d(f, p) = \sqrt{d_x(f, p)^2 + d_y(f, p)^2}$. We then averaged $d(f, p)$ over all patches to obtain a mean displacement for each frame, i.e. $\langle d(f) \rangle_p$. We did not consider patches at the corners of the images as they contained a significant number of pixels that corresponded to areas outside of the fiber bundle and therefore would remain static during acquisition.

By synchronizing calcium acquisition with the videos of the animals moving in the cages, we could then divide the frames according to the animal speed into two groups: f^+ and f^- , for mouse speeds greater or lower than 5cm/s. We then calculated the average and the standard deviation of the mean displacement over relevant frames $\langle d \rangle_{p, f^+}$ and $\langle d \rangle_{p, f^-}$, which are plotted in Fig.3f.

QUANTIFICATION AND STATISTICAL ANALYSIS

Calcium data analysis

After motion correction, we let CalmAn automatically detect active neurons. We confirmed that the detected regions of interest (ROIs) corresponded to actual cells by visually inspected the images and manually removing ROIs that did not match neurons. For each found neuron, we used the SNR value produced by CalmAn, according to the definition given in Ref.⁴¹. To calculate DF/F traces, we used the *detrend_df_f* function from CalmAn.

The algorithm was run with the following parameters, following the CalmAn conventions: *gnb*=1 (global background components); low thresholds: *rval_lowest*=0.3, *SNR_lowest*=0.5, *cnn_lowest*=0.3; high thresholds: *rval_thr*=0.8; *min_SNR*=2 to 2.5; *cnn_thr*= 0.8 to 0.9. A neuron has to exceed all the low thresholds and at least one high threshold to be accepted. Occasionally, after manual inspection we added few cells with *SNR*<0.5. We briefly remind that *rval* measures the spatial footprint consistency of each found component; *SNR* is calculated from strong peaks of fluorescence in a trace and considering the baseline noise over the whole trace; the *cnn* based classification quantifies the resemblance of a component to a neuronal soma using a 4-layer convolutional neuronal network.

For photostimulation data we always repeated the same photostimulation patterns for three consecutive times. We then averaged the DF/F signal over the three consecutive repetitions, generating the average $\langle DF/F \rangle$. We used this average signal to determine if a neuron was or not photostimulated and to calculate the induced increase of fluorescence signal $\langle DF/F \rangle_{\text{Photostim}} = \langle DF/F \rangle_{\text{After}} - \langle DF/F \rangle_{\text{Before}}$ in response to photostimulation. We compare the average signal 2s before photostimulation $\langle DF/F \rangle_{\text{Before}}$ (which constitutes our baseline signal) with the average signal during the 2s following the middle of the photostimulation period $\langle DF/F \rangle_{\text{After}}$. As the photostimulation was composed by 10 pulses, we calculated $\langle DF/F \rangle_{\text{After}}$ by averaging over 2s after the 5th photostimulation pulse. A cell (either targeted or non-targeted) was considered photostimulated if $\langle DF/F \rangle_{\text{Photostim}}$ was greater than 3 times the standard deviation of the baseline signal.

Image treatment

A downside of using disordered bundles is that the transmission and dispersion properties of each core can be slightly different, which results in inhomogeneous 2P signals from different cores even when imaging uniform fluorescent samples. In the images presented here, a Gaussian blur function was used to smooth out the core-to-core differences. Alternatively, this is can be solved, as shown in Ref.¹⁸, by mapping the spatial distribution of the 2P fluorescence on a homogeneous microscope fluorescence slide and correcting for the fiber induced inhomogeneities in post processing.

Tracking data processing

The tracking videos were first analyzed in DeepLabCut, which was trained to recognize the implant and the body center on the freely moving mice. The model was trained with between 15-20 labeled datasets from different mice videos, with different tracking camera-mice cage positions and illumination conditions. From DeepLabCut we extracted the implant and body center part positions in pixels for each frame and a likelihood estimation (value between 0 and 1). We only considered the positions for which the likelihood was at least >0.9 (good confidence estimation). We considered the implant position as the head position of the mouse and the camera frame rate is 50Hz. To calculate the velocity on the mice we divided the distance of the implant between two adjacent frames by the time interval between these two frames ($1/50\text{Hz}$). The same calculation was done for the acceleration but in this case, we divided the velocity in two adjacent frames by the time interval.

References

1. O'Connor, D.H., Huber, D., and Svoboda, K. (2009). Reverse engineering the mouse brain. *Nature* *461*, 923–929. [10.1038/nature08539](https://doi.org/10.1038/nature08539).
2. Emiliani, V., Cohen, A.E., Deisseroth, K., and Häusser, M. (2015). All-Optical Interrogation of Neural Circuits. *The Journal of Neuroscience* *35*, 13917–13926. [10.1523/JNEUROSCI.2916-15.2015](https://doi.org/10.1523/JNEUROSCI.2916-15.2015).
3. Marshel, J.H., Kim, Y.S., Machado, T.A., Quirin, S., Benson, B., Kadmon, J., Raja, C., Chibukhchyan, A., Ramakrishnan, C., Inoue, M., et al. (2019). Cortical layer-specific critical dynamics triggering perception. *Science* (1979) *365*. [10.1126/science.aaw5202](https://doi.org/10.1126/science.aaw5202).
4. Packer, A.M., Russell, L.E., Dagleish, H.W.P., and Häusser, M. (2015). Simultaneous all-optical manipulation and recording of neural circuit activity with cellular resolution in vivo. *Nat Methods* *12*, 140–146. [10.1038/nmeth.3217](https://doi.org/10.1038/nmeth.3217).
5. Rickgauer, J.P., Deisseroth, K., and Tank, D.W. (2014). Simultaneous cellular-resolution optical perturbation and imaging of place cell firing fields. *Nat Neurosci* *17*, 1816–1824. [10.1038/nn.3866](https://doi.org/10.1038/nn.3866).
6. Carrillo-Reid, L., Han, S., Yang, W., Akrouh, A., and Yuste, R. (2019). Controlling Visually Guided Behavior by Holographic Recalling of Cortical Ensembles. *Cell* *178*, 447-457.e5. [10.1016/j.cell.2019.05.045](https://doi.org/10.1016/j.cell.2019.05.045).
7. Gill, J. V., Lerman, G.M., Zhao, H., Stetler, B.J., Rinberg, D., and Shoham, S. (2020). Precise Holographic Manipulation of Olfactory Circuits Reveals Coding Features Determining Perceptual Detection. *Neuron* *108*, 382-393.e5. [10.1016/j.neuron.2020.07.034](https://doi.org/10.1016/j.neuron.2020.07.034).
8. Chen, I.-W., Ronzitti, E., Lee, B.R., Daigle, T.L., Dalkara, D., Zeng, H., Emiliani, V., and Papagiakoumou, E. (2019). In vivo sub-millisecond two-photon optogenetics with temporally focused patterned light. *The Journal of Neuroscience* *39*, 1785–18. [10.1523/jneurosci.1785-18.2018](https://doi.org/10.1523/jneurosci.1785-18.2018).
9. Zhang, Z., Russell, L.E., Packer, A.M., Gauld, O.M., and Häusser, M. (2018). Closed-loop all-optical interrogation of neural circuits in vivo. *Nat Methods* *15*, 1037–1040. [10.1038/s41592-018-0183-z](https://doi.org/10.1038/s41592-018-0183-z).
10. Chong, E., Moroni, M., Wilson, C., Shoham, S., Panzeri, S., and Rinberg, D. (2020). Manipulating synthetic optogenetic odors reveals the coding logic of olfactory perception. *Science* (1979) *368*. [10.1126/science.aba2357](https://doi.org/10.1126/science.aba2357).
11. Aharoni, D., and Hoogland, T.M. (2019). Circuit investigations with open-source miniaturized microscopes: Past, present and future. *Front Cell Neurosci* *13*, 141. [10.3389/fncel.2019.00141](https://doi.org/10.3389/fncel.2019.00141).
12. Skocek, O., Nöbauer, T., Weilguny, L., Martínez Traub, F., Xia, C.N., Molodtsov, M.I., Grama, A., Yamagata, M., Aharoni, D., Cox, D.D., et al. (2018). High-speed volumetric imaging of neuronal activity in freely moving rodents. *Nat Methods*, 1–4. [10.1038/s41592-018-0008-0](https://doi.org/10.1038/s41592-018-0008-0).
13. de Groot, A., van den Boom, B.J.G., van Genderen, R.M., Coppens, J., van Veldhuijzen, J., Bos, J., Hoedemaker, H., Negrello, M., Willuhn, I., De Zeeuw, C.I., et al. (2020). Ninscope, a versatile miniscope for multi-region circuit investigations. *Elife* *9*. [10.7554/eLife.49987](https://doi.org/10.7554/eLife.49987).
14. Zong, W., Wu, R., Li, M., Hu, Y., Li, Y., Li, J., Rong, H., Wu, H., Xu, Y., Lu, Y., et al. (2017). Fast high-resolution miniature two-photon microscopy for brain imaging in freely behaving mice. *Nat Methods* *14*, 713–719. [10.1038/nmeth.4305](https://doi.org/10.1038/nmeth.4305).

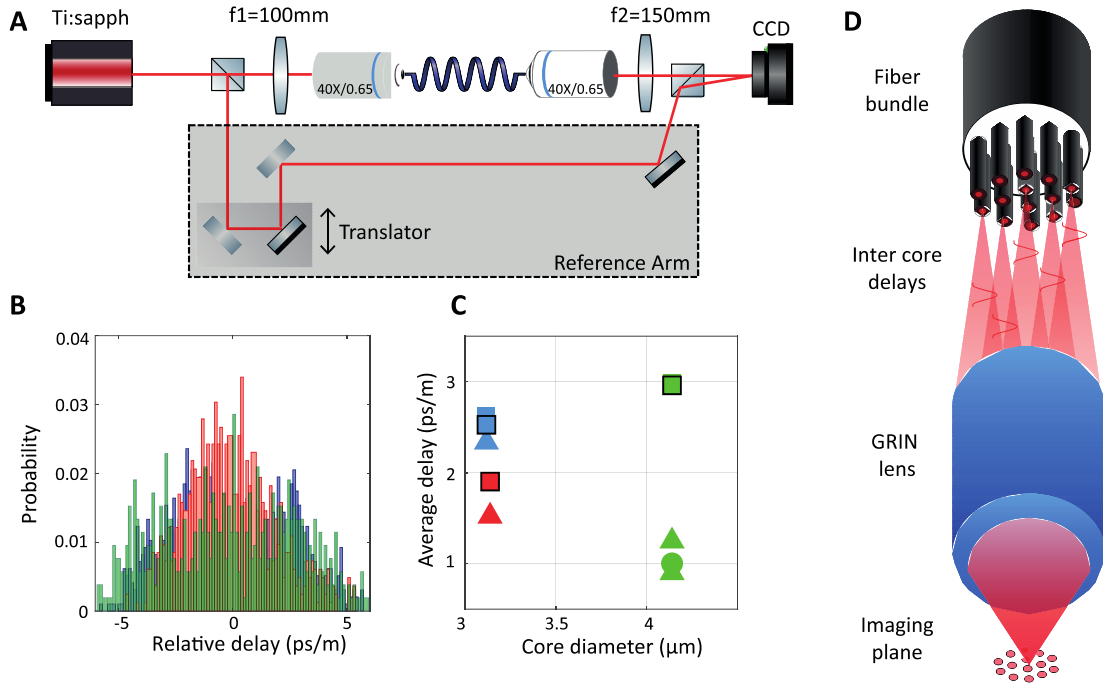
15. Zong, W., Wu, R., Chen, S., Wu, J., Wang, H., Zhao, Z., Chen, G., Tu, R., Wu, D., Hu, Y., et al. (2021). Miniature two-photon microscopy for enlarged field-of-view, multi-plane and long-term brain imaging. *Nat Methods* *18*, 46–49. [10.1038/s41592-020-01024-z](https://doi.org/10.1038/s41592-020-01024-z).
16. Szabo, V., Ventalon, C., De Sars, V., Bradley, J., and Emiliani, V. (2014). Spatially Selective Holographic Photoactivation and Functional Fluorescence Imaging in Freely Behaving Mice with a Fiberscope. *Neuron* *84*, 1157–1169.
17. Dussaux, C., Szabo, V., Chastagnier, Y., Fodor, J., Léger, J.F., Bourdieu, L., Perroy, J., and Ventalon, C. (2018). Fast confocal fluorescence imaging in freely behaving mice. *Sci Rep* *8*, 16262. [10.1038/s41598-018-34472-x](https://doi.org/10.1038/s41598-018-34472-x).
18. Ozbay, B.N., Futia, G.L., Ma, M., Bright, V.M., Gopinath, J.T., Hughes, E.G., Restrepo, D., and Gibson, E.A. (2018). Three dimensional two-photon brain imaging in freely moving mice using a miniature fiber coupled microscope with active axial-scanning. *Sci Rep* *8*, 8108. [10.1038/s41598-018-26326-3](https://doi.org/10.1038/s41598-018-26326-3).
19. Li, A., Guan, H., Park, H.-C., Yue, Y., Chen, D., Liang, W., Li, M.-J., Lu, H., and Li, X. (2021). Twist-free ultralight two-photon fiberscope enabling neuroimaging on freely rotating/walking mice. *Optica* *8*, 870. [10.1364/optica.422657](https://doi.org/10.1364/optica.422657).
20. Aharoni, D., Khakh, B.S., Silva, A.J., and Golshani, P. (2019). All the light that we can see: a new era in miniaturized microscopy. *Nat Methods* *16*, 11–13. [10.1038/s41592-018-0266-x](https://doi.org/10.1038/s41592-018-0266-x).
21. Helmchen, F., Fee, M.S., Tank, D.W., and Denk, W. (2001). A miniature head-mounted two-photon microscope: High-resolution brain imaging in freely moving animals. *Neuron* *31*, 903–912. [10.1016/S0896-6273\(01\)00421-4](https://doi.org/10.1016/S0896-6273(01)00421-4).
22. Sawinski, J., Wallace, D.J., Greenberg, D.S., Grossmann, S., Denk, W., and Kerr, J.N.D. (2009). Visually evoked activity in cortical cells imaged in freely moving animals. *Proc Natl Acad Sci U S A* *106*, 19557–19562. [10.1073/pnas.0903680106](https://doi.org/10.1073/pnas.0903680106).
23. Gu, M., Bao, H., and Kang, H. (2014). Fibre-optical microendoscopy. *J Microsc* *254*, 13–18. [10.1111/jmi.12119](https://doi.org/10.1111/jmi.12119).
24. Lombardini, A., Mytskaniuk, V., Sivankutty, S., Andresen, E.R., Chen, X., Wenger, J., Fabert, M., Joly, N., Louradour, F., Kudlinski, A., et al. (2018). High-resolution multimodal flexible coherent Raman endoscope. *Light Sci Appl* *7*, 10. [10.1038/s41377-018-0003-3](https://doi.org/10.1038/s41377-018-0003-3).
25. Park, H.-C., Guan, H., Li, A., Yue, Y., Li, M.-J., Lu, H., and Li, X. (2020). High-speed fiber-optic scanning nonlinear endomicroscopy for imaging neuron dynamics in vivo. *Opt Lett* *45*, 3605. [10.1364/ol.396023](https://doi.org/10.1364/ol.396023).
26. Klioutchnikov, A., Wallace, D.J., Frosz, M.H., Zeltner, R., Sawinski, J., Pawlak, V., Voit, K.M., Russell, P.S.J., and Kerr, J.N.D. (2020). Three-photon head-mounted microscope for imaging deep cortical layers in freely moving rats. *Nat Methods* *17*, 509–513. [10.1038/s41592-020-0817-9](https://doi.org/10.1038/s41592-020-0817-9).
27. Zong, W., Obenaus, H.A., Skytøen, E.R., Eneqvist, H., de Jong, N.L., Vale, R., Jorge, M.R., Moser, M.-B., and Moser, E.I. (2022). Large-scale two-photon calcium imaging in freely moving mice. *Cell* *185*, 1240–1256.e30. [10.1016/j.cell.2022.02.017](https://doi.org/10.1016/j.cell.2022.02.017).

28. Stamatakis, A.M., Schachter, M.J., Gulati, S., Zitelli, K.T., Malanowski, S., Tajik, A., Fritz, C., Trulson, M., and Otte, S.L. (2018). Simultaneous optogenetics and cellular resolution calcium imaging during active behavior using a miniaturized microscope. *Front Neurosci* 12, 496. 10.3389/fnins.2018.00496.
29. Zhang, J., Hughes, R.N., Kim, N., Fallon, I.P., Bakhurin, K., Kim, J., and Yin, H.H. (2021). All-optical imaging and patterned stimulation at cellular resolution with a one-photon endoscope. *bioRxiv*, 2021.12.19.473349. 10.1101/2021.12.19.473349.
30. Supekar, O.D., Sias, A., Hansen, S.R., Martinez, G., Peet, G.C., Peng, X., Bright, V.M., Hughes, E.G., Restrepo, D., Shepherd, D.P., et al. (2022). Miniature structured illumination microscope for in vivo 3D imaging of brain structures with optical sectioning. *Biomed Opt Express* 13, 2530. 10.1364/boe.449533.
31. Göbel, W., Kerr, J.N.D., Nimmerjahn, A., and Helmchen, F. (2004). Miniaturized two-photon microscope based on a flexible coherent fiber bundle and a gradient-index lens objective. *Opt Lett* 29, 2521. 10.1364/OL.29.002521.
32. Bao, H., Allen, J., Pattie, R., Vance, R., and Gu, M. (2008). Fast handheld two-photon fluorescence microendoscope with a 475 microm x 475 microm field of view for in vivo imaging. *Opt Lett* 33, 1333–1335. 10.1364/OL.33.001333.
33. Helmchen, F., Denk, W., and Kerr, J.N.D. (2013). Miniaturization of two-photon microscopy for imaging in freely moving animals. *Cold Spring Harb Protoc* 2013, 904–913. 10.1101/pdb.top078147.
34. Jung, J.C., and Schnitzer, M.J. (2003). Multiphoton endoscopy. *Opt Lett* 28, 902–904. 10.1364/OL.28.000902.
35. Helmchen, F., Tank, D.W., and Denk, W. (2002). Enhanced two-photon excitation through optical fiber by single-mode propagation in a large core. *Appl Opt* 41, 2930. 10.1364/ao.41.002930.
36. Udovich, J.A., Kirkpatrick, N.D., Kano, A., Tanbakuchi, A., Utzinger, U., and Gmitro, A.F. (2009). Spectral background and transmission characteristics of fiber optic imaging bundles. *Appl Opt* 47, 4560. 10.1364/ao.47.004560.
37. Andresen, E.R., Sivankutty, S., Bouwmans, G., Gallais, L., Monneret, S., and Rigneault, H. (2015). Measurement and compensation of residual group delay in a multi-core fiber for lensless endoscopy. *Journal of the Optical Society of America B* 32, 1221. 10.1364/josab.32.001221.
38. Leith, E.N., and Upatnieks, J. (1963). Wavefront Reconstruction with Continuous-Tone Objects*. *J Opt Soc Am*. 10.1364/josa.53.001377.
39. Qian, Y., Piatkevich, K.D., Mc Larney, B., Abdelfattah, A.S., Mehta, S., Murdock, M.H., Gottschalk, S., Molina, R.S., Zhang, W., Chen, Y., et al. (2019). A genetically encoded near-infrared fluorescent calcium ion indicator. *Nat Methods*. 10.1038/s41592-018-0294-6.
40. Dana, H., Sun, Y., Mohar, B., Hulse, B.K., Kerlin, A.M., Hasseman, J.P., Tsegaye, G., Tsang, A., Wong, A., Patel, R., et al. (2019). High-performance calcium sensors for imaging activity in neuronal populations and microcompartments. *Nat Methods*. 10.1038/s41592-019-0435-6.

41. Giovannucci, A., Friedrich, J., Gunn, P., Kalfon, J., Brown, B.L., Koay, S.A., Taxidis, J., Najafi, F., Gauthier, J.L., Zhou, P., et al. (2019). Caiman an open source tool for scalable calcium imaging data analysis. *Elife* *8*. 10.7554/eLife.38173.
42. Mathis, A., Mamidanna, P., Cury, K.M., Abe, T., Murthy, V.N., Mathis, M.W., and Bethge, M. (2018). DeepLabCut: markerless pose estimation of user-defined body parts with deep learning. *Nat Neurosci*. 10.1038/s41593-018-0209-y.
43. Antonini, A., Sattin, A., Moroni, M., Bovetti, S., Moretti, C., Succol, F., Forli, A., Vecchia, D., Rajamanickam, V.P., Bertoncini, A., et al. (2020). Extended field-of-view ultrathin microendoscopes for high-resolution two-photon imaging with minimal invasiveness. *Elife* *9*, 1–76. 10.7554/eLife.58882.
44. Wang, C., and Ji, N. (2013). Characterization and improvement of three-dimensional imaging performance of GRIN-lens-based two-photon fluorescence endomicroscopes with adaptive optics. *Opt Express* *21*, 27142–27154.
45. Accanto, N., Chen, I.-W., Ronzitti, E., Molinier, C., Tourain, C., Papagiakoumou, E., and Emiliani, V. (2019). Multiplexed temporally focused light shaping through a gradient index lens for precise in-depth optogenetic photostimulation. *Sci Rep* *9*, 7603. 10.1038/s41598-019-43933-w.
46. Andresen, V., Egner, A., and Hell, S.W. (2001). Time-multiplexed multifocal multiphoton microscope. *Opt Lett* *26*, 75. 10.1364/ol.26.000075.
47. Yu, J.Y., Kim, S., Shim, Y.B., Holland, D.B., Allodi, M.A., Yeh, C.Y., Blake, G.A., Han, Y.G., and Guo, C.L. (2018). Fiber-bundle illumination: realizing high-degree time-multiplexed multifocal multiphoton microscopy with simplicity. *Sci Rep* *8*, 14863. 10.1038/s41598-018-33286-1.
48. Zhang, T., Hernandez, O., Chrapkiewicz, R., Shai, A., Wagner, M.J., Zhang, Y., Wu, C.H., Li, J.Z., Inoue, M., Gong, Y., et al. (2019). KiloHertz two-photon brain imaging in awake mice. *Nat Methods* *16*, 1119–1122. 10.1038/s41592-019-0597-2.
49. Podgorski, K., and Ranganathan, G. (2016). Brain heating induced by near-infrared lasers during multiphoton microscopy. *J Neurophysiol* *116*, 1012–1023. 10.1152/jn.00275.2016.
50. Iyer, V., Hoogland, T.M., and Saggau, P. (2006). Fast functional imaging of single neurons using random-access multiphoton (RAMP) microscopy. *J Neurophysiol* *95*, 535–545. 10.1152/jn.00865.2005.
51. Jennings, J.H., Kim, C.K., Marshel, J.H., Raffiee, M., Ye, L., Quirin, S., Pak, S., Ramakrishnan, C., and Deisseroth, K. (2019). Interacting neural ensembles in orbitofrontal cortex for social and feeding behaviour. *Nature* *2019*, 1. 10.1038/s41586-018-0866-8.
52. Dagleish, H.W.P., Russell, L.E., Packer, A.M., Roth, A., Gauld, O.M., Greenstreet, F., Thompson, E.J., and Häusser, M. (2020). How many neurons are sufficient for perception of cortical activity? *Elife* *9*, 1–99. 10.7554/eLife.58889.
53. Carrillo-Reid, L., Yang, W., Bando, Y., Peterka, D.S., and Yuste, R. (2016). Imprinting and recalling cortical ensembles. *Science* (1979) *353*, 691–694. 10.1126/science.aaf7560.

54. Robinson, N.T.M., Descamps, L.A.L., Russell, L.E., Buchholz, M.O., Bicknell, B.A., Antonov, G.K., Lau, J.Y.N., Nutbrown, R., Schmidt-Hieber, C., and Häusser, M. (2020). Targeted Activation of Hippocampal Place Cells Drives Memory-Guided Spatial Behavior. *Cell* 183, 1586-1599.e10. 10.1016/j.cell.2020.09.061.
55. Bonifazi, P., Goldin, M., Picardo, M.A., Jorquera, I., Cattani, A., Bianconi, G., Represa, A., Ben-Ari, Y., and Cossart, R. (2009). GABAergic hub neurons orchestrate synchrony in developing hippocampal networks. *Science* (1979) 326, 1419–1424. 10.1126/science.1175509.
56. Papagiakoumou, E., Ronzitti, E., and Emiliani, V. (2020). Scanless two-photon excitation with temporal focusing. *Nat Methods* 17, 571–581. 10.1038/s41592-020-0795-y.
57. Accanto, N., Molinier, C., Tanese, D., Ronzitti, E., Newman, Z.L., Wyart, C., Isacoff, E., Papagiakoumou, E., and Emiliani, V. (2018). Multiplexed temporally focused light shaping for high-resolution multi-cell targeting. *Optica* 5, 1478. 10.1364/OPTICA.5.001478.
58. Hernandez, O., Papagiakoumou, E., Tanese, D., Fidelin, K., Wyart, C., and Emiliani, V. (2016). Three-dimensional spatiotemporal focusing of holographic patterns. *Nat Commun* 7, 11928. 10.1038/ncomms11928.
59. Flusberg, B.A., Nimmerjahn, A., Cocker, E.D., Mukamel, E.A., Barretto, R.P.J., Ko, T.H., Burns, L.D., Jung, J.C., and Schnitzer, M.J. (2008). High-speed, miniaturized fluorescence microscopy in freely moving mice. *Nat Methods* 5, 935–938. 10.1038/nmeth.1256.
60. Zhang, T., Hernandez, O., Chrapkiewicz, R., Shai, A., Wagner, M.J., Zhang, Y., Wu, C.H., Li, J.Z., Inoue, M., Gong, Y., et al. (2019). KiloHertz two-photon brain imaging in awake mice. *Nat Methods* 16, 1119–1122. 10.1038/s41592-019-0597-2.
61. Bovetti, S., Moretti, C., Zucca, S., Dal Maschio, M., Bonifazi, P., and Fellin, T. (2017). Simultaneous high-speed imaging and optogenetic inhibition in the intact mouse brain. *Sci Rep* 7, 40041. 10.1038/srep40041.
62. Karigo, T., Kennedy, A., Yang, B., Liu, M., Tai, D., Wahle, I.A., and Anderson, D.J. (2020). Distinct hypothalamic control of same- and opposite-sex mounting behaviour in mice. *Nature* 589, 258–263. 10.1038/s41586-020-2995-0.
63. Yu, K., Ahrens, S., Zhang, X., Schiff, H., Ramakrishnan, C., Fenno, L., Deisseroth, K., Zhao, F., Luo, M.H., Gong, L., et al. (2017). The central amygdala controls learning in the lateral amygdala. *Nat Neurosci* 20, 1680–1685. 10.1038/s41593-017-0009-9.
64. Fratzl, A., Koltchev, A.M., Vissers, N., Tan, Y.L., Marques-Smith, A., Stempel, A.V., Branco, T., and Hofer, S.B. (2021). Flexible inhibitory control of visually-evoked defensive behaviour by the ventral lateral geniculate nucleus. *Neuron*. 10.1016/J.NEURON.2021.09.003.
65. Attardo, A., Fitzgerald, J.E., and Schnitzer, M.J. (2015). Impermanence of dendritic spines in live adult CA1 hippocampus. *Nature* 523, 592–596. 10.1038/nature14467.
66. Meng, G., Liang, Y., Sarsfield, S., Jiang, W., Lu, R., Dudman, J.T., Aponte, Y., and Ji, N. (2019). High-throughput synapse-resolving two-photon fluorescence microendoscopy for deep-brain volumetric imaging in vivo. *Elife* 8. 10.7554/eLife.40805.

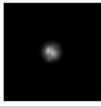


67. Vierock, J., Rodriguez-Rozada, S., Dieter, A., Pieper, F., Sims, R., Tenedini, F., Bergs, A.C.F., Bendifallah, I., Zhou, F., Zeitzschel, N., et al. (2021). BiPOLES is an optogenetic tool developed for bidirectional dual-color control of neurons. *Nat Commun* *12*, 1–20. [10.1038/s41467-021-24759-5](https://doi.org/10.1038/s41467-021-24759-5).
68. Adesnik, H., and Abdeladim, L. (2021). Probing neural codes with two-photon holographic optogenetics. *Nat Neurosci* *24*, 1356–1366. [10.1038/s41593-021-00902-9](https://doi.org/10.1038/s41593-021-00902-9).
69. Guitchounts, G., Masís, J., Wolff, S.B.E., and Cox, D. (2020). Encoding of 3D Head Orienting Movements in the Primary Visual Cortex. *Neuron* *108*, 512-525.e4. [10.1016/j.neuron.2020.07.014](https://doi.org/10.1016/j.neuron.2020.07.014).
70. Bouvier, G., Senzai, Y., and Scanziani, M. (2020). Head Movements Control the Activity of Primary Visual Cortex in a Luminance-Dependent Manner. *Neuron* *108*, 500-511.e5. [10.1016/j.neuron.2020.07.004](https://doi.org/10.1016/j.neuron.2020.07.004).
71. Zahid, M., Vélez-Fort, M., Papagiakoumou, E., Ventalon, C., Angulo, M.C., and Emiliani, V. (2010). Holographic Photolysis for Multiple Cell Stimulation in Mouse Hippocampal Slices. *PLoS One* *5*, e9431-11.
72. Visser, T.D., and Oud, J.L. (1994). Volume measurements in three-dimensional microscopy. *Scanning*. [10.1002/sca.4950160403](https://doi.org/10.1002/sca.4950160403).
73. Binding, J., ben Arous, J., Léger, J.-F., Gigan, S., Boccara, C., and Bourdieu, L. (2011). Brain refractive index measured in vivo with high-NA defocus-corrected full-field OCT and consequences for two-photon microscopy. *Opt Express*. [10.1364/oe.19.004833](https://doi.org/10.1364/oe.19.004833).

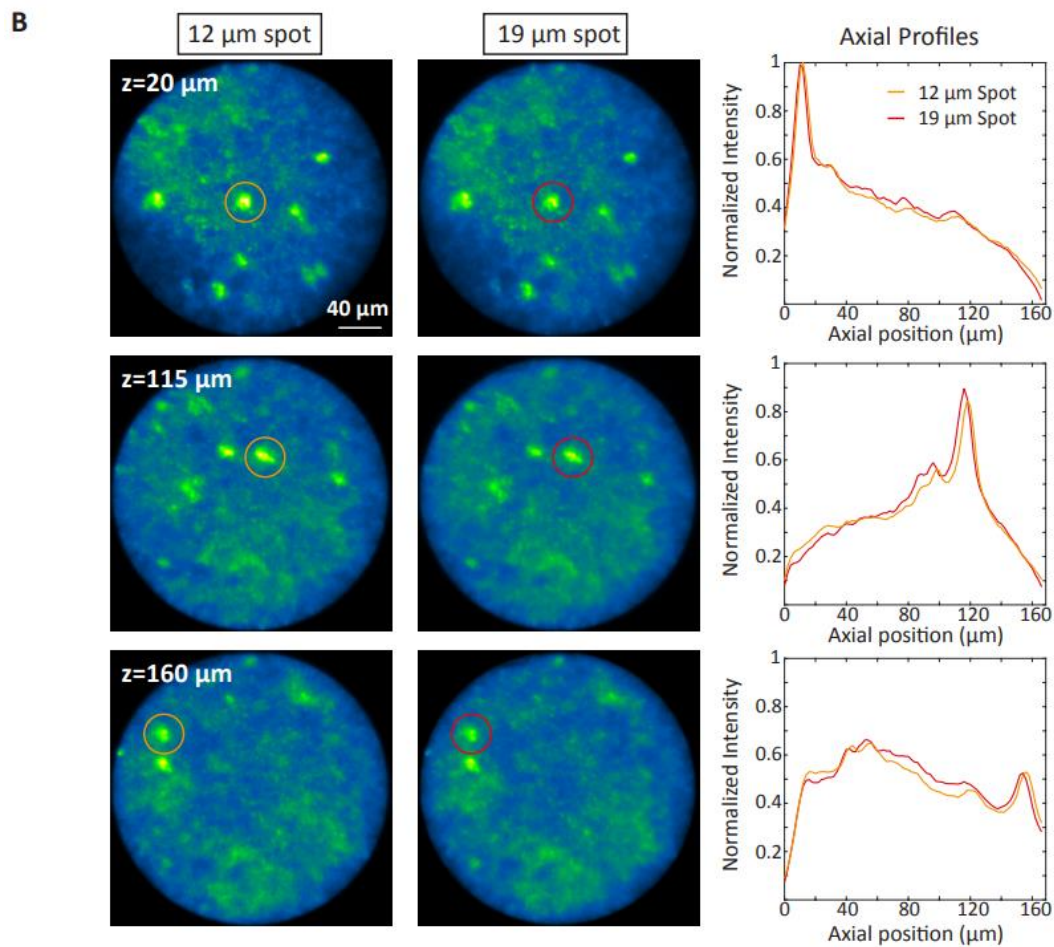


Supplementary Figure 1 | Characterization of inter core delay dispersion for different Fujikura fibers. System and detailed measurements related to Fig. 1.

A. Interferometric setup used for measuring the inter core delay dispersion. A Ti:sapph laser was split into two arms. One arm was sent through the fiber bundle, and the reference arm was delayed using an adjustable delay line. **B.** Distribution of the pulse arrival time in the first mode through the different cores measured for three different Fujikura fiber bundles models: green FIGH-10-500N; red: FIGH-06-300S; blue: FIGH-03-215S). **C.** Average pulse delay for each fiber bundle, defined as the standard deviation of the distribution in (B). The average pulse delay is given in picosecond per meter of fiber and plotted against the core diameter, which is specific of different fiber bundle models. Triangles, squares and circles mark fiber lengths of 0.3, 0.6, 1.82 m respectively. The symbols corresponding to fibers from figure (B) are surrounded by a black contour line. For all the measured bundles, the average pulse delay per meter of fiber is > 1 ps, from which it is apparent that a 2 m long fiber bundle should decouple the cores in time of a sufficient amount to maintain good axial resolution for spatially extended 2P excitations, especially when using ~ 150 fs laser pulses. **D.** Sketch of different fiber bundle cores, illuminated at the same time and re-imaged at the sample plane by using the GRIN lens in the 2P-FENDO configuration. The pulse from each core is coupled out at a slightly different time. The GRIN lens effectively acts as a doublet, making an image of the output facet of the fiber bundle onto the sample plane, with a certain demagnification factor (2.2 or 4.5 depending on the GRIN lens used). Because the beamlet from each core travels with a certain temporal delay, they do not interfere with each other on the way to the sample plane, thus avoiding out of focus excitation. Related to Fig. 1.

A

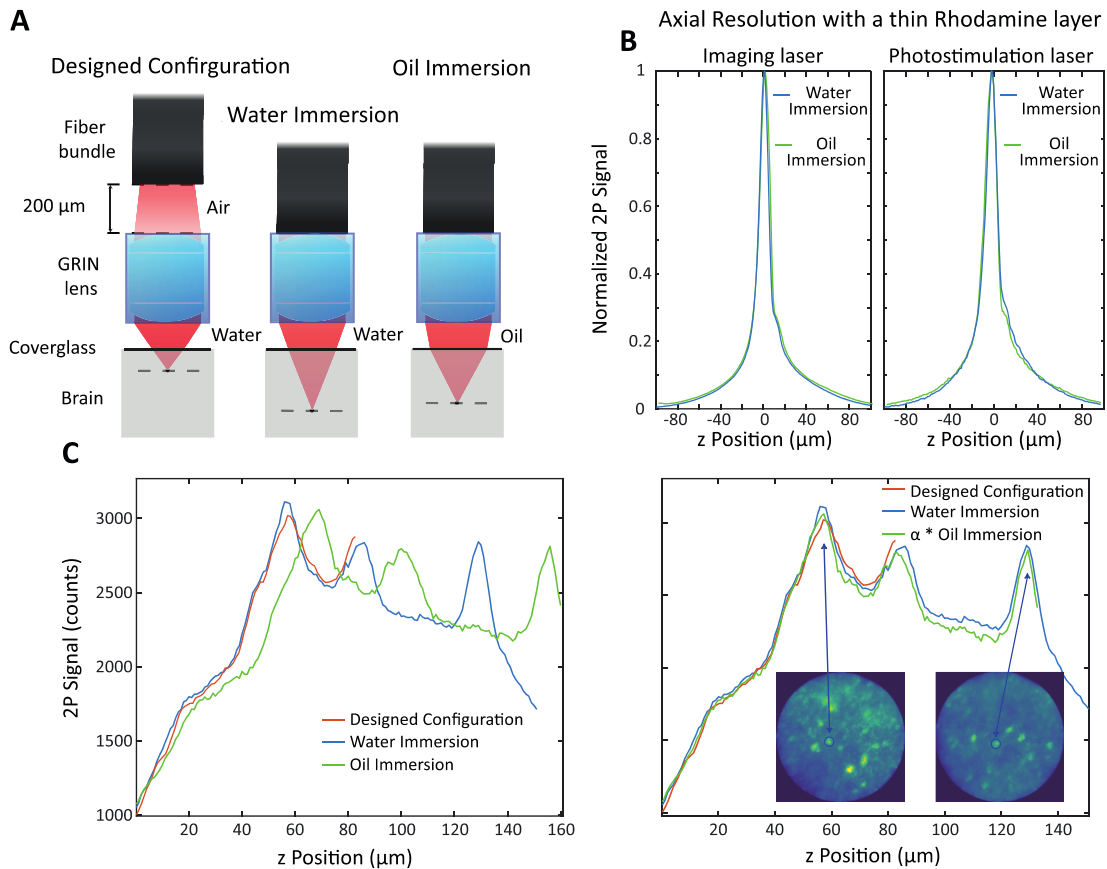
Power before fiber	Power after fiber	Power scanning	Spot size at sample	N cores illuminated	Static spot
400 mW	140 mW	70 mW	12 μm	34	
700 mW	240 mW	120 mW	15 μm	54	
1000 mW	350 mW	170 mW	19 μm	86	



Supplementary Figure 2 | Characterization of 2P imaging for different spot sizes. Characteristics and features of different scanning spot imaging sizes related to **Fig. 2**.

A. Power measurements for the imaging laser for different spot sizes at the sample plane and at different points in the setup when using GRIN lens 2. The coupling objective, fiber bundle, and GRIN lens system transmit $\sim 35\%$ of the light, and an additional factor of 2 is lost when scanning the imaging beam on a larger area than the fiber bundle (see **STAR Methods**). **B.** Three images of a z-stack of a GFP slice at different depths for a small and a large imaging spot. The same features are visible in the two conditions

for the same plane, confirming that the axial confinement is comparable. On the right we plot the axial profiles for the cells circled in the images. For a small and a large imaging spots, the axial profiles largely overlap, excluding additional background when using larger imaging spots. Related to **Fig. 2**.



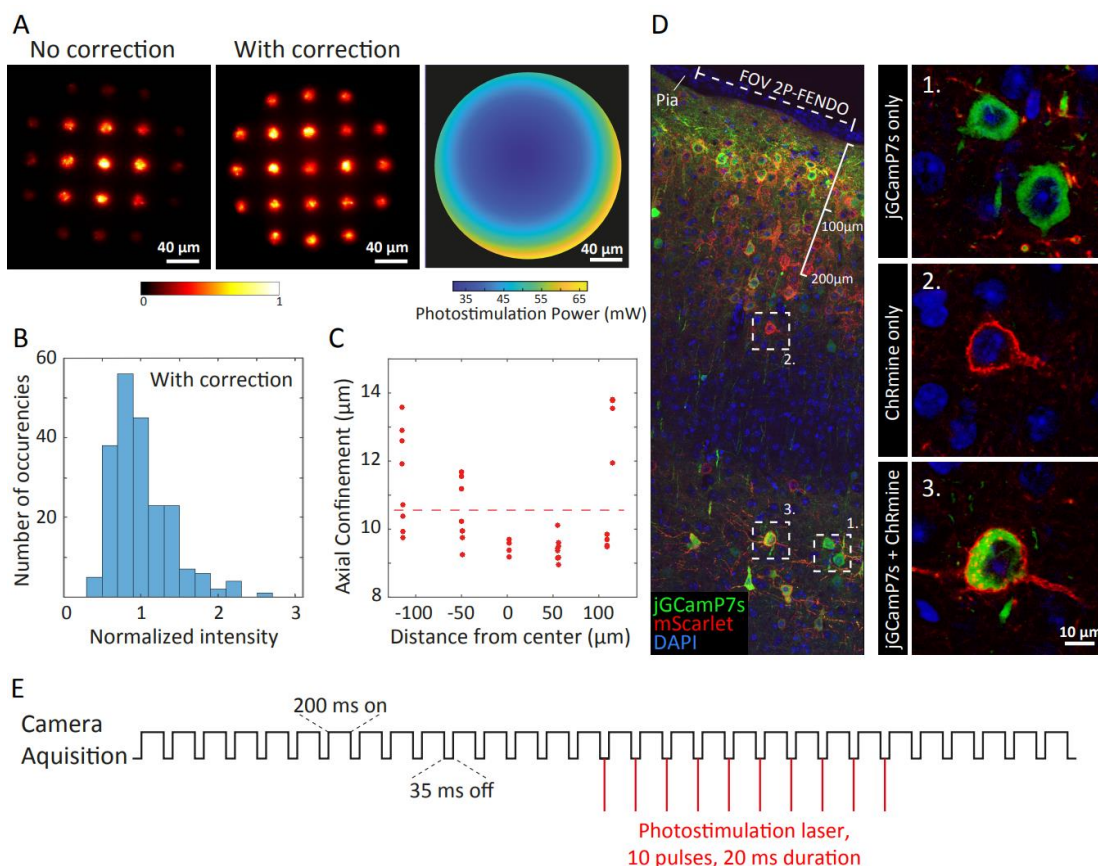
Supplementary Figure 3 | Fiber bundle and GRIN lens configurations. Effect of optical properties of these configurations related to **Fig. 3** and **4**.

A. Scheme of the different configurations used in the experiments. The ‘designed configuration’ refers to the designed parameters according to the manufacturer: the fiber bundle is at the distance of 200 μm from the GRIN lens and the tip of the GRIN lens is immersed in water. It is the configuration leading to the shallowest working distance below the cover glass. In the ‘water immersion’ configuration the fiber is in contact with the GRIN lens and the tip of the GRIN lens is immersed in water. It is the configuration that results in the largest working distance below the cover glass. In the ‘oil immersion’ configuration, the fiber is in contact with the GRIN lens and the tip of the GRIN lens is immersed in oil. This is the configuration used for freely moving experiments to avoid water evaporation (see also **STAR Methods**). **B.** Axial resolution for imaging (*left*) and photostimulation laser (*right*) through GRIN lens 2 in either the oil (green) or the water (blue) immersion configuration, measured on a thin rhodamine layer, showing no difference in axial resolutions. **C.** Characterization of the effective working distance for the 3 different configurations illustrated in A, measured from z-stacks on ~ 150 μm thick GCaMP6 brain slices. The axial profiles in the left-hand plot show 3 different peaks corresponding to cells on different planes that are at the same xy locations. Three effects are apparent: 1) the designed configuration (red curve) has the shortest working distance, allowing to resolve only one peak until the depth of 80 μm below the cover glass; 2) the water immersion configuration (blue curve) is the one producing the largest working distance, allowing to

measure three different peaks and to resolve at least 20 μm below the last peak (located at $z = 130 \mu\text{m}$); 3) the oil immersion configuration (green curve) is able to resolve three peaks, but it can only measure few μm below the last peak, moreover the z axis in the oil immersion configuration is distorted with respect to the water immersion case. As explained in **STAR Methods**, due to the index mismatch between oil and brain tissue on the two sides of the cover glass, a vertical displacement of the endoscope (fiber bundle + GRIN lens) of a quantity Δz with respect to the sample produces a focal shift of $\alpha * \Delta z$ with $\alpha < 1$. In the right-hand plot, we multiplied the z axis for the oil immersion configuration by the factor $\alpha = 0.83$, to match the positions of the peaks measured with the water immersion configuration. The found value is

consistent with the theory of that predicts $\alpha = \frac{\sqrt{n_b^2 - NA^2}}{\sqrt{n_o^2 - NA^2}} = 0.87$, considering the refractive index of the

brain $n_b = 1.35$, the refractive index of the oil $n_o = 1.5$ and the numerical aperture of the GRIN lens $NA = 0.7$. The insets in the right-hand plots show two different planes in the z -stack, with the circled cells corresponding to the axial peaks indicated by the arrows. Related to **Fig. 3** and **4**.



Supplementary Figure 4 | *Spatial resolution and temporal presentation of the holographic photostimulation.* Optical Characteristics of the spatial distributed holographic spots and the photostimulation protocol related to Figure 4. Sagittal brain section jGCamp7s and ChRmine injected mouse in the barrel cortex after viral injections with representative example of 2P-FENDO field of view. Related to **Fig. 6**.

A. 2P excited fluorescence generated on a uniform thick fluorescent slide from a distribution of 15 μm holographic spots without (*left*) and with (*middle*) intensity correction applied on the SLM. The SLM corrects both for the diffraction efficiency and the lower signal at the edges of the FOV (consequence of the larger aberration of the GRIN lens as one moves away from the center). *Right*: Effective power distribution used to photostimulate neurons, measured at the GRIN lens output. In the center of the FOV we used 30 or 40 mW (in the figure we give the case for 30 mW), which were increased smoothly away from the center to generate the same amount of 2P signal. **B.** Distribution of the 2P excited fluorescence from different holographic spots generated with the SLM after the application of the intensity correction. **C.** Axial resolution of holographic spots as a function of the distance from the center. The red dots correspond to individual measurements taken in different days. The dashed line is the average over all the different measurements. **D.** Distribution of transduced cells in the wS1 cortex of mice injected with AAV9-syn-jGCamp7s-WPRE and AAV1-hSyn-ChRmine-mscarlet-Kv2.1-WPRE. The diameter of 2P-FENDO field of view is delineated by the white dotted line. Depth from the brain surface below the pia is indicated to represent the cell distribution in the depth range of 2P-FENDO. Example cells illustrating jGCamp7s expression only (1.), ChRmine expression only (2.) or jGCamp7s + ChRmine (3.). Scale bar= 10 μm . **E.** Photostimulation protocol and camera acquisition timing. During photostimulation experiments, the EM-

CCD camera was driven in external exposure mode, in which a TTL signal, similar to the black curve in figure, was supplied to the camera trigger input. The camera was forced to expose for 200 ms and to remain off for 35 ms. A second signal, synchronized with the camera was then sent to a fast shutter that controlled the photostimulation laser transmission. The shutter was open for 10 times for 20 ms, in correspondence with camera off times, as shown by the red lines in figures. Related to **Fig. 6**

Mouse N	Measurement days	Type of experiment	Imaging depth (μm)	Imaging power at fiber exit (mW)	Data in figures
1	2	Imaging only	80 \pm 10	100-140	Fig. 4C, Video S2
2	5	Imaging/Photostim	70 \pm 10	85-120	Fig. 4A, Fig.6A-E, VideoS2-S3
3	2	Imaging/Photostim	125 \pm 10	110-155	Fig. 6C-E
4	2	Imaging/Photostim	70 \pm 10	85-100	Fig. 6C-E

Supplementary Table 1. Data used. Summary of the parameters used in all the measurements shown in the main manuscript. Related to **Fig. 4, 5 and 6.**

Supplementary Video 1. *In vivo* stack acquisition with 2P-FENDO. *In vivo* stack acquisition of TdTomato expressing neurons in V1 taken with GRIN1 lens, or GFP expressing neurons with either GRIN 1 or GRIN 2 lenses. Depth of imaging is indicated in the upper left corner. The images were filtered with a Gaussian blur function to get rid of the core structure of the fiber bundle and normalized for each plane. Related to **Fig. 3.**

Supplementary Video 2. Spontaneous activity recording at 2 Hz, 5 Hz, and 20 Hz with 2P-FENDO in a freely moving mouse. The calcium data were motion corrected with CalmAn. We applied a 3-frame running average using the Image J plugin. Both the calcium imaging video and the video of the mouse moving in the cage were sped up \sim 8 times. Related to **Fig. 4.**

Supplementary Video 3. High-resolution, multi-cell holographic photostimulation with 2P-FENDO, in a freely moving mouse. The calcium data were motion corrected with CalmAn. We applied a 3-frame running average using the Image J plugin. Both the calcium imaging video and the video of the mouse moving in the cage were sped up \sim 7 times. The video corresponds to the calcium traces reported in Fig. 4 a of the main manuscript. In the calcium images, arrows appear few seconds before the photostimulation laser is switched on and point at the photostimulated cells. The traces in the lower panel correspond to the dF/F signal of the targeted (red traces) and untargeted (white traces) neurons. Related to **Fig. 6.**

B.2.2 Elaboration on 2P-FENDO details

This section aims to provide a more developed explanation of certain aspects that were not extensively covered in the publication (Accanto*, Blot*, Lorca-Cámara* *et al.*, 2023). Specifically, we will delve into the optical methods used to integrate ultrashort 2P excitation pulses with fiber bundles as well as the main optical novelties developed into the system, i.e. GVD compensation and SPM, the ICDD, and the use of GRIN lenses.

GVD and SPM. In the 2P-FENDO system, ultrashort light pulses are employed along a fiber bundle, which as detailed in the introduction, can introduce the effects of GVD and SPM. As for the GVD, the fiber bundle introduces a positive dispersion (figure 22A). To compensate for this effect, a pair of gratings placed inside the lasers are used to impart negative chirp to the laser pulse before its interaction with the fiber bundle (figure 22B). This strategy ensures that after traversing the fiber bundle, the pulse regains its initial pulse duration.

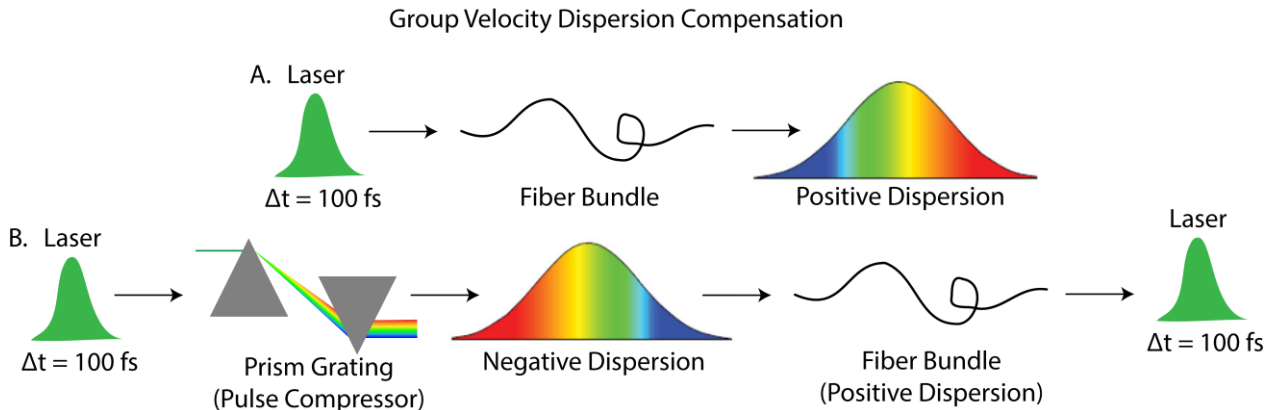


Figure 22. Group velocity dispersion compensation. **A.** GVD of an ultrashort laser pulse propagating in a fiber bundle, where the spectral components of the laser pulse (blue, green and red colors) propagate at different speeds in the fiber. This introduces a positive dispersion to the initial pulse, resulting in pulse broadening after propagating through the fiber bundle. **B.** Grating compensation of the GVD introduced by the fiber bundle with negative dispersion so that after passing through the fiber bundle, the pulse duration is equal to the initial one at the laser output.

The second challenge to overcome when employing fiber bundles with ultrashort light pulses is addressing the effect of SPM. This nonlinear effect becomes apparent when using high laser peak powers. As described in (Ozbay *et al.*, 2018), SPM leads to spectral narrowing when using high powers (1 - 40 mW per core), consequently causing temporal pulse broadening out of

the fiber bundle (increase of pulse duration from 80 fs to 640 fs). One approach to overcome this issue is by initially inducing spectral broadening through the propagation of the pulse in a polarized-maintained fiber (PMF) (Ozbay *et al.*, 2018). With this method, the spectral narrowing effect produced inside the fiber bundle is balanced by the spectral broadening of an unchirped ultrashort pulse in the PMF, to achieve the initial spectral width of the laser. In our approach, we circumvent the issue of SPM by distributing the illumination across a large number of cores in the fiber bundle, effectively lowering the average power per core. To achieve this, our system incorporates an iris to modulate the spot size and therefore the illumination to maintain constant the power per core (power density). This strategy enables to keep a power per core (< 10 mW per core for an 80 MHz repetition rate, 150 fs pulse duration laser) always below the threshold that induces SPM.

ICDD. To perform both 2P imaging and 2P photostimulation of the neuronal activity, we used large spot sizes of 10-20 μm diameter that are created with the illumination of several cores of the fiber bundle (Supp. Fig. 2 Publication). In conventional 2P microscopy, using a large diameter excitation spot size results in an enlargement of the axial extend of the spot, impeding single-cell resolution. In our case instead, the fiber bundle introduces temporal delays among the pulses traversing its various illuminated cores (figure 23). This inter-core delay dispersion (ICDD) reduces the out-of-focus excitation, resulting in the axial resolution of a single core illumination. Consequently, we achieved single-cell resolution even when employing large diameter excitation spot size.

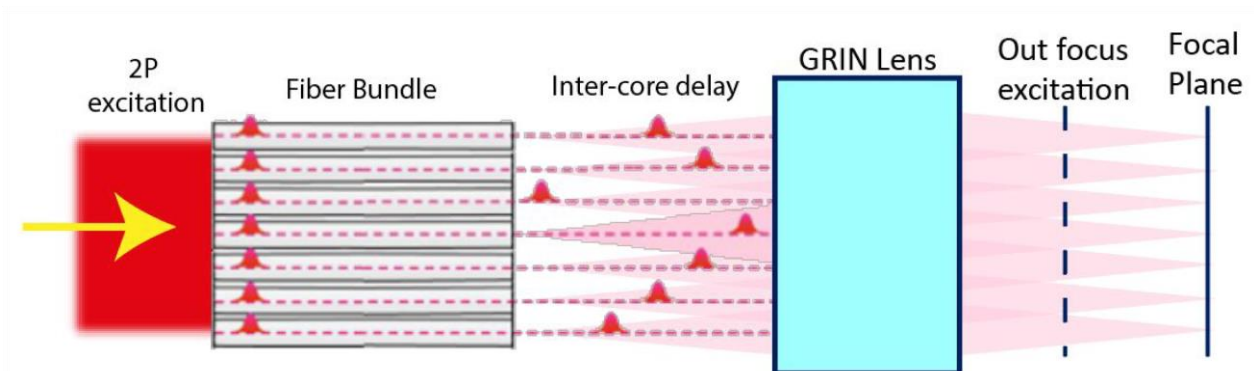


Figure 23. Inter-core delays in the fiber bundle. The fiber bundle temporally decomposes the 2P excitation as it travels through the different cores of the fiber bundle. Although the 2P excitation simultaneously enters the various cores, slight differences between them result in distinct delays

for each part of the excitation, leading to the generation of random delays and the temporal demultiplexing of the excitation. Then, a GRIN lens placed after the fiber recombines the excitation, effectively reducing the probability of out-of-focus excitation due to this temporal effect.

In the 2P-FENDO setup, the large excitation spot generated for two-photon imaging is then scanned across the sample plane using a galvo-resonant scanning device (figure 1 Publication). This choice helps us not only to avoid the negative effects of SPM but to concurrently enhance the acquisition speed in comparison to a scanning diffraction-limited spot strategy. To detect the recorded neuronal activity, a highly-sensitive EM-CCD (Electron Multiplying-Charge Coupled Device) camera is utilized instead of a PMT, which is a direct result of the scanning strategy employed. Consequently, the lateral resolution is not determined by the spot size, but rather by the pixel size of the camera, the inter-core distance in the fiber bundle and the scattering of detected photons at high depths.

GRIN lens. In addition to the fiber bundle, a GRIN lens is used to direct and image the light from the fiber bundle to the mouse brain. GRIN lenses are commonly used in micro-endoscopy as they facilitate the delivery of light into deep brain regions with minimal invasiveness (Jung *et al.*, 2004; Moretti *et al.*, 2016; Jennings *et al.*, 2019; Meng *et al.*, 2019). This is due to the compact dimensions of the devices, typically ranging from 0.7 mm to 1.4 mm in diameter, so that they can be implanted within the brain. However, GRIN lenses often exhibit notable aberrations and field curvature, which generally need to be corrected (Wang and Ji, 2013; Bocarsly *et al.*, 2015; Accanto *et al.*, 2019; Antonini *et al.*, 2020). In our setup, we employed a commercial chromatically and field-corrected GRIN lens with a diameter of 1.3 mm and a length of 5 mm (figure 24). This lens operates as a doublet, re-imaging the output facet of the fiber bundle at the sample plane. However, aberrations occurring at the periphery of the GRIN lens still lead to axial resolution worsening and losses of light efficiency into the sample. When coupled with the two-photon photostimulation system, the efficiency losses can be corrected by using the SLM (Supp. Fig. 3 Publication). This allows us to compensate the light efficiency losses by directing more light towards the periphery of the FOV compared to the central region.

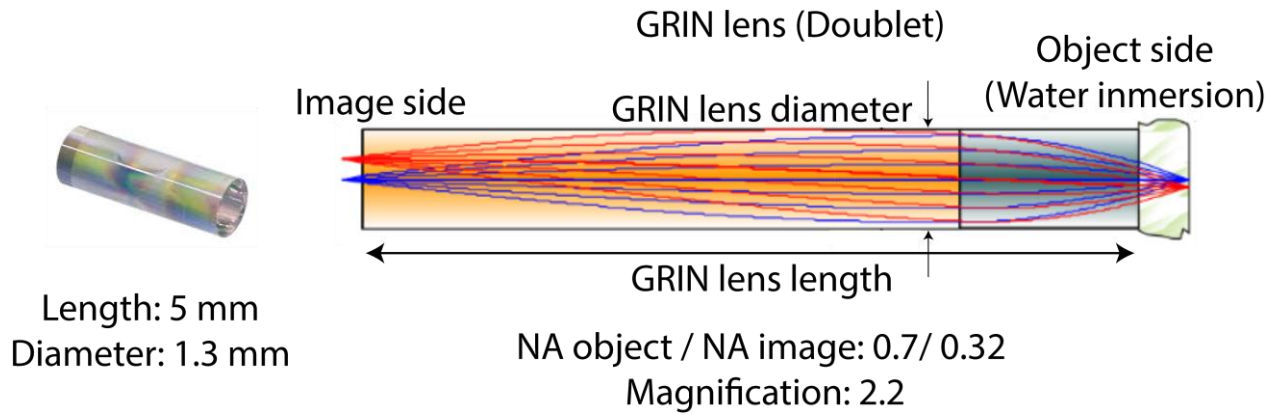


Figure 24. Example of a GRIN lens used in this work. GRIN lens of 1.3 mm diameter and 5 mm length composed by a doublet (two GRIN lenses coupled) that re-image the focal plane from the image side to the object side. The total magnification of the GRIN lens is determined by the ratio between the object and image plane NAs.

B.3 Recent advances enlarging the FOV of 2P-FENDO.

A major advantage of this fiber bundle-based microscope is its simplicity, where minor modifications of a standard 2P imaging system are required. Thanks to this, new optical features can be added to improve the capabilities of the current system. In this section I will present the recent advances and the results we have obtained to improve the performances of 2P-FENDO by enlarging the maximal FOV and enhancing the image quality.

The maximal FOV of 2P-FENDO depends on the fiber bundle diameter (Φ_{fiber}) and on the lens magnification (M) used: $\text{FOV}_{\text{max}} = \Phi_{\text{fiber}}/M$, where the magnification M is given by the object/image lens NA ratio: $M = \text{NA}_{\text{object}}/\text{NA}_{\text{image}}$. The lateral resolution obtained at the sample plane (d_{xy}) is given by the core-to-core distance of the fiber bundle ($d_{\text{core-core}}$) and the magnification of the lens: $d_{xy} = d_{\text{core-core}}/M$. Based on that, several strategies can be developed to extend the maximal FOV, such as larger fiber bundles or different GRIN lenses or mini-objectives, while maintaining single-cell resolution.

In general, to increase the FOV, larger fiber bundles can be used, requiring to increase the number of cores within the bundle with a similar core density, to maintain a good lateral resolution. In the case of the Fujikura fiber bundle tested in (Accanto*, Blot*, Lorca-Cámara* *et al.*, 2023), larger fiber bundles lead to an increase on the fiber bundle rigidity. For example, two Fujikura fiber bundles (FIGH-15-600N and FIGH-100-1500N) have a fiber bundle diameter of 0.55 and 1.5 mm,

which provide a minimum bending radius of 30 and 120 cm, respectively. Thereby, in this case, increasing the FOV with a larger fiber bundle would affect the natural movements of the animal. On the other side, Schott fiber bundles are fabricated with an etching process, where the multiple fibers are separated from each other, leading to the so-called leached fiber bundles, which results in more flexible fibers than the Fujikura fiber bundles, where the material between the cores is glass, leading to bending radius of < 1 cm (Table 1). The downside of large Schott fiber bundles is that they are fabricated with a larger inter-core distance ($d_{\text{core-core}} = 8\text{-}12 \mu\text{m}$) than Fujikura fiber bundles ($d_{\text{core-core}} = 4.5 \mu\text{m}$), which can lead to the reduction of the lateral resolution (d_{xy}).

	Fujikura fiber bundle	Schott fiber bundle (1)	Schott fiber bundle (2)
Bundle diameter	0.55 mm	1.1 mm	1.65 mm
Inter-core distance	4.5 μm	8 μm	11.6 μm
Core diameter	4 μm	6 μm	6 μm
Length	2 m	0.85 m	1.35 m
Bending radius	30 cm	< 1 cm	< 1 cm

Table 1: Fiber bundles parameters. Fiber bundles diameters which refer to the nominal diameter without considering the protective gain surrounding the fiber bundle. Inter-core distance from center of one core to the center of its neighboring cores. Estimated core diameter excluding the material filling the space between cores. Length of the fiber bundle and bending radius indicated by the manufacturer.

However, when using fiber bundles, the image quality is not only based on the resolution given by the inter-core distance but also on two other factors. Firstly, the 2P excitation heterogeneity between the different cores of the bundle, which depends on the differences in propagation of the ultrashort laser pulse through the different cores, induces different power transmission and different GVDs. In a recent work it was shown that, different cores do not only introduce ICDD in the 2P excitation, but they also generate different GVDs. Specifically, in (Garofalakis *et al.*, 2019; Wood *et al.*, 2019), they showed that, for a specific types of fiber bundles (similar to the Fujikura fiber bundle previously used, but with a higher core density), only 50% of the cores can be correctly compensated with a general GVD compressor that compress, with the same factor, each core of the bundle. For the Fujikura fiber bundle, we did not specifically

characterize the GVD for different cores. However, a certain degree of non-homogeneity, that might come from the same effect, was noticed (figure 25A, left). Secondly, the image quality is also based on the aberration introduced by the lens (a GRIN lens or a mini-objective) placed between the fiber bundle and the sample. Notably, aberrations can reduce 2P efficiency and can introduce field curvature when moving from the center to the borders of the FOV.

Considering these factors and parameters, we characterized different fiber bundles (Table 1) and two different lenses (Table 2). A Fujikura fiber bundle and two types of Schott fiber bundles were characterized using the same GRIN lens at the distal end. First of all, we characterized the homogeneity of the 2P excitation through the fiber bundles. As shown in figure 25A, the 2P fluorescence homogeneity between the different cores is higher in the Schott fiber bundles compared to Fujikura fiber bundles (Garofalakis *et al.*, 2019; Wood *et al.*, 2019) in the entire FOV. This means that, in practice, even if the Fujikura fiber presents a smaller inter-core distance ($d_{\text{core-core}} = 4.5 \mu\text{m}$) compared to the inter-core distance of the Schott fiber bundle ($d_{\text{core-core}} = 8 \mu\text{m}$), the imaging quality could be lower with Fujikura fibers than with the Schott fiber bundle due to the higher homogeneity.

Finally, we tested if the higher homogeneity of the Schott fiber bundle affected the ICDD and therefore the axial resolution. We measured that the ICDD is smaller, $\Delta\tau \sim 0.5 \text{ ps/m}$, than with the Fujikura fiber bundle ($\Delta\tau \sim 2 \text{ ps/m}$) (figure 25B). Fortunately, the Schott fiber bundle also provides a good axial resolution (as later shown in figure 27), which results from the effective temporal decoupling of the different pulses propagating through the cores. The decoupling comes not only from the ICDD but also the higher inter-core distance in the Schott fiber bundle compared to the Fujikura fiber.

	GRIN lens	Mini-objective
Lens diameter	1.3 mm	3 mm
Input NA	0.32	0.17
Output NA	0.7	0.5
Magnification	2.2	3
Nominal output WD	200 μm	1 mm

Table 2: Lenses parameters. Input/output NAs refer to the numerical aperture on the fiber bundle side and on the sample side, respectively. M is the calculated magnification from the ration between the output/input lens NAs. Output working distance (WD) refers to the configuration working distance in water immersion and with a cover glass on the sample side.

Then, we characterized the dependence of the FOV and the lateral resolution with two different types of lenses, a GRIN lens (Accanto*, Blot*, Lorca-Cámara* *et al.*, 2023) and a mini-objective, which is the same model as developed in (Zong *et al.*, 2022). For both lenses, we characterized the aberrations introduced by these lenses by measuring the axial resolution and the field curvature when using the same Schott fiber bundle (1) (figure 25C). Optical aberrations lead to a worsening in the axial resolution, notably in the borders of the FOV, and are more evident for the GRIN lens (FWHM = 40-50 μm). Moreover, field curvature is also more significant in the GRIN lens, leading to a curved focal plane as we moved from the center to the periphery of the FOV with an axial shift of 30-35 μm between the center and the border. When using the mini-objective, the aberrations and the field curvature are almost inexistent, with only an axial shift of 2 μm between the center and the border of the FOV.

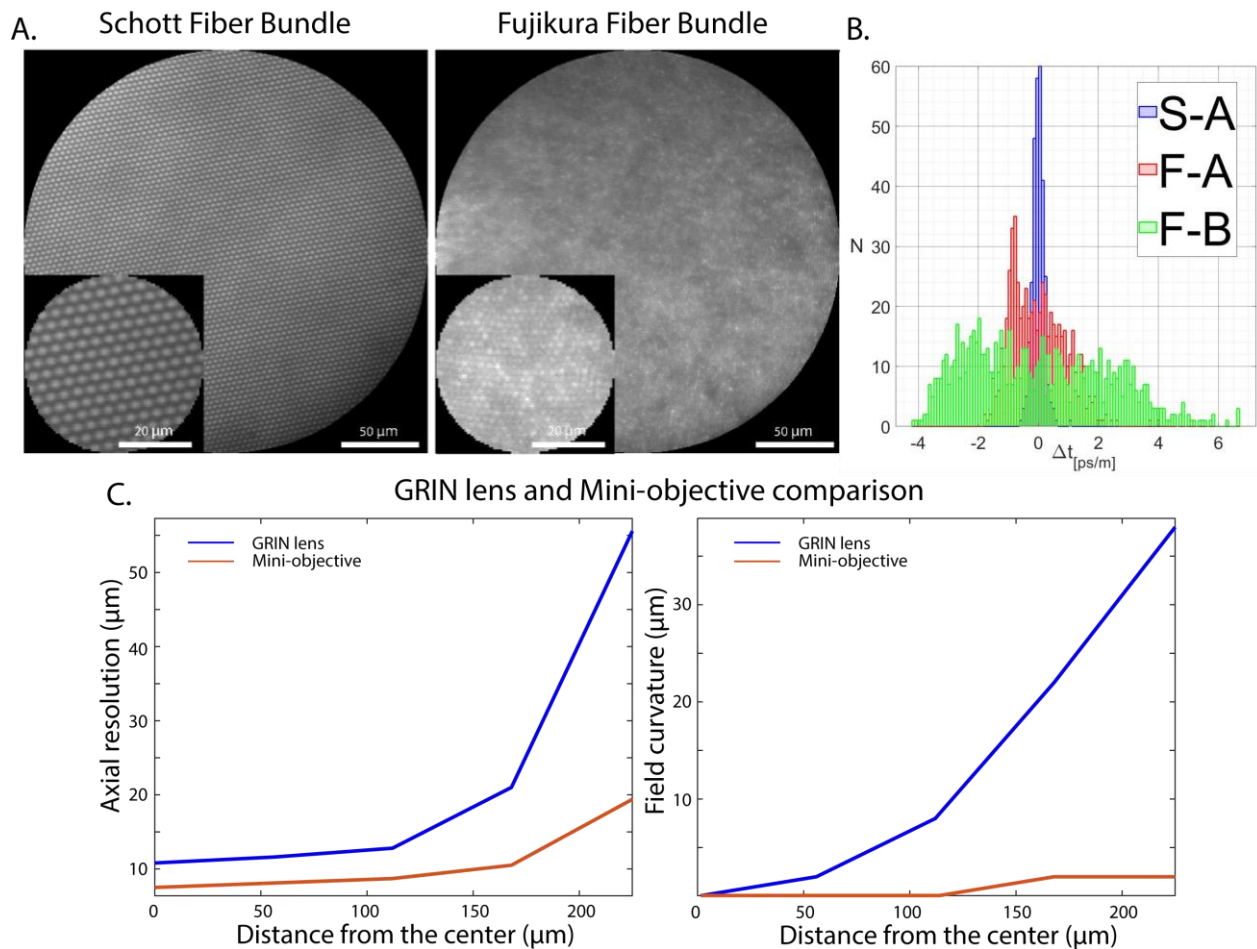


Figure 25. Fiber bundles comparison and GRIN lens and mini-objective aberrations comparison. **A.** Measured two-photon fluorescence when using the fiber bundles to illuminate a uniform rhodamine sample. Image and zoomed views of a 1.1 mm diameter Schott fiber bundle (left) and 0.55 mm diameter Fujikura fiber bundle (right) with 8 μm diameter fiber cores (left) and 4 μm diameter fiber cores (right) with hexagonal configurations. **B.** Distribution of the pulse delay time per meter of fiber through the different cores (N) measured for three different fiber bundle models, including the Fujikura fiber bundle used in the publication (F-A, red) and the Schott fiber bundle (S-A, blue). **C.** Optical measurements of axial resolution (left) and field curvature (right) in the FOV when using a Schott fiber bundle attached to a GRIN lens or a mini-objective.

Considering these characterized parameters, we have tested 4 different optical configurations that lead us to different capabilities as presented below, combination of the previously characterized fiber bundles and lenses. To compare the different achievable FOVs and the lateral resolutions of the different configurations, we imaged with all of them the same fixed brain slice (figure 26).

Configuration 1: This is the original system (Accanto*, Blot*, Lorca-Cámara* *et al.*, 2023) where a Fujikura fiber bundle of $\Phi_{\text{fiber}} = 0.55$ mm in diameter and a GRIN lens of magnification $M = \times 2.2$ is used to achieve a $\text{FOV}_{\text{max}} = \Phi_{\text{fiber}}/M = 250$ μm in diameter (figure 26A). The simple replacement of the fiber bundle used by a larger diameter Schott fiber bundle could increase the FOV of 2P-FENDO.

Configuration 2: A Schott fiber bundle (1) (Table 2) of 1.1 mm in diameter (Φ_{fiber}) and 0.9 mm length could enlarge the achievable FOV in a factor of ~ 2 (from 250 μm 450 μm in diameter), by using the same GRIN lens as before ($M = 2.2$) (figure 26B). The Schott fiber bundle is composed by 18k cores in a 1.1 mm diameter fiber bundle with an inter-core distance of 8 μm (Table 1). Together with the GRIN lens, a lateral resolution of 4 μm is achieved, which, together with the higher core homogeneity of Schott fiber bundles, is sufficient to image neuronal somas and the principal dendrites and neuronal structures (comparison between the zoom of the FOV in figure 26A and 26B). The main disadvantage of this configuration comes from the use of the GRIN lens, which introduces aberrations (Wang and Ji, 2013; Bocarsly *et al.*, 2015; Accanto *et al.*, 2019; Antonini *et al.*, 2020) with a worsening in the axial resolution and field curvature (figure 25C), which are more prominent than in configuration 1 due to the larger FOV obtained in this configuration 2.

Configuration 3: We replaced the GRIN lens by the mini-objective of $\times 3$ magnification ($M = 3$) (Zong *et al.*, 2022) that, with the 1.1 mm Schott fiber bundle ($\Phi_{\text{fiber}} = 1.1$ mm), give us a $\text{FOV}_{\text{max}} = \Phi_{\text{fiber}}/M = 330$ μm in diameter (figure 26C). Even though the FOV is reduced compared to what showed with configuration 2, the field curvature and axial resolution worsening in the entire FOV are less evident or inexistent. Moreover, due the higher magnification, the lateral resolution increased as the cores are now smaller in the sample plane compared to the previous system (lateral resolution $d_{xy} = d_{\text{core-core}}/M = 2.6$ μm).

Configuration 4: To further increase the FOV obtained in configuration 3, we replaced the 1.1 mm diameter fiber bundle by a 1.65 mm diameter (Φ_{fiber}) Schott fiber bundle (2) (Table 2) (1.35 m length) (figure 26D). This fiber bundle is composed by 18k cores with an inter-core distance of 11.6 μm ($d_{\text{core-core}}$), maintaining the good flexibility of the previous Schott fiber bundle (< 1 cm bending radius). Together with the mini-objective, we obtained a large FOV: $\text{FOV}_{\text{max}} = \Phi_{\text{fiber}}/M =$

550 μm in diameter. Due to the larger core diameter of this fiber bundle, the lateral resolution of the system is reduced (lateral resolution $d_{xy} = d_{\text{core-core}}/M = 4 \mu\text{m}$).

All these easily interchangeable configurations give us the opportunity to decide between a large FOV or a higher lateral resolution, or to interchange the use of a large mini-objective or a minimally invasive GRIN lens. Indeed, a large mini-objective (3 mm diameter) cannot be implanted deep in the brain as it was possible with the GRIN lens (1.3 mm diameter) used previously. A solution to use mini-objectives to study deep brain regions is to implant glass rods in the brain as relay (Zong *et al.*, 2022). However, they remain more invasive than the current GRIN lenses.

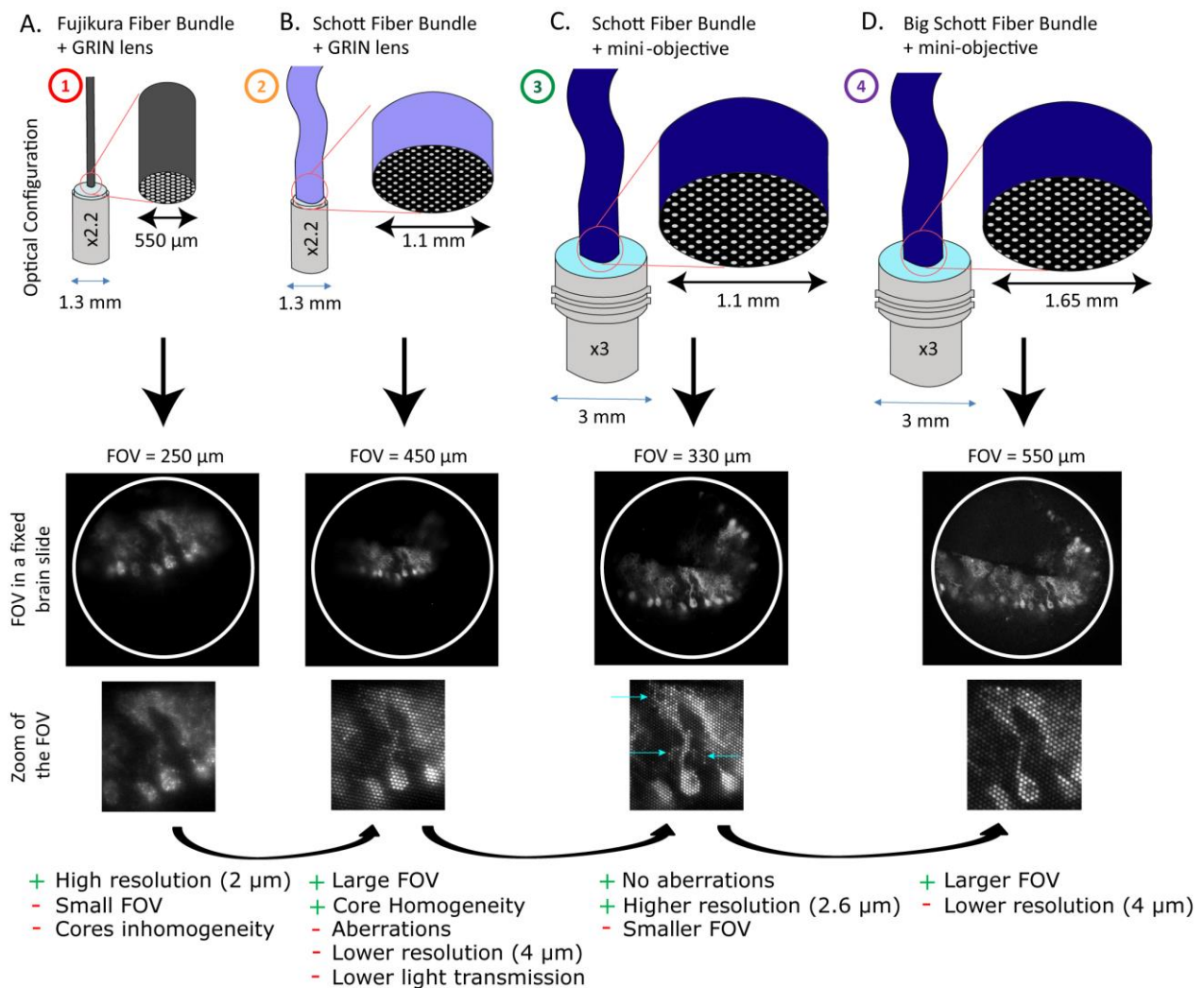


Figure 26. Configurations of 2P-FENDO to achieve a larger FOV and higher lateral resolution. **A.** The original configuration 1 presents a Fujikura fiber bundle coupled to a GRIN lens, providing a FOV of 250 μm wide. **B.** The second configuration replaces the fiber bundle with a Schott fiber bundle, resulting in a FOV of 450 μm wide with higher core homogeneity. **C.** Configuration 3 replaces the GRIN lens with a mini-objective to eliminate aberrations and enhance the lateral resolution in a 330 μm wide FOV. **D.** Configuration 4 improves the third configuration by substituting the fiber bundle with a larger one, to achieve a FOV of 550 μm wide.

B.3.1 Optical characterization of an enlarged FOV 2P-FENDO.

The two most performant configurations previously presented were the 3 and 4, where a trade-off between FOV size and lateral resolution exists. While configuration 3 offers a smaller FOV, it allows to see cell bodies, proximal dendrites, and to discriminate secondary dendritic branches (zoom of the FOV figure 26C). Configuration 4 has a lateral resolution which allow use to see cell bodies and the primary dendrites and axons ($> 4 \mu\text{m}$ size) in a large FOV of 550 μm . Considering this, the last configuration is optically characterized in figure 27 for both the scanning imaging and the holographic photostimulation spots. Figure 27A shows the field curvature between the focal plane in the center and the border of the FOV of 8 μm with axial resolutions ranging from 9-12 μm . Additionally, the axial resolution of holographic spots distributed across the FOV is measured with values from 9-13 μm (figure 27B) obtained from the FWHM of the axial profiles (figure 27C). Once the optical characterization is done, configuration 4 is used to perform 2P calcium activity imaging and 2P optogenetics photostimulation on different brain regions *in vivo* head-fixed and freely moving mice.

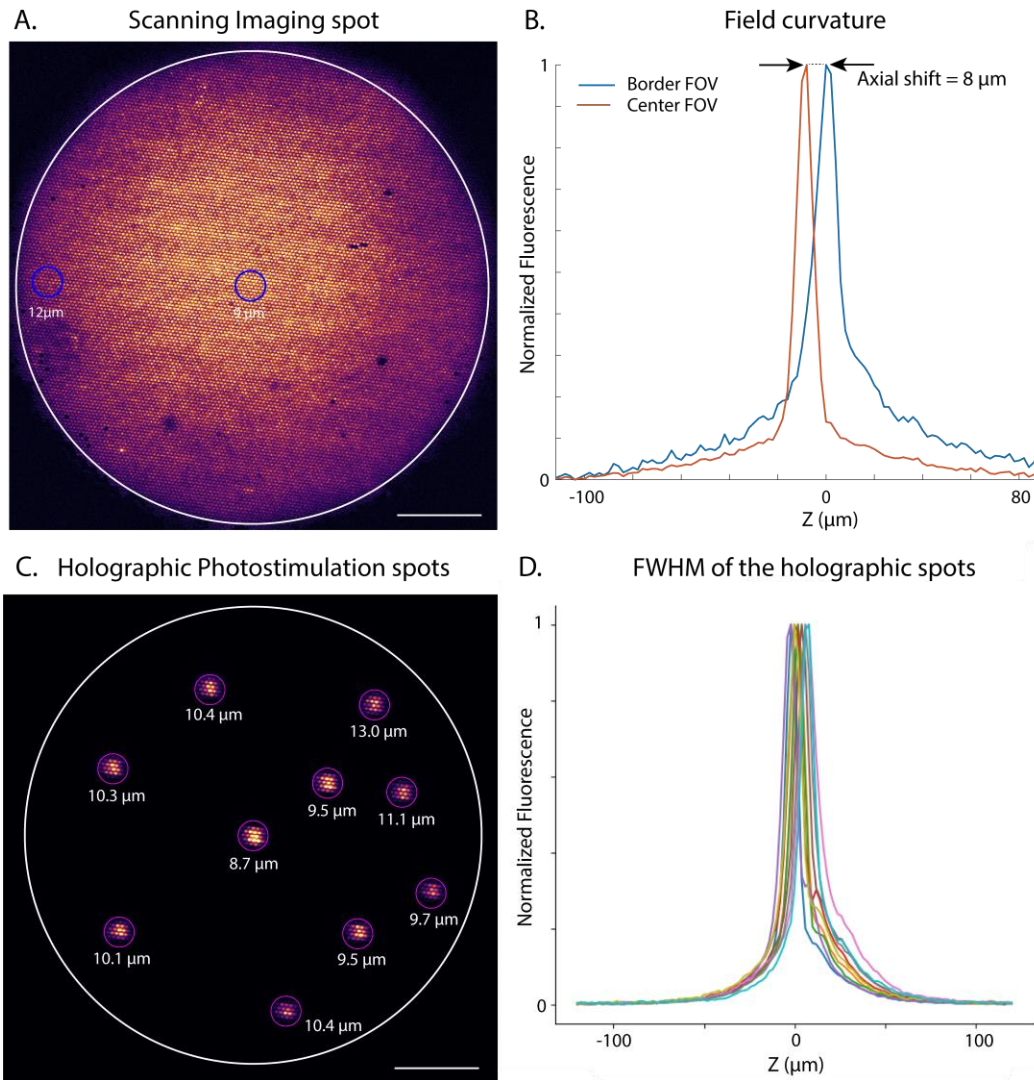


Figure 27. Optical characterization of configuration 4. **A.** Fluorescence image obtained when the imaging spot is scanned through a homogeneous fluorescence slice. **B.** Axial profiles of the regions selected in A, with axial resolutions from 9-12 μm and a field curvature between the center and the border of the FOV of 8 μm (axial shift). **C.** Fluorescence image obtained when holographic spots are displayed within the FOV. FWHM values of the spots are obtained from **D.** Axial profiles of the holographic spots generated in C.

B.3.2 Functional imaging with an enlarged FOV 2P-FENDO.

For experiments in freely moving animals, a new custom-made, lightweight (1.3 g) implant (Figure 28D) was developed to attach the fiber bundle and the mini-objective to the head of the mice. This implant is then connected by screws to a baseplate (black piece) which is cemented into the mice head bar. The fully assembled implant with the baseplate were positioned over the cranial

window of the anesthetized/head-fixed animal. Once a region of interest (ROI) is identified, the implant is cemented over the window. The baseplate is the sole element to be permanently fixed onto the animal's head, thus allowing to make the system fully detachable by unscrewing the implant from the baseplate. The relative position between the fiber bundle and the mini-objective allows to manually change the focal plane of imaging and photostimulation.

Figure 28A shows an example of a large FOV recorded with the configuration 4 of 2P-FENDO in a mouse injected with an AAV9 viral vector for the calcium indicator jGCaMP7s delivered as in Accanto*, Blot*, Lorca-Cámara* et al., 2023 in the barrel cortex. The cranial window surgery and the rest of the procedure were performed as previously. In this example, we characterized the imaging properties with the new fiber bundle and the mini-objective by measuring 5 minutes of spontaneous activity of 78 neurons in the head-fixed mouse (at 130 μm depth from the brain surface) at 10 Hz of imaging frame rate with an average power of 135 mW (power density = $0.6 \text{ mW}/\mu\text{m}^2$) (figure 28B). By using the Caiman software, we semi-automatically detected the neurons with a mean SNR = 2 (figure 28C) and we extracted their calcium transient traces. This present an improvement in the number of detected cells with respect to the results obtained with configuration 1 in freely moving mice (Accanto *et al.*, 2023), where 21 neurons where detected with the same average SNR and by using similar parameters (frame rate = 10 Hz and average power of 100-140 mW ($0.6\text{-}0.7 \text{ mW}/\mu\text{m}^2$)), which is the result of the expanded FOV in configuration 4.

Calcium Activity recording in cortex in head-fixed mouse

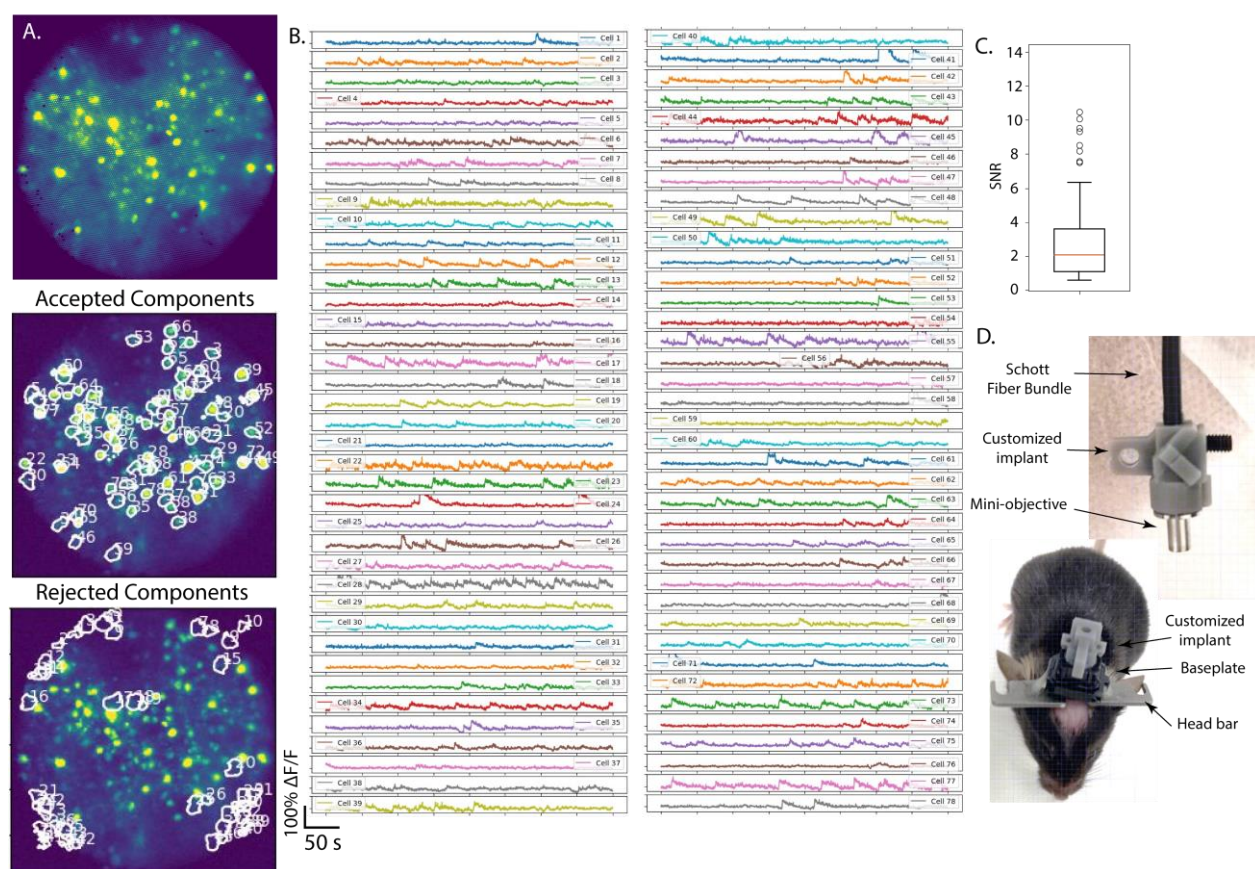


Figure 28. Imaging of spontaneous Ca^{2+} activity in head-fixed mice. **A.** Representative FOV in a mouse from which 78 components are accepted by Caiman software. **B.** Corresponding calcium transients ($\Delta F/F$) for 78 selected cells imaged at 10 Hz acquisition speed. Imaging power and spot size were 135 mW and 16 μm . **C.** SNR quantification for the accepted cells within the FOV. **D.** Image of the implant, composed of a lightweight (1.3 g) 3D printed piece that holds together the fiber bundle and the mini-objective.

By implanting the system over the cerebellum, we recorded the neuronal activity of Purkinje cells dendrites (at 60 μm depth from the brain surface) in a freely moving mouse (figure 29). In this example, 28 Purkinje cells were recorded during 3 minutes while the mouse was freely moving. The mouse was trained to climb a ladder to obtain a reward to prove the stability of our system and the low impact of the mouse natural movements on the FOV (figure 29C.). The recording of the calcium activity is synchronized with the recording of the mouse behavior in its cage.

Calcium Activity recording in the Cerebellum in freely moving mice

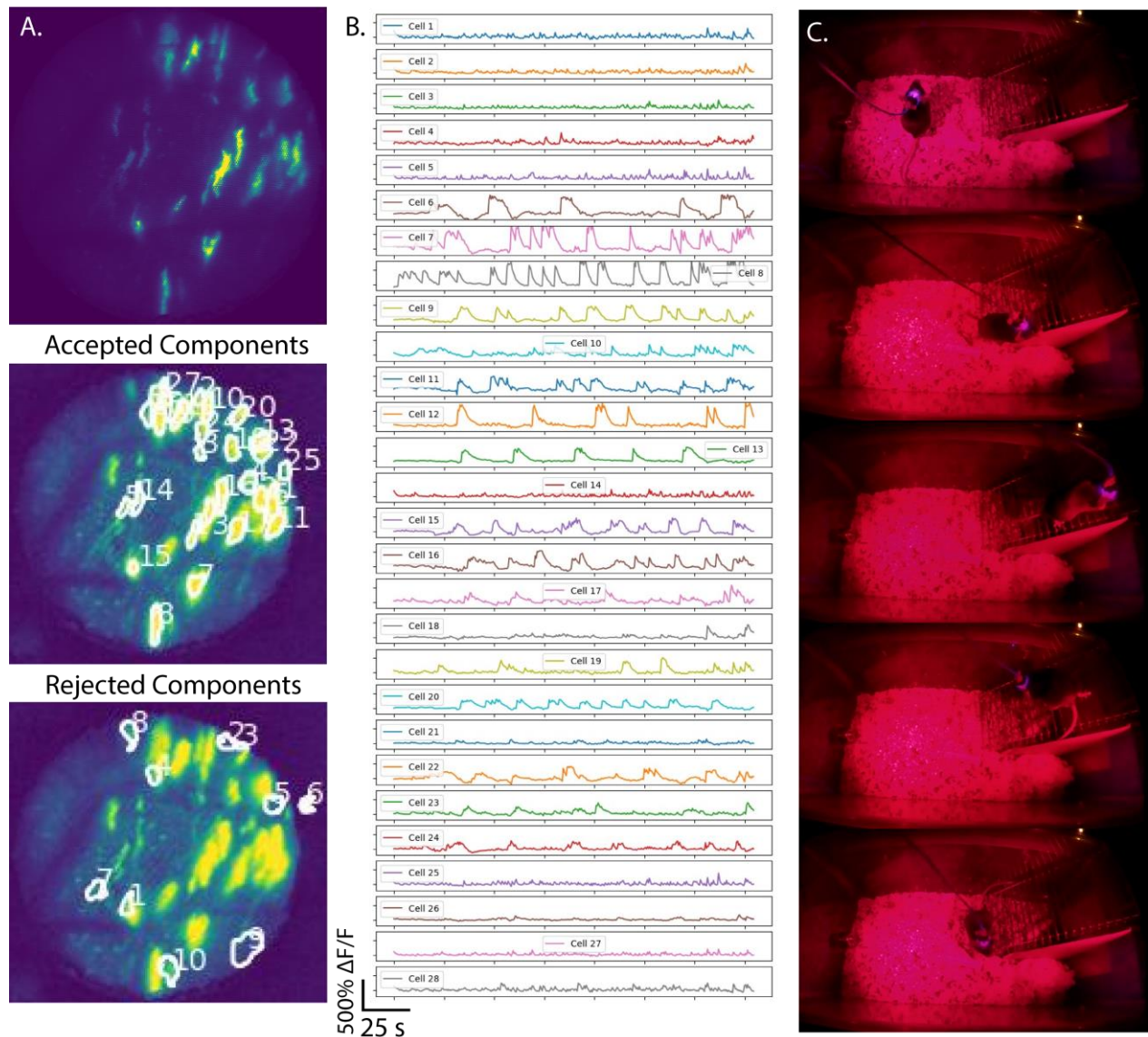


Figure 29. Imaging of spontaneous Ca^{2+} activity in freely moving mice. **A.** Representative FOV in a mouse in which 28 Purkinje cells at the cerebellum were detected by Caiman software. **B.** Corresponding calcium transients ($\Delta F/F$) for the 28 selected cells imaged at 2 Hz acquisition speeds. Imaging power and spot size were 100 mW and 16 μm . **C.** Captures of the video recorded during the experiment in which the mouse is trained to climb stairs to receive a reward. The neuronal activity recording is synchronized with the recording of the mouse's behavior.

B.3.3 *In vivo* all-optical experiment with an enlarged FOV 2P-FENDO.

Finally, we tested the photostimulation capabilities with configuration 4. As in the previous publication, a 2P excitation together with a SLM are used to manipulate individual neurons with

single-neuron precision. In figure 30, preliminary results of neuronal manipulation *in vivo* in head-fixed mouse are shown using the same preparation as in (Accanto*, Blot*, Lorca-Cámara* *et al.*, 2023). In figure 30A-B we show a representative FOV and the calcium activity traces of 5 neurons (yellow circles) recorded at 4 Hz that were photostimulated 4 times, in which we obtained for 4 of them (red circles) a response to all the stimulations (30 seconds between consecutive photostimulations). The traces in figure 30B correspond to the $\Delta F/F$ signal of the targeted cells. In the same FOV, we then targeted 25 neurons (yellow circles) for which 20 showed a clear photostimulation response (red circles) (figure 30C-E), being so far the maximal number of neurons that have been manipulated with our system, which is now limited by the maximal laser power. The higher number of photostimulation spots we were able to create simultaneously by using the same laser source is given by the lower optical aberrations that the mini-objective introduces with respect to the GRIN lens previously used in configuration 1. With this configuration, the power per spot used was 20 mW. With the configuration 1, the power per spot was 30-60 mW. Finally, considering the distance between the targeted neurons and the rest of the neurons we can obtain the cross-activation of non-targeted cells and extrapolate the lateral resolution of the system. Non-targeted cells cross-activation is visible from neurons at distances $< 30 \mu\text{m}$ from one of the targeted neurons, which was also obtained with configuration 1 (Accanto*, Blot*, Lorca-Cámara *et al.*, 2023).

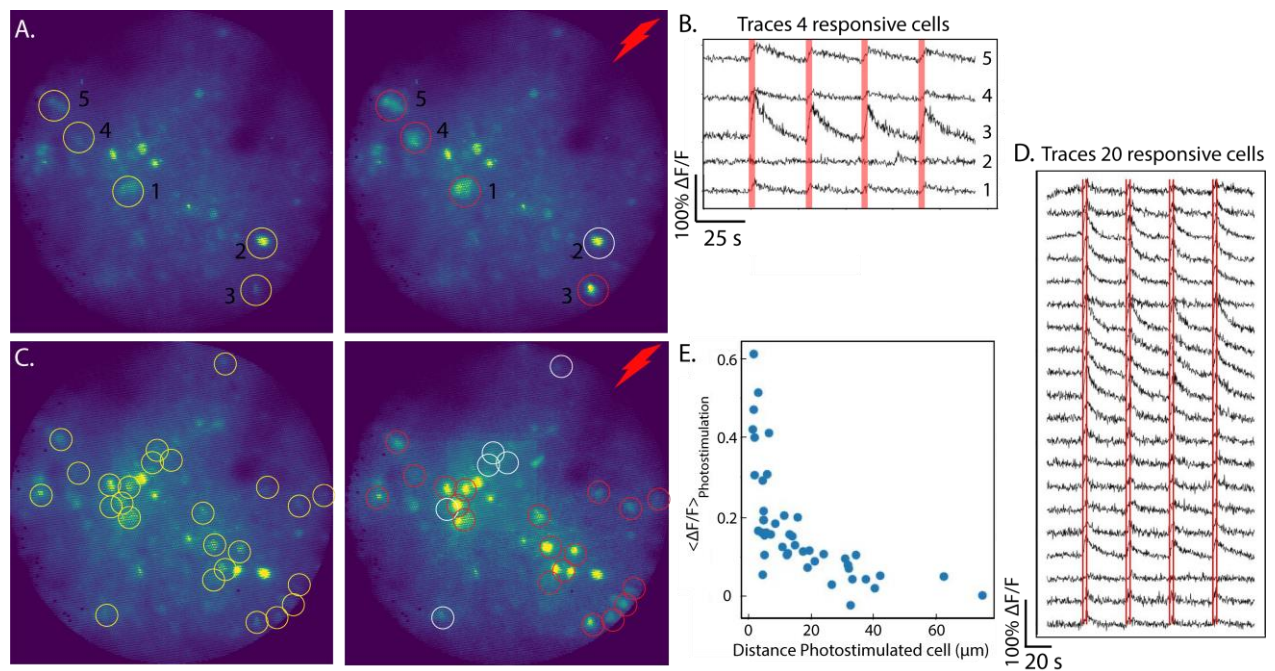


Figure 30. High-resolution photostimulation in head-fixed mice. **A.** Photostimulation of 4 neurons. On the left, a frame of the recorded activity before the photostimulation, with targeted neurons indicated by red circles (5 neurons). On the right, a frame of recorded activity after the photostimulation, with targeted and photostimulated neurons indicated by red circles, and targeted but not photostimulated neurons indicated by blue circles. **B.** Recorded neuronal activity traces (100% $\Delta F/F$) of the 5 targeted neurons. The photostimulation was repeated 4 times during 140 seconds. **C.** High-resolution photostimulation of 20 neurons in head-fixed mice. On the left, a frame of recorded activity before the photostimulation, with targeted neurons indicated by red circles (25 neurons). On the right, a frame of recorded activity after the photostimulation, with targeted and photostimulated neurons indicated by red circles and targeted but not photostimulated neurons indicated by blue circles. **D.** Recorded neuronal activity traces (100% $\Delta F/F$) of the 20 photostimulated neurons. The photostimulation was repeated 4 times during 140-second duration. **E.** $\langle \Delta F/F \rangle_{\text{Photostimulation}}$ for each neuron within the FOV as a function of the distance from the photostimulated cells.

Overall, the new results demonstrate that, with the new configuration of the system, 2P-FENDO can compete with the already existing 2P miniaturized microscopes, in terms of FOV and SNR, while it integrates a feature so far absent to any existing apparatus: 2P holographic photostimulation of multiple neurons with single-neuron resolution. The optimization of the implant, adapted for the new fiber bundle and mini-objective configuration, would allow to perform 2P all-optical experiments in freely moving mice.

B.4 System perspectives

The currently available 2P-FENDO system, developed for freely moving mice, present the advantage of performing all-optical investigation in a large FOV with a good spatial and axial resolution. However, further improvements in the capabilities of 2P-FENDO can be achieved by increasing the maximal imaging frame rate and the SNR, optimizing the motion artifacts correction and adding the capability to image and manipulate FOVs at different depths.

Speed and SNR. Adapting the scanning strategy for 2P functional imaging can enhance the acquisition speeds and the SNR. The increased flexibility of using a tabletop galvo-galvo scanning system in the 2P-FENDO, as opposed to miniaturized MEMs mirrors in 2P miniaturized microscopes (Zong *et al.*, 2022), allows for modifications in the scanning configuration. In 2P-FENDO, a large spot of $\sim 15 \mu\text{m}$ in diameter is used to scan the entire FOV and record the Ca^{2+} activity. This spot can be used to sequentially scan only the cells of interest, rather than the entire FOV, similar to the principles of random access microscopy (RAMP) strategies (Iyer, Hoogland

and Saggau, 2006). This configuration would lead to several benefits, including kHz imaging rates, reduced out-of-focus excitation resulting in improved SNR and less photobleaching during extended acquisitions times.

For example, when using the large FOV configuration of 2P-FENDO (configuration 4, FOV diameter = 550 μm) and a scanning spot of 15 μm in diameter, the number of points that are scanned are $(550 / 15)^2 \approx 1000$ points. With this configuration, we have shown that it is possible to record neuronal activity at 10 Hz (0.1 ms per point) by using ~ 100 mW at the sample plane and an average SNR = 2. Using a strategy in which, for example, only 10 neurons (10 points) of interest are sequentially scanned, one could achieve a higher SNR or a higher imaging frame rate. First, by using the same power at the sample plane (100 mW) and the same imaging rate (10 Hz), the 10 neurons can be imaged at a SNR that is 100 times higher than in the previous case (SNR = 2). Secondly, if the SNR (= 2) and the power (100 mW) are maintained, it is possible to increase the imaging rate of these 10 neurons up to 1 kHz, which could be used to perform voltage imaging, resolving single action potential and subthreshold activity at millisecond time scale.

Another strategy could involve replacing the galvo-galvo device with a SLM, which would generate holographic scanless spots to image the desired neurons at the same time (Sims *et al.*, 2023). In this case, the generation of 10 holographic spots to image the hypothetical 10 neurons would occur in parallel rather than sequentially, as in the galvo-galvo scanning configuration. The simultaneous illumination of the 10 neurons would allow for an increase by a factor N (in this case N = 10 neurons) in the imaging rate or the SNR. For example, it could allow to perform voltage imaging at 1 kHz of 10 neurons with a SNR 10 times bigger than in the previous case (SNR = 2). However, the parallel illumination of multiple neurons also demands a higher laser power. In this case, the power required to image 10 neurons simultaneously is 10 times higher (1 W) than the power used when scanning the neurons sequentially (100 mW), which could result in heating effects.

Motion correction. Although 2P-FENDO presents a high stability when imaging and manipulating the neuronal activity in freely moving mice, we have measured average displacements of the FOV of 2 μm during acquisitions of 300 s (Accanto*, Bot*, Lorca-Cámara* *et al.*, 2023). Larger movements of 5 μm have also been observed during short periods of time. By

using the post-processing analysis software Caiman, motion artifacts can be corrected and therefore these movements can have only minimal impact on the imaging. However, for photostimulations, FOV motion artifacts can be a limitation as the targeted cells might move away from the illumination spot at the photostimulation onset, as they have moved from their reference position. To overcome this limitation, the implementation of an active feedback loop into the SLM software can be used to register the movements during the acquisition and correct the phase on the SLM to retarget the neurons. These active corrections during the recording experiment requires a fast refreshing rate into the SLM to quickly adapt the patterns to the motion to maintain single-neuron resolution (Eybposh *et al.*, 2020). With such device, lateral displacements of the FOV can be corrected, however, axial motion displacements can be only corrected with a miniaturized axial shift device placed after the fiber bundle, such as tunable lenses (Ozbay *et al.*, 2018).

3D FOV. Working with a fiber bundle prevents the SLM to easily axially shift the holographic patterns, to manipulate a neuronal population in 3D. As a result, only the neurons located in a single 2D focal plane can be targeted with 2P-FENDO. Adding a device to axially shift the focal plane, such as a tunable lens (Ozbay *et al.*, 2018; Zong *et al.*, 2022) or a step motor (Flusberg *et al.*, 2008), will displace the focal plane of both the imaging and photostimulation excitations. Thus, if now it is possible to perform 20 Hz in a single plane, with one of these devices, one could perform subsequent acquisition of for example 5 planes at 4Hz of total speed (20Hz per plane), maintaining the same SNR. Another solution is to employ multi-core fibers (MCF) or multi-mode fibers (MMF) (Čižmár and Dholakia, 2012; Turtaev *et al.*, 2018; Tsvirkun *et al.*, 2019; Iyu *et al.*, 2023; Stibůrek *et al.*, 2023), to control the phase propagated through the cores or single-core of the fiber to shift the focal beam at any direction at the sample plane. These techniques use a SLM or a DMD, respectively, to modify the wavefront at the fiber entrance. However, they present limitations due to the slow SLM refresh time to scan the beam at different positions or due to the DMD which is only used for single-photon excitation.

These parameters are considered in the next publication ([under review](#)) in which three theoretical systems are proposed based on possible advances in miniaturized optics, miniaturized wavefront shaping devices and customized fibers.

B.4.1 Review publication

Recent advances in light patterned optogenetic photostimulation in freely moving mice

Antonio Lorca-Cámara^{a 1}, François G. C. Blot^{a 1}, Nicolò Accanto^{a*}

^aSorbonne Université, INSERM, CNRS, Institut de la Vision, F-75012 Paris, France

¹ These authors contributed equally

*Nicolò Accanto, E-mail: nicolo.accanto@inserm.fr

Abstract

Optogenetics opened the door to a new era of neuroscience. New optical developments are under way to enable high resolution neuronal activity imaging and selective photostimulation of neuronal ensembles in freely moving animals. These advancements could allow researchers to interrogate, with cellular precision, functionally relevant neuronal circuits in the framework of naturalistic brain activity. In this manuscript, we provide an overview of the current state-of-the-art of imaging and photostimulation in freely moving rodents, and present a road-map for future optical and engineering developments towards miniaturized microscopes that could reach beyond the currently existing systems.

Keywords: fiber optic applications, optogenetics, multiphoton microscopy, holography applications, functional imaging, neurophotonics.

1. Introduction

Understanding the connections between neuronal activity and behavior stands as a fundamental goal in neuroscience that requires the precise mapping and/or manipulation of neuronal activity. Genetically encoded calcium indicators (GECIs)^{1,2} and voltage indicators (GEVIs)^{3,4} have made it possible to image neuronal activity. Concurrently, the emergence of optogenetics⁵⁻⁷, based on light-gated ion channels (opsins), has provided the means to optically manipulate neurons. On the optical side, advances in multiphoton microscopy^{8,9} have provided tools to image neuronal activity with cellular resolution, deeper into the tissue ($> 1 \text{ mm}^{10,11}$), with fast acquisition rates^{12,13}, and on ultra-large fields of views (FOVs) (up to $5 \text{ mm}^{14,15}$). Simultaneously, progress in wavefront shaping techniques, such as computer-generated holography (CGH)¹⁶ using liquid crystal spatial light modulators (SLMs), coupled with high-energy ultrafast lasers, have unlocked the precise

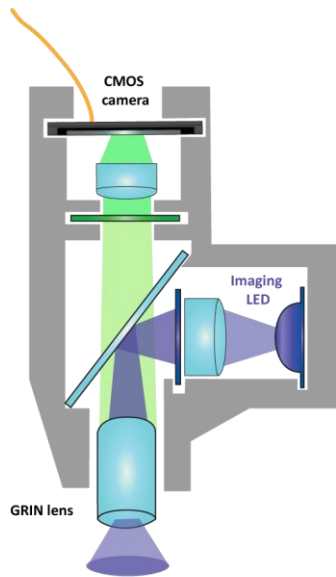
manipulation of groups of neurons, down to the single-cell level¹⁷⁻²⁰. The combination of these approaches has enabled cellular resolution *in vivo* imaging and manipulation studies, often referred to as all-optical studies²¹⁻²⁶, which enabled to identify functionally relevant neuronal ensembles, to replay and/or alter their spatio-temporal activity profile, and to decipher their behavioral implications. Importantly, the selective control of even a reduced number (< 20) of functionally defined neurons showed significant impact on the behavioral output^{22,26}.

Nevertheless, these advanced optical methods were primarily designed for benchtop microscopes and typically necessitate to head-restrain animals under an objective. Head-fixation can alter perception and interaction with the environment, interfering with sensory integration, motor output, and induces stress to the animal, leading to biased neuronal integration²⁷. Head restriction has been showed to affect not only motor related neuronal circuits but also a number of networks related to cognitive functions, such as the recruitment and coding of hippocampal place cells during navigation²⁸, or the multisensory encoding of V1 neurons for visual flow integration²⁹. All together these studies question our ability to reproduce neuronal coding resulting from voluntary real-world exploration, in artificial/virtual settings^{30,31}. While the lack of vestibular and head/neck proprioception inputs have been emphasized to explain the differences in neuronal activity between virtual reality systems and real-world exploration, a larger range of senses could be involved (smell, audition) raising the idea that active free motion is a behavioral state in essence³², comparable to sleep or other known awake states (drowsy, alert, resting). There is thus a need for tools to observe and manipulate neuronal circuits with high resolution in freely moving animals to investigate how natural behaviors shape neuronal processing in the brain.

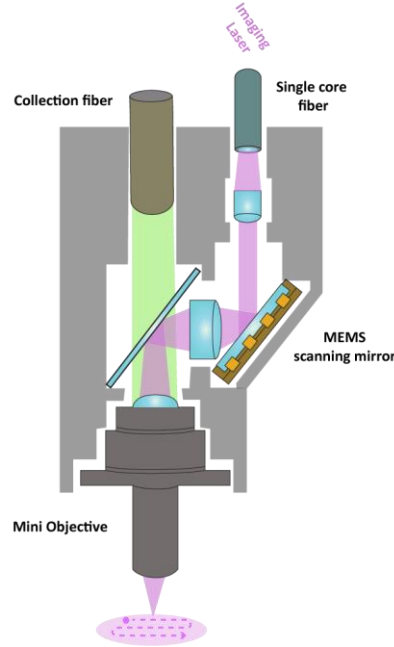
To this end, miniaturized optical systems have been developed to image neuronal activity during natural behaviors. Three main families of systems are widely used today:

- **1P Miniscopes**^{33,34}. One photon (1P) head-mounted wide-field miniscopes use a LED source, micro-lenses, and a miniature CMOS camera to image neuronal activity (Fig. 1a). While these devices enable functional imaging of large FOVs^{35–37} at high acquisition rates³⁸ within a cost-effective system, they suffer from poor optical sectioning, and suboptimal signal to noise ratio (SNR) due to the out-of-focus fluorescence background.
- **Miniaturized multiphoton microscopes**^{39–43}. They are based on single-core optical fibers that propagate infrared light from a pulsed laser to the animal head to generate two-photon (2P)^{44–46} or three-photon (3P)^{47,48} excitation. A light and miniaturized scanner, based either on microelectromechanical system (MEMS⁴⁹) scanning mirrors that deflect the laser beam or on a fiber scanning unit that moves the fiber tip in a spiral trajectory⁴⁵ (Fig. 1b), quickly scans the diffraction limited laser beam on the sample to generate an image. If these systems offer the highest optical resolution and penetration depth compared to other miniaturized optical systems, the single core fiber delivery has so far remained incompatible with different imaging techniques, such as random access microscopy^{12,50} or multipoint scanless excitation⁵¹.
- **Fiber bundle-based microscopes**. In this case, a multicore fiber, also called fiber bundle, composed of many thousands of individual cores, is used to relay a standard optical system to the animal's head (Fig. 1c). Fiber bundle microscopes have been demonstrated in freely moving animals both in the 1P^{52–54} and 2P^{55–57} regime. Thanks to the multicore delivery, the use of fiber bundles is in general compatible with other imaging techniques, such as multipoint excitation⁵², structured illumination^{52,54} or multipoint confocal imaging⁵³. At the same time, the inter-core space limits the optical resolution and lowers the light transmission, especially for the excitation laser.

(a.) 1P Miniscope



(b.) 2P Miniaturized microscope (with MEMs scanning post fiber)



(c.) 2P Fiber bundle microscope (with Galvos scanning pre fiber)

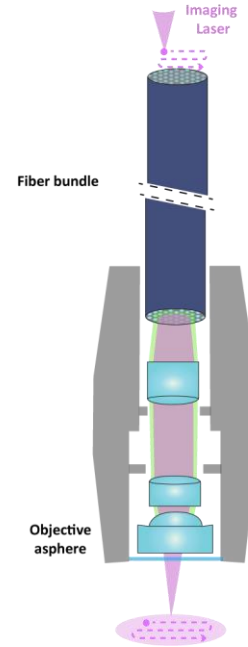


Fig. 1 Optical systems for neuronal activity imaging in freely moving mice. (a-c) Schemes of the optical elements and the light paths of (a) a 1P miniscope, (b) a 2P miniaturized microscope and (c) a 2P fiber bundle-based microscope, and the illumination on the imaging plane, wide field (a) or scanning (b and c) MEMS: miniature electromagnetic mirrors; CMOS: complementary metal-oxide-semiconductor; GRIN lens: gradient refracting-index lens. Detailed information of the three systems is presented in Table 1.

System	Main components	FOV & Resolution	Frame rate	Achievable Depth	3D possible?	Advantages/ Limitations
1P Miniscopes	LED, miniaturized camera	FOV 4.8x3.6 mm ² Lat. Res. 5 μm (Ref. ³⁶)	500 Hz Ref. ³⁸	Superficial layers ~100 μm	With light-field techniques Ref. ^{58,59}	Fast acquisition, large FOV, wireless possibilities/ 1P resolution and depth limitations
		FOV 8x10 mm ² Lat. Res. 50 μm (Ref. ³⁷)				
2P Miniaturized Microscopes	Pulsed laser, single core fiber, MEMS	FOV 420x420 μm ² Lat. Res. 1.2 μm Axial Res. 18 μm (Ref. ⁴⁴)	40 Hz Ref. ⁴⁴	< 400 μm	With tunable lenses. Ref. ^{44,46}	High resolution in deeper regions/ Not shown with different imaging or photostimulation techniques
		FOV 1x0.8 mm ² Lat. Res. 1.47 μm Axial Res. 25 μm (Ref. ⁴⁶)				
3P Miniaturized Microscopes	Pulsed laser, single core fiber, MEMS	FOV 400x400 μm ² Lat. Res. ~ 1 μm Axial Res. ~ 10 μm (Ref. ^{47,48})	~ 15 Hz Ref. ^{47,48}	< 1.2 mm	With tunable lenses. Ref. ⁴⁸	Access to deeper regions/ Lower frame rate
1P fiber bundle microscopes	Visible lasers, benchtop scanners/ DMD	FOV ~250 μm-wide Lat. Res. 2 μm Axial Res. 10-40 μm (Ref. ⁵²⁻⁵⁴)	200 Hz Ref. ⁵³	260 μm in vitro 120 μm in vivo with structured illumination Ref. ⁵⁴	With tunable lenses. Ref. ⁵⁴	Compatible with optimized illumination and photostimulation/ 1P resolution and depth limitations
2P fiber bundle microscopes	Pulsed lasers, benchtop scanners/ SLM	FOV ~250 μm-wide Lat. Res. 2 μm Axial Res. 10-15 μm (Ref. ^{56,57})	50 Hz Ref. ⁵⁷	~150 μm in vivo Ref. ^{56,57}	With tunable lenses. Ref. ⁵⁶	Compatible with optimized illumination and photostimulation/ Optical resolution limited by core size

Table 1. A comparison of the main imaging parameters of recently published 1P miniscopes, 2P/3P miniaturized microscopes and fiber bundle-based microscopes.

Unfortunately, most existing systems are currently only compatible with imaging of neuronal activity and cannot perform optogenetic photostimulation with single-cell spatial resolution, in freely moving animals. The ability to also photostimulate neuronal ensembles in freely moving animal holds major insights to correlate microcircuits control with behavioral outputs. In the following sections, we review the few existing systems to deliver optogenetic photostimulation to the brain in freely moving mice, with a particular attention to systems that can provide near single-cell resolution photostimulation, and explore potential future developments to overcome current limitations.

2. Current optical systems for optogenetic photostimulation in freely moving mice

2.1 Optoelectronics for optogenetic photostimulation

Optogenetics, in its simplest form, employs an optical fiber to deliver wide-field 1P illumination, therefore already compatible with the study of freely moving animals^{60,61}. Various techniques were subsequently developed to increase the spatial precision of light delivery and/or to deliver light at multiple points in the brain⁶². Among those, implantable microLED arrays^{63–66} provide reprogrammable illumination patterns at the millisecond scale for optogenetic control in the brain of freely moving animals. Alternatively, multiple fibers (up to several tens) were implanted at different brain regions and separately addressed for both fiber photometry and optogenetic photostimulation⁶⁷. Finally, tapered optical fibers^{68–70} or photonics waveguides⁷¹ also allow some control over the depth at which light is emitted via mode or wavelength-division multiplexing. However, none of these devices are compatible with simultaneous imaging and photostimulation with single neuron resolution, which is of great importance to understand how neuronal circuits encode information.

2.2 Systems for all optical studies in freely moving animals

Only few innovative systems have emerged for near single-cell resolution imaging and optogenetic photostimulation in freely moving animals. They are mainly based either on subsequent developments of the 1P miniscope architecture, or on the use of fiber bundles.

a) 1P miniscopes for wide-field imaging and photostimulation

Miniscopes can readily be combined with cable-connected LED probes for optogenetic stimulation of brain regions distal from the imaging FOV⁷². Integrating the optoelectronic circuit into the miniscope offers precise synchronization of optogenetic manipulation with imaging recording.

This greatly facilitates accurate post-hoc trace analysis and enables multi-sites optogenetic stimulation with a single imaging FOV, providing insights into long-range connectivity *in vivo*. Alternatively, systems with two LED sources at different wavelength bands⁷³ or different lasers⁷⁴ were developed to enable imaging and photostimulation over the same FOV. However, these systems are limited to wide-field illumination for photostimulation, which does not enable the investigation of refined microcircuits. An interesting future perspective could be to couple microLED arrays from the previous section with a 1P miniscope to provide higher resolution and reconfigurable patterned photostimulation on one brain region, with the simultaneous 1P calcium imaging on a different region.

b) 1P Miniscope and 1P fiber bundle microscopes for patterned illumination

1P miniscopes can be enhanced by incorporating a miniaturized DMD for spatial light patterning in freely moving animals, as demonstrated in the Miniscope with All-optical Patterned Stimulation and Imaging (MAPSI) system⁷⁵ (Fig. 2a). By using a collimated laser beam, MAPSI ensures lateral resolutions of $\sim 10\ \mu\text{m}$ and an axial resolution of $30\text{-}40\ \mu\text{m}$, on a $250\ \mu\text{m}$ wide FOV, sufficient to achieve near single-neuron stimulation in freely moving animals. However, as a consequence of the 1P illumination and the scattering of the brain, the penetration depth at which near single-cell resolution photostimulation was achieved remained limited to the first $\sim 50\ \mu\text{m}$ below the GRIN lens used⁷⁵. Additionally, while conventional miniscopes typically weight less than 5g, the MAPSI system weights 7.8 g (25-30% of the animal weight), which necessitates the use of a weight carrier. An alternative strategy is to use optical fiber bundles to transmit at the same time the imaging source, the patterned photostimulation and to collect the fluorescence from calcium indicators, as shown in Ref.⁵² for the first time (Fig. 2b). Such system offered, on a $240\ \mu\text{m}$ wide FOV, an experimentally defined axial resolution of $18\ \mu\text{m}$ for $5\ \mu\text{m}$ large photostimulation spots, sufficient to achieve near single-cell resolution photostimulation. However, as for the MAPSI system, near

single-cell photostimulation was only possible within $< 60 \mu\text{m}$ deep from the brain surface. To improve penetration depth and spatial resolution of both the imaging and the photostimulation spots, and reduce background noise, multi-photon microscopy can be employed.

c) 2P all-optical studies with a fiber bundle

Recently, we have developed a two-photon fiberscope, 2P-FENDO⁵⁷, based on an optical fiber bundle, to both record and optogenetically manipulate neuronal populations in freely moving mice with single-cell resolution (Fig. 2c). 2P-FENDO uses extended spots encompassing multiple fiber cores for both imaging and photostimulation, thereby reducing the power density and preventing self-phase modulation effects that can disrupt the excitation pulse⁷⁶. Importantly, we have demonstrated that the inherent inter-core delays of a fiber bundle decompose the excitation spot in time, to ensure single-cell axial resolution ($\sim 10 \mu\text{m}$) and prevent out-of-focus excitation, even for extended illumination spots. With 2P-FENDO we have achieved functional imaging at a frame rate of up to 20 Hz within a 2D FOV of $250 \mu\text{m}$ in diameter, together with high resolution photostimulation of selected groups of neurons by using a SLM to pattern the light entering the fiber bundle. 2P-FENDO demonstrated near single-cell photostimulation precision, as it only induced detectable calcium responses in neurons that were within $20 \mu\text{m}$ from the photostimulation spot (spot diameter of $10 \mu\text{m}$). The 2P excitation regime, allowed us to access deeper regions within the brain (depths of up to $160 \mu\text{m}$) below the brain surface.

However, the limited size of the FOV and the lower optical resolution defined by the inter-core spacing, together with the inhomogeneity of 2P excitation through different cores of the fiber bundle (characterized for different type of bundles in Ref. ⁷⁷), result in lower imaging quality compared to the previously described multiphoton miniaturized microscopes^{44,45,47}.

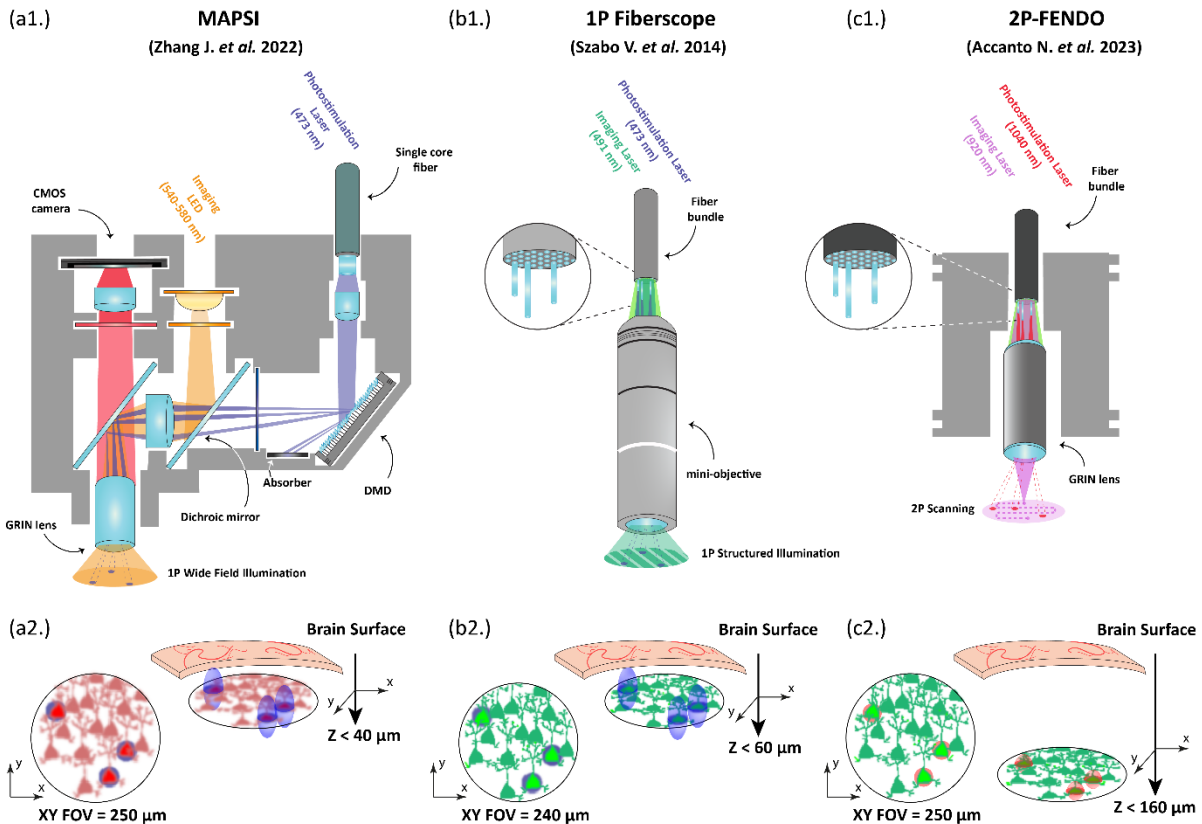


Fig. 2 All-optical systems for patterned illumination in freely moving animals. a1. 1P MAPSI⁷⁵ system using widefield imaging with a LED and patterned photostimulation with a DMD within a FOV of 250 μm -diameter. The fluorescence (in red, as the calcium indicator jRCaMP1b was used in the experiment) is detected with a miniaturized CMOS camera. a2. Single-cell resolution photostimulation was proven down to 40 μm below the GRIN lens surface. b1. 1P fiberscope⁵² that propagates two visible wavelength lasers for imaging and photostimulation from a standard benchtop microscope to the brain using a fiber bundle and a mini-objective. b2. The FOV for the imaging (using the green calcium indicator GCaMP5-G) and the holographic photostimulation is 240 μm -diameter. Single-cell resolution photostimulation was proven down to 60 μm deep. c1. 2P fiberscope (2P-FENDO)⁵⁷ using a fiber bundle and a GRIN lens to transmit the 2P excitation for both the imaging (using the green calcium indicator jGCaMP7s) and holographic photostimulation from the benchtop microscope to the head the mice. c2. The FOV is 250 μm -diameter. Single-cell resolution photostimulation was proven down to 160 μm below the GRIN lens surface. (a2-c2) Representations of the x/y view of the imaged cells (red a2 or green b2/c2) in the FOV (*left*) with the photostimulation spots (1P excitation blue spots in a2/b2 and 2P excitation red spots in c2), and the x/y/z view (*right*) to illustrate the axial extension of the photostimulation spots (better axial resolution is obtained in c2 when using 2P excitation), together with the maximal

reachable depth from the brain surface (largest in c2 for 2P excitation). The imaging quality is qualitatively illustrated with higher or lower blurring applied to the FOV, and is lower for 1P widefield imaging (a2.) and higher for 1P imaging with structured illumination (b2.), and 2P imaging (c2.) DMD: digital micromirror device; CMOS: complementary metal-oxide-semiconductor; GRIN lens: gradient refracting-index lens. Detailed information of the three systems is presented in Table 2.

System	Illumination mode	FOV & Resolution Stim.	Limit depth	Multi-plane	Advantages/ Limitations
μLED	Multiple μLEDs for array illumination	- FOV limited by the size of the array - Cone of illumination	Implant, no theoretical limitations	Yes, along the shaft	Implantable in deep regions + wireless possibilities/ No cellular resolution and no flexibility to target user-desired neurons
1P MAPSI Ref.⁷⁵	1P laser + single core fiber, DMD for patterned illumination	- FOV 250 μm-diameter - Lat. Res. 10 μm - Axial Res. 30 μm	< 40 μm	No	Miniaturized optics/ Lack of cellular resolution in depth and weight (7.8g)
1P fiber bundle microscope Ref.⁵²	1P laser + fiber bundle, SLM for patterned illumination	- FOV 250 μm-diameter - Lat. Res. ~ 5 μm - Axial Res. ~ 18 μm	< 60 μm	No	Light weight/ 1P resolution and depth limitations
2P-FENDO Ref.⁵⁷	2P laser + fiber bundle, SLM for patterned illumination	- FOV 250 μm-diameter - Lat. Res. ~ 10 μm - Axial Res. ~ 10 μm	< 160 μm	No	Light weight, 2P resolution and depth access/ No multiplane, lateral resolution limited by core size

Table 2. A comparison of the main imaging and photostimulation parameters of recently published μLED systems, 1P miniscopes and fiber bundle-based microscopes.

3. Perspectives for all-optical systems in freely moving mice

The currently available all-optical systems developed for the study of freely moving mice all present advantages and disadvantages with respect to spatial resolution, diameter of the FOV, penetration depth, system complexity, flexibility and weight. New efforts from the neurophotonic community will be necessary to improve these technologies to a level comparable to standard benchtop microscopes and ensure their widespread accessibility.

a) Micro optic engineering

One potential improvement is to integrate a multiphoton miniaturized microscope (such as MINI2P, Ref.⁴⁴) for the best image quality with a single-cell resolution patterned photostimulation system based on a fiber bundle, similar to 2P-FENDO⁵⁷ (an example of such a system is depicted in Fig. 3a). This will require substantial optical, mechanical and electronic engineering efforts, especially given the critical need to minimize the weight on the animal's head. The future availability of high performance miniaturized optical components (both active and passive) will undoubtedly ease its implementation. Recent developments in high resolution three-dimensional (3D) printing offer a promising route, allowing for the direct fabrication of aberration corrected and optimized micro-lenses on top of optical fibers⁷⁸⁻⁸⁰, as well as gradient refractive index (GRIN) lenses⁸¹.

b) Miniaturized spatial light modulators

Targeting arbitrary three-dimensional distributions of cells at the sample plane is of great importance in optogenetic applications²⁰. However, this requires phase modulation (such as in CGH), which is challenging in freely moving animals as the phase information is mixed across different modes of a multimode fiber or different cores of a multicore fiber. Wavefront shaping strategies⁸² using a SLM before the fiber have been used to compensate for phase variations and refocus a beam without additional lenses at the fiber output⁸³⁻⁸⁷, but remain highly sensitive to the fiber bending, which has so far prevented their application in freely moving animals, even if progress in this sense is underway^{85,88}. An alternative strategy to achieve 3D light targeting could be to use a miniaturized SLM at the fiber output, in a configuration similar to the MAPSI system⁷⁵. However, the compact DMD used in the MAPSI is highly inefficient when used as amplitude modulator and would require complex (and again inefficient) optical designs to be used as a phase modulator⁷⁵, hindering its application in the 2P regime. The development of a portable, lightweight

phase-only SLM (as illustrated in Fig. 3b) that can be incorporated directly at the animal head would be disruptive for all-optical 2P fiberscopes and thus constitutes a promising direction for the neurophotonics field. Apart from miniaturizing existing liquid crystal SLM technology (starting for example from the LUNA-NIR-147 model from Holoeye), active and reconfigurable metasurfaces could constitute a promising alternative, that has undergone much progress in recent years⁸⁹⁻⁹¹.

b) Fiber optic engineering

All-optical systems based on fiber bundles offer the advantage of requiring minimal optics at the distal end of the fiber (2P-FENDO only uses a single GRIN lens after the fiber), which limits weight and obstruction. Major improvements in these systems^{56,57} will result from enhanced imaging quality, larger FOVs and higher SNR. The image quality is affected by the inhomogeneities in 2P excitation⁷⁷, the core to core coupling⁹² and the inter-core distance of the fiber bundle ($d_{\text{core-core}}$), while the size of the FOV (FOV_{max}) is determined by the diameter of the bundle (ϕ_{fiber}) and the magnification of the optics at the distal end of the fiber (M). Ad hoc design of larger in diameter, and yet flexible, bundles with a sufficiently small inter-core distance ($d_{\text{core-core}}$) to maintain high lateral resolution (d_{xy}), $d_{\text{xy}} = d_{\text{core-core}}/M$, and a reduced 2P inhomogeneity, together with optimized distal optics⁴⁶, will increase the FOV ($\text{FOV}_{\text{max}} = \phi_{\text{fiber}}/M$) and improve the image quality. Fiber engineering, therefore, presents a promising avenue to optimize all-optical studies in freely moving animals (as seen in Fig. 3c).

Finally, one effective way to improve the imaging SNR is by using more complex scanning or multiplexing strategies, which are in general difficult to implement in a multiphoton miniaturized microscope. For instance, one could avoid scanning areas of the FOV that carry no information.

This could be reached with random access microscopy^{12,50} or even with a scanless approach⁵¹ that uses CGH to excite only the cells of interest.

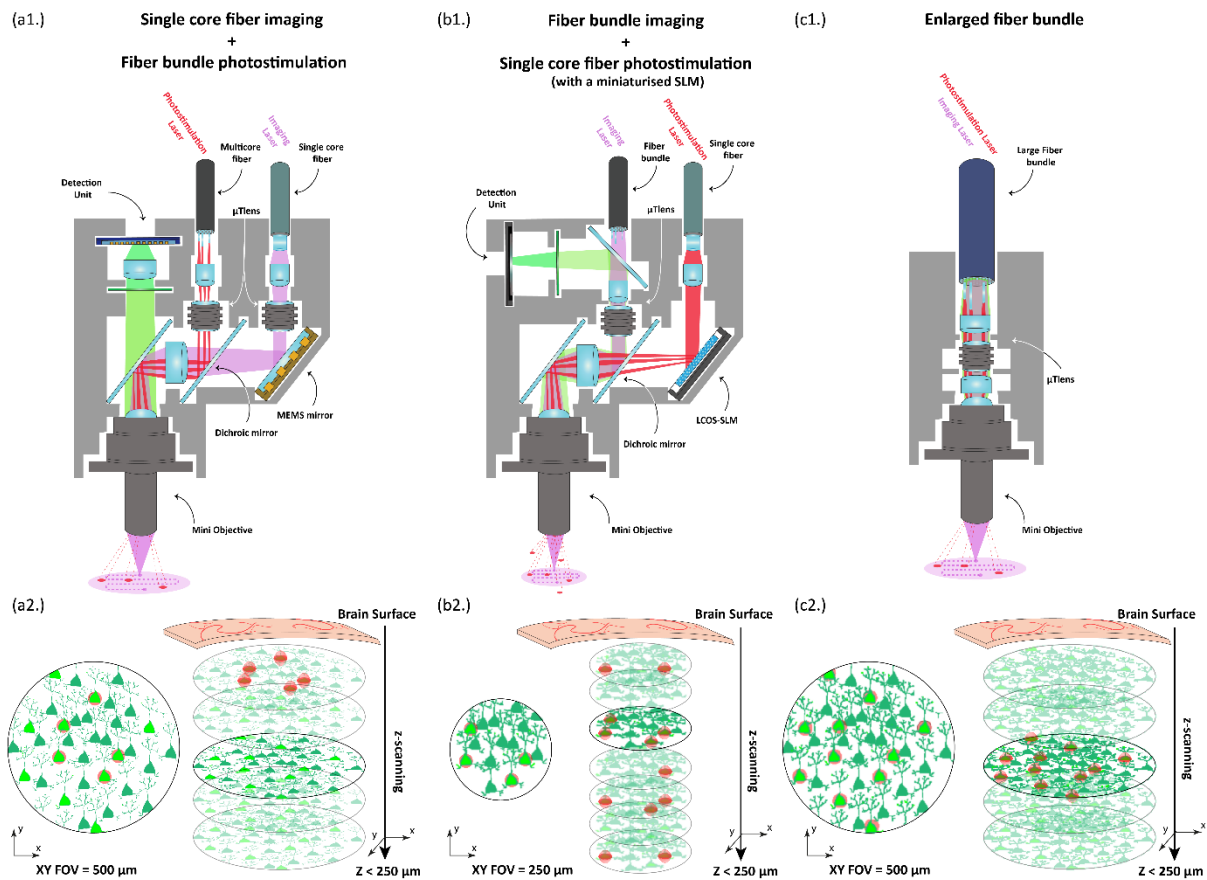


Fig. 3 Possible all-optical architectures for patterned illumination in freely moving animals. (a1-c1) Schemes of the optical elements, the light paths, and the scanning on the imaging plane. (a2-c2) Representations of the x/y view of the imaged cells (green) in the FOV (*left*) with the photostimulation spots (red spots), and the x/y/z view (*right*) to illustrate the axial extension of the photostimulation spots, together with the expected reachable depth from the brain surface. The imaging quality is illustrated by a Gaussian blur applied on the FOV as we compare 2P imaging through a single core fiber (a2.), and 2P imaging through fiber bundles (b2/c2). Representations of the expected imaging quality (green) in the FOV (*left*) and the photostimulation spots (red dots), with the reachable depth from the brain surface (*right*), when using 2P excitation (larger depth could be achieved with 3P excitation^{47,48}). The mini objective and tunable lens (μ Tlens) could be for instance the one presented in Ref.⁴⁴. In a2-b2, we consider the FOV for imaging and photostimulation to be the largest ones so far demonstrated when using a single-core optical fiber and MEMS scanners

(Ref.⁴⁴) and a fiber bundle (Ref.^{56,57}) in the 2P regime, while in c2 a larger FOV comes from the optimization of the fiber bundle and distal optics as explained in the text. (a2) Independent tunable lenses could enable the decoupling of the imaging and photostimulation planes. (b2) The miniaturized SLM at the distal end of the fiber would give access to 3D light multiplexing. c2) A single tunable lens would shift simultaneously the imaging and photostimulation plane, but on a larger FOV. MEMS: micro-electro-mechanical systems; μ Tlens: micro-tunable lens; LCOS-SLM: liquid crystal on silicon spatial light modulators.

4. Concluding remarks

In this manuscript, we have reviewed the state-of-the-art for all-optical studies in freely moving mice and we have given different routes to optimize the performances of these devices to match standards of current benchtop microscopes. Miniaturized systems for all-optical studies will provide an important addition in the near future to understand how discrete neuronal networks shape behavior in animals that are free to move.

It is essential to highlight that a common challenge of all imaging devices working in freely moving animals is motion artefacts. While movements in the recorded image can be compensated with motion correction post-processing algorithms^{93,94}, achieving single-cell optogenetic targeting along the experiment would require online correction to compensate for potential motions of the FOV. Lateral displacements of the FOV could be compensated with a fast SLM, by using a fast phase recalculation⁹⁵ to adapt the stimulation pattern to the FOV movements and maintain single-cell resolution. All-optical studies of freely moving animals will therefore also largely benefit from further algorithm developments as well as computational imaging.

As a final remark, while optogenetic does its very first steps in clinical applications⁹⁶, pre-clinical studies demonstrated the important role that patterned illumination will play in future therapeutic applications⁹⁷⁻⁹⁹. Optical means to implement light delivery targeting are predicted to make important contribution for a novel class of brain-machine interfaces¹⁰⁰, to translate optogenetic

neuronal control to the clinics. We believe that the concepts described in this article will help guiding further developments.

Disclosures

The authors declare no competing interests.

Acknowledgements

We acknowledge support from “Agence National de la Recherche” (grants ANR 19-CE19-0001-01, 2MEnHoloMD; ANR-23-ERCES-0009, 2P-COMFIB).

References

1. Zhang, Y. *et al.* Fast and sensitive GCaMP calcium indicators for imaging neural populations. *Nature* **615**, 884–891 (2023).
2. Lin, M. Z. & Schnitzer, M. J. *Genetically encoded indicators of neuronal activity.* *Nature Neuroscience* **19**, 1142–1153 (2016).
3. Yang, H. H. & St-Pierre, F. Genetically encoded voltage indicators: Opportunities and challenges. *Journal of Neuroscience* **36**, 9977–9989 (2016).
4. Xu, Y., Zou, P. & Cohen, A. E. Voltage imaging with genetically encoded indicators. *Curr. Opin. Chem. Biol.* **39**, 1–10 (2017).
5. Deisseroth, K. Optogenetics: 10 years of microbial opsins in neuroscience. *Nature Neuroscience* **18**, 1213–1225 (2015).
6. Emiliani, V. *et al.* Optogenetics for light control of biological systems. *Nat. Rev. Methods Prim.* **2**, 55 (2022).
7. Boyden, E. S., Zhang, F., Bamberg, E., Nagel, G. & Deisseroth, K. Millisecond-timescale, genetically targeted optical control of neural activity. *Nat. Neurosci.* **8**, 1263–1268 (2005).
8. Svoboda, K. & Yasuda, R. Principles of Two-Photon Excitation Microscopy and Its Applications to Neuroscience. *Neuron* **50**, 823–839 (2006).
9. Helmchen, F. & Denk, W. Deep tissue two-photon microscopy. *Nature Methods* **2**, 932–940 (2005).
10. Ouzounov, D. G. *et al.* In vivo three-photon imaging of activity of Gcamp6-labeled neurons deep in intact mouse brain. *Nat. Methods* **14**, 388–390 (2017).
11. Wang, T. *et al.* Quantitative analysis of 1300-nm three-photon calcium imaging in the mouse brain. *Elife* **9**, 1–22 (2020).

12. Villette, V. *et al.* Ultrafast Two-Photon Imaging of a High-Gain Voltage Indicator in Awake Behaving Mice. *Cell* **179**, 1590-1608.e23 (2019).
13. Wu, J. *et al.* Kilohertz two-photon fluorescence microscopy imaging of neural activity in vivo. *Nat. Methods* **17**, 287–290 (2020).
14. Yu, C.-H. H., Stirman, J. N., Yu, Y., Hira, R. & Smith, S. L. Diesel2p mesoscope with dual independent scan engines for flexible capture of dynamics in distributed neural circuitry. *Nat. Commun.* 2021 121 **12**, 1–8 (2021).
15. Sofroniew, N. J., Flickinger, D., King, J. & Svoboda, K. A large field of view two-photon mesoscope with subcellular resolution for in vivo imaging. *Elife* **5**, (2016).
16. Conti, R., Assayag, O., de Sars, V., Guillon, M. & Emiliani, V. Computer generated holography with intensity-graded patterns. *Front. Cell. Neurosci.* **10**, 236 (2016).
17. Pégard, N. C. *et al.* Three-dimensional scanless holographic optogenetics with temporal focusing (3D-SHOT). *Nat. Commun.* **8**, 1228 (2017).
18. Faini, G. *et al.* Ultrafast light targeting for high-throughput precise control of neuronal networks. *Nat. Commun.* **14**, 2021.06.14.448315 (2023).
19. Chen, I. W., Papagiakoumou, E. & Emiliani, V. Towards circuit optogenetics. *Current Opinion in Neurobiology* **50**, 179–189 (2018).
20. Adesnik, H. & Abdeladim, L. Probing neural codes with two-photon holographic optogenetics. *Nature Neuroscience* **24**, 1356–1366 (2021).
21. Emiliani, V., Cohen, A. E., Deisseroth, K. & Häusser, M. All-Optical Interrogation of Neural Circuits. *J. Neurosci.* **35**, 13917–13926 (2015).
22. Carrillo-Reid, L., Han, S., Yang, W., Akrouh, A. & Yuste, R. Controlling Visually Guided Behavior by Holographic Recalling of Cortical Ensembles. *Cell* **178**, 447-457.e5 (2019).
23. Gill, J. V. *et al.* Precise Holographic Manipulation of Olfactory Circuits Reveals Coding Features Determining Perceptual Detection. *Neuron* **108**, 382-393.e5 (2020).
24. Marshel, J. H. *et al.* Cortical layer-specific critical dynamics triggering perception. *Science (80-.).* **365**, (2019).
25. Zhang, Z., Russell, L. E., Packer, A. M., Gauld, O. M. & Häusser, M. Closed-loop all-optical interrogation of neural circuits in vivo. *Nat. Methods* **15**, 1037–1040 (2018).
26. Robinson, N. T. M. *et al.* Targeted Activation of Hippocampal Place Cells Drives Memory-Guided Spatial Behavior. *Cell* **183**, 1586-1599.e10 (2020).
27. Rector, D. & Harper, R. Imaging of hippocampal neural activity in freely behaving animals. *Behav. Brain Res.* **42**, 143–149 (1991).
28. Aghajan, Z. M. *et al.* Impaired spatial selectivity and intact phase precession in two-dimensional virtual reality. *Nat. Neurosci.* **18**, 121–128 (2015).
29. Ravassard, P. *et al.* Multisensory Control of Hippocampal Spatiotemporal Selectivity. *Science (80-.).* **340**, 1342–1346 (2013).

30. Donato, F. & Moser, E. I. A world away from reality. *Nature* **533**, 325 (2016).
31. Zhou, Z. C. *et al.* Deep-brain optical recording of neural dynamics during behavior. *Neuron* **111**, 3716–3738 (2023).
32. Händel, B. F. & Schölvinck, M. L. The brain during free movement – What can we learn from the animal model. *Brain Res.* **1716**, 3–15 (2019).
33. Aharoni, D. & Hoogland, T. M. Circuit investigations with open-source miniaturized microscopes: Past, present and future. *Frontiers in Cellular Neuroscience* **13**, 141 (2019).
34. Ghosh, K. K. *et al.* Miniaturized integration of a fluorescence microscope. *Nat. Methods* **8**, 871–878 (2011).
35. Guo, C. *et al.* Miniscope-LFOV: A large-field-of-view, single-cell-resolution, miniature microscope for wired and wire-free imaging of neural dynamics in freely behaving animals. *Sci. Adv.* **9**, 1–14 (2023).
36. Scherrer, J. R., Lynch, G. F., Zhang, J. J. & Fee, M. S. An optical design enabling lightweight and large field-of-view head-mounted microscopes. *Nat. Methods* **20**, 546–549 (2023).
37. Rynes, M. L. *et al.* Miniaturized head-mounted microscope for whole-cortex mesoscale imaging in freely behaving mice. *Nat. Methods* **18**, 417–425 (2021).
38. Juneau, J. *et al.* MiniFAST: A sensitive and fast miniaturized microscope for in vivo neural recording. *bioRxiv* 2020.11.03.367466 (2020). doi:10.1101/2020.11.03.367466
39. Helmchen, F., Fee, M. S., Tank, D. W. & Denk, W. A miniature head-mounted two-photon microscope: High-resolution brain imaging in freely moving animals. *Neuron* **31**, 903–912 (2001).
40. Bao, H., Allen, J., Pattie, R., Vance, R. & Gu, M. Fast handheld two-photon fluorescence microendoscope with a 475 microm x 475 microm field of view for in vivo imaging. *Opt. Lett.* **33**, 1333–1335 (2008).
41. Ducourthial, G. *et al.* Development of a real-time flexible multiphoton microendoscope for label-free imaging in a live animal. *Sci. Rep.* **5**, 1–9 (2015).
42. Sawinski, J. *et al.* Visually evoked activity in cortical cells imaged in freely moving animals. *Proc. Natl. Acad. Sci. U. S. A.* **106**, 19557–19562 (2009).
43. Piyawattanametha, W. *et al.* In vivo brain imaging using a portable 29 g two-photon microscope based on a microelectromechanical systems scanning mirror. *Opt. Lett.* **34**, 2309 (2009).
44. Zong, W. *et al.* Large-scale two-photon calcium imaging in freely moving mice. *Cell* **185**, 1240–1256.e30 (2022).
45. Li, A. *et al.* Twist-free ultralight two-photon fiberscope enabling neuroimaging on freely rotating/walking mice. *Optica* **8**, 870 (2021).
46. Zhao, C. *et al.* Millimeter field-of-view miniature two-photon microscopy for brain imaging in freely moving mice. *Opt. Express* **31**, 32925 (2023).
47. Klioutchnikov, A. *et al.* A three-photon head-mounted microscope for imaging all layers of visual cortex in freely moving mice. *Nat. Methods* (2022). doi:10.1038/s41592-022-01688-9

48. Zhao, C. *et al.* Miniature three-photon microscopy maximized for scattered fluorescence collection. *Nat. Methods* **20**, 617–622 (2023).
49. Piyawattanametha, W. *et al.* Fast-scanning two-photon fluorescence imaging based on a microelectromechanical systems two-dimensional scanning mirror. *Opt. Lett.* **31**, 2018 (2006).
50. Grewe, B. F., Langer, D., Kasper, H., Kampa, B. M. & Helmchen, F. High-speed in vivo calcium imaging reveals neuronal network activity with near-millisecond precision. *Nat. Methods* **7**, 399–405 (2010).
51. Sims, R. R. *et al.* Scanless two-photon voltage imaging. *Research square* **Under review**, (2023).
52. Szabo, V., Ventalon, C., De Sars, V., Bradley, J. & Emiliani, V. Spatially Selective Holographic Photoactivation and Functional Fluorescence Imaging in Freely Behaving Mice with a Fiberscope. *Neuron* **84**, 1157–1169 (2014).
53. Dussaux, C. *et al.* Fast confocal fluorescence imaging in freely behaving mice. *Sci. Rep.* **8**, 16262 (2018).
54. Supekar, O. D. *et al.* Miniature structured illumination microscope for in vivo 3D imaging of brain structures with optical sectioning. *Biomed. Opt. Express* **13**, 2530 (2022).
55. Göbel, W., Kerr, J. N. D., Nimmerjahn, A. & Helmchen, F. Miniaturized two-photon microscope based on a flexible coherent fiber bundle and a gradient-index lens objective. *Opt. Lett.* **29**, 2521 (2004).
56. Ozbay, B. N. *et al.* Three dimensional two-photon brain imaging in freely moving mice using a miniature fiber coupled microscope with active axial-scanning. *Sci. Rep.* **8**, 8108 (2018).
57. Accanto, N. *et al.* A flexible two-photon fiberscope for fast activity imaging and precise optogenetic photostimulation of neurons in freely moving mice. *Neuron* **111**, 176-189.e6 (2023).
58. Yanny, K. *et al.* Miniscope3D: optimized single-shot miniature 3D fluorescence microscopy. *Light Sci. Appl.* **9**, 2047–7538 (2020).
59. Skocek, O. *et al.* High-speed volumetric imaging of neuronal activity in freely moving rodents. *Nature Methods* 1–4 (2018). doi:10.1038/s41592-018-0008-0
60. Adamantidis, A. R., Zhang, F., Aravanis, A. M., Deisseroth, K. & De Lecea, L. Neural substrates of awakening probed with optogenetic control of hypocretin neurons. *Nature* **450**, 420–424 (2007).
61. Aravanis, A. M. *et al.* An optical neural interface: in vivo control of rodent motor cortex with integrated fiberoptic and optogenetic technology. *J. Neural Eng.* **4**, (2007).
62. Vázquez-Guardado, A., Yang, Y., Bandodkar, A. J. & Rogers, J. A. Recent advances in neurotechnologies with broad potential for neuroscience research. *Nat. Neurosci.* **23**, 1522–1536 (2020).
63. Scharf, R. *et al.* Depth-specific optogenetic control in vivo with a scalable, high-density μ LED neural probe. *Sci. Rep.* **6**, 1–10 (2016).
64. Stark, E., Koos, T. & Buzsáki, G. Diode probes for spatiotemporal optical control of multiple neurons in freely moving animals. *J. Neurophysiol.* **108**, 349–363 (2012).
65. Shin, G. *et al.* Flexible Near-Field Wireless Optoelectronics as Subdermal Implants for Broad

Applications in Optogenetics. *Neuron* **93**, 509-521.e3 (2017).

66. McAlinden, N. *et al.* Multisite microLED optrode array for neural interfacing. *Neurophotonics* **6**, 1 (2019).
67. Sych, Y., Chernysheva, M., Sumanovski, L. T. & Helmchen, F. High-density multi-fiber photometry for studying large-scale brain circuit dynamics. *Nat. Methods* **16**, 553–560 (2019).
68. Pisanello, F. *et al.* Multipoint-emitting optical fibers for spatially addressable in vivo optogenetics. *Neuron* **82**, 1245–1254 (2014).
69. Pisano, F. *et al.* Depth-resolved fiber photometry with a single tapered optical fiber implant. *Nat. Methods* **16**, 1185–1192 (2019).
70. Spagnolo, B. *et al.* Tapered fiberoptodes for optoelectrical neural interfacing in small brain volumes with reduced artefacts. *Nat. Mater.* **21**, 826–835 (2022).
71. Segev, E. *et al.* Patterned photostimulation via visible-wavelength photonic probes for deep brain optogenetics. *Neurophotonics* **4**, 011002 (2016).
72. de Groot, A. *et al.* Ninscope, a versatile miniscope for multi-region circuit investigations. *Elife* **9**, (2020).
73. Stamatakis, A. M. *et al.* Simultaneous optogenetics and cellular resolution calcium imaging during active behavior using a miniaturized microscope. *Front. Neurosci.* **12**, 496 (2018).
74. Srinivasan, S. *et al.* Miniaturized microscope with flexible light source input for neuronal imaging and manipulation in freely behaving animals. *Biochem. Biophys. Res. Commun.* **517**, 520–524 (2019).
75. Zhang, J. *et al.* A one-photon endoscope for simultaneous patterned optogenetic stimulation and calcium imaging in freely behaving mice. *Nat. Biomed. Eng.* 1–12 (2022). doi:10.1038/s41551-022-00920-3
76. Helmchen, F., Tank, D. W. & Denk, W. Enhanced two-photon excitation through optical fiber by single-mode propagation in a large core. *Appl. Opt.* **41**, 2930 (2002).
77. Garofalakis, A. *et al.* Characterization of a multicore fiber image guide for nonlinear endoscopic imaging using two-photon fluorescence and second-harmonic generation. *J. Biomed. Opt.* **24**, 1 (2019).
78. Gissibl, T., Thiele, S., Herkommer, A. & Giessen, H. Sub-micrometre accurate free-form optics by three-dimensional printing on single-mode fibres. *Nat. Commun.* **7**, 1–9 (2016).
79. Ren, H. *et al.* An achromatic metafiber for focusing and imaging across the entire telecommunication range. *Nat. Commun.* **13**, (2022).
80. Sivankutty, S. *et al.* Miniature 120-beam coherent combiner with 3D-printed optics for multicore fiber-based endoscopy. *Opt. Lett.* **46**, 4968–4971 (2021).
81. Antonini, A. *et al.* Extended field-of-view ultrathin microendoscopes for high-resolution two-photon imaging with minimal invasiveness. *Elife* **9**, 1–76 (2020).
82. Gigan, S. *et al.* Roadmap on Wavefront Shaping and deep imaging in complex media. (2021).

83. Turtaev, S. *et al.* High-fidelity multimode fibre-based endoscopy for deep brain in vivo imaging. *Light: Science and Applications* **7**, 92 (2018).
84. Stibůrek, M. *et al.* 110 μm thin endo-microscope for deep-brain in vivo observations of neuronal connectivity, activity and blood flow dynamics. *Nat. Commun.* **14**, (2023).
85. Tsvirkun, V. *et al.* Flexible lensless endoscope with a conformationally invariant multi-core fiber. *Optica* **6**, 1185 (2019).
86. Ohayon, S., Caravaca-Aguirre, A., Piestun, R. & DiCarlo, J. J. Minimally invasive multimode optical fiber microendoscope for deep brain fluorescence imaging. *Biomed. Opt. Express* **9**, 1492 (2018).
87. Andresen, E. R., Bouwmans, G., Monneret, S. & Rigneault, H. Two-photon lensless endoscope. *Opt. Express* **21**, 20713–20721 (2013).
88. Warren, S. C. *et al.* Adaptive multiphoton endomicroscopy through a dynamically deformed multicore optical fiber using proximal detection. *Opt. Express* **24**, 21474 (2016).
89. Shaltout, A. M., Shalae, V. M. & Brongersma, M. L. Spatiotemporal light control with active metasurfaces. *Science* (80-.). **364**, (2019).
90. Berto, P. *et al.* Tunable and free-form planar optics. *Nat. Photonics* 1–8 (2019). doi:10.1038/s41566-019-0486-3
91. Gu, T., Kim, H. J., Rivero-Baleine, C. & Hu, J. Reconfigurable metasurfaces towards commercial success. *Nat. Photonics* **17**, 48–58 (2023).
92. Chen, X., Reichenbach, K. L. & Xu, C. Experimental and theoretical analysis of core-to-core coupling on fiber bundle imaging. *Opt. Express* **16**, 21598–607 (2008).
93. Giovannucci, A. *et al.* Caiman an open source tool for scalable calcium imaging data analysis. *Elife* **8**, (2019).
94. Pachitariu, M. *et al.* Suite2p: beyond 10,000 neurons with standard two-photon microscopy. *bioRxiv* 1–30 (2016).
95. Hossein Eybposh, M., Caira, N. W., Atisa, M., Chakravarthula, P. & Pégard, N. C. DeepCGH: 3D computer-generated holography using deep learning. *Opt. Express* **28**, 26636 (2020).
96. Sahel, J.-A. *et al.* Partial recovery of visual function in a blind patient after optogenetic therapy. *Nat. Med.* **27**, 1223–1229 (2021).
97. Gauvain, G. *et al.* Optogenetic therapy: high spatiotemporal resolution and pattern discrimination compatible with vision restoration in non-human primates. *Commun. Biol.* **4**, 125 (2021).
98. Kathe, C. *et al.* Wireless closed-loop optogenetics across the entire dorsoventral spinal cord in mice. *Nat. Biotechnol.* **40**, 198–208 (2022).
99. Gao, T. T. *et al.* The clinical potential of optogenetic interrogation of pathogenesis. *Clin. Transl. Med.* **13**, (2023).
100. Ersaro, N. T., Yalcin, C. & Muller, R. The future of brain–machine interfaces is optical. *Nat. Electron.* **6**, 96–98 (2023).

B.5 References

- Accanto, N. *et al.* (2019) 'Multiplexed temporally focused light shaping through a gradient index lens for precise in-depth optogenetic photostimulation', *Scientific Reports*, 9(1), pp. 1–10. doi: 10.1038/s41598-019-43933-w.
- Accanto, N. *et al.* (2023) 'A flexible two-photon fiberscope for fast activity imaging and precise optogenetic photostimulation of neurons in freely moving mice', *Neuron*, 111(2), pp. 176-189.e6. doi: 10.1016/j.neuron.2022.10.030.
- Aghajan, Z. M. *et al.* (2015) 'Impaired spatial selectivity and intact phase precession in two-dimensional virtual reality', *Nature Neuroscience*, 18(1), pp. 121–128. doi: 10.1038/nn.3884.
- Aharoni, D. *et al.* (2019) 'All the light that we can see: a new era in miniaturized microscopy', *Nature Methods*, 16(1), pp. 11–13. doi: 10.1038/s41592-018-0266-x.
- Aharoni, D. and Hoogland, T. M. (2019) 'Circuit investigations with open-source miniaturized microscopes: Past, present and future', *Frontiers in Cellular Neuroscience*. Frontiers Media S.A., p. 141. doi: 10.3389/fncel.2019.00141.
- Antonini, A. *et al.* (2020) 'Extended field-of-view ultrathin microendoscopes for high-resolution two-photon imaging with minimal invasiveness in awake mice'.
- Bao, H. *et al.* (2008) 'Fast handheld two-photon fluorescence microendoscope with a 475 $\mu\text{m} \times 475 \mu\text{m}$ field of view for in vivo imaging', *Optics Letters*, 33(12), p. 1333. doi: 10.1364/ol.33.001333.
- Bocarsly, M. E. *et al.* (2015) 'Minimally invasive microendoscopy system for in vivo functional imaging of deep nuclei in the mouse brain', *Biomedical Optics Express*, 6(11), p. 4546. doi: 10.1364/boe.6.004546.
- Bollimunta, A. *et al.* (2021) 'Head-mounted microendoscopic calcium imaging in dorsal premotor cortex of behaving rhesus macaque', *Cell Reports*, 35(11), p. 109239. doi: <https://doi.org/10.1016/j.celrep.2021.109239>.
- Cai, D. J. *et al.* (2016) 'A shared neural ensemble links distinct contextual memories encoded close in time', *Nature*, 534(7605), pp. 115–118. doi: 10.1038/nature17955.
- Čižmár, T. and Dholakia, K. (2012) 'Exploiting multimode waveguides for pure fibre-based imaging', *Nature Communications*, 3(1), p. 1027. doi: 10.1038/ncomms2024.
- Ducourthial, G. *et al.* (2015) 'Development of a real-time flexible multiphoton microendoscope for label-free imaging in a live animal', *Scientific Reports*, 5(1), pp. 1–9. doi: 10.1038/srep18303.
- Dussaux, C. *et al.* (2018) 'Fast confocal fluorescence imaging in freely behaving mice', *Scientific Reports*, 8(1), p. 16262. doi: 10.1038/s41598-018-34472-x.
- Eybposh, M. H. *et al.* (2020) 'DeepCGH: 3D computer-generated holography using deep learning', *Optics Express*, 28(18), p. 26636. doi: 10.1364/oe.399624.

Flusberg, B. A. *et al.* (2008) 'High-speed, miniaturized fluorescence microscopy in freely moving mice', *Nature Methods*, 5(11), pp. 935–938. doi: 10.1038/nmeth.1256.

Garofalakis, A. *et al.* (2019) 'Characterization of a multicore fiber image guide for nonlinear endoscopic imaging using two-photon fluorescence and second-harmonic generation', *Journal of Biomedical Optics*, 24(10), p. 1. doi: 10.1117/1.jbo.24.10.106004.

Ghosh, K. K. *et al.* (2011) 'Miniaturized integration of a fluorescence microscope', *Nature Methods*, 8(10), pp. 871–878. doi: 10.1038/nmeth.1694.

Giovanniello, J. *et al.* (2020) 'A central amygdala-globus pallidus circuit conveys unconditioned stimulus-related information and controls fear learning', *Journal of Neuroscience*, 40(47), pp. 9043–9054. doi: 10.1523/JNEUROSCI.2090-20.2020.

Göbel, W. *et al.* (2004) 'Miniaturized two-photon microscope based on a flexible coherent fiber bundle and a gradient-index lens objective', *Optics Letters*, 29(21), p. 2521. doi: 10.1364/ol.29.002521.

Grewe, B. F. *et al.* (2017) 'Neural ensemble dynamics underlying a long-term associative memory', *Nature*, 543(7647), pp. 670–675. doi: 10.1038/nature21682.

de Groot, A. *et al.* (2020) 'Ninscope, a versatile miniscope for multi-region circuit investigations', *eLife*, 9, pp. 1–24. doi: 10.7554/eLife.49987.

Guo, C. *et al.* (2023) 'Miniscope-LFOV: A large-field-of-view, single-cell-resolution, miniature microscope for wired and wire-free imaging of neural dynamics in freely behaving animals', *Science Advances*, 9(16), pp. 1–14. doi: 10.1126/sciadv.adg3918.

Händel, B. F. and Schölvinck, M. L. (2019) 'The brain during free movement – What can we learn from the animal model', *Brain Research*, 1716, pp. 3–15. doi: 10.1016/j.brainres.2017.09.003.

Helmchen, F. *et al.* (2001) 'A miniature head-mounted two-photon microscope: High-resolution brain imaging in freely moving animals', *Neuron*, 31(6), pp. 903–912. doi: 10.1016/S0896-6273(01)00421-4.

Iyer, V., Hoogland, T. M. and Saggau, P. (2006) 'Fast functional imaging of single neurons using random-access multiphoton (RAMP) microscopy.', *Journal of neurophysiology*, 95(1), pp. 535–545. doi: 10.1152/jn.00865.2005.

Jacob, A. D. *et al.* (2018) 'A Compact Head-Mounted Endoscope for In Vivo Calcium Imaging in Freely Behaving Mice.', *Current protocols in neuroscience*, 84(1), p. e51. doi: 10.1002/cpns.51.

Jennings, J. H. *et al.* (2019) 'Interacting neural ensembles in orbitofrontal cortex for social and feeding behaviour', *Nature*, 565(7741), pp. 645–649. doi: 10.1038/s41586-018-0866-8.

Juneau, J. *et al.* (2020) 'MiniFAST: A sensitive and fast miniaturized microscope for in vivo neural recording', *bioRxiv*, p. 2020.11.03.367466.

Jung, J. C. *et al.* (2004) 'In vivo mammalian brain imaging using one- and two-photon fluorescence microendoscopy.',

Journal of neurophysiology, 92(5), pp. 3121–3133. doi: 10.1152/jn.00234.2004.

Karigo, T. *et al.* (2021a) 'Distinct hypothalamic control of same- and opposite-sex mounting behaviour in mice', *Nature*, 589(7841), pp. 258–263. doi: 10.1038/s41586-020-2995-0.

Karigo, T. *et al.* (2021b) 'Mounting Behaviour in Mice', *Nature*, 589(7841), pp. 258–263. doi: 10.1038/s41586-020-2995-0.Distinct.

Kim, T. H. and Schnitzer, M. J. (2022) 'Fluorescence imaging of large-scale neural ensemble dynamics', *Cell*, 185(1), pp. 9–41. doi: 10.1016/j.cell.2021.12.007.

Kingsbury, L. *et al.* (2019) 'Correlated Neural Activity and Encoding of Behavior across Brains of Socially Interacting Animals', *Cell*, 178(2), pp. 429–446.e16. doi: 10.1016/j.cell.2019.05.022.

Klioutchnikov, A. *et al.* (2020) 'Three-photon head-mounted microscope for imaging deep cortical layers in freely moving rats', *Nature Methods*, 17(5), pp. 509–513. doi: 10.1038/s41592-020-0817-9.

Klioutchnikov, A. *et al.* (2022) 'A three-photon head-mounted microscope for imaging all layers of visual cortex in freely moving mice', *Nature Methods*. doi: 10.1038/s41592-022-01688-9.

Klioutchnikov, A. and Kerr, J. N. D. (2023) 'Chasing cortical behavior : designing multiphoton microscopes for imaging neuronal populations in freely moving rodents', 10(4), pp. 1–8. doi: 10.1117/1.NPh.10.4.044411.

Kondo, T. *et al.* (2018) 'Calcium Transient Dynamics of Neural Ensembles in the Primary Motor Cortex of Naturally Behaving Monkeys', *Cell Reports*, 24(8), pp. 2191–2195.e4. doi: <https://doi.org/10.1016/j.celrep.2018.07.057>.

Levy, D. R. *et al.* (2019) 'Dynamics of social representation in the mouse prefrontal cortex', *Nature Neuroscience*, 22(12), pp. 2013–2022. doi: 10.1038/s41593-019-0531-z.

Li, A. *et al.* (2021) 'Twist-free ultralight two-photon fiberscope enabling neuroimaging on freely rotating/walking mice', *Optica*, 8(6), p. 870. doi: 10.1364/optica.422657.

Liberti, W. A. *et al.* (2017) 'An open source, wireless capable miniature microscope system.', *Journal of neural engineering*, 14(4), p. 45001. doi: 10.1088/1741-2552/aa6806.

Liberti, W. A. *et al.* (2022) 'A stable hippocampal code in freely flying bats', *Nature*, 604(7904), pp. 98–103. doi: 10.1038/s41586-022-04560-0.

Lyu, Z. *et al.* (2023) 'Sub-diffraction computational imaging via a flexible multicore-multimode fiber', *Optics Express*, 31(7), pp. 11249–11260. doi: 10.1364/oe.481052.

Meng, G. *et al.* (2019) 'High-throughput synapse-resolving two-photon fluorescence microendoscopy for deep-brain volumetric imaging in vivo', *eLife*, 8, pp. 1–22. doi: 10.7554/eLife.40805.

Moretti, C. *et al.* (2016) 'Scanless functional imaging of hippocampal networks using patterned two-photon illumination through GRIN lenses', *Biomed. Opt. Express*, 7(10), pp. 3958–3967. doi: 10.1364/BOE.7.003958.

Olson, J. M. *et al.* (2020) 'Secondary Motor Cortex Transforms Spatial Information into Planned Action during Navigation', *Current Biology*, 30(10), pp. 1845-1854.e4. doi: 10.1016/j.cub.2020.03.016.

Ozbay, B. N. *et al.* (2018) 'Three dimensional two-photon brain imaging in freely moving mice using a miniature fiber coupled microscope with active axial-scanning', *Scientific Reports*, 8(1), pp. 1–14. doi: 10.1038/s41598-018-26326-3.

Park, J. H. *et al.* (2011) 'Head-mountable high speed camera for optical neural recording', *Journal of Neuroscience Methods*, 201(2), pp. 290–295. doi: 10.1016/j.jneumeth.2011.06.024.

Parker, P. R. L. *et al.* (2022) 'Distance estimation from monocular cues in an ethological visuomotor task', *eLife*, 11. doi: 10.7554/eLife.74708.

Piyawattanametha, W. *et al.* (2009) 'In vivo brain imaging using a portable 29 g two-photon microscope based on a microelectromechanical systems scanning mirror', *Optics Letters*, 34(15), p. 2309. doi: 10.1364/ol.34.002309.

Rector, D. and Harper, R. (1991) 'Imaging of hippocampal neural activity in freely behaving animals', *Behavioural Brain Research*, 42(2), pp. 143–149. doi: 10.1016/S0166-4328(05)80005-1.

Roberts, T. F. *et al.* (2017) 'Identification of a motor-to-auditory pathway important for vocal learning', *Nature Neuroscience*, 20(7), pp. 978–986. doi: 10.1038/nn.4563.

Sawinski, J. *et al.* (2009) 'Visually evoked activity in cortical cells imaged in freely moving animals', *Proceedings of the National Academy of Sciences of the United States of America*, 106(46), pp. 19557–19562. doi: 10.1073/pnas.0903680106.

Scherrer, J. R. *et al.* (2023) 'An optical design enabling lightweight and large field-of-view head-mounted microscopes', *Nature Methods*, 20(4), pp. 546–549. doi: 10.1038/s41592-023-01806-1.

Sims, R. R. *et al.* (2023) 'Scanless two-photon voltage imaging', *Research Square*, Under revi. doi: 10.21203/RS.3.RS-2412371/V1.

Srinivasan, S. *et al.* (2019) 'Miniaturized microscope with flexible light source input for neuronal imaging and manipulation in freely behaving animals', *Biochemical and Biophysical Research Communications*, 517(3), pp. 520–524. doi: 10.1016/j.bbrc.2019.07.082.

Stamatakis, A. M. *et al.* (2018) 'Simultaneous optogenetics and cellular resolution calcium imaging during active behavior using a miniaturized microscope', *Frontiers in Neuroscience*, 12(JUL), pp. 1–16. doi: 10.3389/fnins.2018.00496.

Stibůrek, M. *et al.* (2023) '110 Mm Thin Endo-Microscope for Deep-Brain in Vivo Observations of Neuronal Connectivity, Activity and Blood Flow Dynamics', *Nature Communications*, 14(1). doi: 10.1038/s41467-023-36889-z.

Szabo, V. *et al.* (2014) 'Spatially selective holographic photoactivation and functional fluorescence imaging in freely behaving mice with a fiberscope', *Urology*, 84(6), pp. 1157–1169. doi: 10.1016/j.neuron.2014.11.005.

Tsvirkun, V. *et al.* (2019) 'Flexible lensless endoscope with a conformationally invariant multi-core fiber', *Optica*, 6(9),

p. 1185. doi: 10.1364/optica.6.001185.

Turtaev, S. *et al.* (2018) 'High-fidelity multimode fibre-based endoscopy for deep brain in vivo imaging', *Light: Science and Applications*, 7(1). doi: 10.1038/s41377-018-0094-x.

Wang, C. and Ji, N. (2013) 'Characterization and improvement of three-dimensional imaging performance of GRIN-lens-based two-photon fluorescence endomicroscopes with adaptive optics', *Optics Express*, 21(22), p. 27142. doi: 10.1364/oe.21.027142.

Wood, H. A. C. *et al.* (2019) 'High-resolution air-clad imaging fibers', *Optics InfoBase Conference Papers*, Part F168-(21), pp. 5311–5314. doi: 10.1364/BODA.2019.DW2B.4.

Zhang, J. *et al.* (2021) 'All-optical imaging and patterned stimulation at cellular resolution with a one-photon endoscope'.

Zhang, L. *et al.* (2019) 'Miniscope GRIN Lens System for Calcium Imaging of Neuronal Activity from Deep Brain Structures in Behaving Animals.', *Current protocols in neuroscience*, 86(1), p. e56. doi: 10.1002/cpns.56.

Zhao, C., Zhu, Y., *et al.* (2023) 'Millimeter field-of-view miniature two-photon microscopy for brain imaging in freely moving mice', *Optics Express*, 31(20), p. 32925. doi: 10.1364/oe.492674.

Zhao, C., Chen, S., *et al.* (2023) 'Miniature three-photon microscopy maximized for scattered fluorescence collection', *Nature Methods*, 20(4), pp. 617–622. doi: 10.1038/s41592-023-01777-3.

Ziv, Y. *et al.* (2013) 'Long-term dynamics of CA1 hippocampal place codes.', *Nature neuroscience*, 16(3), pp. 264–266. doi: 10.1038/nn.3329.

Zong, W. *et al.* (2017) 'Fast high-resolution miniature two-photon microscopy for brain imaging in freely behaving mice', *Nature Methods*, 14(7), pp. 713–719. doi: 10.1038/nmeth.4305.

Zong, W. *et al.* (2021) 'Miniature two-photon microscopy for enlarged field-of-view, multi-plane and long-term brain imaging', *Nature Methods*, 18(1), pp. 46–49. doi: 10.1038/s41592-020-01024-z.

Zong, W., Obenaus, Horst A, *et al.* (2022) 'Large-scale two-photon calcium imaging in freely moving mice', *Cell*, 185(7), pp. 1240-1256.e30. doi: 10.1016/j.cell.2022.02.017.

C. Multicolor 2P light-patterning

In this chapter, the inter-core delay dispersion (ICDD) produced in the fiber bundles, and introduced in the previous chapter, is harnessed to develop a 2P microscope capable of 3D light targeting multiple laser wavelengths simultaneously. This relatively simple system, which uses a fiber bundle and a single SLM, possesses the capability to generate multiple excitation beams while maintaining extended spots and achieving a single-cell-size axial resolution.

C.1 Introduction

C.1.1 3D generation of TF-patterns

As introduced in Chapter 1, the combination of CGH, GPC or low-NA Gaussian beams with TF enables scanless light targeting with single-cell resolution and millisecond temporal resolution. In TF-based implementations, cellular-resolution is achieved within a 2D region (Papagiakoumou *et al.*, 2008, 2010). To accomplish this, the SLM generates a 2D pattern at the first spatial focal plane, where the diffraction grating surface is placed, which also acts as the temporal focused plane. By imaging this plane onto the sample plane, both spatially and temporally focused 2D patterns are generated. To generate patterns in 3D, the SLM could, in principle, introduce a lens effect to axially displace the patterns. However, this modification only displaces the spatial focus plane, whereas the temporal focus plane, defined by the grating surface, remains fixed. Consequently, this configuration separates the spatial and the temporal focal planes at the sample plane, thereby impeding the achievement of 3D light patterns with TF axial confinement.

One viable solution involves placing the diffraction grating before the SLM, which now can generate diffraction-limited spots in 3D, without axially displacing the light into the grating plane (Sun *et al.*, 2018). In this configuration, a large Gaussian beam illuminates the diffraction grating, which, as introduced in A.4.3, disperses the spectral components (wavelengths) of the ultrashort pulse laser in one of the orthogonal directions relative to the propagation axis while maintaining beam collimation in the other direction. Since the SLM is now placed in the Fourier plane of the diffraction grating (i.e. the focal plane of a lens), this configuration results in a dispersed and focalized illumination forming a line at the SLM and, subsequently, at the objective's

back aperture, which is placed in a conjugated plane to the SLM (after 2 lenses). This enables to generate TF disks at the position defined by the diffraction-limited spots. To optimize the effect of TF and obtain the best axial resolution, the lenses placed before the objective are selected to ensure that the line perfectly fills the objective pupil in the dispersed direction. However, this strategy presents two principal limitations. First, because of the line illumination created by the diffraction grating at the SLM, only a small portion of the SLM is illuminated, thus limiting the maximum number of achievable spots due to the photodamage into the SLM when using high laser powers. Second, in this configuration, the SLM can only replicate the original Gaussian spot that illuminates the diffraction grating. Therefore, this strategy lacks flexibility in the control of the spot shape and size generated.

Several solutions exist to achieve 3D temporally focused light patterning, addressing one or both of the previous limitations. These approaches involve the incorporation of additional optical components, such as a rotating diffuser, a second SLM or a phase mask, or a galvanometric mirror (Hernandez *et al.*, 2016; Pégard *et al.*, 2017; Accanto *et al.*, 2018; Papagiakoumou, Ronzitti and Emiliani, 2020; Faini *et al.*, 2023).

A solution, known as 3D-SHOT (Pégard *et al.*, 2017), employs a lens before the diffraction grating to introduce some convergence of the Gaussian beam illuminating the diffraction grating, thus enlarging the illuminated area on the SLM. However, as explained before, this system results in two different focal planes, one for temporal focusing and one for spatial focusing, compromising the axial confinement of the patterns generated at the sample plane. To mitigate this issue, an optimized version of 3D-SHOT uses a rotating diffuser (Oldenburg, Bounds and Pegard, 2023) positioned after the diffraction grating, resulting in the entire illumination of the SLM to generate targets in 3D with an axial resolution of $\sim 20 \mu\text{m}$. However, if this configuration enlarged the spot size at the SLM, it remains incapable of easily change the spot size or shape.

In our group, a system for 3D TF-CGH has overcome both limitations previously introduced by employing two SLMs, in a configuration arranged as SLM1 + grating + SLM2 (Figure 31A) (Hernandez *et al.*, 2016), and by tiling the SLMs to encode multiple holograms, which independently controlled the lateral shape and position (SLM1) and the axial position (SLM2) of each pattern. This strategy enabled the remote axial displacement of a temporally focused shape,

as well as projecting different TF patterns at axially distinct planes. Additionally, this setup not only overcomes the limitation related to shape and size modulation but also eliminates the issue of line illumination observed on the SLM situated after the grating. Notably, the grating is no longer illuminated by a collimated beam but by a focused light pattern. In the Fourier plane of the grating, where the second SLM is placed, a wide and dispersed illumination is achieved (figure 31A). However, the need of tiling the SLMs physically limited the number of planes that could be addressed. Indeed, in this configuration, the first SLM need to be divided in a maximum of 5 lines that displayed 5 different holograms to efficiently control the shape and the lateral position of the spots. This forced the second SLM to be divided also in 5 lines, each of them controlling the axial position of the spots generated with the first SLM. This strategy limited the number of planes that can be simultaneously targeted to only 5 axial planes. Moreover, this approach has the advantage of enabling multiple shapes but it is hardly compatible with other beam shaping techniques such as GPC or low-NA Gaussian beams, requiring a complicated alignment between the two SLMs and several calibration procedures before using the system.

An alternative configuration of 3D TF-CGH, called MTF-LS (multiplexed temporally focused light-shaping), used two SLMs or a SLM and a phase mask, in combination with a diffraction grating to multiplex the spots at any position within a volume (figure 31A) (Accanto *et al.*, 2018; Papagiakoumou, Ronzitti and Emiliani, 2020). The first SLM (or phase mask) controls the size and shape(s) of the illumination and focuses it onto the grating plane. The second SLM is placed at the Fourier plane of the grating and multiplexes the original spot in 3D while preserving the TF effect. The main difference is that in here the first SLM only controlled the shape of the spots while the second one controlled, not only the axial position, but also the lateral one, which prevented the SLM to be tiled in different holograms. This system was also combined with GPC and showed the possibility to create tens of holographic spots, of 15 μm in diameter, with an average axial resolution of 11 μm in a 3D FOV of 300 μm \times 300 μm \times 500 μm (Accanto *et al.*, 2018).

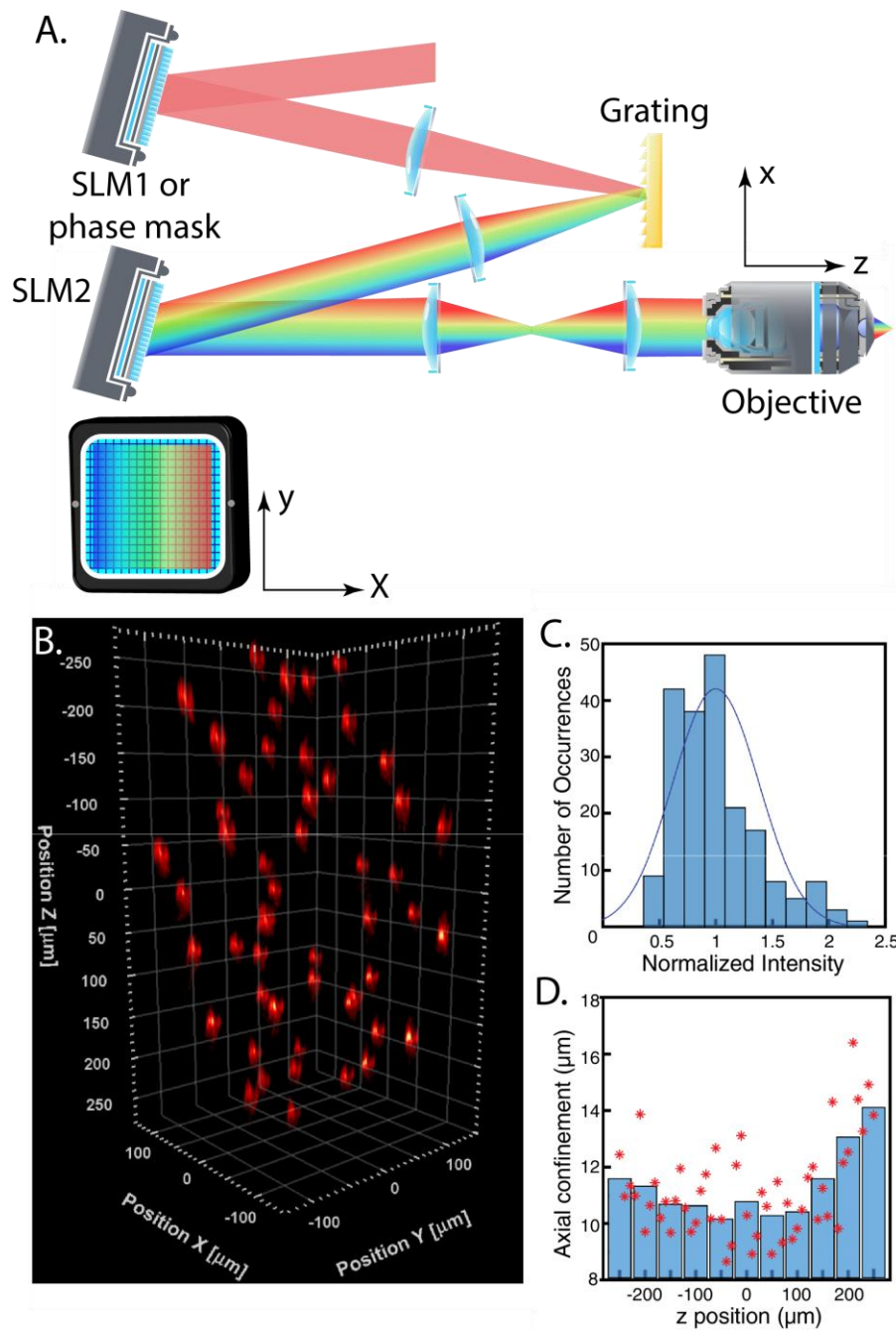


Figure 31. Experimental setup and results of 3D-CGH. **A.** A first SLM (SLM1) or a static phase mask performed the appropriate phase modulation for generating the desired 2D pattern that was then focused on the grating for TF. The first diffraction order was directed to the second SLM (SLM2), which created the predefined 3D distribution of diffraction-limited spots at the sample positions, thereby replicating the 2D pattern generated by SLM1. **B.** 2P excitation fluorescence volume representation of 50 holographic circular spots of 15 μm diameter in a volume of 300 μm × 300 μm × 500 μm. **C.** Histogram of the maximal 2P excitation fluorescence intensity for each spot, normalized to the average intensity of all spots. **D.** Axial confinement, calculated as the FWHM of the axial intensity profile of each spot, as a function of the z position. Red stars represent

the individual measurements for each spot and blue bars show the mean values in a range of 50 μm around the designated z position. The mean value across the whole FOE was $11.1 \pm 1.8 \mu\text{m}$ FWHM. Adapted from (Accanto *et al.*, 2018).

Notably, all these strategies are limited by the SLM refreshing rate to generate multiple light patterns in the millisecond timescale. To overcome this limitation, a novel strategy used the focalized line illumination introduced by the grating into the SLM, when a collimated Gaussian beam illuminates the grating, together with the incorporation of a galvanometric mirror placed in a conjugate plane before the grating (figure 32). The galvanometric mirror is used to rapidly scan the illumination line in one direction across the SLM, enabling the generation of multiple tiled holograms aligned with the scanned illumination line, thus allowing for ultrafast sequential 3D light targeting (FLiT system, Faini *et al.*, 2023). The use of a fast switching element to rapidly scan multiple holograms is used to demonstrate new illumination protocols for optogenetics multi-target stimulation. Two illumination protocols, named hybrid and cyclic illumination, are introduced. Briefly, hybrid illumination consists in controlling the spiking time of two group of cells with a temporal delay ($\sim 100 \mu\text{s}$) shorter than the necessary illumination dwell time, by using three holograms. The first hologram to excite the first group of cells, the third hologram to excite second group of cells and second one to excite both groups. By sequentially illuminating the three holograms it is then possible to sequentially stimulate the two groups of cells with tightly controlled delays, limited by the galvo-mirror switching time only. The cyclic illumination uses the off-time of a photostimulation cycle of illumination pulses to sequentially illuminate other holograms that illuminate other group of cells, so that during the off-time the illumination photostimulate other neurons. This strategy enabled multi-target stimulation with a reduction of laser-induced thermal effects compared to conventional holographic systems, and the increase on the achievable targets.

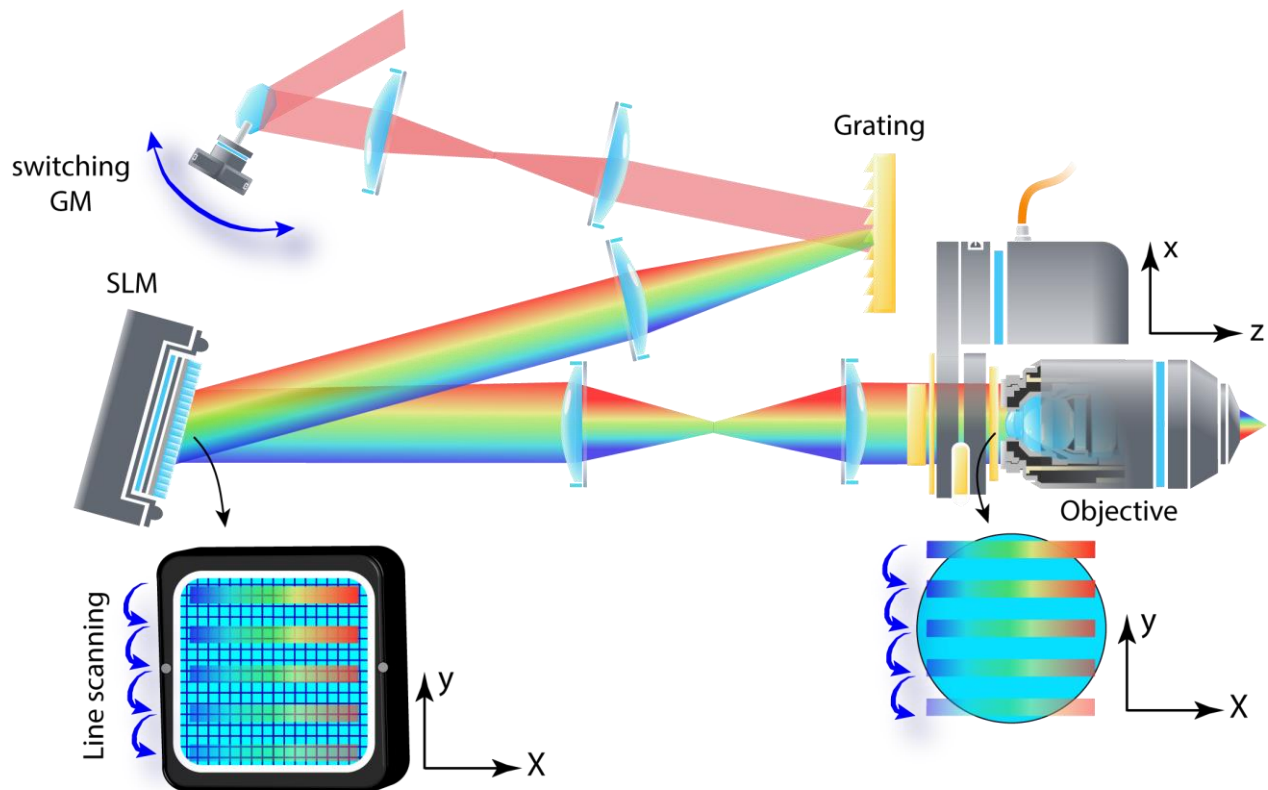


Figure 32. Optical setup of FLiT system. A pulsed collimated beam (red line) is reflected by a galvanometric mirror (GM) onto a diffracting grating via a 4f-telescope. Diffracted off the grating, the beam is projected onto a SLM by a lens in the form of a horizontal (i.e., orthogonal to the orientation of the grating lines) spatially chirped strip of light. The SLM is projected onto the objective's back aperture via a telescope so that the phase modulation on the SLM allows multiplexing the initial beam and generating a multi-site temporally focused pattern of light in the sample. As deflection of the beam by the GM results into a translation of the illuminated bands on the SLM (multicolor lines), addressing the SLM with independent tiled holograms can lead to fast switch of different groups of light patterns into the sample (Adapted from Faini *et al.*, 2023).

All the systems presented here required a minimum of two optical elements to be coupled with the SLM to create multiple TF targets in a 3D, which introduces a certain level of complexity and cost. Additionally, as better explained in the following section, because of the use of the diffraction grating, none of these systems are easily compatible with the use of multiple laser wavelengths at the same time.

C.1.2 TF with multicolor illumination

Using a diffraction grating for TF presents significant challenges when working with multiple lasers at different wavelengths or tunable wavelength lasers. This can be crucial for

experiments that require dual-color scanless imaging and photostimulation (Forli *et al.*, 2018; Shymkiv and Yuste, 2023), bidirectional control of neuronal activity through dual-color activation and inhibition of the same or different cells (Erbguth *et al.*, 2012; Forli *et al.*, 2018; Vierock *et al.*, 2021), or single-color scanless illumination with a tunable laser (Demas *et al.*, 2021).

The use of a diffraction grating (groove density = Λ) for TF relies on the spatial dispersion of the spectral components (wavelengths) of an ultrashort pulse laser beam at different angles (θ). These angles can be calculated as: $\theta = \text{asin}(\lambda / \Lambda - \sin(\theta_i))$, where θ_i is the incident angle to the diffraction grating (Tal, Oron and Silberberg, 2005; Zhu *et al.*, 2005) (figure 33A-B). If we consider typical parameters for an ultrafast laser pulse (central wavelength 900 nm, pulse duration 150 fs), the spectral bandwidth of the laser gives a FWHM of ~ 15 nm. As mentioned earlier, the dispersion of the grating and the lens placed after it is chosen such that, in the Fourier plane of the grating, a dispersed line is generated, filling the objective pupil into the direction of the grating dispersion (figure 33B, $\lambda = 900$ nm). However, if two different lasers with very distinct central wavelengths are used simultaneously, the angles introduced by the grating will be too large, so that only one of the two lasers can effectively hit the objective pupil for the same optical alignment. For instance, commonly used diffraction gratings (600-800 mm/line) reflect the incident beam at around 1° of difference for 15 nm of laser spectrum, which correspond to 18 mm of lateral shift at the objective's back aperture for a lens of 1000mm (as simulated in figure 33C). Conversely, the grating creates an $\sim 8^\circ$ difference between a wavelength of 800 nm and 900 nm. The very divergent reflected angles introduced into the optical path lead to the focalization of spots at very different position (140 mm lateral shift for commonly used lens of 1000 mm) (figure 33B-C). Consequently, these misaligned spots fail to enter into the remaining optical path and the objective's back aperture.

To compensate for this wavelength-dependent effect and realign the different laser central wavelengths to the same location, the introduction of a switching element mirror has been proposed (figure 33D) (Lien *et al.*, 2017, 2017; Cheng *et al.*, 2020). This mirror, placed before the diffraction grating, enables fast adjustments of the incidence or reflected angles for each laser wavelength as they interact with the diffraction grating, ensuring that the reflected angle remains constant for all the laser central wavelengths. Consequently, the line dispersion introduced by the grating continues to illuminate the same region of the objective's back aperture, irrespective of any modification to the laser central wavelength. Although dual-color 2P excitation with TF was used to image

specimens labeled with different fluorophores, the experimental system always needs a switching element (such as galvanometric mirrors) to compensate for the different grating reflected angles, increasing the system's complexity. Moreover, this compensation is limited to a narrow range of excitation wavelengths, and the use of two lasers with very different wavelengths would introduce large incident or reflected angles in the compensation system, which would introduce optical aberrations. Additionally, the coupling of such strategy with 3D-CGH systems using 2 SLMs and a diffraction grating, would complexify the system even more.

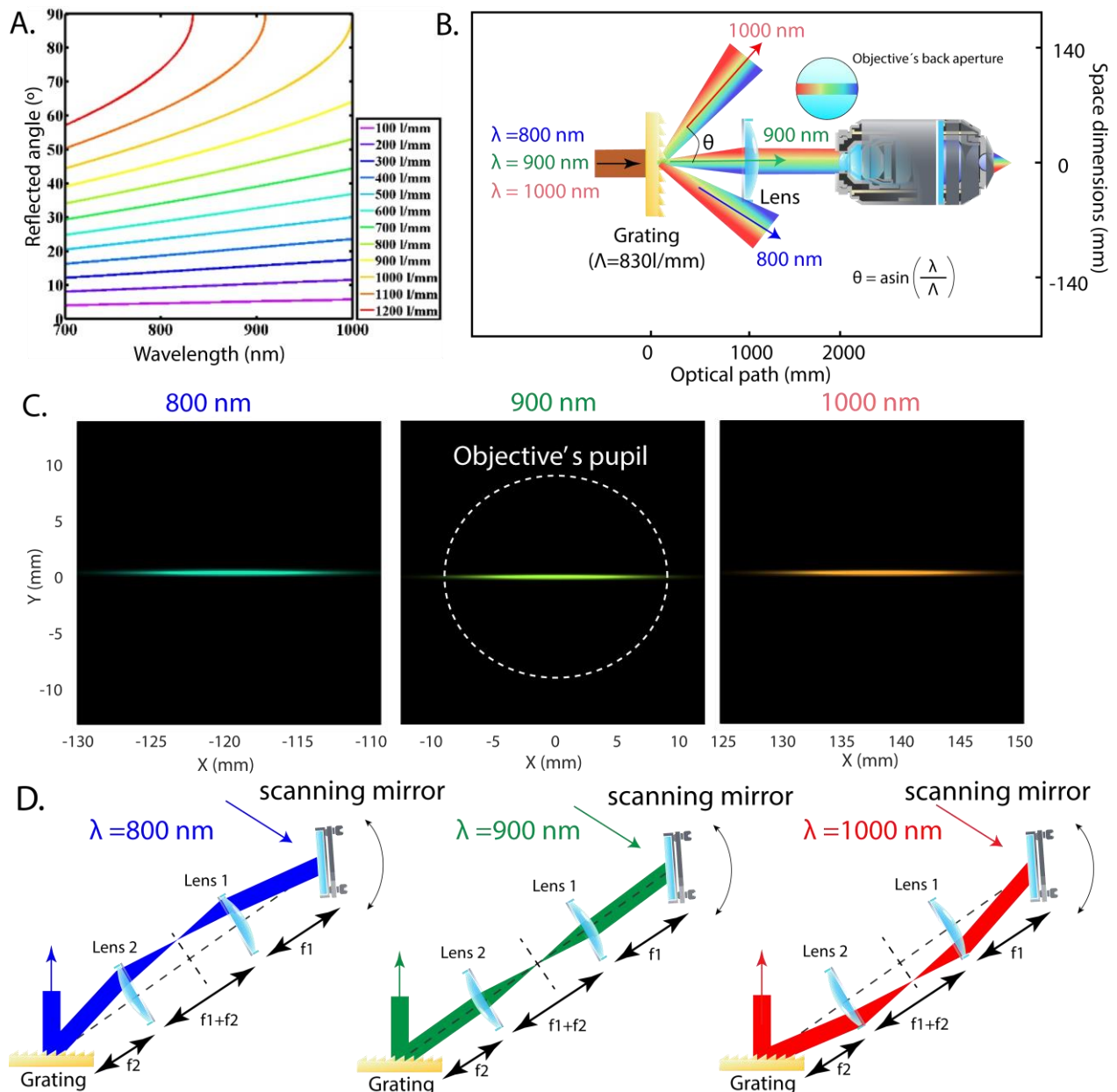


Figure 33. Wavelength dependence of a diffraction grating. **A.** Simulated reflected angles of the excitation light from a diffraction grating with an incident illumination of 0° , as a function of the excitation wavelength for different groove densities (lines/mm) of gratings. (Adapted from Lien *et al.*, 2017, 2019) **B.** Schematic illustrating the simulated light propagation path for the excitation wavelengths of 800, 900 and 1000 nm when using a diffraction grating (groove density of 830 lines/mm) and a lens ($f = 1000$ mm), which laterally shifts the beam 140 mm between 900 and 1000 nm. **C.** Simulation of the beam propagation at the objective's back focal plane for different wavelengths. The beam at 900 nm is simulated to fill the objective's back aperture using a lens of 1000 mm (objective's pupil = 18 mm). The beams at 800 nm and 1000 nm arrive at the objective's back focal plane at shifted position (-120 mm and 138 mm respectively). **D.** Schematics of an optical configuration for excitation wavelength switching at wavelengths of 800, 900, and 1000 nm, respectively. The gray dashed line denotes the optical axis of the beam expander assembled by the lenses (Adapted from Lien *et al.*, 2017, 2019).

C.1.3 Fiber bundles with multicolor illumination

To overcome some of the limitations described in the previous sections and enable multicolor 3D light targeting, we have proposed to replace the grating for TF with a fiber bundle. The system consists in a fiber bundle that is illuminated with beams from lasers operating at different wavelengths. After the fiber bundle and a lens, the SLM is illuminated, and its conjugated image is projected onto the objective's back aperture with two lenses. This configuration, which closely resembles the simplest TF configuration for 3D light patterning using a diffraction grating and a SLM, enables to perform multicolor 3D light targeting. Before presenting the corresponding publication (Lorca-Cámara *et al.*, 2024), I will present optical simulations for comparison with the TF-based systems. Similar to the previous configuration, I consider a laser beam entering the fiber bundle, composed of multiple cores with a size of $4 \mu\text{m}$ and inter-core distance of $4.5 \mu\text{m}$, one lens after the bundle and a microscope objective in the Fourier plane of the bundle. In this simplification, the SLM is not considered so that we can look at what happens right after the fiber bundle. Because fiber bundles diffract the light beam in all the orthogonal directions relative to the beam's propagation, the first effect of this configuration is that, the entire objective's back aperture is fully illuminated without the need for additional active optical elements (figure 34A). Additionally, since each core of the bundle imprints a different phase to the beam travelling through it (Andresen *et al.*, 2013, 2015), this configuration results in a random phase distribution of the beam at the bundle's output. As seen in the simulations in figure 34B, in this condition, the intensity of the 0th order of the diffracted light is maximized and propagated to the objective's back aperture for all the wavelengths simulated. This configuration renders the fiber bundle insensitive to the incident

laser wavelengths (figure 34B). As the propagation angle of the 0th order at the output of the fiber bundle remains constant, regardless of the excitation wavelength, it becomes suitable for multicolor 3D light targeting using a single beam path, after the fiber bundle exit, and reducing the system complexity. The 0th order of the diffracted light cannot be effectively utilized with a diffraction grating because the spectral components are not dispersed in this diffracted order, rendering the TF effect inapplicable. However, the 0th order can be harnessed when using a fiber bundle, thanks to the ICDD effect, which provides temporal demultiplexing of the excitation light even in its 0th order.

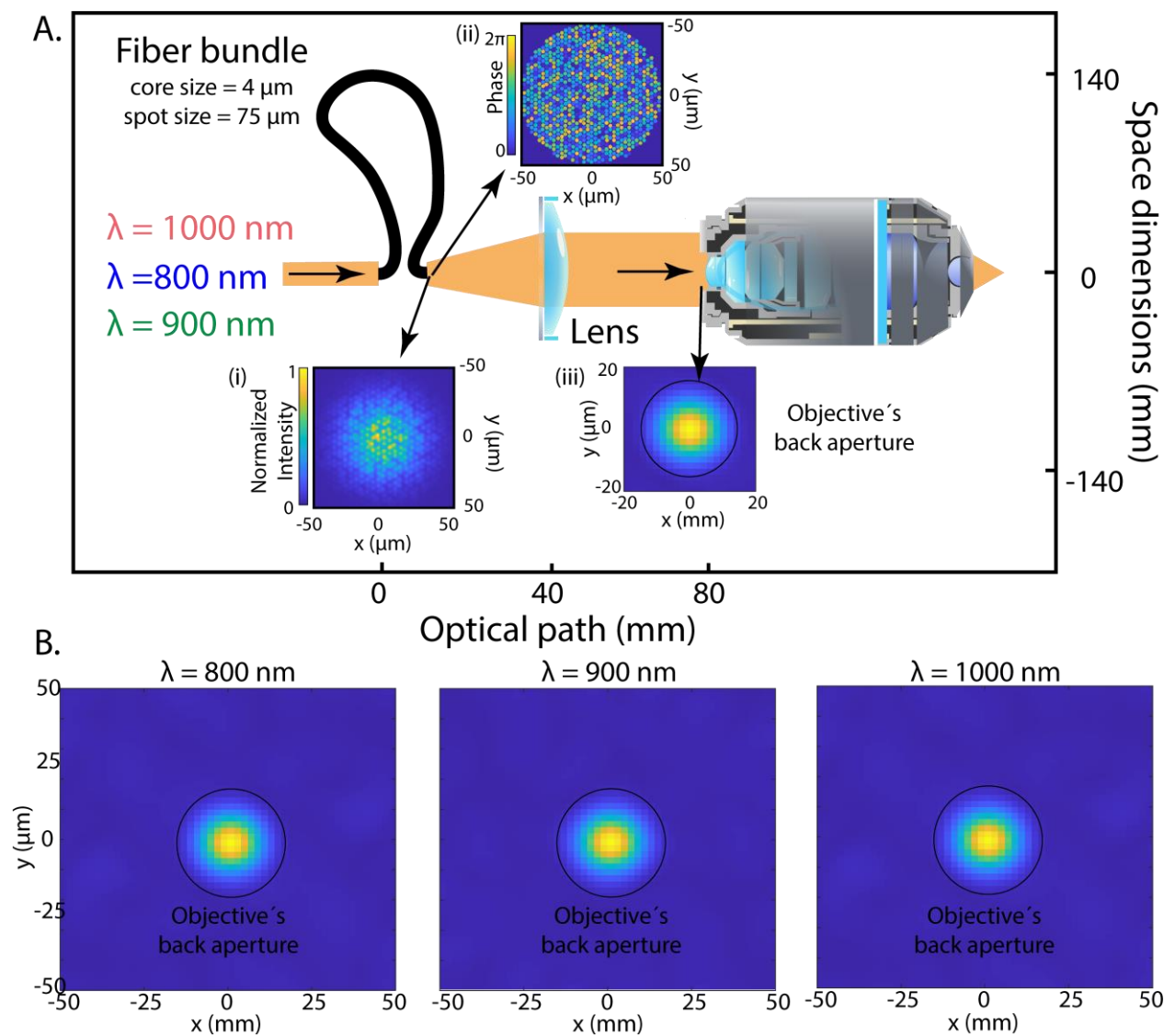


Figure 34. Simulation of beam propagation through a fiber bundle (core diameter = 4 μm). **A.** Simulation of a Gaussian beam (75 μm diameter) illuminating a fiber bundle. (i) The beam initially

illuminates the fiber bundle introduces. (ii) The fiber bundle introduces, on each core, a random phase $[0-2\pi]$. (iii) The beam is then propagated with a lens ($f = 40$ mm) to fill the objective's back aperture to fully illuminates the pupil of the objective. **B.** Different wavelengths, at 800, 900 and 1000 nm are simulated and propagated to the objective's back aperture. In this case, the system is wavelength-independent and the beam arrives at the same position at the objective's back aperture.

The results shown in figure 34 for different wavelengths are directly related to the randomness of the phase, a consequence of the independent propagation through different cores. However, it is worth noting wavefront shaping methods exist that use a SLM to compensate for the phase difference and rephase all the cores at the fiber output (Andresen *et al.*, 2015, 2016; Gajendra Kumar *et al.*, 2023). These methods can force the outgoing beam to be focused at the desired position (and not just on the 0th order) after the fiber bundle. In this case, however, as the rephasing effect is highly dependent on the wavelength, different propagation results and different beam focus positions would be obtained for different laser wavelengths.

In the next section (C.2), I will show how we take advantage of the wavelength independence of the propagation, the full illumination of the SLM, and the ICDD in the fiber bundle to create extended excitation spots at different wavelengths while maintaining micrometer axial resolution, without the addition of other optical components.

C.2 Multicolor 2P light-patterning microscope using a fiber bundle

In this project, my contribution involved the design, the set-up, the full characterization and the optimization of the optical system. Our work demonstrated that the system presents an advantageous strategy to perform multicolor 3D light patterning with a single beam path, although it is limited to the use of low-power lasers, as discussed in the corresponding publication.

C.2.1 Paper

A multicolor two-photon light-patterning microscope exploiting the spatio-temporal properties of a fiber bundle

ANTONIO LORCA-CÁMARA¹, CHRISTOPHE TOURAIN¹, VINCENT DE SARS¹, VALENTINA EMILIANI^{1,2}, NICOLÒ ACCANTO^{1,3}

¹ Sorbonne Université, INSERM, CNRS, Institut de la Vision, 75012 Paris, France.

² valentina.emiliani@inserm.fr

³ nicolo.accanto@inserm.fr

Abstract: The development of efficient genetically encoded indicators and actuators has opened up the possibility of reading and manipulating neuronal activity in living tissues. To achieve precise and reconfigurable targeting of large numbers of neurons with single-cell resolution within arbitrary volume, different groups have recently developed all-optical strategies based on two-photon excitation and spatio-temporal shaping of ultrashort laser pulses. However, such techniques are often complex to set up and typically operate at a single wavelength only. To address these issues, we have developed a novel optical approach that uses a fiber bundle and a spatial light modulator to achieve simple and dual-color two-photon light patterning in three dimensions. By leveraging the core-to-core temporal delay and the wavelength-independent divergence characteristics of fiber bundles, we have demonstrated the capacity to generate high-resolution excitation spots in a 3D region with two distinct laser wavelengths simultaneously, offering a suitable and simple alternative for precise multicolor cell targeting.

© 2022 Optica Publishing Group under the terms of the [Optica Publishing Group Open Access Publishing Agreement](#)

References

1. Boyden, E. S., Zhang, F., Bamberg, E., Nagel, G. & Deisseroth, K. Millisecond-timescale, genetically targeted optical control of neural activity. *Nat. Neurosci.* **8**, 1263–1268 (2005).
2. Fenno L, Yizhar O, D. K. The Development and Application of Optogenetics. *Annu Rev Neurosci.* **34**, 389–412 (2011).
3. Deisseroth, K. Optogenetics: 10 years of microbial opsins in neuroscience. *Nat. Neurosci.* **18**, 1213–1225 (2015).
4. Emiliani, V. *et al.* Optogenetics for light control of biological systems. *Nat. Rev. methods Prim.* **2**, 55 (2022).
5. Svoboda, K. & Yasuda, R. Principles of two-photon excitation microscopy and its applications to neuroscience. *Neuron* **50**, 823–39 (2006).
6. Helmchen, F. & Denk, W. Deep tissue two-photon microscopy. *Nature Methods* vol. 2 932–940 (2005).
7. Conti, R., Assayag, O., de Sars, V., Guillon, M. & Emiliani, V. Computer Generated Holography with Intensity-Graded Patterns. *Front. Cell. Neurosci.* **10**, 236 (2016).
8. Bañas, A. & Glückstad, J. Holo-GPC: Holographic Generalized Phase Contrast. *Opt. Commun.* **392**, 190–195 (2017).
9. Adesnik, H. & Abdeladim, L. Probing neural codes with two-photon holographic optogenetics. *Nat. Neurosci.* **24**, 1356–1366 (2021).
10. Chen, I. W., Papagiakoumou, E. & Emiliani, V. Towards circuit optogenetics. *Current Opinion in Neurobiology* vol. 50 179–189 (2018).
11. Marshel, J. H. *et al.* Cortical layer-specific critical dynamics triggering perception. *Science (80-.)*. **365**, 1–23 (2019).
12. Zhang, Z., Russell, L. E., Packer, A. M., Gauld, O. M. & Häusser, M. Closed-loop all-optical interrogation of neural circuits in vivo. *Nat. Methods* **15**, 1037–1040 (2018).
13. Gill, J. V. *et al.* Precise Holographic Manipulation of Olfactory Circuits Reveals Coding Features Determining Perceptual Detection. *Neuron* **108**, 382–393.e5 (2020).
14. Carrillo-Reid, L., Han, S., Yang, W., Akrouh, A. & Yuste, R. Controlling Visually Guided Behavior by Holographic Recalling of Cortical Ensembles. *Cell* **178**, 447–457.e5 (2019).
15. Bollmann, Y. *et al.* On the prominent influence of single interneurons in the developing barrel cortex in vivo. *Nat. Neurosci.* **26**, 1–45 (2023).
16. Chen, I.-W. *et al.* High-throughput in vivo synaptic connectivity mapping of neuronal micro-circuits using two-photon holographic optogenetics and compressive sensing. *bioRxiv* 2023.09.11.557026 (2023).
17. Printz, Y. *et al.* Determinants of functional synaptic connectivity among amygdala-projecting prefrontal cortical neurons in male mice. *Nat. Commun.* **14**, (2023).
18. McRaven, C. *et al.* High-throughput cellular-resolution synaptic connectivity mapping in vivo with concurrent two-photon optogenetics and volumetric Ca²⁺ imaging. *bioRxiv* 2020.02.21.959650 (2020).
19. Hage, T. A. *et al.* Synaptic connectivity to L2/3 of primary visual cortex measured by two-photon optogenetic stimulation. *Elife* **11**, 1–46 (2022).
20. Two-photon excitation of channelrhodopsin-2 at saturation.pdf.
21. Ronzitti, E. *et al.* Recent advances in patterned photostimulation for optogenetics. *Journal of Optics (United Kingdom)* vol. 19 (2017).
22. Zhu, G., van Howe, J., Durst, M., Zipfel, W. & Xu, C. Simultaneous spatial and temporal focusing of femtosecond pulses. *Opt. Express* **13**, 2153–2159 (2005).
23. Tal, E., Oron, D. & Silberberg, Y. Improved depth resolution in video-rate line-scanning multiphoton microscopy using temporal focusing. *Opt. Lett.* **30**, 1686 (2005).
24. Oron, D., Tal, E. & Silberberg, Y. Scanningless depth-resolved microscopy. *Opt. Express* **13**, 1468 (2005).

25. Papagiakoumou, E. *et al.* Scanless two-photon excitation of channelrhodopsin-2. *Nat. Methods* **7**, 848–854 (2010).
26. Papagiakoumou, E., de Sars, V., Oron, D. & Emiliani, V. Patterned two-photon illumination by spatiotemporal shaping of ultrashort pulses. *Opt. Express* **16**, 22039 (2008).
27. Hernandez, O. *et al.* Three-dimensional spatiotemporal focusing of holographic patterns. *Nat. Commun.* **7**, (2016).
28. Accanto, N. *et al.* Multiplexed temporally focused light shaping for high-resolution multi-cell targeting. *Optica* **5**, 1478 (2018).
29. Papagiakoumou, E., Ronzitti, E. & Emiliani, V. Scanless two-photon excitation with temporal focusing. *Nat. Methods* **17**, 571–581 (2020).
30. Pégard, N. C. *et al.* Three-dimensional scanless holographic optogenetics with temporal focusing (3D-SHOT). *Nat. Commun.* **8**, 1228 (2017).
31. Mardinly, A. R. *et al.* Precise multimodal optical control of neural ensemble activity. *Nat. Neurosci.* **21**, 881–893 (2018).
32. Faini, G. *et al.* Ultrafast light targeting for high-throughput precise control of neuronal networks. *Nat. Commun.* **14**, 1888 (2023).
33. Moretti, C., Antonini, A., Bovetti, S., Liberale, C. & Fellin, T. Scanless functional imaging of hippocampal networks using patterned two-photon illumination through GRIN lenses. *Biomed. Opt. Express* **7**, 3958 (2016).
34. Bovetti, S. *et al.* Simultaneous high-speed imaging and optogenetic inhibition in the intact mouse brain. *Sci. Rep.* **7**, 1–17 (2017).
35. Sims, R. R. *et al.* Scanless two-photon voltage imaging. *Res. Sq. Under rev.*, (2023).
36. Prevedel, R. *et al.* Fast volumetric calcium imaging across multiple cortical layers using sculpted light. *Nat. Methods* **13**, 1021–1028 (2016).
37. Forli, A. *et al.* Two-Photon Bidirectional Control and Imaging of Neuronal Excitability with High Spatial Resolution In Vivo. *Cell Rep.* **22**, (2018).
38. Shymkiv, Y. & Yuste, R. Aberration-free holographic microscope for simultaneous imaging and stimulation of neuronal populations. *Opt. Express* **31**, 33461–33474 (2023).
39. Vierock, J. *et al.* BiPOLES is an optogenetic tool developed for bidirectional dual-color control of neurons. *Nat. Commun.* **12**, 1–20 (2021).
40. Erbguth, K., Prigge, M., Schneider, F., Hegemann, P. & Gottschalk, A. Bimodal Activation of Different Neuron Classes with the Spectrally Red-Shifted Channelrhodopsin Chimera C1V1 in *Caenorhabditis elegans*. *PLoS One* **7**, (2012).
41. Lien, C.-H., Abrigo, G., Chen, P.-H. & Chien, F.-C. Two-color temporal focusing multiphoton excitation imaging with tunable-wavelength excitation. *J. Biomed. Opt.* **22**, 026008 (2017).
42. Cheng, Y. M., Lien, C. H., Ke, J. H. & Chien, F. C. An excitation wavelength switching to enhance dual-color wide-field temporal-focusing multiphoton excitation fluorescence imaging. *J. Phys. D: Appl. Phys.* **53**, (2020).
43. Accanto, N. *et al.* A flexible two-photon fiberscope for fast activity imaging and precise optogenetic photostimulation of neurons in freely moving mice. *Neuron* **111**, 176–189.e6 (2023).
44. Golan, L., Reutsky, I., Farah, N. & Shoham, S. Design and characteristics of holographic neural photo-stimulation systems. *J. Neural Eng.* **6**, (2009).
45. Gerchberg, R. W. and S. W. O. A Practical Algorithm for the Determination of Phase from Image and Diffraction Plane Pictures. *Optik (Stuttg.)* **35**, 237–246 (1971).
46. Lee, J. & Kim, D. Large-scale 3D fast Fourier transform computation on a GPU. *ETRI J.* 1–11 (2023) doi:<https://doi.org/10.4218/etrij.2022-0297>.
47. Chen, S. & Li, X. A hybrid GPU/CPU FFT library for large FFT problems. in *2013 IEEE 32nd International Performance Computing and Communications Conference (IPCCC)* 1–10 (2013). doi:10.1109/PCCC.2013.6742796.
48. Andresen, E. R. *et al.* Measurement and compensation of residual group delay in a multi-core fiber for lensless endoscopy. *J. Opt. Soc. Am. B* **32**, 1221 (2015).
49. Myaing, M. T., Urayama, J., Braun, A. & Norris, T. B. Nonlinear propagation of negatively chirped pulses: maximizing the intensity at the output of a fiber probe. *Opt. Express* **7**, 210–214 (2000).
50. Bao, H., Allen, J., Pattie, R., Vance, R. & Gu, M. Fast handheld two-photon fluorescence microendoscope with a 475 microm x 475 microm field of view for in vivo imaging. *Opt. Lett.* **33**, 1333–1335 (2008).
51. Oberthaler, M. & Höpfel, R. A. Special narrowing of ultrashort laser pulses by self-phase modulation in optical fibers. *Appl. Phys. Lett.* **63**, 1017–1019 (1993).
52. Helmchen, F., Tank, D. W. & Denk, W. Enhanced two-photon excitation through optical fiber by single-mode propagation in a large core. *Appl. Opt.* **41**, 2930 (2002).
53. Backlund, M. P. *et al.* Simultaneous, accurate measurement of the 3D position and orientation of single molecules. *Proc. Natl. Acad. Sci. U. S. A.* **109**, 19087–19092 (2012).
54. Ren, J. & Han, K. Y. 2.5D microscopy with polarization independent SLM for enhanced detection efficiency and aberration correction. *Opt. Express* **29**, 27530 (2021).
55. Garofalakis, A. *et al.* Characterization of a multicore fiber image guide for nonlinear endoscopic imaging using two-photon fluorescence and second-harmonic generation. *J. Biomed. Opt.* **24**, 1 (2019).
56. Ozbay, B. N. *et al.* Three dimensional two-photon brain imaging in freely moving mice using a miniature fiber coupled microscope with active axial-scanning. *Sci. Rep.* **8**, 1–14 (2018).
57. Myaing, M. T., MacDonald, D. J. & Li, X. Fiber-optic scanning two-photon fluorescence endoscope. *Opt. Lett.* **31**, 1076 (2006).
58. Li, A. *et al.* Twist-free ultralight two-photon fiberscope enabling neuroimaging on freely rotating/walking mice. *Optica* **8**, 870 (2021).
59. Zhang, Y. *et al.* Fast and sensitive GCaMP calcium indicators for imaging neural populations. *Nature* vol. 615 (Springer US, 2023).
60. Sridharan, S. *et al.* High-performance microbial opsins for spatially and temporally precise perturbations of large neuronal networks. *Neuron* **110**, 1139–1155.e6 (2022).
61. Packer, A. M., Russell, L. E., Dalglish, H. W. P. & Häusser, M. Simultaneous all-optical manipulation and recording of neural circuit activity with cellular resolution in vivo. *Nat. Methods* **12**, 140–146 (2015).
62. Kalashyan, M. *et al.* Ultrashort pulse fiber delivery with optimized dispersion control by reflection gratings at 800 nm. *Opt. Express* **20**, 25624–25635 (2012).
63. Vierock, J. *et al.* WiChR, a highly potassium-selective channelrhodopsin for low-light one- and two-photon inhibition of excitable cells. *Sci. Adv.* **8**, 1–18 (2022).

1. Introduction

In recent years, the field of neuroscience has been revolutionized by optogenetics, which enables to induce or inhibit neuronal activity in specific populations of neurons by using light¹⁻⁴. To gain a deeper understanding of how spatial and temporal patterns of neuronal activity in the brain influence perception and behavior, advanced optical techniques are required to control the activity of groups of neurons with single-cell resolution and in a reconfigurable manner. In pursuit of this goal, researchers have developed optical systems that combine two-photon excitation (2PE)^{5,6}, which increases optical sectioning and penetration depth through scattering media, with computer-generated holography (CGH)⁷ or generalized phase contrast (GPC)⁸ utilizing spatial light modulators (SLMs) to precisely and dynamically target single or groups of neurons in large volumes^{9,10}. Pioneering experiments using similar methods have started to show that precise optogenetics photostimulation of selected neurons in the mouse brain can influence the animal behavior and affect perception¹¹⁻¹⁴ or influence neuronal population dynamics¹⁵. Sequential optogenetic activation of one or few cells at cellular resolution also enabled in vitro and in vivo high throughput connectivity mapping¹⁶⁻¹⁹.

In general, to efficiently photostimulate groups of neurons with 2PE, a SLM is used to multiplex the excitation onto different targets, in combination with spiral scanning²⁰ or to generate large excitation spots²¹ to cover the whole soma of a neuron. In the latter case, to overcome the loss of axial resolution that a laterally extended excitation spot would cause, lateral light shaping is combined with the temporal focusing (TF²²⁻²⁴) technique. TF is based on a diffraction grating that decomposes the spectral wavelengths of an ultrashort laser pulse, thus increasing the pulse duration and preventing 2PE until all the colors are recombined at the sample plane^{22,23}. Most implementations that combine CGH or GPC and TF can only achieve 2P photostimulation with cellular resolution and high temporal precision within a 2D region^{25,26}, which corresponds to the image plane of the diffraction grating. To extend experiments to a 3D volume, additional optical elements are generally required beyond the diffraction grating and a single SLM. For instance, a second SLM to displace laterally and axially the temporally focused shape generated by the first SLM (or a fixed phase mask) on the TF grating²⁷⁻²⁹. Alternative approaches for the generation of 3D temporally focused patterns used a large Gaussian beam³⁰ and, in its revised form, a rotating diffuser between the diffraction grating and the multiplexing SLM³¹, or a galvanometric mirror, placed before the SLM, to sequentially scan vertically aligned holograms for ultrafast sequential light targeting³².

Besides the use for optogenetics, temporal focused multitarget illumination has been also used for multitarget functional imaging using genetically encoded calcium^{33,34} or voltage indicators³⁵, or for fast scanning volumetric calcium imaging with temporally focused spots³⁶.

One of the significant challenges arising from the use of the diffraction grating for TF occurs when attempting to tune the incident wavelength or coupling multiple colors, which is important in experiments that require, for instance, dual-color scanless imaging and photostimulation^{34,37,38}, bidirectional control of neuronal activity through dual-color activation and inhibition of the same or different cells^{37,39,40} or single color scanless (or TF scanned) illumination^{33,36}.

Because TF is based on the spatial dispersion of the different wavelengths of the laser beam at different angles²³, laser beams with different central wavelengths would be diffracted at different angles. This requires to readjust the angle between the incident or the reflected beam and the grating to maintain a constant deflection for the different wavelengths. Although dual-color 2PE with TF was used to image specimens labeled with different fluorophores^{41,42}, the experimental system always needed a switching element (such as galvanometric mirrors) to compensate for the different grating angles, increasing the system's complexity. Moreover, this compensation is limited to a narrow range of excitation wavelengths.

In this study, we present a novel optical configuration for the generation of single and multicolor 2D and 3D light patterns, where the diffraction grating for TF is replaced by a multi-core optical fiber bundle. This system capitalizes on the core-to-core delay dispersion inherent to the fiber bundle, a concept previously detailed in Ref⁴³, allowing us to maintain micrometer-level axial resolution independently of the resultant spot size. Our results demonstrate that this approach simplifies the optical setup, obviating the necessity of two SLMs for 3D light patterning, or of a rotating diffuser. Furthermore, we demonstrate that substituting the diffraction grating with a fiber bundle preserves the propagation angle after exiting the fiber bundle, irrespective of the excitation wavelength. Consequently, this innovation enables the generation of 2D and 3D multicolor light patterns using a single beam path.

2. Materials and Methods

2.1 Optical setup

The optical setup (Fig. 1a) uses two different laser sources: 1) a low repetition rate laser (Goji, Amplitude, central wavelength of 1030 nm, pulse duration of 150 fs, total power of 4 W, repetition rate of 10 MHz) and 2) a high repetition rate laser (Spark Alcor, central wavelength of 920 nm, pulse duration of 120 fs, total power of 4 W, repetition rate of 80 MHz) whose output powers are controlled by a lambda-half waveplate and a polarizer. The beam coming from each laser, after being combined with a dichroic mirror, is focalized with a short focal length lens ($f_0 = 18$ mm) in the same region of the fiber bundle (Fujikura model FIGH-15-600N, inter-core distance ~ 4.5 μm , length of 2 meters, diameter of 550 μm), illuminating the same number of cores. The spot size that illuminates the fiber bundle, and thus the spots size at the sample plane, are modified by moving the lens (f_0) placed before the fiber bundle with a translational stage that adjusts the distance between f_0 and the fiber bundle and thus the defocus (Fig. 1b).

To compensate for the dispersion of the fiber bundle and additional optical elements, we adjust the pulse compressors inside the lasers with an internal dispersion control (around -90000 fs^2)⁴³. At the fiber bundle output, the beam is collimated with an aspheric lens of $\text{NA} = 0.5$ ($f_1 = 8$ mm, A240-B, Thorlabs). After that, a telescope magnifies the laser beams by a factor of 4 ($f_2 = 150$ mm and $f_3 = 600$ mm) to fill the screen of the SLM (LCOS-SLM X13138-03, Hamamatsu Photonics, resolution 1272×1024 pixels, 12.5 μm pixel size). The SLM is illuminated with an angle of 10 degrees to ensure proper performance. We experimentally verified that, with the beam divergence at the fiber bundle output and the lenses used, the beam at the SLM had a diameter, D , of 12.5 mm, matching the short side of the SLM screen. This value enables deriving the NA of the fiber bundle as $\text{NA}_{\text{fiber}} = \frac{D/2}{f_{eq}} = \frac{12.5/2}{32} = 0.2$, where $f_{eq} =$

$\frac{f_1 \cdot f_3}{f_2}$, represents the equivalent focal lens of the lenses placed between the fiber bundle and the SLM. A second telescope ($f_4 = 200$ mm and $f_5 = 300$ mm) conjugates the SLM plane with the entrance of the microscope objective (Olympus XLUMPlanFL N 18/12 20XW, $\text{NA} = 1$), filling its back aperture. Because the fiber bundle randomizes the input polarization, a polarizing beam splitter is placed before the SLM to select only the horizontal components (half of the total input light) and minimize the intensity of the zero (non-diffracted) order after the SLM. The SLM, placed at the Fourier plane of the fiber bundle output, multiplexes the original spot, which is composed of multiple illuminated fiber bundle cores, to generate 2D and 3D light patterns at the sample plane. The maximal reachable 2D FOV ($\Delta x_{\text{max}} \times \Delta y_{\text{max}}$) depends on the effective objective NA and the number of pixels of the SLM⁴⁴: $\Delta x_{\text{max}} \times \Delta y_{\text{max}} = \frac{\lambda \cdot N}{4 \cdot \text{NA}_{\text{obj}}} \times \frac{\lambda \cdot N}{4 \cdot \text{NA}_{\text{obj}}}$. The phase holograms displayed by the SLM are calculated using a Gerchberg-Saxton algorithm⁴⁵.

Because the SLM is a diffractive optical element, the generated deflection angles depend on the laser wavelength. Different phase masks are therefore calculated for each laser wavelength and displayed on the SLM at different times. A beam blocker is placed in the plane between f_4 and f_5 to block the 0th order of the SLM. A custom-designed software, Wavefront-Designer V, written in C++ and using the open graphic library Qt 5.15.2, controls the SLM for the dynamic CGH configuration. The software also includes phase corrections for the first-order Zernike aberrations and the possibility to add a calibration mask to homogenize the fluorescence intensity distribution in the 3D field of view (FOV). The software also uses the capabilities of the Cuda GPU to accelerate processing speed, which were added to take advantage of both CPU and GPU capacity to calculate 3D patterns even more efficiently^{46,47}.

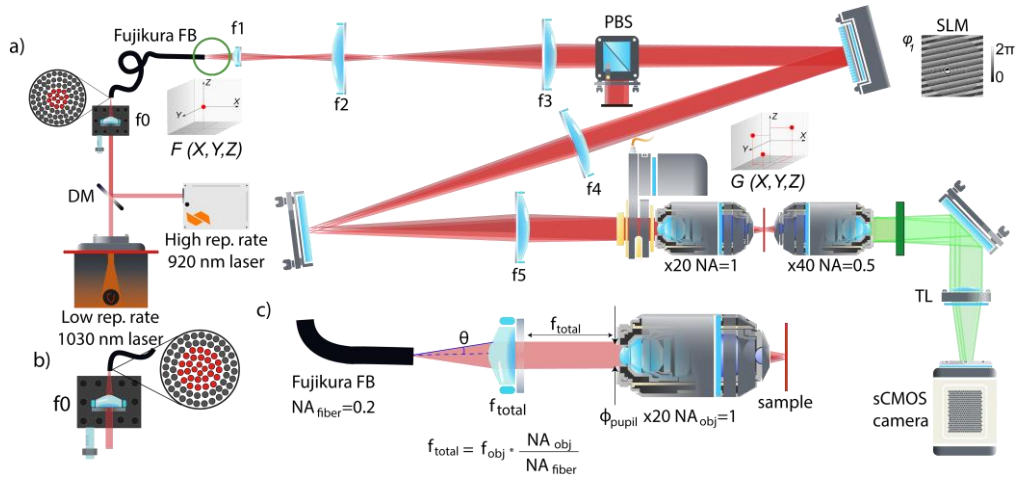


Fig. 1: Experimental setup for a multicolour 3D light-patterning 2P microscope. **a)** The Goji laser (4 W, 1030 nm, 10 MHz, 150 fs) and the Spark laser (4 W, 920 nm, 80 MHz, 120 fs), coupled with a dichroic mirror (DM), are focused ($f_0 = 18$ mm) at the entrance of the fiber bundle (FB) illuminating multiple cores. After the fiber bundle ($NA = 0.2$) the light is collimated with a lens $f_1 = 8$ mm ($NA = 0.5$). A telescope is used to match the beam with the SLM ($f_2 = 150$ mm and $f_3 = 600$ mm) and another telescope to match the size of the objective pupil ($x20 NA = 1$) with lenses ($f_4 = 200$ mm and $f_5 = 300$ mm). The total magnification of the system is $x5.3$, which maximizes the number of cores (around 300 cores for a $15 \mu\text{m}$ diameter spot) thus minimizing the power per core for a given total power. A polarized beam splitter (PBS) ensures that the correct polarization is sent to the SLM and rejects half of the light coming from the fiber bundle. The excitation objective can be moved axially with a piezoelectric motor to measure the axial profiles of the spots in the sample plane. The 2P fluorescence is measured using an inverted objective ($x40 NA = 0.5$) and a lens (TL = 180 mm) with an sCMOS camera. **b)** Input side of the fiber bundle illumination, showing that by moving the f_0 lens - fiber bundle relative position, we can defocus the light to change the number of spots we illuminate, thus changing the spot size in the sample plane. **c)** Simplified optical scheme of the system where all the lenses between the fiber bundle and the excitation objective are reduced to an equivalent lens of focal f_{total} , which is determined by the excitation objective we use, considering a complete illumination of the objective back aperture, and the NA_{fiber} .

The magnification of the system, from the fiber bundle output to the sample plane can be expressed as $\approx \frac{NA_{obj}}{NA_{fiber}}$, under the condition that the excitation beam completely fills the objective pupil (ϕ_{pupil}). This expression can be derived by looking at the simplified schema of fig. 1c) where the lenses (f_{1-5}) between the fiber bundle and the objective are replaced with a single lens of equivalent focal length $f_{total} = \frac{f_1 \cdot f_3 \cdot f_5}{f_2 \cdot f_4}$, and considering the corresponding expressions for the fiber bundle and objective numerical apertures: $NA_{fiber} \approx \tan(\theta) = \frac{\phi_{pupil}}{2 \cdot f_{total}}$ and $NA_{obj} \approx \frac{\phi_{pupil}}{2 \cdot f_{obj}}$. The total magnification (M) of the system can be then expressed as $M = \frac{f_{total}}{f_{obj}} \approx \frac{NA_{obj}}{NA_{fiber}}$. This, given that, in our system $NA_{obj} = 1$ and $NA_{fiber} = 0.2$, results in a total magnification of ≈ 5 in agreement with the measured value of 5.3. As a result, the generation of e.g. a spot of $\sim 15 \mu\text{m}$ of lateral size corresponds to a spot of $80 \mu\text{m}$ diameter at the fiber bundle input corresponding to the illumination of ~ 300 cores.

2.2 Detection System and axial resolution measurements

The patterns generated by the SLM and focused by the excitation objective illuminate a thin fluorescent film made of a spin coated layer of rhodamine-6G in polymethyl methacrylate (2% w/v in chloroform), and the 2P-excited fluorescence is collected by a second objective (Nikon, PLAN 40X, 0.7 NA) in transmission geometry and detected by a sCMOS camera (Orca Flash 4.0 C11440, Hamamatsu) using a tube lens (TL = 180 mm) and 2 IR blocking filters (Thorlabs TF1) (Fig. 1a). For characterizing the axial resolution, a z-step piezoelectric scanner (PI N-725.2A PIFOC) is used to axially scan the excitation objective over the desired z range in steps of $2 \mu\text{m}$ to obtain 3D stacks of images, while the second objective is fixed and focused on the fluorescent film plate.

The sCMOS camera is controlled with MicroManager and synchronized with the z-stack piezoelectric scanner of the excitation objective to measure the axial profiles of the spots created in the fluorescent sample. The recorded stacks

are analyzed using Matlab and ImageJ. The 2P fluorescence values for each spot are obtained by integrating the intensity of all the pixels of the camera in a circular area containing the spot. Axial intensity distributions are obtained by integrating the intensity of the pixels in the same area for each plane of the recorded stack. The axial confinement values are reported as the full-width at half maximum (FWHM) of the axial profiles of the spots fitted with a Lorentzian model. Statistical data in axial resolution measurements are reported as mean \pm standard deviation, and as averaged normalized mean \pm standard deviation for 2P fluorescence signal measurements.

3. Results

3.1 Axial resolution for extended spots with a fiber bundle

We first characterized the axial resolution of a single spot that encompasses ~ 300 cores of the fiber bundle and results in a disk of $15 \mu\text{m}$ in diameter at the sample plane, at the center of the FOV. As recently demonstrated, the inter-core delay dispersion of these fiber bundles, enables maintaining micrometer size axial resolution through a 2P fiberscope⁴³ independently of the laterally extension of the excitation spots. In practice, when multiple cores are illuminated simultaneously with an extended spot, the pulses from each core arrive at the sample plane at slightly different times due to small variations in the shape and size of the cores (Fig. 2a)⁴⁸. This has the same consequence of TF, namely, a decrease of the out-of-focus 2PE, and maintains the axial confinement independent on the lateral spot size.

This effect is demonstrated in fig. 2b where we compare the axial confinement of spots of different sizes generated at the center of the FOV by conventional CGH with spots that are propagated through the fiber bundle. As one can clearly see, the axial resolution of the spots is reduced to $\sim 8 \mu\text{m}$ when using a fiber bundle and it shows little dependence on the lateral spot size compared to the axial resolution of CGH spots (axial resolution = $20 - 40 \mu\text{m}$).

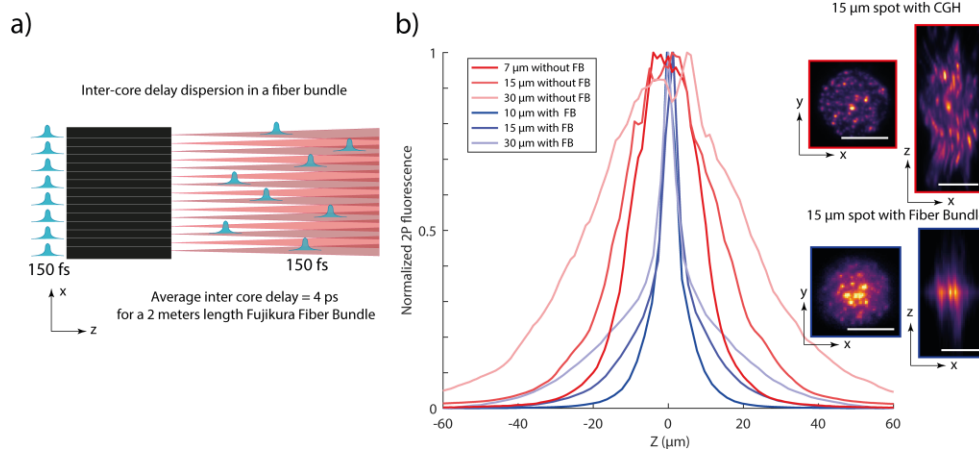


Fig. 2: Characterization of the axial resolution for extended spots with and without the fiber bundle. a) Schematic representation of the inter-core delays experienced by an ultrashort laser pulse ($\tau_0 = 150$ fs) when propagating through multiple cores of a ~ 2 m length Fujikura fiber bundle. b) Axial profiles of extended spots of 7, 15 and $30 \mu\text{m}$ created with fiber bundle (FB), corresponding to 65, 300 and 1200 illuminated cores, and with CGH without the fiber bundle. Insets: example of the front view (x,y) and the side view (x,z) of the 2P fluorescence signals generated by the $15 \mu\text{m}$ diameter spot with and without the fiber bundle. The axial confinement obtained with the fiber bundle is $\sim 8 \mu\text{m}$ i.e. 2-4 times smaller than what achievable without the fiber bundle (~ 20 - $40 \mu\text{m}$) by using $1\text{mW}/\text{core}$. Scale bar = $10 \mu\text{m}$.

3.2 The effect of self-phase modulation on 2PE efficiency and axial resolution

In this section, we characterize the effect of the laser powers on the 2PE efficiency and axial resolution. As described in the methods, in the current system, the spots at the sample plane are all replicas, generated by the SLM, of the same original spot created at the fiber bundle exit. To produce many excitation spots at the sample with sufficient power per spot, we therefore need to increase the total power at the fiber bundle entrance. As previously shown⁴⁹⁻⁵², one of the main challenges associated with using high laser powers through optical fibers or fiber bundles, is the occurrence of nonlinear effects as self-phase modulation (SPM), which can distort the laser pulses traveling through the fiber bundles, and correspondingly reduce the 2PE efficiency and axial resolution. For fibers similar to the one used in this study, the

threshold for SPM when using an 80 MHz repetition rate laser at a wavelength of 850 nm is of $\sim 10\text{mW/core}^{52}$, which corresponds to a pulse energy per core of 0.12 nJ.

To characterize the effects of SPM on the pulse broadening and axial resolution, for the lasers and wavelengths used in this study (920 nm and 1030 nm; 80 and 10 MHz repetition rate) we performed two separate sets of measurements. In a first set of experiments, we measured the 2P fluorescence generated by a 15 μm spot at constant power into the rhodamine sample, while increasing the power per core. This was achieved by adding a second power control at the output of the fiber bundle which maintains constant the power at the sample plane while a first power control increases the power per core sent to the entrance of the fiber bundle. The power per core was calculated by dividing the power measured at the output of the fiber bundle (which is $\sim 60\%$ of the power at the entrance of the fiber bundle) by the number of cores illuminated (~ 300 cores). Because the 2PE is inversely proportional to the laser pulse duration (τ), measuring the fluorescence decrease as a function of the power per core (P_{core}), for a constant power into the sample, gives an indirect measurement of the effect of the SPM on the pulse broadening. Considering that the measurements of 2PE when low P_{core} are used, i.e. $2PE_0$, correspond to the shortest pulse duration τ_0 , we can write the following equation: $\frac{2PE(\tau)}{2PE_0} = \frac{\tau_0}{\tau}$, where $\tau_0 = 150$ fs and $\tau_0 = 120$ fs (i.e. the nominal pulse durations from the laser manufacturers) for the low and high repetition rate laser, respectively. Using this equation, we obtained the values for τ reported in Fig. 3 for different laser powers. A linear relation $\tau(P_{\text{core}}) = \tau_0 + \Delta\tau(P_{\text{core}}) = \tau_0 + K \cdot P_{\text{core}}$ was found to well represent the experimental data in the range of powers used in the graphs. We therefore used such a curve to fit the data point by letting the parameters τ_0 and K vary freely. We obtained the values of ~ 123 fs and ~ 160 fs for the two lasers respectively, and found that at the maximum power used of 8 mW/core (corresponding to 0.1 and 0.8 nJ for the high and low repetition rate lasers, respectively), the laser pulse increased to 190 fs and 480 fs, for each laser (Fig. 3a and 3b) which corresponds to a 50% and 210% of pulse broadening ($\Delta\tau$) with respect to the initial laser pulse duration (see Supp. Fig. 1 for pulse broadening dependence on the peak power for both lasers used). Secondly, we measured the axial profile of a single 15 μm spot focused on a thin fluorescent layer of rhodamine in the center of the FOV ($x = y = z = 0$) using different powers per core for both lasers. As shown in (Fig. 3c and 3d), the FWHM of the axial profiles increases when illuminating the fiber bundle with higher powers per core. Specifically, the axial resolution changes from ~ 6 to ~ 7 μm for the high repetition rate laser and from ~ 5 to ~ 8 μm for the low repetition rate laser. This effect can be explained by the broadening of pulses due to SPM, discussed earlier. Specifically, with a constant inter-core delay dispersion (as it depends on a property of the fiber), the longer the pulses, the more likely pulses from different cores will overlap, resulting in an increased out-of-focus excitation and therefore loss of axial resolution.

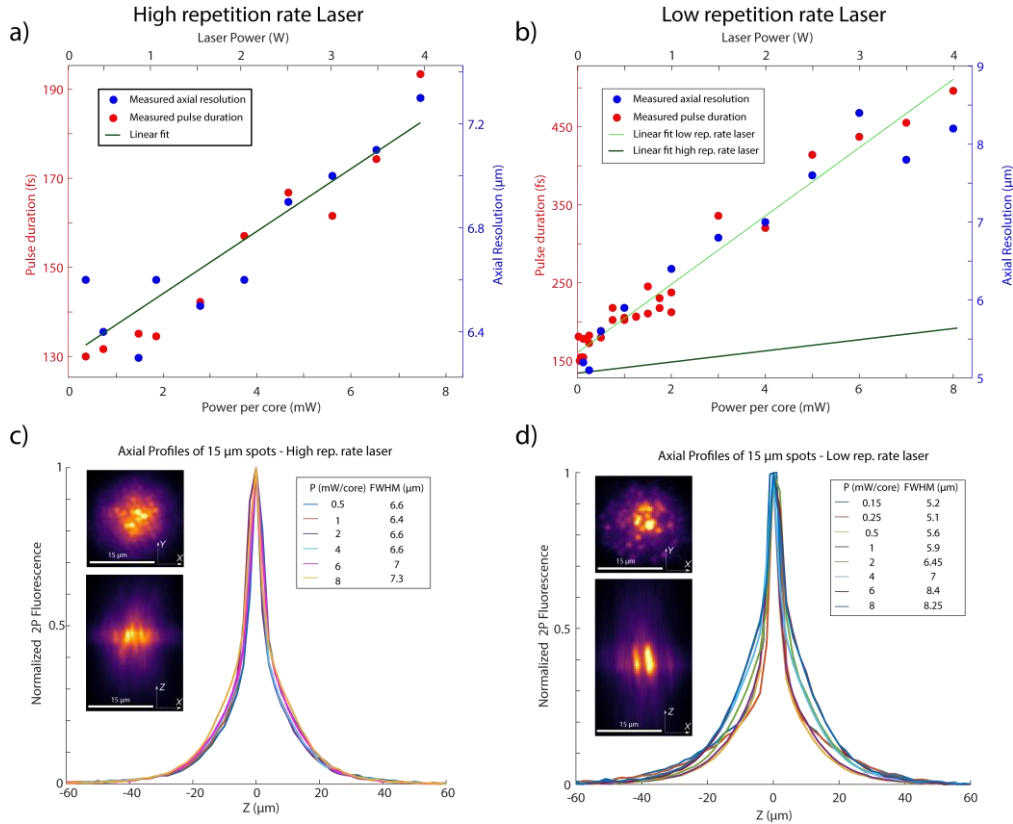


Fig. 3: Optical characterization of a single spot through a fiber bundle. **a, b)** In blue, measurements of the FWHM of the axial profiles in **c, d)** and in red, the calculated pulse duration of a 15 μm diameter spot in the sample plane for different powers, for the high and low repetition rate laser respectively. The pulse duration after the fiber bundle is obtained from the 2P fluorescence measured in the sample as described in the text. The laser pulse duration increases as the power density in the fiber bundle increases due to the SPM. The solid red line indicates a linear fit $\tau = K \cdot P_{\text{core}} + \tau_0$ between the power per core (P_{core}) and the pulse duration (τ). From the fit we obtain $K = 7.8 \text{ fs/mW}$ and $\tau_0 = 123 \text{ fs}$ for the high repetition rate laser, and $K = 43.8 \text{ fs/mW}$ and $\tau_0 = 160 \text{ fs}$ for the low repetition rate laser, respectively. **c, d)** Measurements of the normalized axial profile of the 2P fluorescence of a 15 μm diameter spot in the sample plane at different powers, while illuminating ~ 300 cores in the fiber bundle with the 920 nm (**c**) and 1030 nm (**d**) laser. The power per core is determined by dividing the power measured at the fiber bundle output by the number of cores. Bottom right insets: front (x,y) and side (x,z) view of a 15 μm spot when using 2 mW/core.

3.3 Optical Characterization of 2D and 3D pattern generation

In this section, we demonstrate the capability of the system for creating multiple 2PE spots, in a volume, using two wavelengths (920nm and 1030nm). To this end the two lasers are focused to illuminate the same cores at the fiber bundle entrance, and the SLM, positioned after the fiber bundle, is used to multiplex and displace the replicas of the original spots by using for each wavelength the corresponding phase mask. To be noted that, to simulate experimental conditions in which the setup is used to target the largest number of cells, in what follows, we always use the highest input laser power (4 W, $\sim 8 \text{ mW/core}$). This leads to suboptimal pulse durations and axial resolutions, particularly for the low repetition rate laser.

We first demonstrate the possibility of creating a two-color distribution of 2PE spots on a single plane, on the largest 2D FOV allowed by the system (limited by the maximal angles the SLM can produce⁴⁴). To homogenize the relative intensity of different spots at different distances from the center of the FOV, we applied for the two wavelengths the same diffraction efficiency correction mask on the SLM²⁷ (Fig. 4a).

As the SLM is a diffractive element, the deflection angles, and consequently, the x and y positions of the spots at the sample plane, depend on the incoming wavelength (Fig. 4b). This results in a wavelength-dependent calibration offset required to match the intended and effective positions of the spots. To compensate for this effect, when generating spatially overlapping spot distributions for the two wavelengths, we added a further relative scaling factor of 0.88 to

the phase masks that control the spot generation with the laser at 1030 nm. This enables the creation of overlapping patterns at the sample plane, with the appropriate and sequentially applied phase mask for each wavelength, as shown in fig. 4b.

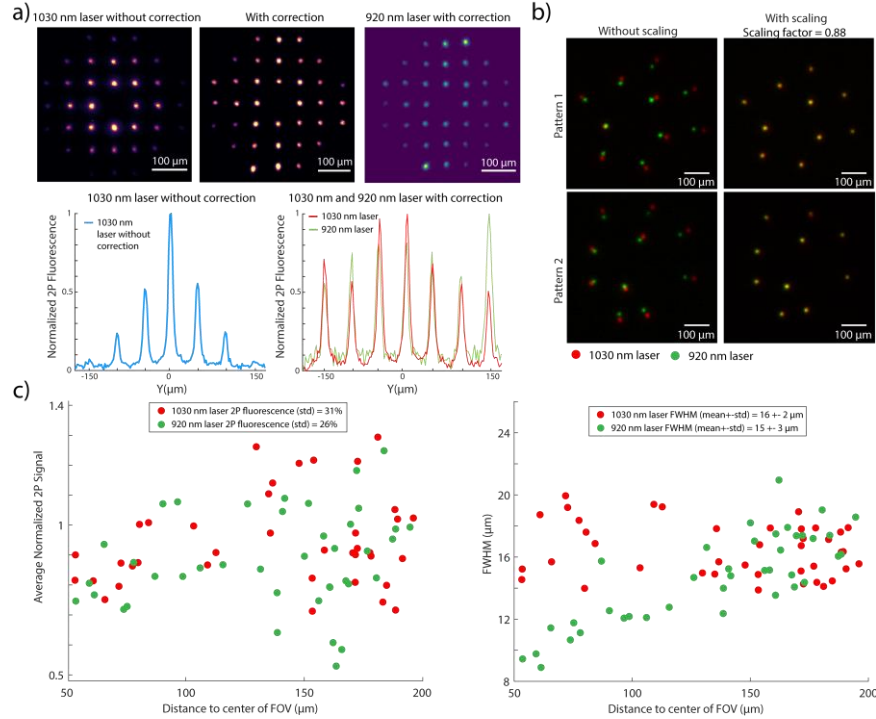


Fig. 4: Optical characterization of multiple spots multiplexed in 2D with the SLM through a fiber bundle. a) Top: Example of the recorded 2P fluorescence signal in the sample plane when a pattern (36 spots) without (left) and with (center and right) the correction is created for the two lasers in the 2D FOV. Bottom: Examples of the 2P fluorescence signal (a. u.) for a line of spots distributed along the Y axis. Left (blue): Diffraction efficiency correction is not applied so that a clear dependence of the 2P fluorescence with the distance to the center is shown. Right (red and green): diffraction efficiency correction is applied after a calibration to homogenize the 2P intensity distribution for both lasers. b) Example of 2P fluorescence signal in the sample plane when two patterns (10 spots per pattern) are created with the two different lasers. On the left, patterns 1 and 2 are applied to both lasers without applying the scaling factor. On the right, the scaling factor (= 0.88) is applied to the 1030 nm laser to produce overlapping spots. c) Left: Average normalized 2P signal of the spots randomly distributed in a 2D FOV of $380 \times 380 \mu\text{m}^2$ as a function of the distance to the center of the FOV for the two different lasers after the diffraction efficiency correction mask is applied. Right: FWHM of the axial profiles of the spots randomly distributed in a 2D FOV of $380 \times 380 \mu\text{m}^2$ as a function of the distance to the center of the FOV for the two different lasers.

In fig. 4c we show the obtained 2P fluorescence signal and the axial resolution of multiple spots generated from different patterns using the two lasers simultaneously (10 spots per pattern, 4 different patterns). We found values for the axial resolutions comprised between 8 and 18 μm , with a mean FWHM = 15 μm (standard deviation = 3 μm) at 920 nm and between 14 and 20 μm , with a mean FWHM = 16 μm (standard deviation = 2 μm) at 1030 nm.

Finally, we demonstrate the ability to create 3D two-color excitation patterns in a volume of $380 \times 380 \times 300 \mu\text{m}^3$ (Fig. 5). The average axial resolution (FWHM) of the spots is 20 μm at 920 nm and 24 μm at 1030 nm. There is a worsening of the axial resolution in both x-y plane and in z direction as we moved away from the center of the FOV, which we attribute to larger aberrations. The lateral profile for different spots in the volume for both lasers was also characterized to confirm that the properties of the spots were well-maintain throughout the entire FOV (Supp. Fig. 2). Similar to what was done for 2D two-color generation of spots, a scaling factor (= 0.88) was added to the phase masks that control the 1030 nm beam.

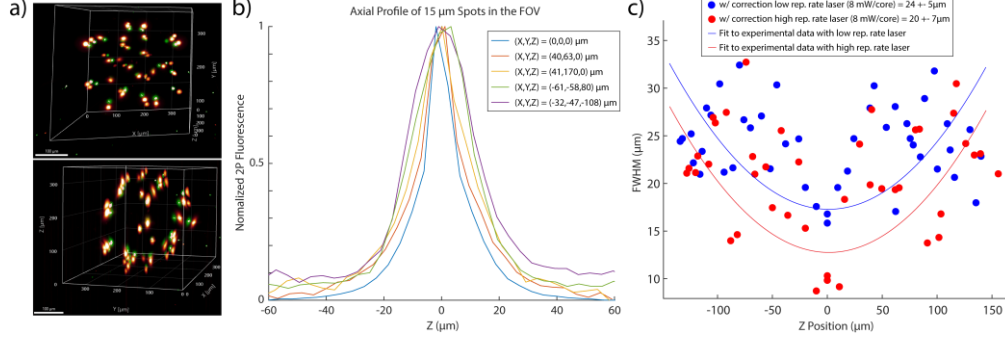


Fig. 5: Optical characterization of multiple spots multiplexed in a 3D volume with the SLM through a fiber bundle. a) Example of the recorded 2P fluorescence signal in the sample plane when 42 spots are created in a 3D FOV of $380 \times 380 \times 300 \mu\text{m}^3$ with both colors (green for the laser at 920 nm and red for the laser at 1030 nm) Top: (x,y) front view. Bottom: (y,z) side view. b) Axial profiles of some spots distributed in the 3D FOV in different (x, y, z) positions in a with the 1030 nm laser. c) FWHM of the axial profiles of the distributed in the 3D FOV in function of the depth position (z) for spots in random (x, y) positions in two different wavelengths propagated through the fiber bundle (920 nm in red and 1030 nm in blue).

With these results, we have demonstrated that our method can produce nearly uniform (std $\sim 30\%$) two-color distributions of axially confined spots across a FOV of at least $380 \times 380 \times 300 \mu\text{m}^3$.

3.4 System capabilities

Here, we analyze the different parameters that need to be considered when designing an optical system tailored to diverse experimental conditions. This involves finding a balance between optimizing the available power (and consequently the achievable number of spots), and the achievable axial resolution and FOV. This is especially relevant for the current system, where increasing the number of spots at the sample plane requires increasing the power per core, P_{core} , at the fiber bundle, which, because of the SPM effect, can be detrimental for the 2PE efficiency and the axial resolution.

As explained in the methods, the condition on the optical magnification between the fiber output and the sample plane required to fill the pupil of the objective becomes $M \approx \frac{NA_{obj}}{NA_{fiber}} \sim 5$ when considering $NA_{fiber} = 0.2$ and an objective with $NA_{obj} = 1$. An excitation spot of diameter ϕ_{sample} at the sample plane corresponds to a diameter of $\phi_{fiber} = M \cdot \phi_{sample}$ at the fiber bundle. If we call the inter-core distance of the fiber bundle ϕ_{core} , then the total number of cores illuminated by a spot can be expressed as $N_{cores} = \left(\frac{\phi_{fiber}}{\phi_{core}}\right)^2 = \left(M \cdot \frac{\phi_{sample}}{\phi_{core}}\right)^2 \approx \left(\frac{NA_{obj}}{NA_{fiber}} \cdot \frac{\phi_{sample}}{\phi_{core}}\right)^2$. For our experimental conditions $\phi_{core} = 4.5 \mu\text{m}$ and considering a spot size at the sample of diameter $\phi_{sample} = 15 \mu\text{m}$, we obtain $N_{cores} \cong 300$ cores.

To calculate the total power at the sample plane and the 2PE efficiency, which depends on the pulse broadening, we first consider the power losses between the laser output and the sample plane within our experimental system. These losses are given by several components: the fiber bundle (transmission of 60%, T_{fiber}), the PBS (transmission of 50%), the SLM (reflection of the 1st diffraction order of 70%) and the excitation objective (transmission of 50-60% at the wavelengths used, T_{obj}), resulting in a total transmission $T_{total} = 12\%$. Denoting P_{laser} as the laser power at the fiber entrance, the total available power at the sample plane is $P_{sample} = P_{laser} \cdot T_{total}$.

However, for a fixed spot diameter at the fiber bundle, an increase in P_{laser} beyond a specific threshold results in an elevated power per core, causing pulse duration broadening. For the range of laser powers used here, the pulse duration, denoted as τ , can be approximated as $\tau = K \cdot P_{core} + \tau_0$, where K and τ_0 represent the slope and the nominal pulse duration obtained from the linear fit in fig. 3b respectively. As P_{core} is the power per core, $P_{core} = P_{laser} \cdot T_{fiber} / N_{cores}$, we obtain:

$$\tau \approx \tau_0 + K \cdot P_{laser} \cdot T_{fiber} \cdot \left(\frac{NA_{fiber}}{NA_{obj}} \cdot \frac{\phi_{core}}{\phi_{sample}}\right)^2 \quad (1)$$

Subsequently, designating P_{spot} as the power needed to efficiently excite a target in the 2P regime (it can be the power needed to photostimulate or to image a cell for instance), the total number of targets that can be excited for a given P_{sample} is $N_{spots} = \frac{P_{sample}}{P_{spot}}$, where P_{spot} depends on the pulse duration. Calling P_{spot_0} the power needed to excite a target when the pulse duration is τ_0 , we obtain $P_{spot} = P_{spot_0} \cdot \left(\frac{\tau}{\tau_0}\right)^{1/2}$ and $N_{spots} = \frac{P_{sample}}{P_{spot_0}} \left(\frac{\tau_0}{\tau}\right)^{1/2}$.

To introduce the effects of the pulse broadening, we can also define an effective power at the sample plane: $P_{eff} = P_{sample} \cdot \left(\frac{\tau_0}{\tau}\right)^{1/2}$. The total number of excitable targets is then proportional to P_{eff} . By combining this expression with equation (1), we obtain the dependence between P_{eff} and NA_{obj} :

$$P_{eff} = P_{laser} \cdot T_{total} \left(1 + \frac{K \cdot P_{laser} \cdot T_{fiber}}{\tau_0} \cdot \left(\frac{NA_{fiber}}{NA_{obj}} \cdot \frac{\phi_{core}}{\phi_{sample}} \right)^2 \right)^{-1/2} \quad (2).$$

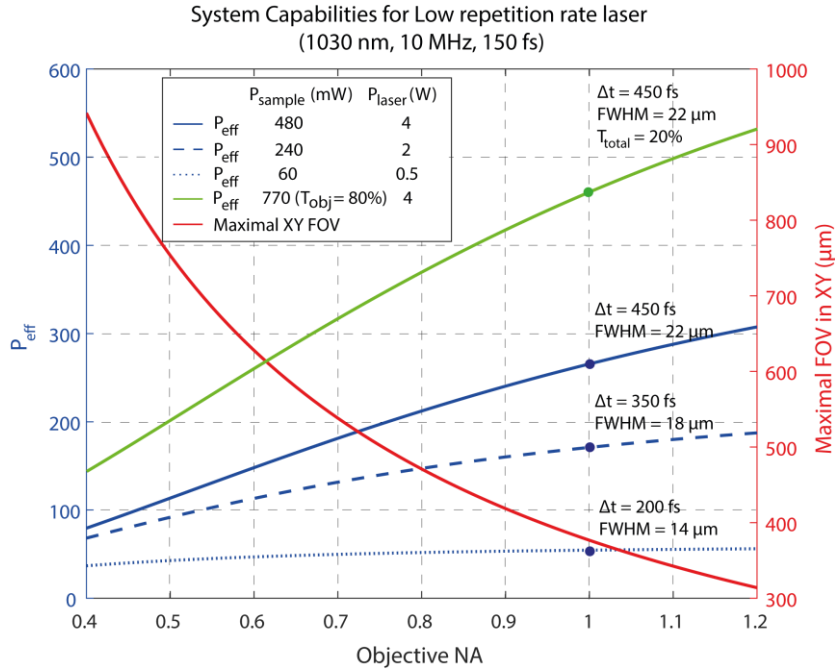


Fig. 6: Systems capabilities and comparisons for different objective NAs. Left vertical axis: Calculated output power from the excitation objective as a function of the effective objective NA, for the objective used in this work (with 50% transmission) and an incident wavelength of 1030 nm at a repetition rate of 10MHz. Three different laser powers at the fiber bundle entrance are considered: 0.5 W (dashed-dotted blue curve), 2 W (dashed blue curve) and 4 W (solid blue curve), leading to different pulse broadening (200 fs, 350 fs and 450 fs respectively as indicated on top of each curve) with the corresponding measured axial resolutions. The green curve represents the maximal P_{eff} that can be created considering an incident power of 4 W and an 80% transmission objective. Right vertical axis (red curve): calculated 2D FOV for different effective objective NAs using a SLM of 1272x1024 pixels.

In fig. 6, we plot the effective power from Eq. (2) as a function of the objective NA, for different values of P_{sample} , obtained either by changing P_{laser} (blue curves), or by optimizing the transmission of the system (such as by using a higher transmission objective, green curve). The graph assumes $\phi_{sample} = 15 \mu m$ and considers the parameters of the 1030 nm laser previously discussed in this manuscript ($K = 43.8 \text{ fs/mW}$, $\tau_0 = 160 \text{ fs}$). A similar graph for the 920 nm laser is given in Supp. Fig. 3.

Notably, the choice of the objective NA also defines the achievable FOV (see equation in Methods) (red curve, right axis). To change the objective NA does not necessarily involve replacing the objective as it is possible to underfill the objective pupil by using a different magnification between the SLM and the objective.

As illustrated, there exists a clear tradeoff between the effective power at the sample plane, which increases for higher objective NAs, and the achievable FOV's size. In practice, for a fixed P_{laser} and ϕ_{sample} , increasing NA_{obj} results in a greater number of illuminated cores, lowering the power per core. This leads to a decrease of SPM, shorter laser

pulse durations and more efficient 2PE. At the same time, a larger NA_{obj} increases the magnification between the SLM and the objective pupil, which reduces the maximal FOV at the sample plane, for the same angles produced by the SLM.

The difference among the three blue curves demonstrates that increasing P_{sample} of a given factor by turning up P_{laser} only leads to an increase in P_{eff} of a smaller factor (Supp. Fig. 4). This is due to the fact that as the power per core increases, the 2PE becomes less efficient, especially for lower NA_{obj} . However, within the power range considered in our analysis, it is still beneficial to increase P_{laser} , up to the full 1030 nm laser power (4 W at the fiber entrance) to maximize P_{eff} and, consequently, N_{spots} , even though it comes with a worse axial resolution. Alternatively, it is possible to increase P_{sample} by minimizing the losses between the fiber and the sample. In this case, P_{eff} increases by the same factor as P_{sample} . For example, with a 0.8 NA excitation objective with 80% transmission (which is a typical commercially available objective) and the SLM used here, one could obtain $P_{eff} = 370$ mW on a FOV of $470 \times 470 \mu\text{m}^2$ in diameter.

Another major source of power losses (50%) in our system is introduced by the PBS placed before the SLM. One possibility to compensate for this loss is to redirect the deviated beam to the SLM after rotating its polarization as shown in Supp. Fig. 5a, where we could reach an almost two-fold increase of the total system transmission T_{total} (from 12% to 20%). An alternative solution could use a pyramidal 4-faces mirror system⁵³. Because in this configuration the two beams illuminate separately the two halves of the SLM⁵⁴, and therefore of the objective back aperture, the achievable FOV is also reduced by the half and is equal to $190 \times 190 \times 200 \mu\text{m}^3$. Larger FOVs could be reached by using a SLM with a higher pixel number.

4. Discussion.

We have demonstrated a simple 2P microscope for multicolor axially confined 3D light patterning that uses a fiber bundle and exploits its intrinsic inter-core delay dispersion. A first advantage of using a long and flexible fiber bundle is that it makes the setup highly modular. It could for instance allow different optical setups to be coupled to the same laser sources, just by displacing the distal end of the fiber, or it could ease the integration of a photostimulation branch to an already existing imaging only 2P microscope.

Previous approaches for 2D or 3D generation of axially confined spots have used one or two SLMs for spot shaping and beam multiplexing and a diffraction grating for temporal focusing^{25–28,30–32}. Here we have demonstrated that, the diffraction grating can be replaced with similar light losses (both cases corresponding to 20–40% light loss), by a ~ 2 -m fiber bundle. One of the primary advantages of this configuration lies in simplifying the previously proposed multiplexed temporally focused light shaping (MTF-LS²⁸) configurations for the generation of three-dimensional illumination patterns. Specifically, the use of a fiber bundle, replaces the first SLM and the diffraction grating used in MTF-CGH so that one only needs the SLM for 3D light multiplexing²⁸. Notably, this also preserves the flexibility to change the size (even if not the shape) of the generated spot, a flexibility that would be lost when using MTF-CGH with a fixed phase mask⁸. Typical photostimulation and neuronal imaging experiments commonly use a round-shaped spot, which aligns well the capabilities of this system.

Our configuration has also advantages with respect to the 3D-SHOT³⁰ configuration, which reaches three-dimensional light generation by using a single SLM but is tied to the generation of a fixed spot size, as defined by the laser's expansion. Moreover, the most recent version of 3D-SHOT³¹ requires the addition of a rotating diffuser to expand the illumination to the size of the SLM, which increases the complexity of the system.

The spots generated through the fiber bundle at the sample plane present some level of inhomogeneity (see Fig.3). This could be due to the differences in group velocity dispersion among different cores, as was experimentally demonstrated, especially for high density fibers in Ref.⁵⁵. Nonetheless, the same type of fiber bundles was already used both for imaging^{43,56} and for photostimulation⁴³ of neurons in freely moving mice. Additionally, spots with inherent inhomogeneities, such as those generated by CGH that present speckles, have been employed for both 2P photostimulation and voltage imaging³⁵ of neuronal somas. We therefore do not expect the inhomogeneity shown here to significantly affect the imaging and/or photostimulation of somas. However, it could pose higher challenges when trying to image, with camera detection, smaller compartments of a neuron, such as dendrites or axons. In such a situation, the core-to-core inhomogeneities could be mitigated by introducing, for example, a rapid vibration based on

a resonant cantilever at the output of the fiber^{57,58}. This strategy would homogenize more the generated spots, at the cost of adding complexity to the optical system.

Apart from the advantage of making the system more compact and straightforward the major benefit of this configuration is that it allows for tuning the excitation wavelength or coupling multiple colors simultaneously without modifications to the optical system^{41,42}. The use of a grating, in fact, requires adjusting the angle of incidence or exit for each wavelength, and for multicolor excitation, it would necessitate the use of two gratings and therefore two distinct optical paths and multiplexing SLMs. On the contrary, in our configuration, beams of different colors can be coupled into the same fiber bundle without being deflected, thus enabling using a single multiplexing SLM without beam path readjustment.

We have shown that, multicolor excitation of even the same targets can only be done accurately with an appropriate phase mask for each wavelength. This can only be achieved by sequentially applying the corresponding phase masks, with a minimum temporal interval that is dictated by the SLM's refresh time, i.e. 3-16 ms with standard SLMs (refresh rates of 300-60 Hz)¹¹. This is not truly a limitation for all experimental configurations in which the temporal dynamics of the phenomenon under study is longer than the refresh time. This is the case e.g. when scanless photostimulation is combined with scanless Ca²⁺ imaging given the long (~80-200 ms) decay time of commonly used calcium indicators⁵⁹. In this case, as the refresh time of the SLM is faster than the decay time of the indicators, one can sequentially switch between the photostimulation and imaging to record the effects of the photostimulation. Similarly, for experiments designed to analyze the impact on a defined behavior of an alternating sequence of activations and inhibitions, the refresh rate of the SLM should not pose a limitation.

Truly simultaneous two colors projection could otherwise be achieved by adopting the configuration reported in Supp. Fig. 5, integrating the variant schematized in Supp. Fig. 5b to control one color at each side of the SLM.

While the solution presented in this work offers many advantages compared to traditional systems, it also has its limitations in terms of maximum power, which is constrained by SPM effects^{49,52}. The resulting pulse broadening has a dual detrimental effect on signal loss and axial resolution. Considering that SPM depends on the peak power⁵², these effects are particularly significant for low repetition rate, short pulse lasers, as the 1030 nm laser used here. We have observed that for a laser with high repetition rate of 80 MHz and 920nm excitation wavelength, it is possible to couple the total laser output power (4W) through the fiber and keep a pulse duration < 200 fs, without significant losses in the 2PE or the axial resolution. For low repetition rate lasers with comparably short initial pulses (~150 fs), the broadening effects are more pronounced, resulting in a pulse of ~400 fs for the highest powers used here. However, such a pulse duration remains comparable to the one of higher power laser systems used in conventional holographic optogenetics (10-50 W, 500 kHz-10 MHz, 300-400 fs)^{11,60,61} and will thus be compatible with photostimulation. At the same time, it is possible that, for lasers with longer initial pulse durations (400 fs), the pulse broadening effect as a result of SPM, might not be as significant as in the case of shorter pulses (100-150 fs), even for the same peak power. It was indeed shown in Ref.⁶² that a pulse with larger initial spectral bandwidth (shorter initial pulse duration) is more distorted and harder to temporally recompress after propagation through a fiber. This might open the way to the use of our setup to even lower repetition rate lasers with longer initial pulses. A complete characterization of SPM with different spectral bandwidths and repetition rates will allow more certain conclusions to be drawn.

To prove the capabilities of our system, we have estimated the total number of cells that we could target for photostimulation of previously reported opsins (ChroMe³¹ and ChRmine¹¹, WicHR⁶³ and BIPOLE³⁹); for scanless voltage imaging using the indicator JEDI-2P³⁵; for scanless calcium imaging using GCaMP6^{33,34}. To do that, we have compared the P_{eff} given in Fig.6 and Supp. Fig. 3, for an objective with NA=1 and $T_{\text{obj}} = 80\%$, with the power per cell used in previous works. The detailed calculation of the maximal numbers of cells that can be targeted in different situations is provided in Supp. Table 1. In the case of photostimulation and scanless voltage imaging, by using the 1030 nm laser at 10 MHz, our system could already efficiently excite ~ 10 to 30 cells. For scanless calcium imaging, by using the 920 nm laser at 80 MHz, similar calculations show that we could target several tens, up to ~ 140 cells.

These numbers of achievable targets are compatible with a wide range of applications. They can be applied, e.g., to study how the activation of a portion or the entirety of a specific cell assembly, or even just a single hub neuron¹⁵, can impact the circuit dynamics or to perform high-throughput intra and inter-layer connectivity mapping¹⁶⁻¹⁹. For applications where, higher total power or a greater number of achievable targets are required¹¹, it becomes imperative

to conduct a thorough assessment of signal losses, axial resolution, and attainable output power for evaluating the benefit of using this approach compared to more traditional configurations.

5. Conclusions

In this study, we developed and characterized a novel fiber-based optical configuration to generate multiple axially confined illumination spots within a 2D and 3D volume using the intrinsic inter-core delay dispersion of the fiber bundles.

This configuration has two main advantages with respect to conventional optical system for multi temporal focusing light shaping, which is its simplicity and capability for multicolor excitation using a single beam path.

Despite the power per core limitation caused by SPM, we showed that the system should be already compatible with the photostimulation of few tens of cells (< 30) on a lateral FOV of 470 x 470 μm^2 by using commercially available objectives and SLMs.

We believe that the current system will be a suitable and simple alternative in all the situations in which very large number of photostimulated cells are not needed, or in experiments requiring to project extended 2PE spots with two different colors.

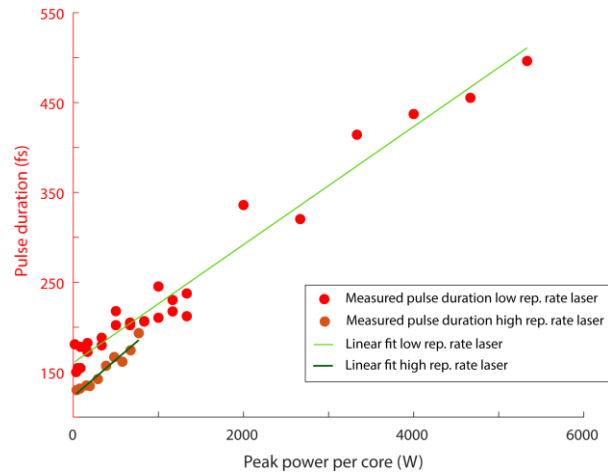
Funding. We acknowledge support from the Fondation Bettencourt Schueller (Prix Coups d'élan pour la recherche française), the AXA research funding, the "Agence National de la Recherche" (grants ANR-19-CE19-0001-01, 2MEnHoloMD; ANR-23-ERCS-0009, 2P-COMFIB), the ERC advanced Grant HOLOVIS (ERC-2019-AdG; Award no. 885090), the ERC Horizon 2020 H2020-ICT (DEEPER, 101016787), and the NIH Brain initiative (Grant 1RF1NS128772-01).

Disclosures. The authors declare that there are no conflicts of interest related to this article.

Data availability. Data underlying the results presented in this paper are not publicly available at this time but may be obtained from the authors upon reasonable request.

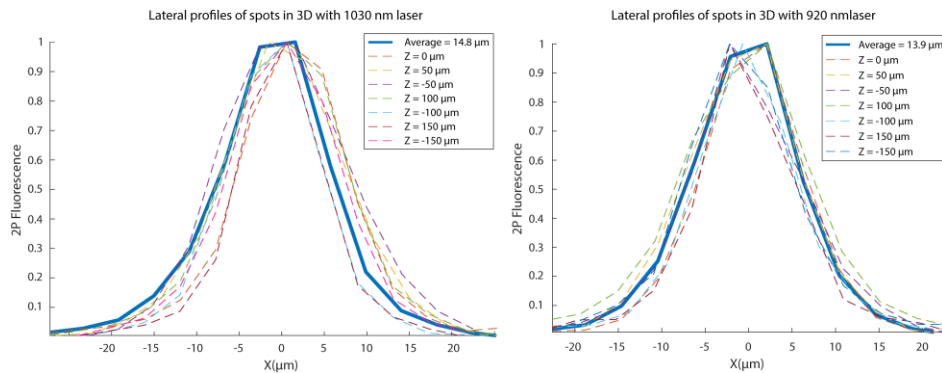
Supplemental document.

Supplementary Figure 1



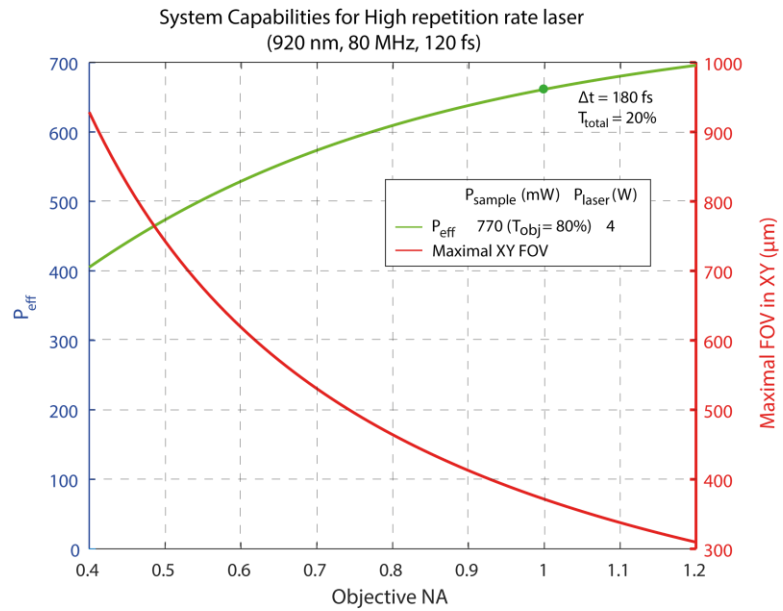
Supp. Fig. 1: Dependence of the pulse broadening when using high peak power per core. Measured pulse durations for both lasers (red dots for 1030 nm laser and orange dots for the 920 nm laser) when using different peak power per core (P_{peak}). Linear fit for the measurements of each laser ($\tau = m \cdot P_{\text{peak}} + \tau_0$) shows a similar dependence on the pulse broadening with the peak powers ($m = 66$ fs/kW for low repetition rate laser, light green curve and $m = 81$ fs/kW for high repetition rate laser, dark green curve). The use of a low repetition rate laser presents a higher peak power per core compared to the use of a high repetition rate laser.

Supplementary Figure 2



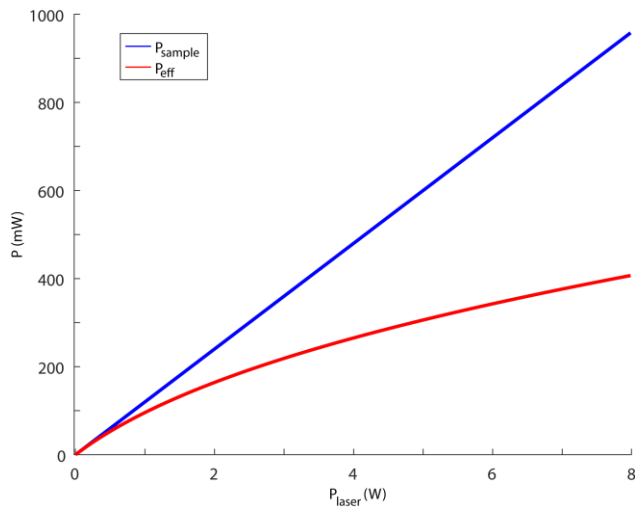
Supp. Fig. 2: Lateral profile of multiple spots multiplexed in a 3D volume with the SLM through a fiber bundle. Characterization of the lateral profiles for different spots created with the laser at 1030 nm (left) and the laser at 920 nm (right) at different depths (Z positions) throughout the entire FOV in Fig. 5. The average lateral profile for these spots is shown in solid blue line with FWHM = 14.8 μm (for the 1030 nm laser) and FWHM = 13.9 μm (for the 920 nm laser).

Supplementary Figure 3



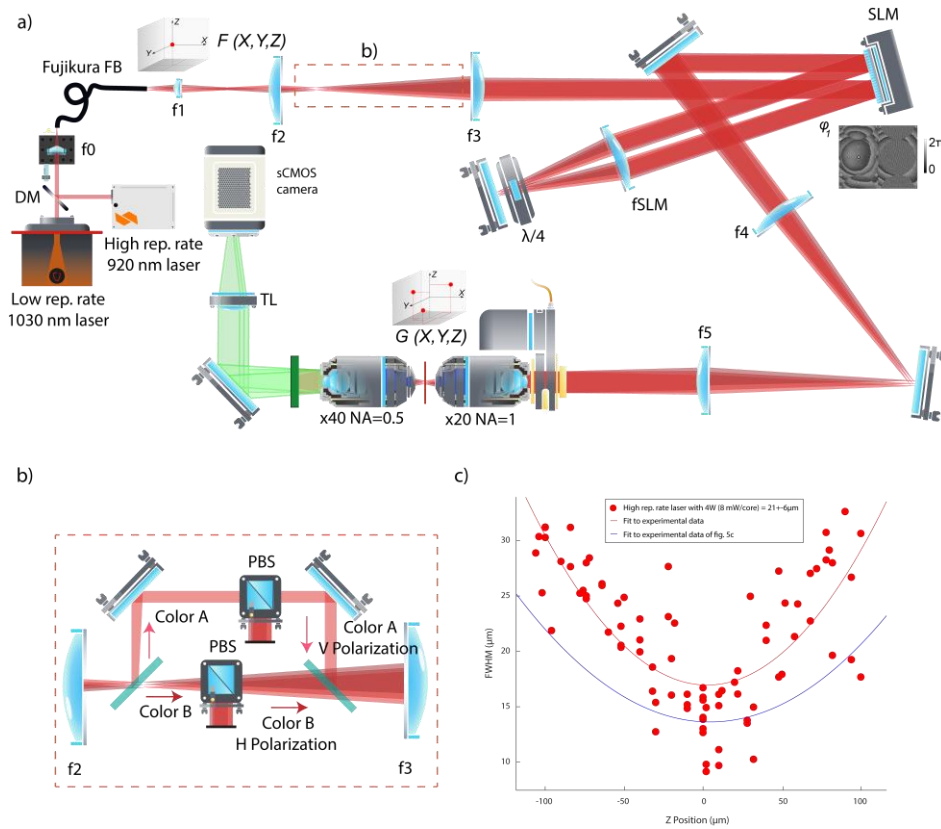
Supp. Fig. 3: Systems capabilities and comparisons for different objective NAs. Left vertical axis (green curve): Calculated P_{eff} at the sample plane considering an incident power of 4 W and an 80% transmission objective as a function of the effective objective NA, for an incident wavelength of 920 nm at a repetition rate of 80 MHz. Right vertical axis (red curve): calculated 2D FOV for different effective objective NAs using a SLM of 1272x1024 pixels.

Supplementary Figure 4



Supp. Fig. 4: Dependence between P_{eff} and P_{sample} with P_{laser} . Due to pulse broadening when using high power per core, the 2PE becomes less efficient so that a different factor of dependence is obtained between P_{sample} and P_{laser} (curve in blue) compared to P_{eff} and P_{laser} (curve in red). Even though, it is shown that is advantageous to use the maximal laser power to maximize P_{eff} .

Supplementary Figure 5



Supp. Fig. 5: Second approach of experimental setup for a multicolour 3D light-patterning 2P microscope. **a)** The lasers illuminate the fiber bundle as in Fig. 1. In this configuration, a telescope is used to match the beam with one half (right side) of the SLM ($f_2 = 300$ mm and $f_3 = 600$ mm). We use a 4f 1:1 system (two times $f_{\text{SLM}} = 500$ mm) with a quarter-wave plate $\lambda/4$ (AQWP10M-1030, Thorlabs) to rotate 90 degrees the light polarization and illuminate the other half of the SLM (left side). Finally, another telescope is used to match the size of the objective pupil ($x20$ NA = 1) with lenses ($f_4 = 400$ mm and $f_5 = 1000$ mm). **b)** Inset of a) to perform dual color 3D light targeting simultaneously by separating the two colors (color A and B) to polarized them with vertical (V) and horizontal (H) linear polarizations and recombining them to illuminate the SLM, which displays a single-phase mask. **c)** FWHM of the axial profiles of the distributed in a 3D FOV of $210 \times 210 \times 200 \mu\text{m}^3$ in function of the depth position (z) for spots in random (x, y) positions when using 4W to illuminate the fiber bundle (8 mW/core). Red: quadratic fit of the measured resolutions and in blue of the measured FWHMs in Fig. 5c.

Supplementary Table 1

(1) Opsins/ indicators	(2) Laser ($f_{REF}, \tau_{REF}, \lambda_{REF}$) reference	(3) Power per cell (P_{cell}^{REF}), reference	(4) Laser (f , τ , λ) current system	(5) Power per cell current system (P_{cell})	(6) Number of cells (N^{cell})
ChRmine ³¹	2 MHz, 350 fs, 1030 nm	10 mW	10 MHz, 150 fs, 1030 nm	14.6 mW	31
ChroMe ³¹	2 MHz, 350 fs, 1030 nm	25 mW	10 MHz, 150 fs, 1030 nm	36.5 mW	12
WicHR ⁶³	0.5 MHz, 300 fs, 1030 nm	7-8 mW	10 MHz, 150 fs, 1030 nm	22-25 mW	18-20
JEDI-2P ³⁵	0.25 MHz, 100 fs, 940 nm	2.5-5 mW	10 MHz, 150 fs, 1030 nm	19-38 mW	12-24
GCaMP6 ^{33,34}	80 MHz, 140 fs, 920 nm	5-30 mW	80 MHz, 120 fs, 920 nm	4.6-27.8 mW	24-143

Supp. table 1. Estimation of the number of cells that could be targeted with the current system, based on previously published works. Column (1) lists the opsins and indicators considered, together with the reference to the corresponding works. Column (2) gives the properties of the lasers used in the reference works, particularly the pulse duration τ_{REF} , the repetition rate f_{REF} and the central wavelength λ_{REF} . Column (3) indicates the power per cell at the sample plane used in the reference works (P_{cell}^{REF}). Column (4) lists the parameters of the lasers used in the current manuscript. To match the excitation wavelengths of the reference works we have considered to use the 1030 nm laser with effective pulse duration of $\tau = 150$ fs, and repetition rate $f = 10$ MHz for the first 4 lines in the table, and the 920 nm laser with effective pulse duration of $\tau = 120$ fs, and repetition rate $f = 80$ MHz for the last line. In column (5) we estimate the power per cell that we would need with our 1030 nm laser for the first 4 lines and 920 nm laser for the last line to produce the same 2P excitation as with the powers per cell and lasers parameters listed in column (2) and (3). This can be derived as follows: $P_{cell} = P_{cell}^{REF} \cdot \sqrt{\frac{\tau \cdot f}{\tau_{REF} \cdot f_{REF}}}$. In column (6) we give the total number of cells N^{cell} that could be simultaneously targeted with our system when considering an 80% transmission excitation objective (NA = 0.8) and using a total effective power at the sample plane $P_{eff} \approx 450$ mW in the case of the first 4 lines (related to Fig. 6) and $P_{eff} \approx 660$ mW in the case of the last line (related to Supp. Fig. 3). This number can be derived as follows:

$$N^{cell} = \frac{P_{eff}}{P_{cell}} = \frac{P_{eff}}{P_{cell}^{REF}} \sqrt{\frac{\tau_{REF} f_{REF}}{\tau f}}$$

C.2.2 Details on the system for multicolor 3D light-patterning using a fiber bundle

To perform 3D light targeting with a SLM and CGH, a custom-designed software, Wavefront V, was utilized to display into the SLM screen the desired phase mask, previously calculated in function of the desired light pattern, into the sample plane. The software is based on a Fourier-based iterative algorithm (GS algorithm, Gerchberg, 1971) that calculates and displays into the SLM the phase mask necessary to modify the wavefront of the beam. The calculated phase $[0-2\pi]$ value for each pixel is displayed by applying an input voltage to each pixel of the SLM (Lutz *et al.*, 2008). In figure 35, the main view of the software is shown, where the green circle represents the maximal (x, y) FOV. Within this FOV, it is possible to define the (x, y, z) positions for the targeted spots (yellow squares) to be generate in the sample plane. Once the targets are displayed in the software, a phase mask is calculated and sent to the SLM (calculated phase mask in figure

35). Depending on the illuminated area on the SLM, the phase mask can be displayed into the entire SLM or in a small and specific region, allowing for the generation of multiples phase masks to be displayed in different areas of the SLM. The software can also calculate, in function of the optical path used, the diffraction efficiency of the SLM within the FOV so that a correction mask can be used to correct for this effect. The software also offers other features such as Zernike polynomials to correct for optical aberrations and the incorporation of cylindrical lenses (introduced in section A.4.2, figure 8) into the calculated phase mask displayed into the SLM.

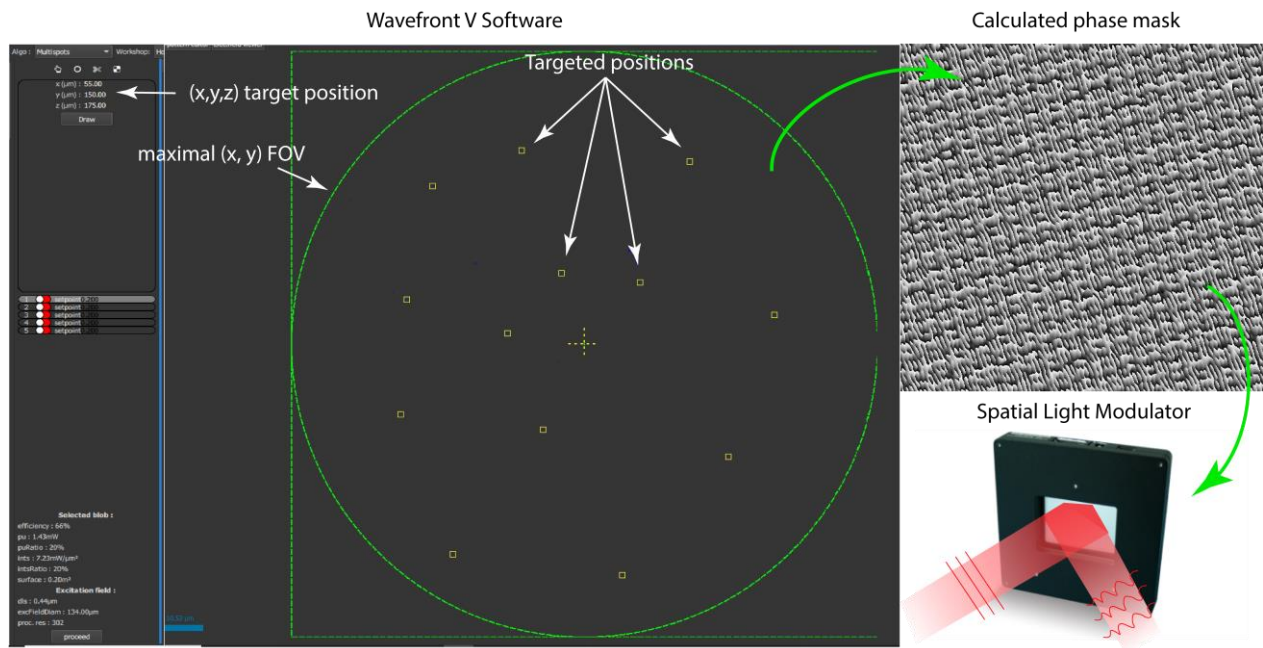


Figure 35. View of Wavefront V software (left), which is use to display the calculated phase mask (top right) into the SLM screen. The phase mask corresponds to the desired targets at any (x, y, z) positions in the sample plane within the maximal FOV.

C.3 Discussion and future perspectives

In our study, we introduced a new 2P microscope configuration tailored for multicolor 3D light patterning. Our approach is based on a fiber bundle and exploits its inherent ICDD to achieve precise axial confinement of targeted spots.

Beyond its benefits in terms of compactness and simplicity, our configuration stands out for its ability to tune the excitation wavelength or accommodate multiple colors simultaneously without requiring alterations to the optical system, as is common in traditional methods using a

diffraction grating (Lien *et al.*, 2017; Cheng *et al.*, 2020). However, the SLM still remains a wavelength dependent element in the system and different phase masks need to be generated sequentially to control each wavelength. This imposes a minimum temporal delay of 3 - 16 ms (SLM refresh time) between the generation of two consecutive phase masks (Marshel *et al.*, 2019). While this may impose limitations for applications that demand the simultaneous projection of two colors (Vierock *et al.*, 2021), it is worth noting that it is not a constraint in experimental configurations with response times longer than the SLM's refreshing time, such as in scanless photostimulation combined with scanless Ca²⁺ imaging (Forli *et al.*, 2018), bidirectional control of neuronal activity through dual-color activation and inhibition of the same or different neurons (Erbguth *et al.*, 2012; Forli *et al.*, 2018) or single color scanless illumination with a tunable laser. To achieve simultaneous two-color projection, we proposed (see Publication, Supp. fig. 4) a strategy in which each color illuminates a different region of the SLM.

An alternative solution for simultaneous dual-color could be the use of new phase mask calculation algorithms that enable the SLM to simultaneously modulate two different lasers at different wavelengths with a single phase mask (figure 36) (Jesacher, Bernet and Ritsch-Marte, 2014b, 2014a; Shechtman *et al.*, 2016). This was achieved through an algorithm that optimizes the modulation of two different visible wavelengths at 459 and 699 nm into a single phase mask, with a minimal deviation to the real phase mask needed for each wavelength independently. However, the implementation of this phase calculation has certain limitations, such as the range of phase modulation that it can accept. Indeed, this approach relies on finding voltages values for the SLM's pixels that can generate sufficient phase delays for the different wavelengths used. If the phase range at visible wavelengths can go up to 10π at 400 nm or 4.2π at 700 nm, for infrared wavelengths this modulation is currently limited to $\sim 2\pi$, which could be insufficient for the algorithm to simultaneously modulate two infrared wavelengths. Another challenge is the need of the algorithm of using two wavelengths that are spectrally well-separated, as the approach depends on finding voltage values that results in significantly different phase delays for the different wavelengths.

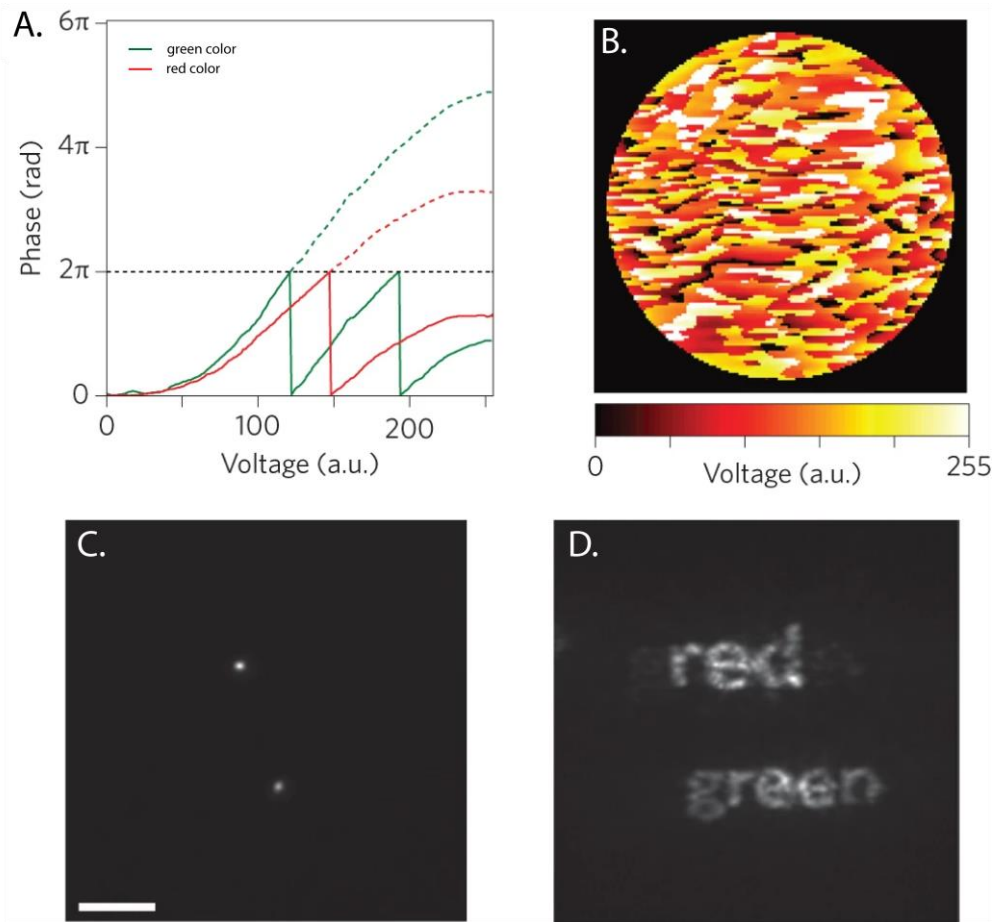


Figure 36. Encoding multicolor phase modulation into the SLM. **A.** A SLM pixel's phase response as a function of input voltage for two visible wavelengths: 559 nm (green) and 699 nm (red). The dotted lines show unwrapped phases. **B.** Input 'red-green' SLM voltage pattern (8 bit). **C.** Two fluorescent microspheres (red and green) imaged with the SLM off. Scale bar, 5 μm . **D.** The same two microspheres imaged with the pattern in B on. Adapted from (Shechtman *et al.*, 2016).

While this system has been tested with 2P excitation, its adaptability for 3P excitation lasers operating at different wavelengths, such as 1300 nm and 1700 nm, through a fiber bundle, can lead to several application in optogenetics. In this scenario, it is important to characterize the pulse duration properties after the fiber bundle, as the peak power for typical 3P excitation lasers (50 fs pulse duration, 1 - 2 MHz repetition rate, 2 - 3 W output power) could reach a factor 2 - 5 times higher than the pulse energy (0.8 nJ/core) tested in this project (150 fs pulse duration, 10 MHz repetition rate, 4 W output power). Experimental demonstrations in fibers have been already performed using low pulse duration lasers at 800 nm (Kalashyan *et al.*, 2012). In the investigation, 1 nJ of pulse energy have been transmitted through the fiber and temporally compressed to achieve 29 fs of pulse duration after the fiber by using a grism-pair (grating + prism pair), which is placed

before the fiber to stretch the pulse by compensating for second and third order of dispersion. And even by using higher energy levels of 2.5 nJ, small pulse duration of 50 fs was obtained at the output of the fiber.

Finally, the main limitation of this system lies in its maximum power usability due to the SPM constraint, which limits the maximum number of achievable targets. This limitation becomes notable when using low repetition rate lasers or high-power lasers (10 - 50 W, 500 kHz-10 MHz, 300-400 fs) (Marshel *et al.*, 2019; Sridharan *et al.*, 2022). A characterization of these lasers through fiber bundles, where the initial pulse duration is higher than the ones used in this project, would provide information into pulse broadening effects under these conditions. If in our work we studied two lasers at different wavelengths and repetition rates, the pulse duration was similar between both lasers (130 fs and 150 fs), which did not provide any information in the SPM effects of the fiber bundle with different pulse duration lasers.

Future developments in fiber bundles, particularly those with small core sizes and smaller fiber bundle NAs, have the potential to increase the maximal power per core that can be transmitted in the system. This advancement would be highly advantageous as it could help reduce the detrimental effects of nonlinear phenomena such as SPM, thus allowing for the simultaneous generation of more targets. Combining this capability with the ability for 3D light targeting of multiple colors (wavelengths) and the overall simplicity of the system would make it even more advantageous for various applications in neuroscience, such as circuit dynamics studies and connectivity mapping.

C.4 References

Accanto, N. *et al.* (2018) 'Multiplexed temporally focused light shaping for high-resolution multi-cell targeting', *Optica*, 5(11), p. 1478. doi: 10.1364/optica.5.001478.

Andresen, E. R. *et al.* (2013) 'Two-photon lensless endoscope', *Optics Express*, 21(18), pp. 20713–20721.

Andresen, E. R. *et al.* (2015) 'Measurement and compensation of residual group delay in a multi-core fiber for lensless endoscopy', *Journal of the Optical Society of America B*, 32(6), p. 1221. doi: 10.1364/josab.32.001221.

Andresen, E. R. *et al.* (2016) 'Ultrathin endoscopes based on multicore fibers and adaptive optics: a status review and perspectives', *Journal of Biomedical Optics*, 21(12), p. 121506. doi: 10.1117/1.jbo.21.12.121506.

Cheng, Y. M. *et al.* (2020) 'An excitation wavelength switching to enhance dual-color wide-field temporal-focusing multiphoton excitation fluorescence imaging', *Journal of Physics D: Applied Physics*, 53(23). doi: 10.1088/1361-6463/ab7acc.

Demas, J. *et al.* (2021) 'High-speed, cortex-wide volumetric recording of neuroactivity at cellular resolution using light beads microscopy', *Nature Methods*, 18(9), pp. 1103–1111. doi: 10.1038/s41592-021-01239-8.

Erbguth, K. *et al.* (2012) 'Bimodal Activation of Different Neuron Classes with the Spectrally Red-Shifted Channelrhodopsin Chimera C1V1 in *Caenorhabditis elegans*', *PLoS ONE*, 7(10). doi: 10.1371/journal.pone.0046827.

Faini, G. *et al.* (2023) 'Ultrafast light targeting for high-throughput precise control of neuronal networks', *Nature communications*, 14(1), p. 1888. doi: 10.1038/s41467-023-37416-w.

Forli, A. *et al.* (2018) 'Two-Photon Bidirectional Control and Imaging of Neuronal Excitability with High Spatial Resolution In Vivo', *Cell Reports*, 22(11), pp. 3087–3098. doi: 10.1016/j.celrep.2018.02.063.

Gajendra Kumar, N. *et al.* (2023) 'Coupling optimized bending-insensitive multi-core fibers for lensless endoscopy', *Optics Express*, 31(10), p. 15334. doi: 10.1364/oe.485550.

Gerchberg, R. W. and S. W. O. (1971) 'A Practical Algorithm for the Determination of Phase from Image and Diffraction Plane Pictures', *Optik*, 35, pp. 237–246. doi: 10.1070/qe2009v039n06abeh013642.

Hernandez, O. *et al.* (2016) 'Three-dimensional spatiotemporal focusing of holographic patterns', *Nature Communications*, 7. doi: 10.1038/ncomms11928.

Jesacher, A., Bernet, S. and Ritsch-Marte, M. (2014a) 'Colour hologram projection with an SLM by exploiting its full phase modulation range', *Optics Express*, 22(17), p. 20530. doi: 10.1364/oe.22.020530.

Jesacher, A., Bernet, S. and Ritsch-Marte, M. (2014b) 'Combined holographic optical trapping and optical image processing using a single diffractive pattern displayed on a spatial light modulator', *Optics Letters*, 39(18), p. 5337. doi: 10.1364/ol.39.005337.

Kalashyan, M. *et al.* (2012) 'Ultrashort pulse fiber delivery with optimized dispersion control by reflection grisms at 800 nm', *Opt. Express*, 20(23), pp. 25624–25635. doi: 10.1364/OE.20.025624.

Lien, C.-H. *et al.* (2017) 'Two-color temporal focusing multiphoton excitation imaging with tunable-wavelength excitation', *Journal of Biomedical Optics*, 22(2), p. 026008. doi: 10.1117/1.jbo.22.2.026008.

Lien, C.-H. *et al.* (2019) 'Simulation design of wide-field temporal-focusing multiphoton excitation with a tunable excitation wavelength', *OSA Continuum*, 2(4), p. 1174. doi: 10.1364/osac.2.001174.

Lorca-Cámara, A. *et al.* (2024) 'A multicolor two-photon light-patterning microscope exploiting the spatio-temporal properties of a fiber bundle', *Biomedical Optics Express*. doi: 10.1364/BOE.507690.

Lutz, C. *et al.* (2008) 'Holographic photolysis of caged neurotransmitters', *Nature Methods*, 5(9), pp. 821–827. doi: 10.1038/nmeth.1241.

- Marshel, J. H. *et al.* (2019) 'Cortical layer-specific critical dynamics triggering perception', *Science*, 365(6453), pp. 1–23. doi: 10.1126/science.aaw5202.
- Oldenburg, I. A., Bounds, H. A. and Pegard, N. C. (2023) 'High-Speed All-Optical Neural Interfaces with 3D Temporally Focused Holography', in *Neuromethods*, pp. 187–230. doi: 10.1007/978-1-0716-2764-8_7.
- Papagiakoumou, E. *et al.* (2008) 'Patterned two-photon illumination by spatiotemporal shaping of ultrashort pulses', *Optics Express*, 16(26), p. 22039. doi: 10.1364/oe.16.022039.
- Papagiakoumou, E. *et al.* (2010) 'Scanless two-photon excitation of channelrhodopsin-2', *Nature Methods*, 7(10), pp. 848–854. doi: 10.1038/nmeth.1505.
- Papagiakoumou, E., Ronzitti, E. and Emiliani, V. (2020) 'Scanless two-photon excitation with temporal focusing', *Nature Methods*, 17(6), pp. 571–581. doi: 10.1038/s41592-020-0795-y.
- Pégard, N. C. *et al.* (2017) 'Three-dimensional scanless holographic optogenetics with temporal focusing (3D-SHOT)', *Nature Communications*, 8(1), p. 1228. doi: 10.1038/s41467-017-01031-3.
- Shechtman, Y. *et al.* (2016) 'Multicolour localization microscopy by point-spread-function engineering', *Nature Photonics*, 10(9), pp. 590–594. doi: 10.1038/nphoton.2016.137.
- Shymkiv, Y. and Yuste, R. (2023) 'Aberration-free holographic microscope for simultaneous imaging and stimulation of neuronal populations', *Optics Express*, 31(20), pp. 33461–33474.
- Sridharan, S. *et al.* (2022) 'High-performance microbial opsins for spatially and temporally precise perturbations of large neuronal networks', *Neuron*, 110(7), pp. 1139–1155.e6. doi: 10.1016/j.neuron.2022.01.008.
- Sun, B. *et al.* (2018) 'Four-dimensional light shaping: Manipulating ultrafast spatiotemporal foci in space and time', *Light: Science and Applications*, 7(1). doi: 10.1038/lsa.2017.117.
- Tal, E., Oron, D. and Silberberg, Y. (2005) 'Improved depth resolution in video-rate line-scanning multiphoton microscopy using temporal focusing', *Optics Letters*, 30(13), p. 1686. doi: 10.1364/ol.30.001686.
- Vierock, J. *et al.* (2021) 'BiPOLES is an optogenetic tool developed for bidirectional dual-color control of neurons', *Nature Communications*, 12(1), pp. 1–20. doi: 10.1038/s41467-021-24759-5.
- Zhu, G. *et al.* (2005) 'Simultaneous spatial and temporal focusing of femtosecond pulses.', *Optics Express*. 2005/03/21, 13(6), pp. 2153–2159. doi: 83023 [pii].

D. General conclusion and future outlook

This PhD thesis aimed to develop and characterize new advanced techniques for 2P all-optical studies using fiber bundles. In this work, two new and distinct, yet interrelated, approaches were presented, each addressing challenges in the fields of 2P all-optical studies and optogenetics. The common ingredient of all these approaches is what we called inter-core delay dispersion, or in other words, the fact that the fiber bundle decomposes in time an ultrafast laser pulse travelling through multiple cores, which can be used to maintain single cell-axial resolution for extended excitation spots that have been used for both 2P imaging and 2P holographic photostimulation.

(1) A 2P fiberscope for all-optical studies in freely moving mice with single-cell axial resolution. While current systems offer the possibility to perform imaging with subcellular resolution in freely moving mice, only a few configurations are capable of combined imaging and optogenetic photostimulation. The primary focus on this thesis was the development of the first fiberscope, 2P-FENDO, capable of performing 2P calcium imaging and 2P holographic photostimulation in freely moving mice. The use of fiber bundles and their inherent ICDD, demonstrated in these fibers, allowed for fast neuronal activity recordings, at 20Hz, and high-resolution optogenetics photostimulation at brain depths of up to 160 μm , leading to the most important publication during my PhD. Additionally, we showed that new optical improvements, still ongoing in the lab, have already greatly improved the size of the accessible 2P-FENDO FOV to up to 550 μm in diameter, representing one of the largest FOVs so far achieved in the 2P regime in freely moving mice. Future technological developments of 2P-FENDO will likely lead to even larger volumetric FOVs, in deeper brain regions through endoscopy, and higher acquisition rates. 2P-FENDO holds the potential to record and manipulate neuronal activity in different brain regions with single-cell resolution, enabling the study of behaviors related to orientation, navigation, complex motor tasks, and social interaction, among others. Especially with the larger FOV now available, as shown in the last part of chapter 2, 2P-FENDO is capable of imaging ~ 100 neurons and stimulating > 20 neurons in freely moving mice, capabilities that already match what is typically done in all-optical experiments in head fixed mice.

(2) A simple 2P multicolor microscope for 3D light targeting. This strategy offers a simplified alternative to typical 3D scanless light targeting systems with TF by substituting the diffraction grating with a fiber bundle. This approach enables to couple multiple laser wavelengths

in the same path to achieve 3D light patterning with a single SLM. I have showed through simulations that this property derives from the random phase that is imprinted by the propagation through multiple cores of the fiber bundle. We conducted a characterization of SPM effects in the fiber bundles to find the values for which the power per core does not considerably enlarge the laser pulse duration. These measurements were then use to derived the system's capabilities in terms of maximum FOV, which is limited by the SLM used and the excitation objective, and the maximum power at the sample plane, that depends on the fiber bundle and the excitation objective. This analysis points to a tradeoff between the maximal FOV and the maximal power. For instance, larger objectives NAs increase the available power while the accessible FOV decreases. Despite this, combination of these values were found showing that this strategy can generate a sufficient number of spots with single-cell axial size in a large 3D volume. This versatile system can be used in essential experiments, including dual-color imaging and photostimulation, as well as dual-color activation and inhibition of individual neurons.

In conclusion, these projects collectively represent significant strides toward creating more precise and flexible advanced optical tools for 2P all-optical optogenetics experiments in the quest to deeper understand neuronal circuits with specific patterns and their relationship to animal behavior. These optical developments, among others, would propelled optogenetics into a new dimension in combination with recent progresses in the engineering of genetic actuators and reporters and multiphoton excitation microscopy with various illumination strategies.